Karlsruhe Institute of Technology

Martin F. Schumann

Transformation optics for optoelectronic devices

Cloaking contact fingers and enhancing light extraction

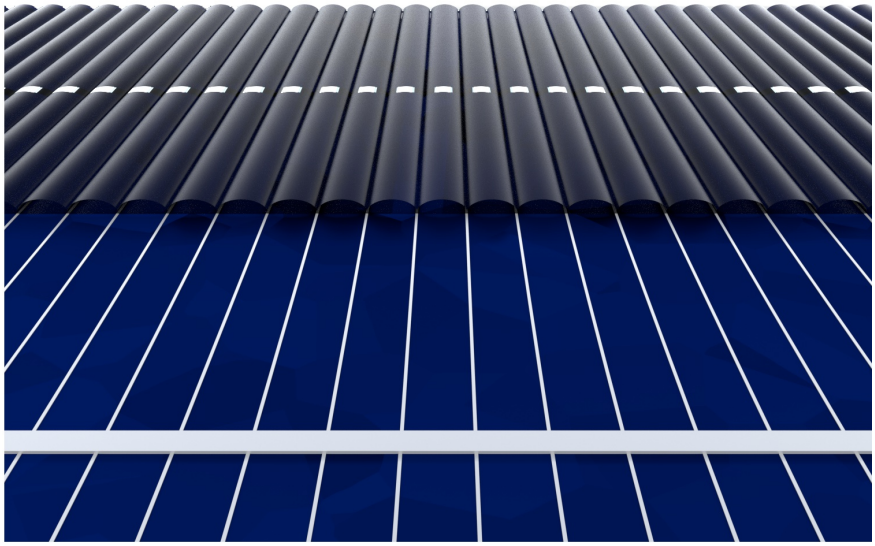

2018
Dissertation

Transformation optics for optoelectronic devices

Zur Erlangung des akademischen Grades eines
DOKTORS DER NATURWISSENSCHAFTEN
von der Fakultät für Physik des
Karlsruher Instituts für Technologie (KIT)

genehmigte

DISSERTATION

von

Martin Fabian Schumann, M.Sc.
geboren in St. Wendel

Tag der mündlichen Prüfung: 9. Februar 2018
Referent: Prof. Dr. Martin Wegener
Korreferent: Prof. Dr. Carsten Rockstuhl

Contents

Acronyms

2D two-dimensional
3D three-dimensional

ALD atomic-layer deposition

DLW direct laser writing

EQE external quantum efficiency
EVA ethylene vinyl acetate

fcc face-centered cubic
FEM finite-element method
FFS free-form surface

GRIN graded–refractive-index

HOMO highest occupied molecular orbital

IPA isopropyl alcohol
IQE internal quantum efficiency
ITO indium tin oxide

LED light-emitting diode
LUMO lowest unoccupied molecular orbital

MIBK methyl isobutyl ketone
MM metamaterial
MPP maximum-power point
MPS 3-methacryloxypropyltrimethoxysilane

OLED organic light-emitting diode
OTS octadecyltrichlorosilane

PCE power conversion efficiency

PDMS polydimethylsiloxane
PECVD plasma-enhanced chemical vapor deposition
PFOTS trichloro(1H,1H,2H,2H-perfluorooctyl)silane
PMMA poly(methyl methacrylate)

SC Schwarz-Christoffel
SEM scanning electron microscope
SHJ silicon heterojunction
SISC spatially resolved short-circuit current

TCO transparent conductive oxide
TO transformation optics

UV ultraviolet

Publications

Parts of this thesis have already been published ...
... in scientific journals:

- M. F. Schumann, S. Wiesendanger, J. C. Goldschmidt, B. Bläsi, K. Bittkau, U. W. Paetzold, A. Sprafke, R. B. Wehrspohn, C. Rockstuhl, and M. Wegener, "Cloaked contact grids on solar cells by coordinate transformations: designs and prototypes", *Optica* **2**, 850 (2015)

- M. F. Schumann, A. Abass, G. Gomard, S. Wiesendanger, U. Lemmer, M. Wegener, and C. Rockstuhl, "Single-pass and omniangle light extraction from light-emitting diodes using transformation optics", *Opt. Lett.* **40**, 5626 (2015)

- M. F. Schumann, M. Langenhorst, M. Smeets, K. Ding, U. W. Paetzold, and M. Wegener, "All-angle invisibility cloaking of contact fingers on solar cells by refractive free-form surfaces", *Adv. Opt. Mater.* **5**, 1700164 (2017)

- M. F. Schumann, B. Fritz, R. Eckstein, U. Lemmer, G. Gomard, and M. Wegener, "Cloaking of metal grid electrodes on Lambertian emitters by free-form refractive surfaces", *Opt. Lett.* **43**, 527 (2018)

... at scientific conferences (only own presentations):

- M. F. Schumann, S. Wiesendanger, J. C. Goldschmidt, B. Bläsi, K. Bittkau, U. W. Paetzold, A. Sprafke, R. B. Wehrspohn, C. Rockstuhl, and M. Wegener, "Cloaking of Metal Contacts on Solar Cells", CLEO 2015, San Jose, CA, USA, May 2015

- M. F. Schumann, A. Abass, S. Wiesendanger, C. Rockstuhl, and M. Wegener, "Cloaking of Contact Fingers on Solar Cells Enabled by Transformation Optics", OSA Light, Energy and the Environment Congress, Suzhou, China, November 2015

- M. F. Schumann, S. Wiesendanger, J. C. Goldschmidt, B. Bläsi, K. Bittkau, U. W. Paetzold, A. Sprafke, R. B. Wehrspohn, C. Rockstuhl, and M. Wegener, "Cloaked contact fingers on solar cells enabled by 3D laser lithography" (invited talk), SPIE Photonics West, San Francisco, CA, USA, February 2016

- M. F. Schumann, A. Abass, G. Gomard, S. Wiesendanger, U. Lemmer, C. Rockstuhl, and M. Wegener, "Graded photonic crystal structures for single-pass all-angle light extraction from light-emitting diodes" (invited talk), SPIE Photonics West, San Francisco, CA, USA, February 2016

- M. F. Schumann, M. Langenhorst, M. Smeets, K. Ding, U. W. Paetzold, B. Fritz, R. Eckstein, G. Gomard, and M. Wegener, "Cloaking of contacts on solar cells and OLEDs using free-form surfaces designed by coordinate transformations" (invited talk), SPIE Optics + Photonics, San Diego, CA, USA, August 2017

Additional related work has already been published ...
... in scientific journals:

- M. Schumann, T. Bückmann, N. Gruhler, M. Wegener, and W. Pernice, "Hybrid 2D–3D optical devices for integrated optics by direct laser writing", *Light Sci. Appl.* **3**, e175 (2014)

- S. Paul, V. S. Lyubopytov, M. F. Schumann, J. Cesar, A. Chipouline, M. Wegener, and F. Küppers, "Wavelength-selective orbital-angular-momentum beam generation using MEMS tunable Fabry–Perot filter", *Opt. Lett.* **41**, 3249 (2016)

- V. Lyubopytov, A. P. Porfirev, S. O. Gurbatov, S. Paul, M. F. Schumann, J. Cesar, M. Malekizandi, M. T. Haidar, M. Wegener, A. Chipouline, and F. Küppers, "Simultaneous wavelength and orbital angular momentum demultiplexing using tunable MEMS-based Fabry-Perot filter", *Opt. Express* **25**, 9634 (2017)

Chapter 1

1 Introduction

What do ancient burning glasses used several centuries BC and modern microscope or camera objectives have in common? Certainly not a lot when comparing their focusing and imaging performance, but surprisingly much when it comes to the process of designing them. In ancient times, when the physics of refraction of light was not yet understood, finding the best geometrical shape for such an optical element must have been a tedious process of trial and error. It was not until 1621 that the law of refraction was discovered by Willibrord Snellius. Even with this mathematical foundation, designing lenses largely remained a question of shaping a transparent homogeneous dielectric material. The geometrical shape needed to obtain a prescribed functionality was found in a cumbersome optimization process. This still applies today, even though the possibility to numerically simulate the behavior of the optical element has sped up the process tremendously. Strictly speaking, however, this approach of designing optics can still be considered a brute-force method. Wouldn't it be more elegant to calculate the structure of the optical element directly from the desired light path?

A novel design scheme, that is known today as transformation optics (TO), promised to offer that possibility. In essence, TO relies on the fact that light propagation is influenced by the geometry of space-time, which was already discussed in the 1920s [1, 2] after Albert Einstein's introduction of the theory of general relativity [3] in 1916. It was discovered in the 1960s and 1970s that Maxwell's equations keep their mathematical form under spatial transformations and that deformed space can alternatively be understood as a spatial distribution of material parameters [4, 5]—the key idea of TO as we know it today. Back then, however, the material parameters associated with useful spatial transformations were considered too exotic to ever be realized. Designs based on TO commonly required anisotropic magnetodielectric materials

involving near-zero, negative, or very large relative permissivity and permeability. These extreme properties are not to be found in nature, and it was not before the turn of the millennium that some of them were demonstrated to be feasible in carefully designed artificial compounds, so-called metamaterials [6]. The field was pioneered by John Pendry [7–9], who was also among the first to rediscover the concept of TO and the possibilities it offered in the dawning age of artificial materials [10]. An equally important contribution was made by Ulf Leonhardt [11], who proposed the use of conformal transformations in the TO design process [12]. This enabled the realization of a class of TO designs via a locally isotropic distribution of refractive index, facilitating experimental implementation significantly.

The new design freedom offered by the TO method was embraced by the community, and many designs offering novel optical functionality were proposed over the following decade, some of which were also realized experimentally. The range of devices included perfect lenses and collimators [13–16], lossless waveguide bends [17–20], and invisibility cloaks [21–26]. These devices impressively demonstrate the capabilities of the TO method. An application of the method outside of an academic context, however, has been rare.

Particularly, a real-world challenge not yet tackled with a transformation-optical approach is the improvement of optoelectronic devices such as solar cells or light-emitting diodes (LEDs). In the ongoing transformation toward a more ecological society, these devices have shown a large potential. Solar cells have already found widespread application for eco-friendly generation of electricity [27]. The growth of photovoltaic energy generation critically depends on the levelized costs at which the cells can provide electricity. The costs in turn are directly related to the power-conversion efficiency. Thus, maximizing efficiency of solar cells has been the aim of intense research over the past decades with new efficiency records reported every year [28].

Similarly, LED-based light sources have replaced conventional light bulbs in many applications, because they offer significantly higher efficiencies in converting electricity to light. Nevertheless, there is still a large potential to increase their efficiency even further [29, 30]. Also, especially organic light-emitting diodes (OLEDs) play an increasing role in display applications. Nevertheless, some challenges still remain, for instance when using them as large-area sources for lighting [31].

In this work, we explore the possibilities that the TO approach offers to improve optoelectronic devices, with special attention given to experimental

feasibility. The following specific questions are investigated:

1. Metallic contact fingers on solar cells are necessary for efficient extraction of the generated current, but shadow a part of the active area, hence reducing the efficiency of the cell. An optical structure guiding the incident light around the contact fingers could eliminate this shadowing loss.

2. The brightness homogeneity of large-area OLEDs can profit from metallic contacting grids that—on the other hand—cause visible shadows that may be unwanted. This issue could be remedied by an optical structure that conceals the metal grids from being seen.

3. Formation of substrate or waveguide modes in LEDs reduces their external quantum efficiency because not all the generated light can be coupled out. By eliminating Fresnel reflections at the interface between air and the substrate or LED stack, the extraction efficiency could be increased.

OUTLINE Before discussing the applications sketched above, the mathematical framework of the TO method is introduced in chapter 2, along with a brief review of band structure calculations of photonic crystals and a concise introduction to radiometry and its conservation laws.

Chapter 3 first gives an overview of the fabrication methods used for making experimental demonstrators, namely direct laser writing (DLW), soft-imprinting, and electron-beam lithography. Secondly, ray-tracing as the method of choice for numerical characterization of the investigated optical designs is introduced.

In chapter 4, the operation of solar cells is reviewed, and the effect of metallic contact fingers on their performance is outlined. Two TO-inspired approaches for optical cloaking of the contact fingers are discussed; their cloaking ability is investigated both experimentally and in detailed ray-tracing simulations.

Chapter 5 deals with metallic contact grids on OLEDs. After deriving that—under realistic conditions—this problem is equivalent to the shadowing of contact fingers on solar cells, a similar cloaking approach is applied and assessed experimentally. Remaining imperfections are analyzed via ray-tracing calculations.

In chapter 6, an optical structure is designed via TO that can provide efficient light extraction from LEDs via complete elimination of Fresnel reflections at a dielectric interface. Several modifications of the device are studied numerically.

The work is concluded by a summary of the most important results in chapter 7, along with a brief outlook.

Chapter 2

2 Fundamentals

In this chapter, the physical concepts most relevant for this work are discussed briefly. After an introduction to transformation optics, the basics of light propagation in photonic crystals are reviewed. Finally, radiometric quantities and their conservation laws are introduced.

2.1 Transformation optics

TO [10, 12] is a powerful mathematical tool enabling the design of optical devices that almost arbitrarily manipulate the propagation of light. To understand the concept, it is instructive to consider propagation of a light wave in a material with refractive index n over a small distance Δx [32]. The corresponding phase change is $\omega/c_0 n\Delta x$, where ω is the angular frequency and c_0 is the speed of light in vacuum. In an alternate coordinate system that is stretched by a factor n with respect to the original coordinate system, we expect the light to accumulate the same phase change as before, because Maxwell's equations are scale invariant. In the stretched system, however, the phase change can be expressed as $\omega/c_0\Delta x'$, where x' is the propagation distance given in the stretched coordinates. Scale invariance then dictates that $\Delta x' = n\Delta x$, yielding a relationship between spatial coordinates and a material parameter, in this simple example the refractive index n of the material.

2.1.1 Mathematical foundation

This example illustrates the basic idea behind the concept of TO. In order to end up with a cooking recipe for material parameter distributions enabling prescribed optical functionality, however, a mathematically more rigorous

treatment is necessary. In a sense, the following argumentation can be understood as a generalization of the invariance of Maxwell's equations under a *global* scaling operation: When applying a coordinate transformation, space is *locally* (and possibly anisotropically) scaled.

We start our discussion in a space that is filled with a medium described by complex tensors of relative permittivity and relative permeability, ε and μ, respectively. At a fixed frequency ω and in absence of free currents and charges, Maxwell's equations for the electric field $\boldsymbol{E}$ and the magnetic field $\boldsymbol{H}$ can be expressed as [33]:

$$\nabla \times \boldsymbol{E} + \mathrm{i}\,\omega\mu_0\mu\boldsymbol{H} = 0\,, \quad \nabla \times \boldsymbol{H} - \mathrm{i}\,\omega\varepsilon_0\varepsilon\boldsymbol{E} = 0 \tag{2.1}$$

Here, the two divergence equations are left out because they only ensure transversality of the electromagnetic waves.

Let us now turn to a second coordinate system that is obtained from the original one via the spatial mapping $\boldsymbol{x} \to \boldsymbol{x'}(\boldsymbol{x})$. The relationship between the two coordinate systems can be described in terms of the Jacobian matrix J, given by its elements

$$J_{jk} = \partial_k x'_j \equiv \frac{\partial x'_j}{\partial x_k}\,. \tag{2.2}$$

Remarkably, Maxwell's equations retain their form under the mapping transformation [5, 11, 33–35], i.e., they read

$$\nabla' \times \boldsymbol{E'} + \mathrm{i}\,\omega\mu_0\mu'\boldsymbol{H'} = 0\,, \quad \nabla' \times \boldsymbol{H'} - \mathrm{i}\,\omega\varepsilon_0\varepsilon'\boldsymbol{E'} = 0 \tag{2.3}$$

in the transformed coordinate system, where the fields and material tensors are given as

$$\boldsymbol{E'} = \left(J^{\mathrm{T}}\right)^{-1}\boldsymbol{E}\,, \quad \boldsymbol{H'} = \left(J^{\mathrm{T}}\right)^{-1}\boldsymbol{H}\,, \tag{2.4}$$

$$\mu' = J\mu J^{\mathrm{T}}/\det J\,, \quad \varepsilon' = J\varepsilon J^{\mathrm{T}}/\det J\,. \tag{2.5}$$

For a more intuitive view on the meaning of this form invariance, let's assume that the original space, which will be called *virtual space* from now on, is empty, i.e., $\varepsilon = \mu = 1$. Obviously, light propagating in this space will behave according to Maxwell's equations in vacuum. Particularly, if virtual space is flat, light will travel along straight lines, because this behavior minimizes optical path length. Form invariance implies that in a distorted space (called *physical space*) filled with a medium exhibiting the material parameters dictated

by eq. (2.5), light behaves the same way as in virtual space. For instance, if light happens to propagate along a particular coordinate axis in virtual space, it will travel along the distorted version of the axis in physical space. This correspondence of coordinate transformations and material property distributions can be exploited to design devices with specialized optical functionality, e.g. for invisibility cloaking.

The extreme freedom of design for optical devices that TO offers, however, comes at a price. The medium present in physical space has to exhibit material tensors ε and μ that follow from the chosen coordinate transformation as per eq. (2.5). As a consequence, spatially inhomogeneous coordinate mappings result in inhomogeneous spatial distributions of ε and μ, strong deformations of space automatically lead to extreme values of ε and μ, and an anisotropic transformation will translate to anisotropic material tensors. From a theoretical point of view, these aspects might not seem bothersome, but they can significantly hinder the practical implementation of transformation-optical designs.

2.1.2 *Practical material parameters*

In the following section, which loosely follows the argumentation in [36], we will explore how TO can be exploited to design devices with realizable material parameters. Implementing TO designs using only naturally occurring materials is difficult at least, because there is no straight-forward way to realize arbitrary, possibly anisotropic gradients in optical parameters. Furthermore, the range of parameter values for materials found in nature is limited to values of ε and μ above or equal unity, whereas TO designs frequently request close-to-zero or even negative material parameters. As outlined in chapter 1, at the time when TO was proposed, the emerging field of optical metamaterials (MMs) [6] received tremendous attention when demonstrating that extreme effective material parameters are feasible [37–40]. Moreover, MMs can show electrical and magnetic response with tailored anisotropy [41–45]. MMs providing these uncommon properties, however, oftentimes are based on coupling to geometric resonances [46, 47]. This has two key disadvantages: Resonances typically go hand in hand with losses due to absorption. Especially when using metals as constitutive materials, this can be a problem: For metals, dissipation due to resistive losses usually increases with frequency, so that this effect can present a major drawback in the optical regime. Another problem can be the narrow operating bandwidth that follows from the strong

dispersion around the resonance frequency.

These issues can be circumvented by restricting the discussion to coordinate transformations with special properties, most prominently conformal [12, 48] and quasi-conformal mappings [23, 36]. These mapping approaches can result in devices that (approximately) realize the TO design, but only need dielectric materials with positive permittivity. Hence, non-resonant, dielectric MMs suffice for realization, enabling low-loss and broadband operation of the TO device [49, 50]. While devices designed using (quasi-)conformal mappings are usually based on a two-dimensional geometry, they have been demonstrated to work for three-dimensional light trajectories and all polarizations under certain circumstances [15, 25, 49, 51].

CONFORMAL MAPPING Mappings are called *conformal* when they locally preserve angles. This type of mappings is particularly useful for coordinate transformations between two-dimensional domains. In the following, we therefore assume all materials and fields to be invariant along the x_3-direction. The conformal map is then characterized by its Jacobian matrix

$$J = \begin{pmatrix} \partial_1 x_1' & \partial_2 x_1' \\ \partial_1 x_2' & \partial_2 x_2' \end{pmatrix} . \tag{2.6}$$

When starting the transformation in a virtual space filled with an isotropic material, ε and μ are scalars, and eq. (2.5) becomes

$$\mu' = \frac{\mu}{\det J} \begin{pmatrix} JJ^{\mathrm{T}} & \begin{matrix} 0 \\ 0 \end{matrix} \\ \begin{matrix} 0 & 0 \end{matrix} & 1 \end{pmatrix} , \quad \varepsilon' = \frac{\varepsilon}{\det J} \begin{pmatrix} JJ^{\mathrm{T}} & \begin{matrix} 0 \\ 0 \end{matrix} \\ \begin{matrix} 0 & 0 \end{matrix} & 1 \end{pmatrix} . \tag{2.7}$$

Moreover, it has been shown that conformal mappings satisfy Laplace's equation [52]

$$(\partial_{11} + \partial_{22})\, \boldsymbol{x}' = 0 , \tag{2.8}$$

where ∂_{ij} is shorthand notation for the second partial derivative $\partial^2 / \left(\partial x_i \partial x_j\right)$. Inserting eq. (2.6) into eq. (2.7) and using eq. (2.8), we find

$$\mu' = \mu \operatorname{diag}\left(1, 1, \det J^{-1}\right) , \quad \varepsilon' = \varepsilon \operatorname{diag}\left(1, 1, \det J^{-1}\right) . \tag{2.9}$$

Here, the diag function denotes a diagonal matrix with its entries specified starting at the top left. Obviously, the in-plane part of the resulting material tensors are isotropic. For the special case of a light wave that propagates

within the $x_1'x_2'$-plane and has its electric field oriented along the x_3-axis (TE polarization), only μ_1', μ_2', and ε_3' are relevant. Hence, the TO device designed using the conformal mapping approach can be realized by a non-magnetic material with an isotropic permittivity given by

$$\varepsilon' = \varepsilon / \det J \,. \tag{2.10}$$

Complex Helmholtz equation A particularly handy formulation of eq. (2.10) can be found if light propagation is described in terms of complex spatial coordinates $u = x_1 + \mathrm{i}\, x_2$ and $\overline{u} = x_1 - \mathrm{i}\, x_2$ [12]. Here, we consider TE-polarized light to propagate within the x_1x_2-plane through an isotropic, but inhomogeneous dielectric with refractive index $n(u)$ that is invariant along the x_3-direction. Under these conditions, propagation is governed by a scalar Helmholtz equation for the out-of-plane component of the electric field,

$$\left(4\partial_{\overline{u}u} + n^2 k_0^2\right) E_3 = 0 \,, \tag{2.11}$$

where the Laplace operator $\partial_{11} + \partial_{22} = 4\partial_{\overline{u}u}$ has been expressed in terms of partial derivatives with respect to the complex variables u and $\overline{u}$ using $\partial_1 = \partial_u + \partial_{\overline{u}}$ and $\partial_2 = \mathrm{i}\,\partial_u - \mathrm{i}\,\partial_{\overline{u}}$, and k_0 denotes the free-space wave number.

Let us now consider a conformal mapping $u \to w(u) = x_1' + \mathrm{i}\, x_2'$. Conformity implies that the mapping function $w(u)$ does not explicitly depend on $\overline{u}$. Thus, we can rewrite the partial derivatives in eq. (2.11) as

$$\partial_{\overline{u}u} = \left|\frac{\mathrm{d}w}{\mathrm{d}u}\right|^2 \partial_{\overline{w}w} \,. \tag{2.12}$$

Inserting this result into eq. (2.11), we find the Helmholtz equation for w-space,

$$\left(4\partial_{\overline{w}w} + \left|\frac{\mathrm{d}u}{\mathrm{d}w}\right|^2 n^2 k_0^2\right) E_3 = 0 \,, \tag{2.13}$$

which takes the same form as in the original space. The effect of the coordinate transformation only appears in form of a modified refractive index n' related to the original one according to

$$n(u) = n'(w(u)) \left|\frac{\mathrm{d}w}{\mathrm{d}u}\right| \,. \tag{2.14}$$

SCHWARZ-CHRISTOFFEL MAPPING As discussed above, once the function $w(u)$ is given, the needed refractive-index distribution can be computed in a straight-forward way. Depending on the type of TO device to be realized, obtaining $w(u)$, for example by solving Laplace's equation, can be challenging [53]. For many problems, however, the physical and virtual domains can be approximated as polygons with a finite number of vertices, so that a Schwarz-Christoffel (SC) mapping [54] between the domains becomes possible.

Let us consider the situation sketched in fig. 2.1, where the complex half-plane $\mathrm{Im}(u) \leq 0$ shall be mapped to a polygon. The latter is specified by its complex vertices w_i and interior angles φ_i ($i = 1..N$). Note that the polygon depicted in fig. 2.1 extends from the green line toward the right, excluding the gray region. The SC map

$$w(u) = C_1 + C_2 \int^u \prod_{i=1}^{N-1} (\tilde{u} - u_i)^{\varphi_i/\pi - 1} \, \mathrm{d}\tilde{u} \tag{2.15}$$

defines a conformal mapping between the two domains. Such a mapping can be used to derive a refractive-index distribution with a prescribed optical functionality. For instance, the resulting TO device can guide incident light around the gray region (see section 4.2). In eq. (2.15), C_1 and C_2 are complex constants that need to be determined and $w(u_N = \infty) = w_N$. u_i are called *prevertices*, because they are the points in the half-plane that are mapped to the vertices of the polygon, i.e., $w_i = w(u_i)$ for $i = 1..N$. Since the w_i lie on the boundary of the domain after mapping, the u_i have to lie on the boundary of the original domain. As a consequence, the prevertices must be real.

The SC map has three degrees of freedom: one for scaling (corresponding to the magnitude of C_2), one for rotation (corresponding to the phase of C_2), and one for translation (determined by C_1 and the lower bound of integration). One of the degrees of freedom is already fixed by requiring $u_N = \infty$, so two more can be specified by choosing two more prevertices. The remaining $N - 3$ prevertices then have to be found by solving a non-linear parameter problem. In general, this is only possible using a numerical method. For instance, a specialized Matlab toolbox [55, 56] can be employed for this purpose.

For the special case of $N = 3$, i.e., the polygon being a generalized triangle, the need of solving the parameter problem vanishes. Instead, u_1 and u_2 can be specified freely (again $u_3 = \infty$), so that C_1 and C_2 become fixed and eq. (2.15)

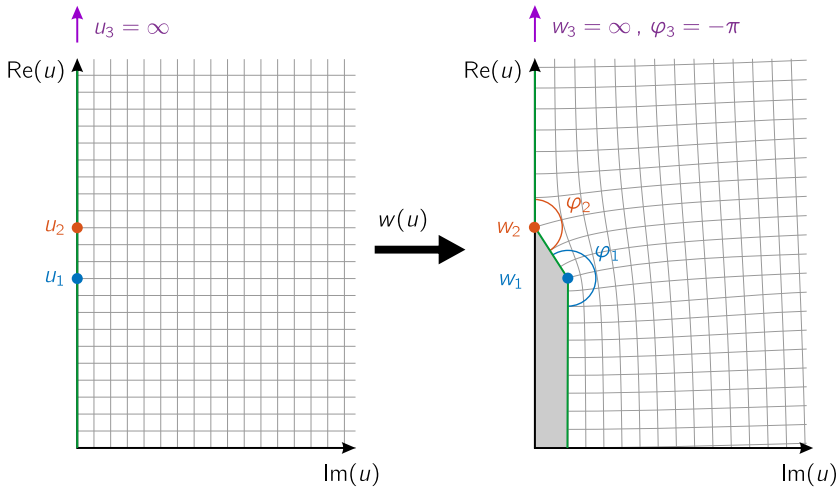

Figure 2.1: Schwarz-Christoffel mapping of the half-plane $\mathrm{Im}(u) \geq 0$ to a semi-infinite polygon, bounded by the green line. The gray region is excluded from space after transformation.

turns into the explicit equation

$$w(u) = C_1 + C_2 \frac{(-1)^{1-\alpha_1} (u-u_2)^{\alpha_2} (u_1-u_2)^{\alpha_1-2}}{\alpha_2 (1+\alpha_2)} \cdot \left[\alpha_2 (u-u_2)\, {}_2F_1\left(1-\alpha_1, 1+\alpha_2; 2+\alpha_2; \frac{u-u_2}{u_1-u_2}\right) + (1+\alpha_2)(u_1-u_2)\, {}_2F_1\left(-\alpha_1, \alpha_2; 1+\alpha_2; \frac{u-u_2}{u_1-u_2}\right)\right] \tag{2.16}$$

with the constants

$$C_1 = w_2\,,$$
$$C_2 = \frac{(-1)^{1+\alpha_1} \alpha_2 (1+\alpha_2)(w_1-w_2)(u_1-u_2)^{1-\alpha_1-\alpha_2} \Gamma(1+\alpha_1+\alpha_2)}{(1+\alpha_2)\Gamma(1+\alpha_1)\Gamma(1+\alpha_2) + \alpha_2 \Gamma(\alpha_1)\Gamma(2+\alpha_2)}\,. \tag{2.17}$$

Here, α_i is shorthand notation for φ_i/π, Γ denotes the Euler gamma function, and ${}_2F_1$ is the ordinary hypergeometric function.

Now that the mapping function $w(u)$ is fully determined, it can be translated to the refractive-index distribution that implements the designed optical functionality. Assuming that virtual space is filled with a homogeneous isotropic dielectric with refractive index n_0, the refractive index $n'(w(u))$ in physical space follows from eq. (2.14) as

$$n'(w(u)) = n(u) \left|\frac{\mathrm{d}w}{\mathrm{d}u}\right|^{-1} = \frac{n_0}{|C_2|} \left|(u-u_1)^{1-\varphi_1/\pi} (u-u_2)^{1-\varphi_2/\pi}\right|\,. \tag{2.18}$$

While the analytical treatment might seem advantageous at first sight, taking the numerical route can be more practical: For the realization of a TO device it is oftentimes sufficient to know the values of the corresponding refractive-index distribution on a discretized grid, as fabrication accuracy limits spatial resolution of the resulting structure anyway. Evaluating the analytic functions occurring in eqs. (2.16) to (2.18) on a dense grid can be computationally intensive, whereas the numerical SC toolbox is optimized for quick evaluation of the map with high numerical accuracy. For these reasons, the SC maps and corresponding refractive-index distributions computed in this work were obtained using the numerical approach.

2.2 Photonic crystals

Photonic crystals are materials that show a spatially periodic variation in their optical parameters on a length scale comparable to the wavelength of light. This periodic modulation has similar effects on photons propagating in the material as the periodic potential formed by the atomic nuclei in a solid state crystal has on its electrons. In both cases, only certain modes can propagate in the crystal, which are described by the dispersion relation $\omega(\boldsymbol{k})$. The modes can form bands that are separated energy-wise. Electrons / photons with energies between the band edges are therefore disallowed to propagate. If a band separation is observed for all possible propagation directions, it is called a *(photonic) band gap*, while it is termed a *stop band* otherwise. Since the pioneering work of Sajeev John [57] and Eli Yablonovitch [58] in 1987, the unique properties of photonic crystals have been exploited to enable a multitude of different applications [59–65].

In this work, three-dimensional photonic crystals were used in the long-wavelength limit to realize the refractive-index distributions designed by conformal mapping. For wavelengths much longer than the crystal periodicity, the light cannot resolve the internal structure of the crystal. Thus, light propagation can be described by effective material parameters—in our case of a purely dielectric photonic crystal by an effective refractive index n_{eff}. The latter can be calculated from the group velocity in the medium, v_{g}, via

$$\frac{c_0}{n_{\mathrm{eff}}} = v_{\mathrm{g}} = \frac{\partial \omega}{\partial |\boldsymbol{k}|}, \tag{2.19}$$

where isotropic dispersion is assumed. Equation (2.19) indicates that once the dispersion relation is known, the effective refractive index can be calculated.

The method to obtain the dispersion relation in a photonic crystal is outlined in the following section, where the argumentation follows that in [66].[1] To simplify the treatment, we assume that the constitutive materials of the photonic crystal are homogeneous and isotropic, so that their material properties become scalar functions $\varepsilon(\boldsymbol{x})$ and $\mu(\boldsymbol{x})$ that vary according to the crystal periodicity. Again, we start with the time-harmonic Maxwell equations for fixed frequency ω (eq. (2.1)), from which we derive the wave equation

$$\nabla \times \left(\frac{1}{\varepsilon(\boldsymbol{x})} \nabla \times \boldsymbol{H}(\boldsymbol{x}) \right) = \left(\frac{\omega}{c_0} \right)^2 \mu(\boldsymbol{x}) \boldsymbol{H}(\boldsymbol{x}) \,. \tag{2.20}$$

At optical frequencies natural materials are non-magnetic, so we can let $\mu(\boldsymbol{x}) = 1$. Furthermore, we can understand the left-hand side of eq. (2.20) as an operator $\hat{O}$ acting on $\boldsymbol{H}(\boldsymbol{x})$. Like that, we obtain the eigenvalue equation

$$\hat{O}\boldsymbol{H}(\boldsymbol{x}) = \left(\frac{\omega}{c_0} \right)^2 \boldsymbol{H}(\boldsymbol{x}) \,. \tag{2.21}$$

Solutions to this eigenvalue equation are the modes that propagate in the photonic crystal, specified by their spatial distribution of the magnetic field $\boldsymbol{H}(\boldsymbol{x})$ (corresponding to the eigenvectors) and their squared angular frequency ω (proportional to the eigenvalues). Once $\boldsymbol{H}(\boldsymbol{x})$ is known, the distribution of the electric field can be computed from eq. (2.1).

For solid-state crystals, the corresponding eigenvalue equation is the one-electron Schrödinger equation. This equation can be solved by employing a Bloch ansatz that exploits the periodicity of the potential. The same treatment can be applied here to find solutions to eq. (2.21), since the permittivity is periodic in lattice vectors $\boldsymbol{X}$, i.e.,

$$\varepsilon(\boldsymbol{x} + \boldsymbol{X}) = \varepsilon(\boldsymbol{x}) \,, \quad \boldsymbol{X} = \sum_i c_i \boldsymbol{a_i} \,. \tag{2.22}$$

Here, $\boldsymbol{a_i}$ are the primitive vectors of the Bravais lattice generating the photonic crystal. In analogy to the electronic case, solutions to the eigenvalue equation can be written as the product of a complex exponential function and a lattice-periodic function $\boldsymbol{u}_{km}(\boldsymbol{x})$, i.e.,

$$\boldsymbol{H}_{km}(\boldsymbol{x}) = \boldsymbol{u}_{km}(\boldsymbol{x}) \exp(\mathrm{i}\, \boldsymbol{k}\boldsymbol{x}) \,. \tag{2.23}$$

[1] A more detailed discussion can be found in [67].

As indicated by the band index m, several solutions exist for a given $\boldsymbol{k}$-point, corresponding to the different bands. Using the Bloch ansatz, eq. (2.21) can be solved for its eigenvalues, yielding the dispersion relations $\omega_m(\boldsymbol{k})$ of the individual bands. Plotting the band dispersions in the first Brillouin zone, one obtains the band structure of the photonic crystal.

While for very simple geometries the band structure can be found analytically, in most cases a numerical solution of eq. (2.21) is necessary. All band dispersions computed in this work were obtained using the MIT Photonic Bands package [68].

2.3 Radiometry

Radiometry summarizes a set of physical quantities that measure electromagnetic radiation. Radiometric quantities and corresponding conservation laws are essential to the field of astronomy, for instance. In this work, some radiometric concepts will be used to describe brightness transfer when imaging an emitting surface. The definitions presented in this section are taken from [69].

2.3.1 *Radiometric quantities*

The most basic quantity in radiometry is the radiant energy that is received, emitted, reflected, or transmitted per unit time. This quantity is called *radiant flux* Φ and is measured in W. For many problems (including the current density generated by a solar cell), it is not the total flux that is the relevant quantity, but the radiant flux that is received per unit area, called *irradiance* or *flux density* E. It is measured in $\mathrm{W\,m^{-2}}$ and is defined as the derivative

$$E = \frac{\mathrm{d}\Phi}{\mathrm{d}A}\,, \tag{2.24}$$

where $\mathrm{d}\Phi$ is the infinitesimal flux element received by the surface element $\mathrm{d}A$. Instead of relating the radiant flux to the receiving area, it can be normalized to the solid angle Ω that the flux is emitted to or received from. This form of description is especially useful to quantify the angular emission profile of point-like light sources. The corresponding directional quantity, *radiant*

intensity[2] I is defined as [69]

$$I = \frac{\mathrm{d}\Phi}{\mathrm{d}\Omega} \tag{2.25}$$

and measured in $\mathrm{W\,sr^{-1}}$. Yet another quantity, *radiance* L, is a measure for the radiant flux emitted, received, reflected, or transmitted per unit solid angle per unit projected area of a surface. Radiance can be understood as the flux received by an optical system with a given entrance pupil that views an extended light source (e.g. an emitting surface) from a certain direction. Generally, radiance is defined as

$$L = \frac{\mathrm{d}^2\Phi}{\mathrm{d}\Omega\,\mathrm{d}A\cos\theta}\,, \tag{2.26}$$

and is measured in $\mathrm{W\,sr^{-1}\,m^{-2}}$. In the given example, Ω is the solid angle subtended by the entrance pupil and θ is the angle between the source surface normal and the viewing direction. For a general light source, L is a directional quantity, i.e., it varies with θ and the azimuthal viewing angle. In the special case that L does not depend on the viewing direction, the reflecting, transmitting, or emitting surface is called *Lambertian*. As the flux received by an imaging system (e.g. the human eye) directly determines the perceived brightness of the viewed object, this angle-independence means that a Lambertian surface looks equally bright from any direction. For a Lambertian emitter, the radiant intensity profile $I_\mathrm{L}(\theta)$ can be computed by integrating the radiance over the projected emitting area, yielding

$$I_\mathrm{L}(\theta) = \frac{\mathrm{d}\Phi}{\mathrm{d}\Omega} = \int_A L\cos\theta\,\mathrm{d}A = I_0\cos\theta\,, \tag{2.27}$$

where $I_0 = LA$.

2.3.2 Conservation laws

As we will see in the following, (basic) radiance is a conservation quantity under certain circumstances. This fact can be used to simplify the computation of radiation transfer through an optical system significantly. To derive the conservation law, we consider an emitting surface with a given radiance distribution $L_0 = L_0(\boldsymbol{r_0}, \theta_0)$. Let the surface radiate into a medium with

[2] In radiometric literature and in this thesis, the term *intensity* is used consistently to describe flux per solid angle. In other fields of physics, however, "intensity" may denote several other quantities, including radiance, irradiance, or exitance.

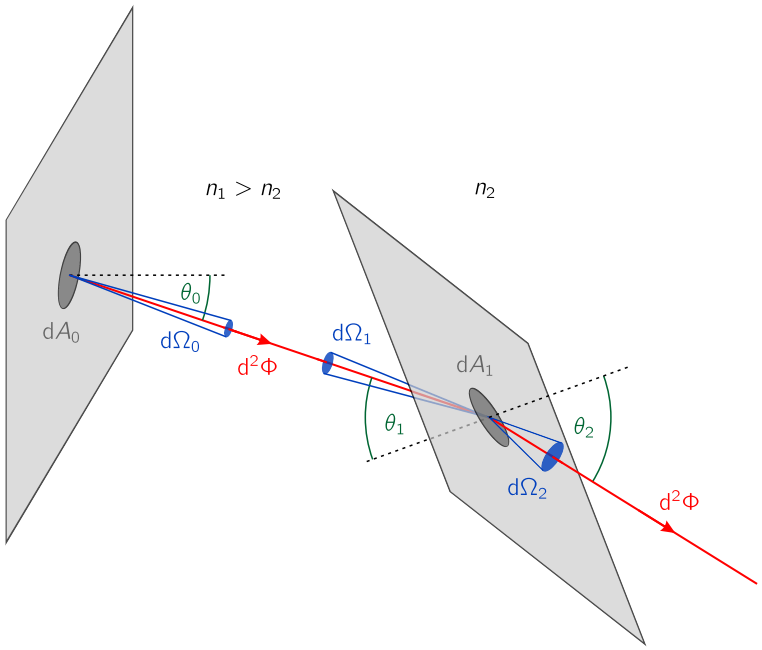

Figure 2.2: Geometry considered for the derivation of conservation of (basic) radiance.

refractive index n_1 toward a second surface, as depicted in the left part of fig. 2.2. A radiant flux $\mathrm{d}^2\Phi$ is radiated from the surface element $\mathrm{d}A_0$ into the solid angle element $\mathrm{d}\Omega_0$, corresponding to an area element $\mathrm{d}A_1$ on the second surface. Per definition,

$$L_0 = \frac{\mathrm{d}^2\Phi}{\mathrm{d}\Omega_0 \, \mathrm{d}A_0 \cos\theta_0} \,. \tag{2.28}$$

At the same time, the radiance received at $\mathrm{d}A_1$ from solid angle element $\mathrm{d}\Omega_1$ becomes

$$L_1 = \frac{\mathrm{d}^2\Phi}{\mathrm{d}\Omega_1 \, \mathrm{d}A_1 \cos\theta_1} \,. \tag{2.29}$$

In homogeneous, absorption-free media the optical flux $\mathrm{d}^2\Phi$ is conserved, so that

$$\begin{aligned} \mathrm{d}^2\Phi &= L_0 \, \mathrm{d}\Omega_0 \, \mathrm{d}A_0 \cos\theta_0 \\ &= L_1 \, \mathrm{d}\Omega_1 \, \mathrm{d}A_1 \cos\theta_1 = \mathrm{d}^2\Phi \,. \end{aligned} \tag{2.30}$$

The solid angle elements can be expressed as

$$\mathrm{d}\Omega_0 = \frac{\mathrm{d}A_1 \cos\theta_1}{R^2} \,, \quad \mathrm{d}\Omega_1 = \frac{\mathrm{d}A_0 \cos\theta_0}{R^2} \,, \tag{2.31}$$

where R denotes the distance between the two surface elements. Using these geometric relations, eq. (2.30) yields $L_0 = L_1$, i.e., radiance is conserved along rays within homogeneous, absorption-free media.

But what happens to radiance once the light ray crosses an interface between two media with different refractive indices? To answer this question, it is instructive to consider the situation sketched in the right part of fig. 2.2, where a ray of light is refracted at the interface between two homogeneous media with refractive indices n_1 and $n_2 < n_1$.

In spherical coordinates, the relevant solid angle elements can be expressed as

$$\mathrm{d}\Omega_i = \sin\theta_i \,\mathrm{d}\theta_i \,\mathrm{d}\Phi_i \,, \tag{2.32}$$

where $i = 1, 2$ and Φ_i is the azimuthal angle element. The refracted ray stays in the plane of incidence, so that $\mathrm{d}\Phi_1 = \mathrm{d}\Phi_2$. Thus, the ratio of solid angle elements simplifies to

$$\frac{\mathrm{d}\Omega_1}{\mathrm{d}\Omega_2} = \frac{\sin\theta_1 \,\mathrm{d}\theta_1}{\sin\theta_2 \,\mathrm{d}\theta_2} \,. \tag{2.33}$$

Refraction at the interface obeys Snell's law

$$n_1 \sin\theta_1 = n_2 \sin\theta_2 \,, \tag{2.34}$$

which is differentiated to yield

$$n_1 \cos\theta_1 \,\mathrm{d}\theta_1 = n_2 \cos\theta_2 \,\mathrm{d}\theta_2 \,. \tag{2.35}$$

Equations (2.34) and (2.35) are used to express the ratio of sines and the angle elements $\mathrm{d}\theta_i$ in eq. (2.33):

$$\frac{\mathrm{d}\Omega_1}{\mathrm{d}\Omega_2} = \frac{n_2^2 \cos\theta_2}{n_1^2 \cos\theta_1} \,. \tag{2.36}$$

Using eqs. (2.26), (2.29) and (2.36), we find

$$\begin{aligned} L_2 &= \frac{\mathrm{d}^2\Phi}{\mathrm{d}A_1 \cos\theta_2 \,\mathrm{d}\Omega_2} \\ &= \frac{L_1 \,\mathrm{d}\Omega_1 \,\mathrm{d}A_1 \cos\theta_1}{\mathrm{d}\Omega_2 \,\mathrm{d}A_2 \cos\theta_2} \\ &= L_1 \frac{n_2^2}{n_1^2} \,. \end{aligned} \tag{2.37}$$

Obviously, the quantity L_i/n_i^2, called *basic radiance*, is conserved upon refraction at an interface between two media. Note that in the derivation, again Fresnel reflections at the interface were neglected, so that $\mathrm{d}^2\Phi$ is conserved.

Conservation of basic radiance is closely related to conservation of *etendue*, a quantity characterizing the geometric extent of light in an optical system. To define etendue, the situation sketched in the right part of fig. 2.2 is considered. Here, the light confined to solid angle $\mathrm{d}\Omega_1$ in the material with refractive index n_1 passing area element $\mathrm{d}A_1$ is assigned the etendue

$$\mathrm{d}G = n_1^2 \, \mathrm{d}\Omega_1 \, \mathrm{d}A_1 \cos\theta_1 \, . \tag{2.38}$$

The purely geometric factor $\mathrm{d}\Omega_1 \, \mathrm{d}A_1 \cos\theta_1$ can also be understood as the volume in phase space (the product of spatial and angular space) occupied by the light. Comparing the definition of etendue to eq. (2.29), we find a relationship connecting basic radiance, etendue, and flux as

$$\mathrm{d}\Phi = \mathrm{d}G \frac{L_1}{n_1^2} \, . \tag{2.39}$$

As has been discussed above, basic radiance L_1/n_1^2 and radiant flux $\mathrm{d}\Phi$ are conserved along rays propagating through an ideal optical system (in which absorption, scattering, and Fresnel back-reflections are absent). Therefore, it follows that the etendue of the light, $\mathrm{d}G$, is a conserved quantity as well. Note that imperfections in the optical system, such as scatterers, can increase etendue, because they increase the angular spread of light. Decreasing etendue is fundamentally impossible in a passive optical system, as this would correspond to decreasing entropy, which is forbidden by the second law of thermodynamics [70].

Optical systems can be characterized by the largest ray bundle that is transmitted through them. Hence, a certain volume in phase space can be attributed to the optical system that follows from its geometry. The system can be populated with light until all the phase space it offers is occupied. Light with etendue $\mathrm{d}G$ transported through the system can be understood to occupy a phase space volume given by eq. (2.38) as $\mathrm{d}G/n_1^2$. Thus, more light can "fit" in higher-index media.

As a simple illustration of this notion, let us consider the interface between two half-spaces filled with homogeneous dielectrics of refractive indices n_1 and $n_2 < n_1$. Let the interface be completely absorbing except for a window region with a size $\mathrm{d}A$. Since the geometry of the two half-spaces is identical,

they offer the same phase space volumes. As a consequence, if phase space in the high-index region is completely filled, conservation of etendue of light across the interface forbids that all the light be transmitted to the low-index region, because light would need a larger phase space volume there. This manifests in the well-known phenomenon of total internal reflection, trapping a part of the light in the high-index half-space.

REDUCING DIMENSIONALITY While the above derivation has been based on a three-dimensional problem, it can sometimes be useful to limit discussion to two spatial dimensions. In that case, all solid angle elements $\mathrm{d}\Omega_i$ have to be replaced by angle elements $\mathrm{d}\theta_i$, so that eq. (2.35) can be used directly to find the two-dimensional (2D) version of eq. (2.36), reading

$$\frac{\mathrm{d}\theta_1}{\mathrm{d}\theta_2} = \frac{n_2 \cos\theta_2}{n_1 \cos\theta_1} \,. \tag{2.40}$$

Using this result while calculating the ratio of radiances L_i, we find

$$L_2^{(2\mathrm{D})} = L_1^{(2\mathrm{D})} \frac{n_2}{n_1} \,, \tag{2.41}$$

meaning that in two dimensions, the ratio of radiance and the (un-squared) refractive index, L_i/n_i, is conserved upon refraction. Accordingly, two-dimensional etendue is defined as

$$\mathrm{d}G^{(2\mathrm{D})} = n_i \,\mathrm{d}A_i \cos\theta_i \,\mathrm{d}\theta_i \quad (i = 1, 2) \,. \tag{2.42}$$

3 Chapter 3 Methods

In the following, an overview of the experimental and numerical methods most prominently used in this work is given: electron beam lithography, direct laser writing, and soft-imprinting as the main fabrication methods and ray-tracing in homogeneous and inhomogeneous media as the method of choice for simulation of the investigated TO devices.

3.1 Direct laser writing

Direct laser writing, also frequently called *two-photon polymerization*, is a three-dimensional (3D) printing technique that allows for structuring polymers in three spatial dimensions, with feature sizes well below 1 µm. Since its introduction in 2001 [71], the concept has been applied to fabricate a multitude of different functional devices, including 3D metamaterials [25, 72–78], 3D scaffolds for biological applications [79–83], microoptical [84–88], and microfluidic [89, 90] devices.

Principle The working principle of DLW is based on non-linear absorption of light in a liquid photoresist. Upon exposure using a tightly focused femtosecond-pulsed laser, the photoresist solidifies only in the laser focus, enabling the realization of spatially distinct features. Photoresists used for DLW typically consist of a monomer (for example a multi-functional acrylate) and a photoinitiator. Solidification of the photoresist happens in a two-step process: After a photosensitive initiator molecule is excited by the impinging light, it generates a radical molecule that initiates polymerization of the monomer.

The photoinitiator is chosen such that its absorption cross-section is negligible at the operation wavelength of the laser (usually close to 800 nm), and

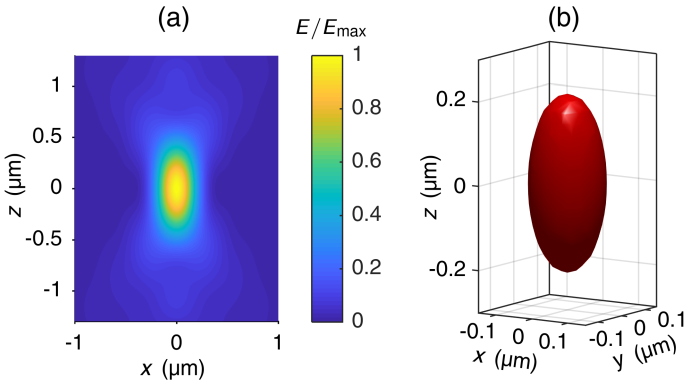

Figure 3.1: Calculated laser irradiance and voxel shape in DLW for an objective with NA $= 1.4$, immersed in a medium with $n = 1.5$, and a vacuum wavelength of $\lambda = 780\,\mathrm{nm}$. z is the optical axis; calculation followed the method proposed in [91]. (a) Irradiance distribution $E(x,z) \propto |\boldsymbol{E}(x,z)|^2$ around the focus. (b) Iso-surface ($E^2 = 2/3 E^2_{\mathrm{max}}$) of the squared irradiance distribution, representing the typical shape of a voxel.

much larger around half the wavelength. Like this, one-photon absorption in the photoinitiator is strongly suppressed and two-photon absorption becomes the dominant absorption mechanism. Thus, the probability to excite the initiator in a given duration is proportional to the squared irradiance. Since irradiance shows a maximum in the center of the laser focus (fig. 3.1(a)), excitation probability is highest there, too. Additionally, polymerization can be regarded as a threshold process. Only regions of the photoresist that have been exposed with a dose higher than a certain threshold form a polymer cross-linked strongly enough to withstand the subsequent development step.

Together with the non-linear response of the initiator, the thresholded polymerization leads to a spatial confinement of the solidification to a volume around the laser focus that is bounded by an iso-surface of the squared irradiance, as shown in fig. 3.1(b). This *voxel*, the three-dimensional analog to a pixel, is the elementary building block of DLW. By moving the voxel during exposure, almost arbitrary three-dimensional trajectories can be polymerized.

LIMITATIONS While it is not the focus of this work to investigate or improve DLW as a method, its limitations in terms of spatial resolution became apparent in several experimental results. Therefore, a brief overview of the effects leading to resolution limitations is given in the following.

In principle, the smallest achievable voxel size is not limited by diffraction, but is solely determined by the choice of exposure dose relative to the poly-

merization threshold. If the dose is set just below the threshold, the voxel size can become arbitrarily small. Moreover, there is no fundamental limit as to how close to each other two distinguishable voxels can be polymerized in two subsequent exposures.

In practice, however, polymerization thresholds of common photoresists are not perfectly sharp, but smeared out, leading to a finite minimum voxel size. And even more importantly, typical photoresists seem to "remember" sub-threshold doses, so that doses can accumulate across subsequent exposures. As a consequence, the resolution of DLW becomes effectively limited by diffraction. To quantify resolution, Sparrow's criterion [92] can be applied. Originally formulated for spectroscopy, it states that two adjacent lines can be resolved as long as the corresponding irradiance distribution features a local minimum in the center. In lithography, the criterion can be understood as follows: Two point-like, spatially separated features will appear distinct after exposure if the response of the photoresist shows a local minimum upon exposure with the two corresponding point-spread functions. Considering a resist response based on two-photon absorption, one can find approximations for the lateral and axial resolution limits [93]

$$\begin{aligned} a_{12} &\gtrsim \frac{\lambda}{2\sqrt{2}\mathrm{NA}} \approx 200\,\mathrm{nm}\,, \\ a_3 &\gtrsim \frac{\lambda}{\sqrt{2}\left(n - \sqrt{n^2 - \mathrm{NA}^2}\right)} \approx 600\,\mathrm{nm}\,. \end{aligned} \tag{3.1}$$

Here, λ denotes the vacuum wavelength of the laser light used for exposure and $\mathrm{NA} = n \sin \alpha$ is the numerical aperture of the objective used for focusing, where n is the refractive index of the immersion medium and α is the maximum collection half-angle of the objective. The numbers stated in eq. (3.1) were found for typical DLW conditions ($\lambda = 780\,\mathrm{nm}$, $\mathrm{NA} = 1.4$, $n = 1.52$).

Another effect comes into play when exposing a pair of lines that are separated by more than the minimum separation discussed above. Despite the larger distance, an influence of the line written first on the second line is commonly observed. Typically, the second line becomes wider than the first line or random tiny connections between the lines form [94, 95]. In analogy to electron-beam lithography [96], these observations are summarized as *proximity effect*. The cause for line broadening specifically has recently been found to be diffusion of radical molecules or oxygen[1] between adjacent,

[1]The cross-linking chain reaction taking place during solidification of the photoresist

sequentially exposed features [97].

DLW is a very convenient scheme to fabricate polymeric devices on, e.g., glass substrates. However, since DLW is an optical method, the writing process can be influenced by the optical properties of the substrate. More specifically, a non-negligible reflectance of the substrate can cause detrimental effects: Focusing the writing laser close to the resist-substrate interface may lead to interference of the laser beam with its reflection, producing a standing wave pattern in the irradiance distribution. Like this, the local exposure dose oscillates strongly along the axial direction, leading to an oscillation in cross-linking density. For very strong oscillations (occurring for strongly reflective substrates and low exposure powers) a structure designed as a bulk block can turn into individual, disconnected polymer layers that delaminate during development. If interference is less pronounced, a periodic corrugation at the surface of the fabricated structures can be observed (see fig. 4.17 for instance).

While delamination is primarily caused by the minima of the standing wave pattern, constructive interference can also have effects detrimental to structure quality. At the positions of irradiance maxima, the exposure dose is amplified, leading to overexposure of the photoresist. As a consequence, the resist can heat up locally by several hundred Kelvins, causing microexplosions, i.e., the monomer locally evaporates and forms gas bubbles in the liquid resist [98]. Due to strong refraction and reflection at the bubbles, deterministic focusing of the laser is prevented in their vicinity. To avoid the deteriorations of structural quality that come along with overexposure, the laser power is usually reduced when writing features close to a strongly reflective substrate. For bare substrates (e.g. silicon wafers), the power compensation can be applied globally. Once DLW shall be used to add polymer structures to a pre-patterned substrate, however, power compensation has to be adjusted to the *local* reflectivity. This can be very challenging for substrates with pronounced spatial variations in reflectivity (e.g. silicon with metallic contact fingers). For this reason, a soft-imprinting scheme (section 3.2) was applied to fabricate the polymeric free-form surfaces on solar cells and OLEDs discussed in section 4.4 and chapter 5.

is terminated by oxygen. Therefore, the presence of oxygen and oxygen diffusion play an important role in the polymerization process.

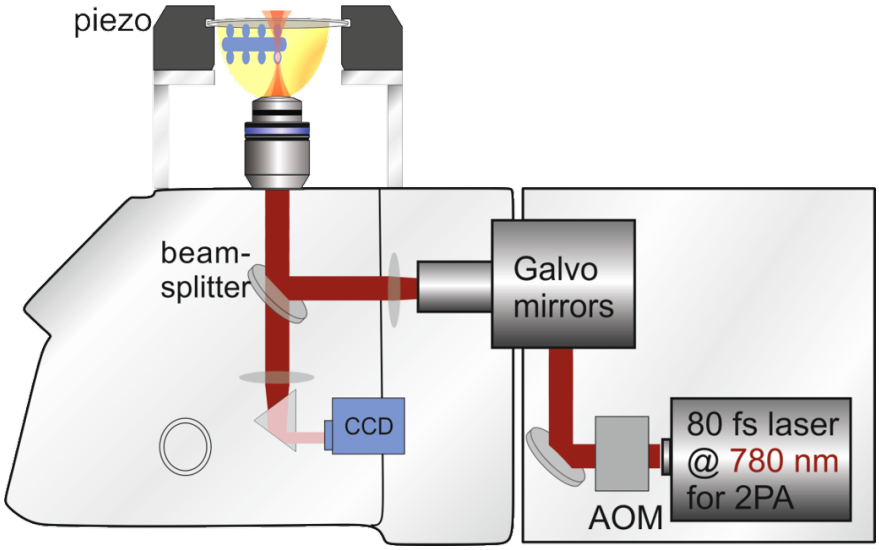

Figure 3.2: Schematic structure of the Photonic Professional GT system used for DLW. Image courtesy of Nanoscribe GmbH.

SETUP In this work, a commercial DLW setup (Photonic Professional GT, Nanoscribe, Germany) was employed (fig. 3.2). The instrument is based on a near-infrared femtosecond pulsed laser source with a central emission wavelength of 780 nm. The beam is fed into a microscope body and then focused to the substrate using an immersion objective. The objective is immersed in the photoresist (so-called dip-in configuration) and looks at the substrate from below, so that fabricated structures are written to the bottom side of the substrate. In order to anchor the structures to the substrate in a controlled fashion, the instrument features an optical interface finder that is able to precisely determine the axial position of the interface between substrate and photoresist. As the interface finding routine is based on reflection at the interface, it only works reliably if there is a sufficient difference in refractive indices of substrate and photoresist.

Before entering the microscope body, the laser beam passes an acousto-optic modulator (AOM) that controls the laser irradiance. A galvanometric mirror system enables rapid lateral scanning (typically $1\,\mathrm{cm\,s^{-1}}$ to $10\,\mathrm{cm\,s^{-1}}$) of the laser focus within a field of view of a few hundred micrometers in diameter. As the galvanometric mirrors cannot scan the laser focus along the axial direction, the substrate is moved by a piezo stage instead to provide access to the third dimension. The piezo stage moves relatively slow (around $100\,\mu\mathrm{m\,s^{-1}}$) compared to the lateral scan speed. Therefore, 3D structures are

sliced into lateral layers that are exposed consecutively.

Structures larger than the field of view are split into smaller parts that fit into a single writing field. These parts are written one after another, using a linear stage to displace the substrate laterally when advancing from one field to the next. This stitching procedure allows fabricating samples with lateral dimensions of several mm^2 within few hours, depending on the structure height and desired fabrication accuracy.

WORKFLOW The typical protocol followed in this work for fabricating samples by DLW is detailed in the following list. All the samples were treated with 3-methacryloxypropyltrimethoxysilane (MPS) before the polymer writing [80]. The silanization step is employed to increase adhesion between the substrate and the fabricated polymer structures: While the silane side of MPS covalently bonds to OH-groups present at the substrate surface (typically SiO_2) after plasma activation, the methacrylate group is incorporated via radical polymerization into the acrylate network that forms during DLW. Thus, MPS establishes a covalent bond between the fabricated polymer structure and the substrate [99, 100].

1. Cleaning the substrate: The substrate[2] was wiped with isopropyl alcohol (IPA) using a paper towel, then blown dry using a nitrogen gun.

2. Silanization for adhesion promotion: The substrate was activated in air plasma for 15 min, then immersed in a 1 mM solution of MPS in toluene for 1 h. Excess silane was washed away in toluene, followed by a rinse in IPA. Finally, the substrate was blown dry using a nitrogen gun.

3. Writing the polymer structure: Photoresist was drop-cast onto the substrate, which was then inserted into the DLW instrument. Two combinations of photoresists and objectives were used in this work: IP-S was written using a 25×/0.8 NA objective (LCI Plan-Neofluar Imm Corr DIC, Carl Zeiss Microscopy, Germany), while IP-Dip was used with a 63×/1.4 NA objective (Plan-Apochromat Oil DIC, Carl Zeiss Microscopy, Germany). Both resists were bought from Nanoscribe and were written in dip-in configuration. For structure designs featuring large solid volumes the shell-writing technique was applied to reduce fabrication time.

[2] In this work, two types of substrates were used: either 700 µm thick glass with an additional layer of indium tin oxide ($n \approx 1.7$) to simplify interface finding (Nanoscribe, Germany), or 525 µm thick n-doped silicon (Siegert Wafer, Germany)

Only a several µm thick outer shell of the structure was exposed along with a stabilizing scaffold in the inside, leaving the largest portion of the interior unexposed.

4. Developing: Excess photoresist was washed away in a bath of mr-Dev 600 (Micro Resist Technology, Germany) for 20 min to 30 min, followed by a brief rinse in IPA. Drying was carried out using a nitrogen gun.

5. UV-curing: The shell-written structures were exposed to ultraviolet (UV) light for 5 min at an approximate irradiance of 50 mW cm^{-2} to solidify the photoresist that remained unexposed during the DLW step. As a light source, a WEPUV3-S2 light-emitting diode (Winger Electronics, Germany) with its emission peak at a wavelength of 400 nm was employed.

3.2 Soft-imprinting

As discussed above, several challenges arise when applying DLW to print polymeric devices onto pre-structured substrates. To avoid these difficulties, the refractive free-form surfaces developed in this work to cloak contact fingers on solar cells and OLEDs were not printed onto the respective substrates via DLW directly. Instead, the samples were fabricated by a sequence of DLW of a master structure, a two-step polydimethylsiloxane (PDMS) replication and soft-imprinting. The process is schematically shown in fig. 3.3 and described in detail in the following.

1. The inverted structure was printed onto an ITO-covered glass substrate using the standard DLW procedure described above. The photoresist IP-S and the 25×/0.8 NA objective were employed here.

2. 20 nm of Al_2O_3 were conformally deposited onto the resulting polymer master using atomic-layer deposition (ALD) to enable subsequent silanization. This step was carried out in a Savannah ALD system (Cambridge Nanotech, USA). The material was grown at 150 °C using trimethylaluminum and water as precursors.

3. The alumina-covered polymer master was activated in air plasma for 1 min and immersed in a 3 mM solution of octadecyltrichlorosilane (OTS)

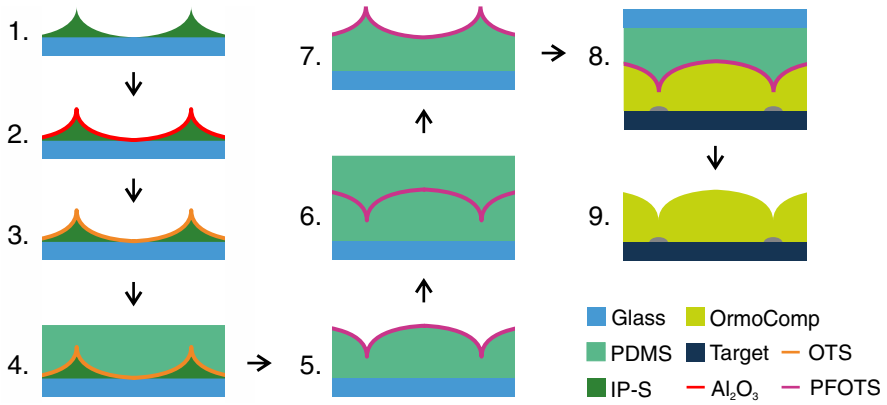

Figure 3.3: Soft-imprinting scheme. Adapted with permission from [101], © 2017 WILEY-VCH Verlag GmbH & Co. KGaA, Weinheim.

in toluene for 5 min. Excess silane was rinsed off in consecutive toluene and IPA baths. The sample was then dried using a nitrogen gun. Similar to MPS, the silane used here can covalently bond to the substrate surface. OTS, however, was used to turn the surface hydrophobic and thus make it antiadhesive to PDMS.

4. PDMS needed for replication of the master was prepared by mixing Sylgard 184 Elastomer Base and the corresponding thermal curing agent (ratio 10:1 by weight; both from Dow Corning, USA). The mixture was degassed in vacuum for 30 min and poured over the silanized master. For curing, the PDMS was placed on a hot plate at 60 °C for 2 h.

5. The PDMS replica was removed from the master and silanized with antiadhesive silane before the next replication step. While OTS would provide the desired antiadhesive effect, it cannot be applied to the PDMS replica from a toluene solution, as toluene leads to strong, partly irreversible swelling of PDMS. Therefore, trichloro(1H,1H,2H,2H-perfluorooctyl)silane (PFOTS), which can be deposited from the gas phase, was applied. First, the surface of the replica was activated in air plasma for 30 s. Then, a solution of 0.3 vol% PFOTS in cyclohexane was prepared. A 20 µL droplet of the solution was kept in vacuum (650 mbar below atmosphere) together with the PDMS replica for 2 h.

6.–7. After PFOTS silanization was complete, the PDMS replication step was repeated using the previously fabricated PDMS replica as a master.

Through this double-replication process, a PDMS replica of the original polymer master made by DLW was obtained.

8.–9. In the following soft-imprinting step, 60 µL to 70 µL of the UV-curable transparent OrmoComp photoresist (micro resist technology, Germany) were drop-cast onto the substrate. The PDMS stamp was aligned to the pre-fabricated structures on the substrates and pushed into the photoresist until the desired spacing between stamp and substrate was reached. Curing of the resist was carried out using the same UV LED as for IP-S curing, but split into three consecutive steps with increasing irradiance to prevent crack formation. The sequence of $2\,\mathrm{mW\,cm^{-2}}$ for 2 min, $10\,\mathrm{mW\,cm^{-2}}$ for 1 min, and $50\,\mathrm{mW\,cm^{-2}}$ for 30 s was applied here.

The initial motivation to use the double-replication process presented above was to avoid difficulties with writing directly to the surface of a pre-structured substrate. Apart from this aspect, there are some beneficial side effects in applying this scheme.

Most importantly, the imprinting process allows choosing different photoresists for DLW and subsequent soft-imprinting. Like this, the optimum resists for both steps can be selected. In this work, IP-S was chosen for the DLW step, because it can be structured at high writing speeds (typically around $10\,\mathrm{cm\,s^{-1}}$), is very tolerant to exposure dose variations and exhibits low shrinkage [102]. These properties make it an ideal resist for writing large volumes through DLW, such as the master structure used for replication and imprinting. On the other hand, the resist shows a yellow tint after UV-curing, indicating that some of its ingredients absorb a part of the visible spectrum. If the resist was to be used to write structures directly onto solar cells or OLEDs, absorption would present a major drawback. This potential disadvantage was overcome by choosing a different resist for the imprinting step, namely the hybrid polymer OrmoComp. After UV exposure, it is mechanically stable and shows no absorption through the visible regime down to 400 nm [103], both advantageous properties when applying the resist to solar cells or OLEDs.

Another benefit lies in the reusability of the master. DLW of the several $\mathrm{mm^2}$ sized master structure typically takes around 24 h. It would therefore need an impractical amount of time to write structures with that size directly onto solar cells or OLEDs.

Finally, the double-inversion scheme provides two more advantages. Firstly, the free-form refractive surfaces are relatively bulky structures in the sense that

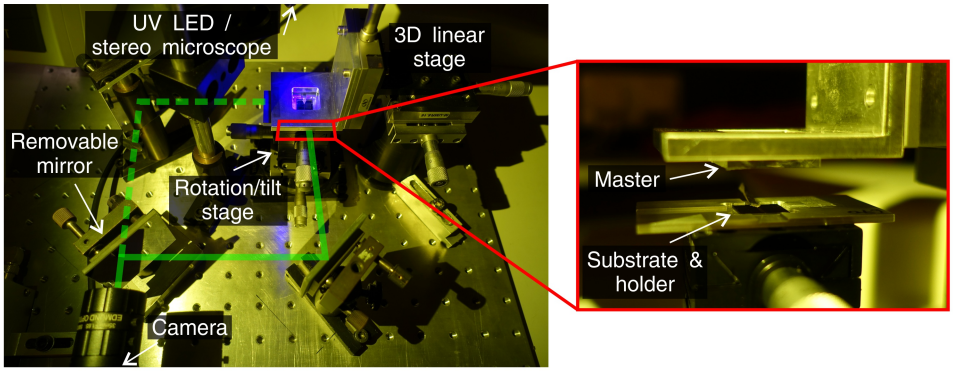

Figure 3.4: Photograph of the setup used for soft-imprinting. After aligning substrate and master, photoresist was drop-cast to the substrate, the master was lowered to make contact to the substrate holder, and the resist was cured using an UV LED.

they have a large volume filling. Inverting the structure reduces the volume to be written, so it is beneficial in terms of fabrication time to make the inverse structure in the DLW step. Secondly, using the inverse structure on a stamp sized larger than the final sample has the benefit that around the structured region a flat polymer layer will be produced during soft-imprinting. When measuring the cloaking efficiency of the free-form structures as discussed in section 4.4.4, the region covered with flat polymer can be used as reference.

A photograph of the soft-imprinting setup is depicted in fig. 3.4. The PDMS master was attached to a 3D linear stage to allow for pushing it against the substrate holder. The holder served as a spacer, ensuring the correct distance between master and substrate during curing of the resist. Fixing the holder on rotational and goniometric stages allowed for rotation and tilt alignment of the substrate with respect to the master surface. Lateral alignment was done visually using a stereoscopic microscope providing a 5× magnification. A camera and removable mirror allowed for monitoring the process of approaching the master toward the substrate from two directions.

3.3 Electron beam lithography

The samples discussed in section 4.2.3 were fabricated in a two-step lithographic process. In the first step, a metal was structured into strips—mimicking metallic contact fingers on solar cells—using electron beam lithography on a silicon substrate, physical vapor deposition of the metal, and a lift-off process.

Then, polymeric cloaking devices were added in the second step by DLW.

The metal structures on silicon were obtained by the process described in the following.

1. The diced silicon wafer was cleaned by wiping it with spectroscopy-grade acetone and subsequent drying using a nitrogen gun.

2. Poly(methyl methacrylate) (PMMA) served as the resist for electron beam lithography. A solution of PMMA with a molecular weight of 950000 in anisole (4 % by weight; 950 PMMA A 4, MicroChem, USA) was spun onto the silicon substrate; first, at 300 rpm for 5 s, then at 4000 rpm for 90 s. The resist was baked at 165 °C for 45 min.

3. The desired structure was exposed in a commercial electron beam lithography instrument (eLine, Raith, Germany) using an acceleration voltage of 30 kV, an aperture of 120 µm, and a square writing field with 1 mm edge length.

4. Developing of the resist was carried out at room temperature by first holding the sample into a 1:3 mixture of methyl isobutyl ketone (MIBK) and IPA for 15 s, followed by 30 s in pure IPA. The sample was dried by nitrogen blow-drying. As PMMA is a positive-tone resist, the unexposed regions survived the development step.

5. 5 nm of chromium and 60 nm of gold were deposited on the sample subsequently in a home-built electron-beam physical vapor deposition instrument. Gold was chosen as the main material for the metal structures to mimick high reflectivity of contact fingers on solar cells; the thin chromium layer acted as adhesion promoter between gold and the silicon substrate.

6. The final lift-off process served for removing the metal layer in the unexposed regions of the samples, i.e., where the metal was deposited onto the resist layer. The metal layer was scratched using tweezers in the outskirts of the sample, which was then immersed face-down in a remover solution (AR 300-70, Allresist, Germany) for several hours. After that, the metal layer was removed by thoroughly rinsing with acetone and subsequent sonication while immersed in the remover solution. Finally, the sample was quickly immersed in IPA and blown dry using a nitrogen gun.

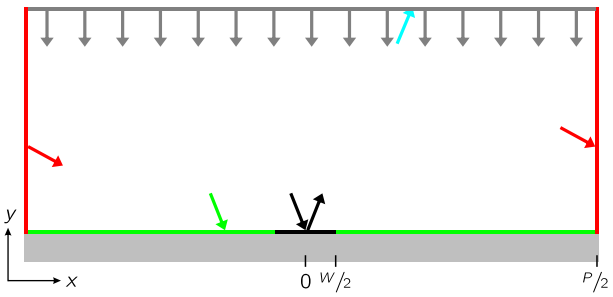

Figure 3.5: Unit cell for ray-tracing. N_0 rays are launched at equidistant positions at the top and are traced until they either leave the simulation region (cyan ray) or reach the region between contact fingers (green ray). Rays hitting the contact finger (black) are reflected specularly. Right and left boundaries are periodic, i.e., rays leaving the simulation region at the right re-enter at the left and vice versa (red rays).

3.4 Ray-tracing

Ray-tracing is the simulation method of choice for optically large systems without features exhibiting dimensions or periodicities comparable to the wavelength of light. In this case, light waves can locally be described as plane waves that propagate along the direction perpendicular to the local wavefront. The propagation direction defines the direction of the light ray. In homogeneous media, light rays are straight lines. They underlie refraction and reflection at interfaces between homogeneous media. In inhomogeneous media, light rays can be curved.

In this work, a dedicated Matlab program was developed to compute ray trajectories in optical systems comprising several homogeneous media with free-form interfaces or media with inhomogeneous refractive index. The program allowed tracing of rays through the unit cell of the periodic arrangement of contact fingers that can be present on solar cells or OLEDs (see fig. 3.5). Periodic boundaries were employed, so that rays leaving the unit cell on one side re-entered on the opposite side, while keeping their direction. The contact fingers were assumed to be infinitely extended along the z-direction, so that the geometry was effectively 2D. Light propagation was considered in three dimensions, however.

For simulations of contact fingers on solar cells as discussed in chapter 4, a set of $N_0 = 1000$ rays was launched at equidistant starting points at the top of the simulation region. The rays were traced until they either hit the solar cell interface, or they left the simulation region through the top boundary (after being reflected off of the contact finger, for instance). The complete ray

trajectories were stored for later visualization and analysis.

3.4.1 Homogeneous media

While light travels along straight lines within homogeneous media, rays are refracted according to Snell's law at interfaces between different media. Thus, the main computational task when implementing a ray-tracing algorithm is to find intersections of rays with interfaces between media. This was done by solving a linear equation of the type $\boldsymbol{x}_{\text{int}} = \boldsymbol{x}_{\text{ray}} + \boldsymbol{v}t$, where $\boldsymbol{x}_{\text{int}}$ is the intersection point, bound to lie on the interface, $\boldsymbol{x}_{\text{ray}}$ is a point on the ray with velocity $\boldsymbol{v}$, and t is the time of the intersection. The solution can be found analytically if the interfaces are simple enough. The free-form surface designed in this work for contact finger cloaking, however, can only be described numerically. Therefore, the intersection between rays and that surface had to be found numerically. This was achieved by first computing the surface height $y(x)$ on a discretized grid (section 4.2.2). The discrete version was then interpolated linearly using `griddedInterpolant`, and the point of intersection was found using `fzero`. Both procedures are built-in optimized Matlab functions, allowing for a quick and reliable evaluation.

For solar cell simulations, each of the rays were assigned a radiant flux $\delta\Phi$. At launch, it was set to $\delta\Phi = \delta\Phi_0$ for all rays. Together with the equidistant spacing of the rays, this situation mimicks a homogeneous incident irradiance, as expected for sunlight. Upon hitting an interface, rays were split into a reflected and a transmitted sub-ray. These continued propagation along the directions given by the law of reflection and Snell's law in their vectorial forms,

$$\begin{aligned}\hat{\boldsymbol{v}}_{\text{r}} &= \hat{\boldsymbol{v}} - 2\left(\hat{\boldsymbol{v}}\cdot\hat{\boldsymbol{n}}\right)\cdot\hat{\boldsymbol{n}}\,,\\ \hat{\boldsymbol{v}}_{\text{t}} &= -{}^{n_0}\!/_{n_1}\left(\hat{\boldsymbol{n}}\times\left(\hat{\boldsymbol{n}}\times\hat{\boldsymbol{v}}\right)\right) - \hat{\boldsymbol{n}}\sqrt{1-\left({}^{n_0}\!/_{n_1}\right)^2\left|\hat{\boldsymbol{n}}\times\hat{\boldsymbol{v}}\right|^2}\,.\end{aligned} \tag{3.2}$$

Here, both interface normal vector $\hat{\boldsymbol{n}}$ and the velocity before reflection or refraction, $\hat{\boldsymbol{v}}$, are normalized to unit length. $\hat{\boldsymbol{n}}$ is oriented to point against the direction of $\hat{\boldsymbol{v}}$. n_0 and n_1 are the refractive indices of the two media separated by the interface.

The sub-rays were assigned reduced fluxes, $R\delta\Phi$ and $T\delta\Phi$, respectively, with R and T being the polarization-averaged reflectance and transmittance

according to the Fresnel equations

$$
\begin{aligned}
R_\mathrm{s} &= \left| \frac{n_0 \cos\theta_0 - n_1 \cos\theta_1}{n_0 \cos\theta_0 + n_1 \cos\theta_1} \right|^2 , \\
R_\mathrm{p} &= \left| \frac{n_0 \cos\theta_1 - n_1 \cos\theta_0}{n_0 \cos\theta_1 + n_1 \cos\theta_0} \right|^2 , \\
R &= \frac{1}{2} \left(R_\mathrm{s} + R_\mathrm{p} \right) , \\
T &= 1 - R \, .
\end{aligned} \tag{3.3}
$$

Here θ_0 and θ_1 denote the angle of the ray toward the interface normal before and after refraction, respectively. Sub-rays were traced recursively until either their flux $\delta\Phi$ dropped below a threshold of $1 \times 10^{-3} \delta\Phi_0$, or a recursion depth of 100 reflections/transmissions was exceeded. The total radiant flux transmitted to the solar cell was computed by summing over the fluxes $\delta\Phi$ assigned to the sub-rays that reached the active area of the cell.

3.4.2 *Inhomogeneous media*

Ray trajectories in media with inhomogeneous refractive index can be found by several approaches. In the most straight-forward scheme, space is discretized into small domains. Their size is reduced so far that the variation of refractive index within them becomes negligible. Therefore, the domains can be treated as if they had a homogeneous refractive index, so that rays are straight within each of the domains. Finding the overall ray trajectory then consists of repeatedly finding the intersection of the ray with domain interfaces and applying Snell's law of refraction. While being simple to implement, this approach has shown some limitations [104].

Therefore, an alternative method is employed to find the ray trajectory. The scheme is based on the analogy between ray optics in inhomogeneous media and Hamiltonian mechanics [35, 105, 106]. More precisely, propagation of light through a refractive-index distribution can be described as a moving particle subject to an acceleration. In mechanics, acceleration is the consequence of a force acting on the particle, as dictated by Newton's second law. In ray optics it is the variation of the refractive index that causes the acceleration and a corresponding bending of the trajectory. The following derivation of the ray-optical equation corresponding to Newton's second law is taken from [104].

In classical mechanics, Hamilton's variation principle is the basis for the derivation of Newton's second law. It states that for physical trajectories of a particle the action integral becomes stationary, i.e.,

$$\delta \int_{t_0}^{t_1} L(\boldsymbol{x}, \boldsymbol{v}, t)\, \mathrm{d}t = 0\,, \tag{3.4}$$

where $L(\boldsymbol{x}, \boldsymbol{v}, t)$ is the Lagrangian function of the system. This can be reformulated as a requirement for the components of generalized coordinate $\boldsymbol{x}$ and generalized velocity $\boldsymbol{v}$, known as the Euler-Lagrange equations:

$$\frac{\partial L}{\partial x_i} - \frac{\mathrm{d}}{\mathrm{d}t}\frac{\partial L}{\partial v_i} = 0\,. \tag{3.5}$$

The first term can be interpreted as a component of a force $\boldsymbol{F}$, the second term as the temporal derivative of the momentum component, leading to Newton's second law

$$\frac{\mathrm{d}\boldsymbol{v}}{\mathrm{d}t} = \frac{\mathrm{d}^2\boldsymbol{r}}{\mathrm{d}t^2} = \frac{\boldsymbol{F}}{m} \tag{3.6}$$

under the assumption that the particle mass m is constant.

For propagation of light in ray optics, Fermat's principle plays the role that Hamilton's principle plays in mechanics. It requires the optical path length to be stationary for physical ray trajectories, i.e.,

$$\delta \int_{t_0}^{t_1} n(\boldsymbol{x})\, |\boldsymbol{v}|\, \mathrm{d}t = 0\,, \tag{3.7}$$

where $n(\boldsymbol{x})$ is the spatial distribution of refractive index. This can be translated to an equation analog to eq. (3.5), which reads

$$|\boldsymbol{v}|\, \nabla n - \frac{\mathrm{d}}{\mathrm{d}t}\left(n\frac{\boldsymbol{v}}{|\boldsymbol{v}|}\right) = 0\,. \tag{3.8}$$

Finally, by inserting the local phase velocity $v = c_0/n$, the Newtonian equation of motion for ray optics becomes

$$\frac{\mathrm{d}\boldsymbol{v}}{\mathrm{d}t} = \frac{\mathrm{d}^2\boldsymbol{x}}{\mathrm{d}t^2} = \frac{|\boldsymbol{v}|^2\, \nabla n - 2\,(\nabla n \cdot \boldsymbol{v})\,\boldsymbol{v}}{n}\,. \tag{3.9}$$

As expected, acceleration vanishes in a homogeneous medium ($\nabla n = 0$), so that light rays are straight lines.

In this work, Newtonian ray-tracing was implemented as a Matlab program. It was based on `ode15s` to numerically solve eq. (3.9). At discontinuities of the refractive-index distribution, Snell's law and Fresnel equations were applied as in the ray-tracer for homogeneous media.

Chapter 4

4 Cloaking contact fingers on solar cells

In this chapter, the basic principle of operation of solar cells is outlined. After discussing the key figures to quantify solar cell performance, the concept of contact finger cloaking is introduced. Two cloak designs based on a transformation-optical method are presented. Experimental evidence of cloaked contact fingers is shown along with supplementary numerical results obtained by ray-tracing calculations.

4.1 Operation of solar cells

Generally speaking, the generation of electrical power in a solar cell is a process comprising four steps [107]:

1. A photon is absorbed by the absorber material, triggering a transition of an atom or a molecule of the material to an excited state.
2. The excited state is converted into a pair of free positive (holes) and negative (electrons) charge carriers.[1]
3. A transport mechanism that distinguishes between electrons and holes takes care of moving the electrons toward one of the contacts (the cathode) and the holes toward the other contact (the anode).
4. The electron is extracted from the cathode and travels through the external electrical circuit, where its energy can be converted into electrical work. Arriving at the anode, it recombines with the hole, closing the circuit.

[1] Oftentimes, steps 1 and 2 coincide, because the photon directly creates a free electron-hole pair upon absorption. This is the case for crystalline silicon solar cells, for instance.

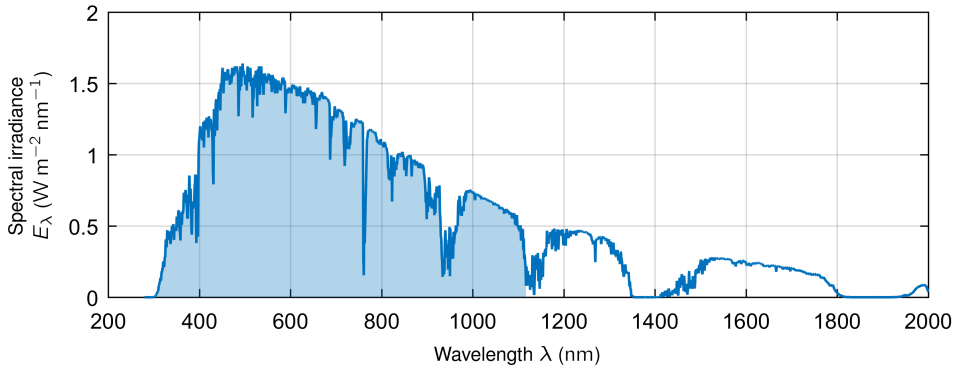

Figure 4.1: Reference AM1.5 terrestrial solar spectrum (ASTM G173-03), corresponding to the average solar irradiation over a typical year in the United States of America [108, 109]. This spectral irradiance distribution represents a standard for performance evaluation of terrestrial solar cells. Silicon solar cells with a band gap of 1.11 eV can harvest a large part of the spectrum (shaded region).

The most popular way of realizing such a process is by building a p–n junction, i.e., by putting together two pieces of semiconducting material, one being p-doped, the other one being n-doped. The semiconductor is chosen such that its bandgap allows efficient absorption in the visible regime, for example silicon. With its bandgap of 1.1 eV—corresponding to a wavelength of around 1100 nm—it can absorb photons with higher energies or shorter wavelengths, covering a large portion of the solar spectrum (see fig. 4.1). Upon absorption, an electron is lifted to the conduction band, leaving behind a hole in the valence band.

Sticking with the example of silicon as an absorber material, the effect of doping can easily be understood. In an intrinsic (doping-free) piece of silicon, all four valence electrons take part in covalent bonds to the neighboring atoms. At absolute zero temperature, all the electrons occupy states in the valence band, since the Fermi energy lies in the band gap. At elevated temperatures, some of the electrons are excited thermally, so they take part in conduction, leading to a temperature-dependent carrier density. For silicon, around 10^{10} carriers are available in $1\,\mathrm{cm}^3$ of material at room temperature.

By doping, this value can be changed drastically. Extra electrons can be provided for conduction by replacing some of the silicon atoms with phosphorous, an element of group V of the periodic table. It has five valence electrons, but only four take part in covalent bonds to the surrounding silicon. Therefore, one excess electron per phosphorous atom can contribute to conduction. At typical doping densities of $1 \times 10^{17}\,\mathrm{cm}^{-3}$, electron density is increased by up

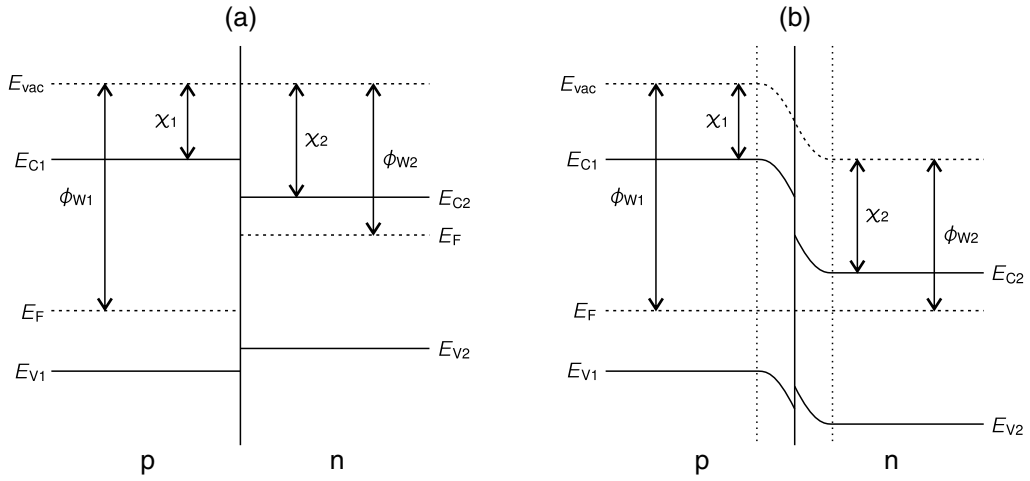

Figure 4.2: Band diagram of a p–n junction (a) during contact, (b) in thermodynamic equilibrium. E_{Ci} and E_{Vi} denote the band edges of conduction and valence band, respectively. E_F is the Fermi energy, E_{vac} is the vacuum energy level, and ϕ_{Wi} and χ_i denote the work function and the electron affinity, respectively.

to seven orders of magnitude as compared to the intrinsic material. This type of doping is called n-doping, because negatively-charged electrons constitute the majority of charge carriers in this material. The same game can be played with atoms from group-III-elements (such as boron) who miss an electron in comparison with silicon. Here, the missing electron can be interpreted as an excess hole that can take part in hole conduction in the valence band. Due to the positive charge of the majority carriers, such a material is called p-type.

In terms of the band diagram, adding dopant atoms introduces localized states at the position of the atoms. In order to increase carrier density, these states are ideally located in the band gap and close to the conduction (n-type) or valence (p-type) band. Like this, electrons can be excited by thermal excitation either from the dopant state to the conduction band (n-type) or from the valence band to the dopant state (p-type). As can be seen in the band diagrams of generic n-type and p-type semiconductors (fig. 4.2(a)), this effect leads to a shift of the Fermi energy toward conduction band and valence band for n-type and p-type doping, respectively.

As indicated above, a p–n junction is needed to build a photovoltaic device. What happens to the band diagram when bringing the p-type and n-type semiconductors in contact and allowing them to find a thermodynamic equilibrium can be observed in fig. 4.2(b). First of all, equilibrium requires the Fermi

energies of the two materials to align. Secondly, far away from the junction, the two materials have to exhibit the same properties as before contact, i.e., the same work functions ϕ_{Wi} and electron affinities χ_i. These two requirements can only be fulfilled by a bending of the local vacuum level and the band edges in the region close to the junction. In the n-region, the conduction band bends away from the Fermi energy whereas the valence band bends toward it. This indicates a positive space charge that is present in the n-part of the central region, and vice versa a negative space charge in the p-type part. This effect can be explained by diffusion of the majority carriers to the opposite material: Electrons from the n-type semiconductor diffuse to the p-type material and leave behind the positively charged ions. After arriving on the p-type side, the electrons recombine with holes, so that negatively charged ions are left on that side. The static electric field that builds up between the positively and negatively charged ions hinders presents a barrier to the diffusion, effectively limiting the width of this so-called space-charge or depletion region.

Now, when an electron-hole pair is generated by absorption of a photon close to the junction, the hole drifts to the left in the built-in field, while the electron is pushed to the n-type material, where it can be extracted through the cathode (not shown in the band diagram). From the band diagram it is clear that the maximum amount of energy the electron can deliver to an electric load is limited by the energy it acquires while drifting through the built-in field.

But what else limits the performance of a solar cell? To discuss this question, let us first take a look at the general structure of a solar cell from a device perspective (fig. 4.3). To efficiently extract the generated current, the cathode is typically made of an array of metallic strips, called contact fingers. They reflect some of the incoming photons, so that they never reach the absorber (1). The same is true for photons reflected at the front surface of the solar cell (2) or at the back-contact (3), which is usually a metal sheet. Photons that make it into the absorber and are absorbed close to the depletion region (4,5) undergo the ideal process described above and contribute most to the current. Those absorbed further away from the junction (6) are somewhat less efficient, since the minority carrier (in this case the electron) first has to find its way to the junction to be guided toward the contact fingers by the built-in field. As the electron is a minority carrier in the p-type material, chances are that it recombines with a hole before reaching the junction, reducing the efficiency of this process.

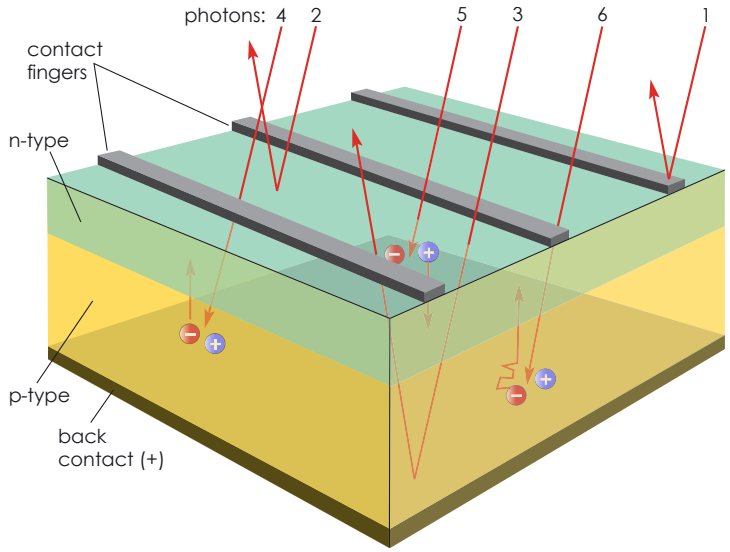

Figure 4.3: Scheme of solar cell operation. Reproduced with permission from [110], © 2010 John Wiley & Sons, Ltd.

The maximum attainable efficiency of a solar cell can be estimated from a thermodynamic consideration [111]. Apart from the forward process of generating charge carriers from absorbed photons, the reverse process of generating photons from recombining charge carriers occurs in the cell as well. Therefore, it can be described as a black body radiator that is in radiative equilibrium with the sun. The maximum efficiency of power conversion achievable under this assumption is determined mainly by the spectrum of the incident light and the band gap energy of the absorber material: While photons with energies below the band gap cannot be absorbed at all, light with energies much larger than the band gap creates charge carriers far away from the band edges. Over time, these dissipate their excess energy to the atomic lattice via phononic interactions to end up in an energetically more favorable state close to the band edge. This thermalization process is typically much faster than the time it takes to separate and guide the carriers to the external contacts. Therefore, a fraction of the energy of the incident photon is not available for electricity generation, reducing the overall efficiency of power conversion of the cell. For single-junction silicon solar cells, these considerations yield a maximum efficiency of 32 % for non-concentrated insolation under an AM1.5 spectrum [112]. Adding other parasitic processes, such as Auger recombination or free-carrier absorption to the picture, the efficiency limit reduces to around 29 % [113, 114]. With experimentally demonstrated

efficiencies near 26 % [115], current cell designs already provide performances near the theoretical limit. In order to reach the limit eventually, advanced cell designs have to be considered that overcome the remaining loss mechanisms, one of which can be shadowing of the active area by the front metallization.

Now that we have established a basic understanding of the internal function and loss mechanisms in a solar cell, let us try to answer the question how a solar cell looks from the perspective of an external electric circuit. As the heart of the cell is the p–n junction, it behaves as a p–n diode as long as it is not illuminated. Current can only flow strongly along one direction, as dictated by the built-in field. Under illumination, an additional current is generated by the process described above. An ideal solar cell will therefore produce a current that consists of the diode current, I_D, and the light-induced current, I_L. As the diode is a passive device that dissipates power, its I–V characteristics lie in the first and third quadrant, where the product of I and V is positive. An illuminated solar cell generates power, so its I–V characteristics must be dragged into the fourth quadrant by the light-induced current. Therefore, the total current becomes

$$I = I_\mathrm{D} - I_\mathrm{L}\,, \quad \text{where } I_\mathrm{D} = I_0 \left(\exp\left(\frac{qV}{k_\mathrm{B}T} \right) - 1 \right)\,, \tag{4.1}$$

I_0 is the dark saturation current, I_L is the light-induced current, q is the charge of the carriers, V is the voltage at the external load, k_B is the Boltzmann constant, and T denotes the temperature. Both contributions I_D and I_L are proportional to the cross-sectional area A of the p–n junction, which can be divided out to yield the total current density

$$J = J_0 \left(\exp\left(\frac{qV}{k_\mathrm{B}T} \right) - 1 \right) - J_\mathrm{L}\,, \tag{4.2}$$

where J_0 and J_L are the current densities corresponding to I_0 and I_L, respectively.

Typical J–V characteristics for an ideal solar cell under different levels of insolation are depicted in fig. 4.4(a). Three points along each of the characteristics are commonly used to quantify solar cell performance:

1. Short-circuit current density J_sc, the current density at which the J–V curve crosses the vertical axis, is the maximum current that the solar cell delivers. Unless parasitic series resistance (discussed below) is very high,

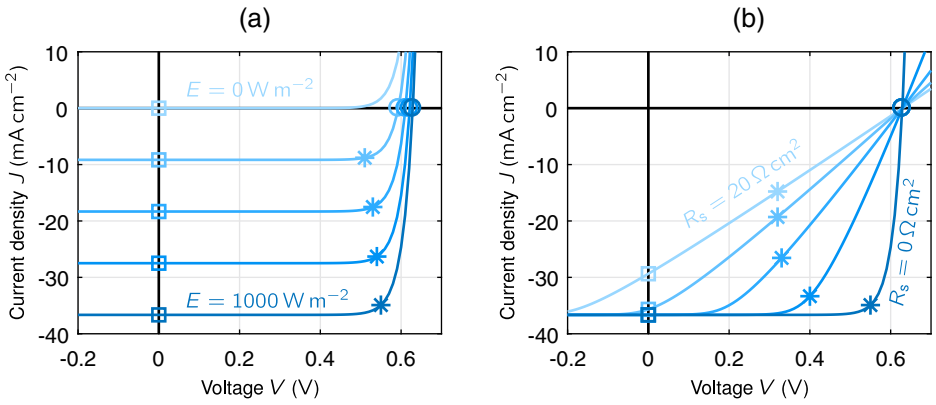

Figure 4.4: Computed current-density–voltage characteristics $J(V)$ (lines), J_{sc} (squares), V_{oc} (circles), and maximum power points (stars) at $T = 300\,\mathrm{K}$ (a) for an ideal solar cell under different levels of irradiance E and (b) for an otherwise ideal solar cell with series resistance R_s under an irradiance of $E = 1000\,\mathrm{W\,m^{-2}}$. J_L was obtained by integrating eq. (4.3), assuming EQE $= 1$ for $400\,\mathrm{nm} \leq \lambda \leq 1000\,\mathrm{nm}$ and EQE $= 0$ otherwise, and illumination with the solar spectrum shown in fig. 4.1. A dark saturation current density $J_0 = 1 \times 10^{-9}\,\mathrm{mA\,cm^{-2}}$ was assumed [116].

the short-circuit current density is equal to J_L. Particularly, J_{sc} is then proportional to the irradiance onto the solar cell. The proportionality factor (which usually depends on wavelength) is given by the external quantum efficiency (EQE), which is defined as the ratio of collected electrons and incident photons. This condenses optical properties of the solar cell (back-reflection at front surface or contact fingers, parasitic absorption, ...) and its carrier collection probability into one wavelength-dependent quantity EQE(λ). It is related to the spectral light-induced current density (given in $\mathrm{A\,m^{-2}\,nm^{-1}}$) via

$$J_{L,\lambda} = q \cdot \mathrm{EQE}(\lambda) \frac{E_\lambda}{hc_0/\lambda}\,, \tag{4.3}$$

where E_λ denotes the spectral irradiance in $\mathrm{W\,m^{-2}\,nm^{-1}}$.

2. Open-circuit voltage V_{oc}, the maximum voltage available from the solar cell, occurs when no net current flows through the cell, i.e., at $J = 0$. From eq. (4.2) V_{oc} can be derived as

$$V_{oc} = \frac{k_B T}{q} \ln\left(\frac{J_L}{J_0} + 1\right)\,. \tag{4.4}$$

V_{oc} is most prominently determined by the dark saturation current density J_0 for a given device, since J_0 can vary by orders of magnitude,

whereas J_L is relatively constant. J_0 depends on the parasitic recombination in the solar cell, turning V_{oc} into a measure of recombination.

3. Maximum-power point (MPP), the point (V_{MPP}, J_{MPP}) along the J–V characteristic at which the product of $-J$ and V is maximized. It is used to define the fill factor FF of the solar cell, which is a measure of the similarity of the J–V curve to a rectangle:

$$\mathrm{FF} = \frac{J_{MPP} V_{MPP}}{J_{sc} V_{oc}} . \tag{4.5}$$

The fill factor is strongly influenced by parasitic series resistance R_s or parallel resistance R_p that might be present in the solar cell. For an ideal cell, $R_s = 0$ and $R_p \to \infty$. In a real device, a high series resistance can be caused by low carrier mobility, high contact resistance at the semiconductor-metal interface, or low conductivity of the contact, for instance. Fabrication defects can lead to internal short-circuits that help the carriers to avoid the p–n junction, so that a low parallel resistance occurs. As can be seen in fig. 4.4(b), non-negligible series resistances primarily reduce the fill factor before reducing J_{sc} at very high values.

The quantities defined above are straight-forward to extract from a measured J–V characteristic. With their help, we can calculate the ultimate measure of solar cell performance, the power conversion efficiency (PCE). It is defined as the ratio of the maximum generated electrical power and the incident radiant flux and can be derived from the properties of the J–V characteristic as

$$\eta = \frac{\text{max. output power}}{\text{incident flux}} = \frac{V_{MPP} I_{MPP}}{\Phi} = \frac{V_{oc} I_{sc} \mathrm{FF}}{EA} = \frac{V_{oc} J_{sc} \mathrm{FF}}{E} , \tag{4.6}$$

where E denotes the irradiance of the incident light and A is the illuminated area.

Based on this formula, we can gain an understanding of the effect of metallic contact fingers on the efficiency of a solar cell. On the one hand, contact fingers reduce the series resistance, as they pick up charge carriers close to the location where they are generated. As discussed above, a low series resistance leads to a high fill factor. On the other hand, however, metallic contact fingers present an optical obstacle. They can reflect, scatter, or absorb photons that hit the fraction of the total area that is covered by the contact fingers. We call this relative area *contact finger filling fraction* f in the following. The shadowing effect reduces the external quantum efficiency and thereby

the short-circuit current density of the solar cell. Both FF and J_{sc} enter into eq. (4.6) as factors that scale oppositely with f. As a consequence, an optimum value for f has to be found to yield the highest possible PCE. Optimized filling fractions of typical non-concentrating silicon solar cells are around 5 % [117]; in concentrator cells, the metal fraction can be even higher [118].

The idea pursued in this work was to decouple the two effects by optically cloaking the contact fingers. More specifically, the incident light was to be guided around the contact fingers, so that contact finger shadowing becomes effectively zero. Like this, R_s can be minimized by choosing a suitable finger filling fraction without conveying a shadowing-induced loss in J_{sc}. Consequently, FF and J_{sc} become maximal independently of each other, maximizing the overall PCE.

Several approaches to minimize shadowing losses while preserving the electrical properties of the contacting have been discussed in the literature. Contact fingers or bus bars with a tailored geometry have been suggested that redirect a part of the reflected light toward the active area of the cell [119–122]. Like this, they reduce the optical width of the metal structures.

Similarly, different types of optical elements embedded in the cover glass or the encapsulation were proposed for guiding the light around the contact fingers or bus bars. When based on diffraction [117, 123], the functionality of the optical elements is inherently wavelength- and angle-sensitive. Approaches based on scattering can only provide partial relief of the shadowing problem [124]. Refractive air voids in the encapsulant have been investigated, but their performance was found to be limited for oblique incidence [125, 126].

Solar cells with contact fingers of sub-wavelength geometrical dimensions [127–129] were suggested, as well as cells that have all contacting on their backside [130, 131]. Both approaches can fully solve the shadowing problem, but they involve technological challenges. Due to the high complexity and cost of fabrication, back-contact cells have not yet found wide-spread commercial application, making up a world market share of few percent only [27].

Finally, prismatic covers based on refraction at a specially shaped interface promise to solve the shadowing problem for a wide range of incidence angles [132]. Due to the lack of appropriate fabrication methods, however, only approximations of the proposed shape have been demonstrated so far [133–135].

In this work, a novel route for designing optical elements for solar cells was taken: Transformation-optical concepts were employed to design a structure that can solve the shadowing problem.

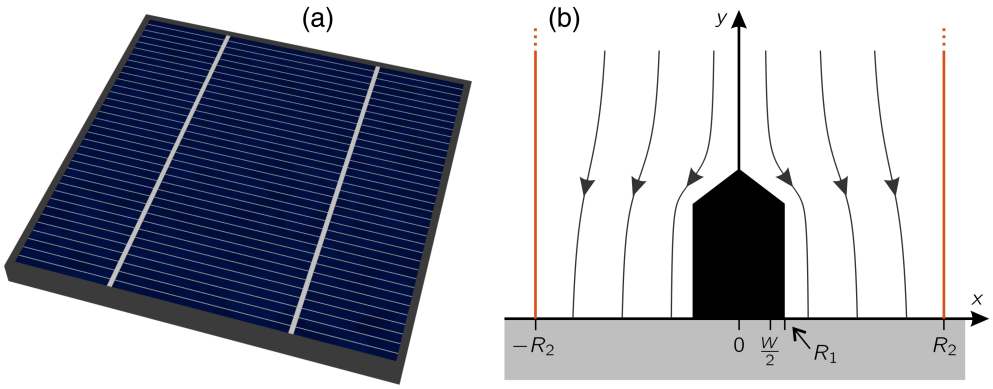

Figure 4.5: (a) Rendering of a typical silicon solar cell with front electrode comprising two bus bars and many contact fingers. (b) Schematic cross-section of a solar cell (gray region) with a grid of contact fingers (width W, period $2R_2$). Normally incident light is guided around the forbidden region (black) by a cloaking device. The semi-infinite 2D unit cell of the problem is marked in red.

4.2 Cloak design & experimental implementation[2]

The front electrode of a typical silicon solar cell is schematically shown in fig. 4.5(a). It comprises a grid of narrow contact fingers that collect the carriers from the p–n junction and wider bus bars that conduct the current toward the external contact. Contact fingers are around 100 µm wide and are arranged with a period of few millimeters. They meet bus bars every several centimeters, so the length of the contact finger is at least one order of magnitude larger than their period. This makes the problem of contact finger cloaking effectively invariant with respect to translations along the direction of the contact finger. Also, if contact fingers can be cloaked independent of their filling fraction, the filling fraction can be increased as far as necessary to remove the need for bus bars in the first place. Therefore, bus bars are ignored altogether in the following and the problem is described in terms of the 2D unit cell that is depicted in fig. 4.5(b). The contact fingers with width W are centered at $x = 2mR_2$ ($m \in \mathbb{Z}$). The cloaking structures presented in the following optically hide a region of width $2R_1$ that is a bit wider than the contact finger to allow for alignment tolerances in fabrication.

[2]The cloak designs and the corresponding proof-of-principle experiments presented here and in the next section have been discussed in one of the author's journal publications [136].

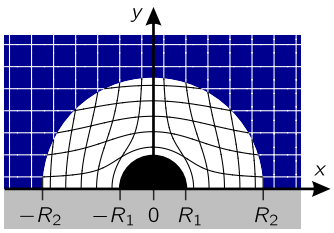

Figure 4.6: Cylindrical TO cloak based on a linear coordinate transformation, embedded in a homogeneous medium (blue). It can be employed for hiding a contact finger placed in the forbidden region (black). Light is guided around this region by an anisotropic magnetodielectric transformation medium (white). Adapted with permission from [136], © 2015 Optical Society of America.

4.2.1 Graded–refractive-index cloak

DESIGN To find a TO design suitable for contact finger cloaking, let us start by reviewing Pendry's famous invisibility cloak [10, 22], one of the first cloak designs proposed to illustrate the power of TO. He considers a coordinate transformation of a point to a cylinder with radius R_1. The transformation is limited to a radius $R_2 \geq R_1$. In cylindrical coordinates with radial coordinate r, azimuthal angle θ, and axial coordinate z, the transformation reads

$$r \to r' = \frac{R_2 - R_1}{R_2} r + R_1 \tag{4.7}$$

for $0 \leq r \leq R_2$ and $r' = r$ otherwise. No transformation is applied to azimuth and axial coordinate, i.e., $\theta' = \theta$ and $z' = z$. Since a point is invisible by definition, the cylinder obtained through the coordinate transformation is invisible, too. The spatial distribution of material parameters, ε and μ, calculated using eq. (2.5), ensures that light is guided around the cylinder. Its volume can therefore be used to conceal objects from an observer.

In principle, this concept can be translated directly to the problem of cloaking contact fingers. Here, the upper half of the cloak suffices to cloak the finger, as illustrated in fig. 4.6. Implementation of such a TO device poses a major challenge, since the design requires an anisotropic magnetodielectric material. As discussed in section 2.1.2, when using conformal maps instead of arbitrary coordinate transformations, spatial distributions of a locally isotropic refractive index $n(x, y)$ are enough to realize the desired behavior. Therefore, this is the route taken in this work.

The concept and initial design of the cloak presented in this section were developed by Samuel Wiesendanger [137], whereas the implementation in an experimental demonstrator and the corresponding ray-tracing simulations were carried out by the author. As the unit cell of the problem is mirror symmetric, it is sufficient to consider the right half of the unit cell depicted in fig. 4.5. To find $n(x \geq 0, y)$, a SC mapping from a half-plane to a semi-infinite

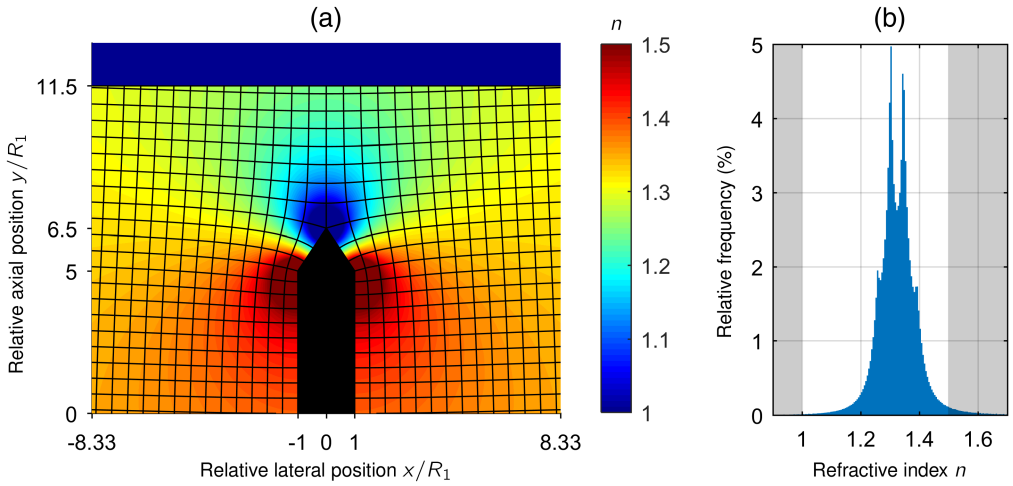

Figure 4.7: (a) Exemplary refractive-index distribution $n(x, y)$ for contact finger cloaking, obtained by SC mapping with subsequent spatial cropping. $R_2 = 8^1/_3 R_1$ corresponds to the finger half-period chosen in the experimental realization, where $W = {}^5/_3 R_1$ and $R_1 = 24\,\mu\text{m}$. The color scale is truncated to the experimentally accessible interval $n \in [1, 1.5]$. (b) Relative frequency of refractive index values occurring in the index distribution shown in (a); the shaded region is experimentally inaccessible.

polygon as shown in fig. 2.1 was applied. The refractive-index distribution in the polygon was then calculated according to eq. (2.18). Since conformal maps transform all space, the resulting $n(x, y)$ prescribes the refractive index in the complete semi-infinite polygon. To fit the actual geometry of a unit cell with finite dimensions, $n(x, y)$ was spatially cropped to the region $x \in [0, R_2]$, $y \in [0, 11.5R_1]$.

It has to be noted that spatial cropping has two side-effects. Firstly, cropping the infinitely extended conformal map to a finite region introduces interfaces at which Fresnel reflections can occur. That might lead to unwanted effects that will be discussed later by means of ray-tracing simulations. The second side-effect relates to the cloaking of the phase of the light wave that traverses the cloak. For the phase to be cloaked, any two light rays entering the cloak with the same phase have to leave the cloak without acquiring a phase difference. In the cropped conformal map discussed here, this is not true, as can be seen from fig. 4.7. Consider two rays that enter the refractive-index distribution along transformed coordinate lines at the top, one at $x \approx 0.5R_1$, the other one at $x \approx 7R_1$. Both will travel along the respective coordinate line. Now the length of the ray paths, as measured in terms of the transformed coordinates,

corresponds to the respective optical path length. These are different for the two rays, since the boundaries of the cropped refractive-index distribution do not coincide with transformed coordinate lines.

Generally, when talking about ideal or perfect invisibility cloaking, it is demanded that both amplitude and phase be cloaked. If this requirement is met, the presence of the cloaking device cannot be detected by looking at the irradiance or phase profile behind the cloaked region. In the case of a solar cell, however, the requirement for ideal cloaking can be relaxed significantly. Solar cells are not sensitive to the phase of the light, so this requirement can be dropped altogether. Furthermore, the incident irradiance pattern does not have to be resembled exactly after the cloak, because solar cells are usually tolerant to local variations of irradiance. Therefore, in this work, ideal cloaking only refers to the fact that all incident light is guided around the contact finger toward the active area of the solar cell.

In order to define the polygon for the SC mapping, the imaginary parts of the complex vertex coordinates were set to $\mathrm{Im}(w_1) = R_1$ and $\mathrm{Im}(w_2) = 0$ to open up a forbidden region that can accommodate half a contact finger (fig. 4.5). The real parts of the polygon vertices were optimized to yield $n(x, y)$ with a minimal refractive index gradient along the interface between cloak and solar cell. Furthermore, the refractive index in virtual space was set to $n_0 = 1.5$ and the prevertices were fixed to $u_i = \mathrm{Re}(w_i)$, because the occurring values of refractive index were found to be distributed in the most favorable manner: For these parameters, $n(x, y)$ was distributed symmetrically around a central value of 1.33. Values below 1 and above 1.5 that are particularly hard to implement experimentally, were avoided almost entirely (fig. 4.7(b)). By mirroring the resulting spatial refractive-index distribution $n(x, y)$ to the left, the index map for the complete unit cell as depicted in fig. 4.7(a) was obtained.

IMPLEMENTATION For an experimental demonstration of contact finger cloaking, the translationally invariant refractive-index distribution has to be realized in a 3D device. It is extremely challenging to experimentally adjust the refractive index of a bulk material according to a prescribed index distribution $n(x, y)$. Therefore, an artificial material was used in this work. As discussed in section 2.2, the propagation of light in photonic crystals can be described by an effective refractive index for wavelengths that are long enough. This means that locally changing the geometric parameters of the photonic crystal allows

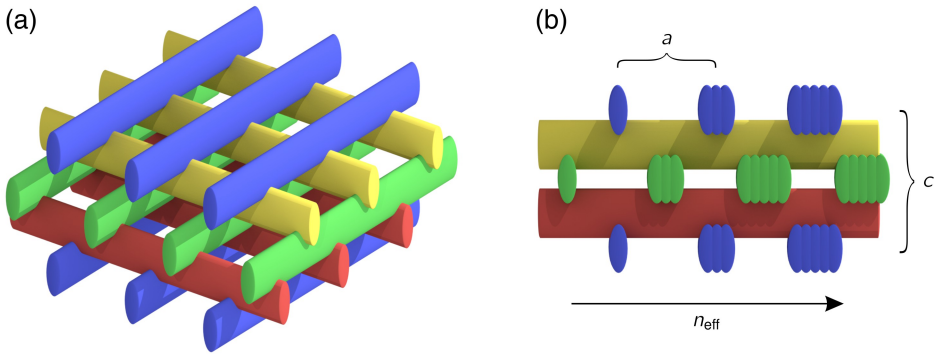

Figure 4.8: Structure of an fcc-type woodpile photonic crystal. The elliptical cross-section of the rods resembles the shape of the DLW voxel. (a) Several cubic unit cells of the woodpile with rod spacing a and lattice constant $c = \sqrt{2}a$. The structure repeats every four layers. (b) The local effective refractive index n_{eff} is tuned by changing the number of lines written per rod.

for adjusting the effective refractive index locally. Like this, the prescribed $n(x, y)$ can be realized in terms of the local effective refractive index of the photonic crystal.

In this work, dielectric *woodpile photonic crystals* served as the effective material. The geometry of these photonic crystals resembles a stack of wooden log, hence their name. They comprise layers of periodically arranged dielectric rods, as depicted in fig. 4.8(a). Adjacent layers are rotated by 90° and every second layer is shifted by half the rod spacing a. Like this, the pattern repeats every four layers, corresponding to the lattice constant c. The symmetry of the crystal is determined by the ratio c/a. In the special case of $c/a = \sqrt{2}$, the photonic crystal takes on a face-centered cubic (fcc) symmetry, leading to favorable properties [25]: In the long-wavelength limit, fcc-type woodpiles exhibit isofrequency surfaces that are nearly spherical in $\boldsymbol{k}$-space, corresponding to an almost perfectly isotropic effective refractive index n_{eff}. Also, n_{eff} can be tuned in the range defined by the refractive indices of the rods and the surrounding.

Here, the woodpiles were fabricated using DLW, so the rods consisted of a polymer with a refractive index of 1.5 and were surrounded by air after development. The local n_{eff} was controlled by adjusting the local volume filling fraction. As illustrated in fig. 4.8(b), this was achieved by making the rods running along the z-direction consist of N lines in proximity.

Before the refractive-index distribution could be translated to a spatial

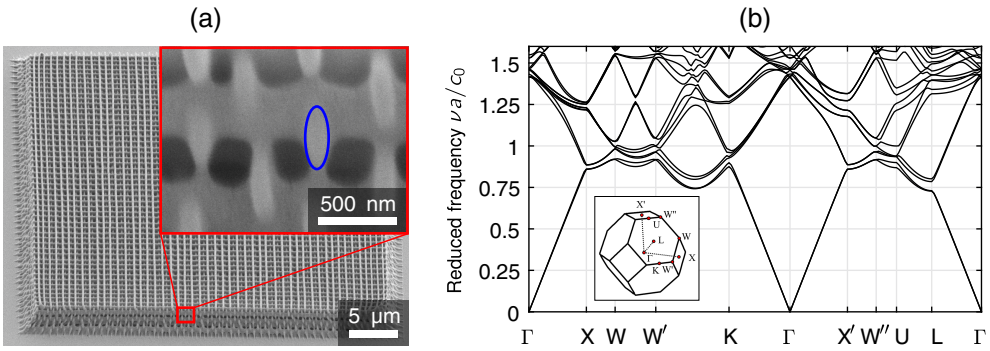

Figure 4.9: DLW-fabricated fcc-type woodpile with rod spacing $a = 800\,\text{nm}$ and $N = 1$ lines per rod. (a) Oblique-view (45°) electron micrograph and estimated voxel shape (inset). (b) Band structure calculated for rods with an elliptical cross-section of $150\,\text{nm} \times 565\,\text{nm}$ and corresponding first Brillouin zone (inset, taken from [138]).

distribution of N, the relation between the two quantities had to be found. For this purpose, the size and shape of the rod cross-section was estimated via scanning electron microscope (SEM) inspection of woodpiles with rod spacing $a = 800\,\text{nm}$ fabricated by DLW on a glass substrate. Here, the $63\times/1.4\,\text{NA}$ objective was used with IP-Dip photoresist. Exposure took place just above the polymerization threshold to minimize voxel size. For these parameters, an elliptical cross-section of $150\,\text{nm} \times 565\,\text{nm}$ was found, as depicted in fig. 4.9(a). The experimental voxel shape served as an input for the numerical calculation of the band structure of the woodpile (see fig. 4.9(b) and section 2.2). The lowest band shows a linear and isotropic dispersion close to the Γ-point, so that for long wavelengths the material can be described by a single effective refractive index. According to eq. (2.19), n_{eff} was obtained from the slope of the dispersion curve near the Γ-point.

The minimum wavelength at which the woodpile photonic crystal behaves as an effective material can also be estimated from the calculated band structure. The reduced frequency plotted on the vertical axis in fig. 4.9(b) can be expressed in terms of the vacuum wavelength λ as $\nu a/c_0 = a/\lambda$. This means the vertical axis directly provides the ratio of rod spacing and wavelength. For the directions investigated in this band structure, a linear dispersion is observed for reduced frequencies up to $a/\lambda \approx 0.7$. Consequently, a woodpile with rod spacing $a = 800\,\text{nm}$ would be expected to act as an effective medium for wavelengths above $\lambda = 1140\,\text{nm}$. This estimate corresponds well to the minimum wavelength of 1400 nm that was found in previous experiments

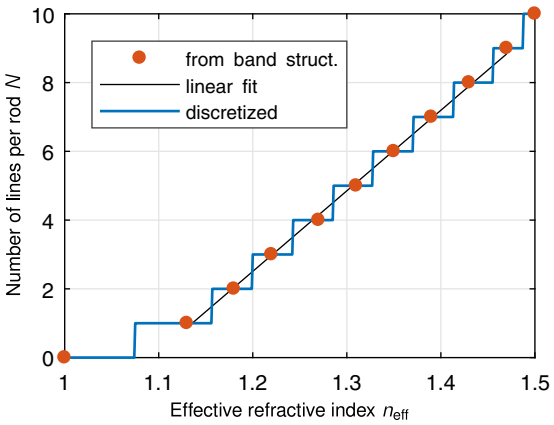

Figure 4.10: Relationship between number of lines per rod of the woodpile and effective refractive index as extracted from band structure calculations (red points), linear fit of $N = 1..9$ (black curve), discretized relationship used for woodpile fabrication (blue curve).

with similar graded–refractive-index (GRIN) cloaks [25].

The band structure calculation was carried out for several volume filling fractions of the woodpile, corresponding to different numbers of lines per rod N. Like this, a relationship between n_{eff} and N was found. It is shown in fig. 4.10 for a line spacing of 100 nm. For $N = 10$ lines per rod the voxels overlap far enough to form bulk material, so that the refractive index of the polymer is restored. $N = 0$ on the other hand corresponds to no polymer at all, i.e., positions where the required refractive index is mapped to $N = 0$ will show up as an air void in the final structure.

All in all, this method of implementation allowed realization of a discretized version of the index distribution shown in fig. 4.7 that was truncated to the accessible interval $n_{\text{eff}} \in [1, 1.5]$. Despite the fact that only a small portion of the original cloak design exhibits index values outside of this interval (see fig. 4.7), index truncation was found to affect the cloaking performance. This effect is discussed numerically in section 4.3.3.

Before fabricating the final structure comprising regions with different numbers of lines per rod N, writing parameters were optimized: Writing speeds of $30\,\text{mm}\,\text{s}^{-1}$ were found to provide a good compromise between structure quality and duration of fabrication. It took near 1 h to fabricate the structure shown in fig. 4.16 that is 107.25 woodpile unit cells high.

The writing power had to be optimized for each value of N individually due to the proximity effect discussed in section 3.1. The higher the volume filling fraction, the higher is the effective dose that a voxel written in proximity sees. Thus, writing power has to be decreased for higher values of N. Woodpiles with 1 to 10 lines per rod were fabricated at different exposure powers to find the polymerization threshold. Close to the threshold, structures tend

to be mechanically instable and show strong shrinkage. Therefore, the first power value above the threshold that provided good structure quality (as judged by SEM inspection) was chosen as the power for fabrication of the complete cloaking device. The resulting optimum exposure powers for each N are presented in appendix A.1.1, along with a comprehensive listing of DLW parameters.

As for isolated woodpiles, post-writing shrinkage was also observed in the full device, leading to an upward bending of the bottom of the structure and subsequent partial delamination from the substrate. To counteract this effect, a 7 µm high solid polymer block was written below the actual graded-index part of the final structure. This significantly increased mechanical stability of the device and reduced shrinkage-induced delamination considerably.

Another aspect relevant to the experimental implementation of the GRIN cloak is the following. The refractive-index distribution obtained from the SC mapping does not specify n in the cloaked region above the contact finger, since this region is excluded from physical space by the coordinate transformation. When fabricating the structures, however, this region (called *core* in the following) has to consist of some material. To increase the mechanical stability of the overall structure, the core was made of bulk polymer in the experiments discussed below. The opposite extreme of an air-filled core was discussed numerically by ray-tracing simulations (section 4.3).

4.2.2 *Free-form refractive cloak*

DESIGN As discussed above, it is not necessary to restore the wavefront of the light when hiding contact fingers on solar cells. In principle, however, TO devices designed by conformal mapping do cloak the phase. For the graded-index cloak, this property was lost only because of post-processing of the index distribution, namely spatial cropping. But what if we ignore phase cloaking from the beginning of the cloak design? Can we obtain a structure that is easier to realize than the GRIN cloak?

To answer this question, let us reconsider the cloak design. For now, let us assume that light approaches the solar cell sketched in fig. 4.5(b) under normal incidence. All we want to achieve is that none of the incident light rays hit the contact finger, but all rays make it to the active area. Additionally, we demand the irradiance between the contact fingers to be homogeneous. Put more formally, the cloaking device shall implement a mapping between the intersection point of an incident ray with the top of the cloak, (x, y), and

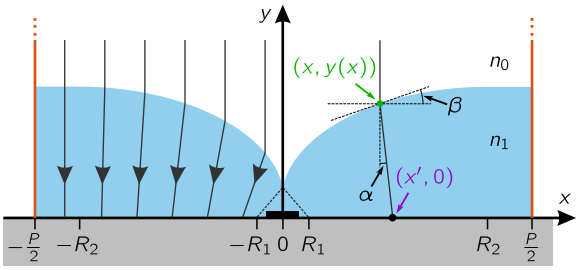

Figure 4.11: The free-form surface described by $y(x)$ refracts normally incident light such that it avoids the region $x' \in]-R_1, R_1[$ and is distributed homogeneously between the contact fingers (black rectangle with width W and period P). Adapted with permission from [136], © 2015 Optical Society of America.

the position where it reaches the solar cell surface, $(x', 0)$. The relevant part of the mapping is that of the respective x-coordinates, which can be written as

$$x' = \frac{R_2 - R_1}{R_2} x + R_1 \tag{4.8}$$

for $x \geq 0$, in close similarity to eq. (4.7). Mirror symmetry of the problem allows for computing the cloak for $x \geq 0$ only and obtaining the left half by mirroring. Therefore, we will limit the following discussion to positive values of x. The formula dictates that light approaching the cloak at $x \in [0, R_2]$ be redistributed to the interval $x' \in [R_1, R_2]$ on the solar cell surface, sparing out the region $x' \in [0, R_1[$ containing the contact finger. Different from the GRIN cloak, the upper limit of the transformation, R_2, does not necessarily need to coincide with the half-period of the contact fingers, $P/2$. Therefore, R_2 is considered as a free parameter here.[3]

The mapping of the ray positions as given by eq. (4.8) can be understood as a redistribution of the incident radiant flux to the region between contact fingers. Neglecting Fresnel reflections, this redistribution can be implemented by refraction at a surface of a homogeneous isotropic dielectric that is added to the front side of the solar cell, as shown in fig. 4.11. To find the shape of the free-form surface (FFS), we consider a ray that travels along the vertical axis and hits the FFS at position $(x, y(x))$. Here, $y(x)$ is a function describing the local height of the dielectric material. The local inclination angle $\beta(x)$ of the FFS is then given by

$$\frac{\mathrm{d}y}{\mathrm{d}x} = \tan(\beta(x)) \ , \tag{4.9}$$

[3] Strictly, homogeneous irradiance across the full unit cell (excluding the cloaked region) is only possible if $R_2 = P/2$. Since finger filling fractions are typically a few percent, irradiance in the region $x' \in [R_1, R_2]$ will only deviate from the irradiance in the rest of the unit cell ($x' \in [R_2, P/2]$) by a similar percentage. This effect is considered negligible.

which can be reformulated as

$$y(x) = y(0) + \int_0^x \tan(\beta(\tilde{x}))\ \mathrm{d}\tilde{x}\,. \tag{4.10}$$

After refraction at the inclined surface, the ray propagates at an angle $\alpha(x)$ with respect to the y-axis. Since rays are just straight lines within homogeneous media, $\alpha(x)$ is connected to x and x' via

$$\tan(\alpha(x)) = \frac{x' - x}{y(x)} = \frac{R_1}{y(x)}\left(1 - \frac{x}{R_2}\right)\,. \tag{4.11}$$

The right equation was obtained by inserting eq. (4.8). Applying Snell's law at the free-form surface we find the relationship

$$\beta(x) = \alpha(x) + \arcsin\left(\frac{n_0}{n_1}\sin(\beta(x))\right) \tag{4.12}$$

between the local inclination angle of the FFS, $\beta(x)$, and the angle of propagation after refraction, $\alpha(x)$. n_0 and n_1 denote the refractive inidices of the surrounding medium and the homogeneous dielectric, respectively. Inserting eqs. (4.10) and (4.11) yields the defining equation for the surface inclination angle,

$$y(0) + \int_0^x \tan(\beta(\tilde{x}))\ \mathrm{d}\tilde{x} = \frac{R_1\left(1 - \frac{x}{R_2}\right)}{\tan\left[\beta(x) - \arcsin\left(\frac{n_0}{n_1}\sin(\beta(x))\right)\right]}\,. \tag{4.13}$$

This equation has four parameters that influence the shape of the resulting free-form surface, n_0/n_1, R_1, R_2, and $y(0)$. While the ratio of refractive indices n_0/n_1 follows from the material chosen for realization of the free-form layer, the other three have a direct geometric meaning. Limitations to the choice of these parameters apply if perfect cloaking of the contact finger is desired, as will be discussed later. Let us assume for the following description of the solution of eq. (4.13) that all parameter values are fixed.

NUMERICAL SOLUTION To find $\beta(x)$ from eq. (4.13), the interval $[0, R_2]$ was discretized into N equidistant steps of width $\Delta x = R_2/N$, so that $x_k = k\Delta x$ ($k = 0\,..\,N$). At the point $x = x_k$, eq. (4.13) can be written as

$$y(0) + I_k = \frac{R_1\left(1 - \frac{x_k}{R_2}\right)}{\tan\left[\beta(x_k) - \arcsin\left(\frac{n_0}{n_1}\sin(\beta(x_k))\right)\right]}\,, \tag{4.14}$$

where I_k is short-hand notation for

$$I_k = \int_0^{x_k} \tan(\beta(\tilde{x}))\ \mathrm{d}\tilde{x}\,. \tag{4.15}$$

For small enough discretization steps Δx, the integral can be approximated by its lower sum, so that we obtain the recursion relation

$$I_k = I_{k-1} + \Delta x \tan(\beta(x_{k-1}))\ . \tag{4.16}$$

In order to use eq. (4.16), the start value $\beta(x_0 = 0)$ has to be known. It was obtained from inserting $x_0 = 0$ into eq. (4.14), leading to

$$y(0) = \frac{R_1}{\tan\left[\beta(0) - \arcsin\left(\frac{n_0}{n_1}\sin(\beta(0))\right)\right]}\,. \tag{4.17}$$

Matlab's `fzero` routine was applied to numerically solve this equation for $\beta(0)$, which was then inserted into eq. (4.16) to obtain I_1. Inserting I_1 enabled the numerical solution of eq. (4.14) for $\beta(x_1)$, again using `fzero`. This procedure was repeated until $\beta(x_k)$ had been computed for all k. Note that the numerical solution for $y(x)$ immediately follows from the computed I_k, since $y(x_k) = y(0) + I_k$.

Small-angle approximation In the special case that $\alpha(x)$ and $\beta(x)$ are much smaller than 90°, the trigonometric functions in eq. (4.13) can be replaced by their respective arguments. Employing eq. (4.9), the analytically solvable differential equation

$$y(x) \cdot \frac{\mathrm{d}y}{\mathrm{d}x} = \frac{R_1}{1 - \frac{n_0}{n_1}}\left(1 - \frac{x}{R_2}\right) \tag{4.18}$$

is found, which is solved by the function

$$y(x) = \sqrt{y^2(0) + \frac{R_1}{1 - \frac{n_0}{n_1}}\left(2x - \frac{x^2}{R_2}\right)}\,. \tag{4.19}$$

For realistic parameters, the analytical small-angle approximation resembles the numerically obtained solution to the full problem very well (fig. 4.12). Nevertheless, all free-form surfaces presented in this work were obtained via the numerical method. The analytical approximations of $y(x)$ and $\beta(x)$ were, however, used as the starting guesses for Matlab's `fzero` routine in the numerical solution process discussed above.

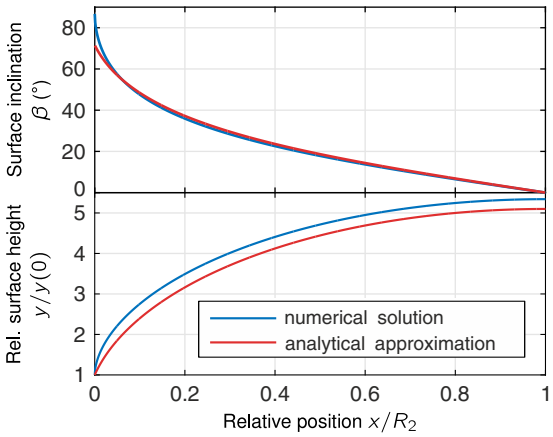

Figure 4.12: FFS shape from numerical solution and analytical small-angle approximation, both for geometric parameters $R_1 = 0.6W$, $R_2 = 5W$, $y(0) = 0.6W$, and refractive indices $n_0 = 1$ and $n_1 = 1.5$, corresponding to the situation in the transmission experiments (see section 4.2.3).

PARAMETER CHOICE As indicated above, the requirement of perfect cloaking sets limits to the range of values that can be chosen for R_1, R_2, and $y(0)$. According to eq. (4.8), R_1 determines the width of the cloaked region. Hence, the half-width of the contact finger, $W/2$, represents a lower limit for reasonable values of R_1. By definition of the coordinate mapping, $R_2 \geq R_1$, setting an upper limit for R_1 and a lower limit for R_2. R_2 cannot increase beyond $P/2$ to ensure a horizontal tangent of the free-form surface in the middle between two adjacent contact fingers. The choice of the third parameter, the minimum distance between the solar cell and the free-form surface, $y(0)$, is limited by the following consideration. To obtain a sensible surface shape, the local inclination angle $\beta(x)$ cannot exceed 90°. As seen from fig. 4.12, $\beta(x)$ decreases monotonically, so that the argument just made effectively imposes the limit $\beta(x = 0) \leq 90°$. This can be translated to a lower limit for $y(0)$ by evaluating eq. (4.13) at $x = 0$ and $\beta = 90°$. There is no physical reason that would put an upper limit to $y(0)$, so that we can summarize the parameter requirements as

$$R_1 \in \left[\frac{W}{2}, R_2\right], \quad R_2 \in \left[R_1, \frac{P}{2}\right],$$
$$y(0) \geq R_1 \left[\tan\left(90° - \arcsin\left(\frac{n_0}{n_1}\right)\right)\right]^{-1}. \tag{4.20}$$

All parameter sets fulfilling these requirements deliver ideal cloaking performance at normal incidence. However, it is not immediately clear how the performance changes for more oblique incidence, and how the parameter choice influences oblique-angle performance. Considering that diffuse light makes up a substantial part of the radiation that a solar cell receives in a location with temperate climate such as Karlsruhe, oblique incidence cannot

be neglected when finding the optimal parameters for the FFS. To include the effect of non-normal incidence into the discussion, ray-tracing simulations were run for a range of parameter sets and incidence angles for given finger filling fraction $f = W/P = 0.1$, refractive indices $n_0 = 1$, $n_1 = 1.5$, and finger width W. From the simulation results, the expected relative increase in short-circuit current caused by the cloak, ζ, was calculated (see section 4.3). ζ was averaged over a typical calendar year under Karlsruhe conditions, yielding the annual average current increase, $\langle\zeta\rangle$, for each of the parameter sets.[4] It was found that $\langle\zeta\rangle$ was highest when R_2 was maximal while R_1 and $y(0)$ were minimal, so that

$$R_1 = \frac{W}{2}\,, \quad R_2 = \frac{P}{2} = \frac{W}{2f} = 5W\,,$$
$$y(0) = \frac{W}{2}\left[\tan\left(90° - \arcsin\left(\frac{n_0}{n_1}\right)\right)\right]^{-1} \approx 0.45W\,. \tag{4.21}$$

Note that it is sufficient to specify the design parameters relative to the contact finger width W (alternatively to their period P), because the FFS is designed by geometrical optics. Like this, its shape and functionality are independent of an overall scaling as long as the ray-optical approximation stays valid.

Choosing exactly the above parameter set for fabrication is not advisable, because minimizing R_1 causes the cloaked region to be just as wide as the contact finger. Thus, no tolerance for misalignment in the fabrication process is provided. Moreover, fixing $y(0)$ at the minimum possible value leads to a local surface inclination angle of 90° at $x = 0$, corresponding to a very sharp notch that is challenging to realize when fabricating the FFS by means of DLW. The two issues were mitigated by choosing modified parameter values, $R_1 = 0.6W$ and $y(0) = R_1 = 0.6W$. It was confirmed by ray-tracing simulations that the parameter modification did not severely impact the cloaking performance: With both parameter sets an annual average current increase of $\langle\zeta\rangle = 11\,\%$ was found when neglecting Fresnel reflections. This value indicates perfect cloaking in both cases, since the maximum achievable current increase is determined by the finger filling fraction as $\zeta_{\max} = f/1-f \approx 11\,\%$. When partial reflections at all interfaces were included in the simulations, $\langle\zeta\rangle$ for the modified parameter set was less than 0.5 % below that for the optimal set. In conclusion, the discussed modification of parameters was therefore considered to have a negligible influence on cloaking performance.

[4] Details on this procedure can be found in section 4.3.4.

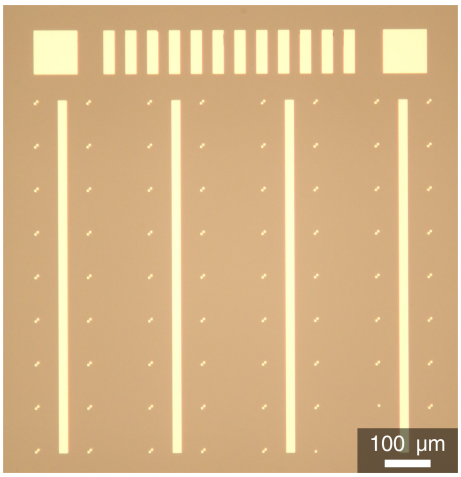

Figure 4.13: Optical micrograph of the metal structures on silicon after electron beam lithography, metal evaporation, and lift-off. Long metal strips emulated contact fingers on solar cells and were accompanied by alignment markers for the following DLW. The array of shorter lines was used for piezo calibration and the square metal patches served as knife edges for determination of the focus shape.

4.2.3 Transmission experiments

The cloaking performance of the two concepts discussed above was compared experimentally. To emulate the surface of a solar cell with contact fingers, $W = 20\,\mu m$ wide metal strips were added to a silicon wafer via electron beam lithography, metal evaporation, and a lift-off process (see section 3.3 and fig. 4.13). FFS and GRIN cloaks were designed to fit the finger width as described above, and added to the sample using DLW (see appendix A.1.1 for the writing parameters). The minimal rod spacing achieved reproducibly for the GRIN cloaks was $a = 800\,nm$. To enable the woodpile photonic crystals to act as an effective medium, the measurement was conducted at a vacuum wavelength of $\lambda = 1510\,nm$. Above a wavelength of 1.1 µm, silicon is transparent, so that transmission through the complete sample could be measured. The FFS cloak was designed by ray-optical principles and comprises a homogeneous material. Apart from material dispersion, it therefore not expected to show any wavelength dependence. Thus, transmission through the FFS cloaks was measured at the same wavelength of $\lambda = 1510\,nm$ to allow for direct comparison. Cloaking quality was judged by analyzing the spatial dependence of the recorded transmittance.

MEASUREMENT SETUP The setup serving for characterization of the contact finger cloak samples is shown schematically in fig. 4.14. The light from a fiber-coupled continuous-wave diode laser emitting around 1 mW of optical

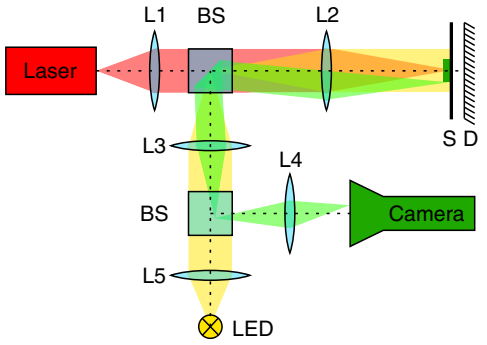

Figure 4.14: Measurement setup for transmission measurements with beam paths of the infrared laser (red), illumination (yellow), and imaging (green). Sample (S) and Detector (D) were moved relative to the optical axis to obtain spatial profiles of transmission through the sample.

power at a wavelength of 1510 nm was guided through a single-mode fiber[5] (not depicted). Its output was collimated and then focused onto the surface of the sample by two $10\times/0.25\,\mathrm{NA}$ objectives[5] (L1, L2). The sample (S) was mounted onto a germanium photodiode[5] (D) with an active area of $1\,\mathrm{cm}^2$, such that the region of interest on the sample was roughly in the center of the photodiode. The separation of the front-side of the sample and the active area of the detector was approximately 1 mm. Like this, all light leaving the sample at angles up to 75° toward the optical axis was collected by the detector. Two beam splitters[5] (BS) enabled separate beam paths for illumination and imaging of the sample (lenses[5] L3–L5). A light-emitting diode[5] with a peak wavelength of 940 nm served as the light source for sample illumination. The sample was imaged using an infrared camera[5], facilitating orientation on the sample. The sample-detector assembly was mounted to a piezo positioning stage[5] that allowed moving it within the plane normal to the optical axis.

For sample characterization, spatial profiles of transmission through the sample were analyzed. These were obtained by moving the sample-detector assembly such that the laser focus was scanned across the metal fingers in the sample. Simultaneously, the light-induced current through the photodiode was recorded.

SETUP CHARACTERIZATION Before the measurement setup could be used to characterize the cloaking performance of GRIN and FFS cloaks it had to be calibrated and characterized itself. Since the aim of the measurements was to record spatial profiles of transmission, two aspects were essential:

[5]Fiber: Thorlabs 1060XP, L1: Olympus 604490 ($f = 18\,\mathrm{mm}$), L2: Newport F-L10B ($f = 12\,\mathrm{mm}$), L3: Thorlabs AC508-150-C ($f = 150\,\mathrm{mm}$), L4: Thorlabs AL5040-C ($f = 40\,\mathrm{mm}$), L5: Thorlabs AC254-035-C ($f = 35\,\mathrm{mm}$), D: Thorlabs FDG1010, BS: Thorlabs BP245B3, LED: Thorlabs M940D2, camera: Hamamatsu C2741, piezo stage: Piezosystem Jena PX400 and PZ100

Firstly, the prescribed displacement of the piezo stage had to match its physical displacement. The piezo stage model employed in this work was of the open-loop type, i.e., it had no internal closed control loop that ensured correspondence between commanded and actual position of the stage. Instead, the relationship between the piezo voltage V and its displacement x was determined experimentally. To achieve good reproducibility of positioning, conservative scanning speeds of few tens of micrometers per second were chosen along with a fixed scanning direction when recording measurement data. The silicon wafers with metal fingers that were equipped with the cloaking structures comprised additional metal structures useful for calibration and characterization of the measurement setup (fig. 4.13). For instance, the array of equidistant metal strips was used to obtain the V–x curve for the piezo stage: The laser focus was scanned across the strip array by sweeping the piezo voltage V, resulting in a movement of the detector-sample assembly. Simultaneously, transmission through the sample was recorded. The minima of transmission were then correlated to the known positions x of the centers of the metal strips. Like this, a discretized relationship between V and x was established; in between the measured points, linear interpolation was applied.

The second important fact was that the laser focus was small enough to make sure that the shadowing by the metal strips left a clear trace in the transmission profile. The focus was characterized by the knife-edge method discussed in the following. The idea of this method is to move a sharp edge of an opaque material into the laser beam while recording the optical flux that the beam carries behind the obstacle. This sharp edge can be a razor blade (hence an actual knife-edge), or—as in this experiment—the edge of the $100\,\mu\text{m} \times 100\,\mu\text{m}$ large metal patches on the sample (fig. 4.13). The irradiance profile of the laser beam is then derived from the measured spatial profile of the transmitted flux. Assuming that the beam propagates along the y-direction and the knife-edge is moved along the x-direction, while being infinitely extended along the z-direction, the transmitted flux Φ can be computed by integrating the irradiance $E(x,z)$ over the region not covered by the knife-edge:

$$\Phi(x_0) = \int_{-\infty}^{\infty} \int_{-\infty}^{x_0} E(x,z)\,\mathrm{d}x\,\mathrm{d}z\,. \tag{4.22}$$

Here, the transmitted flux is a function of the position of the knife-edge, x_0. Without further assumptions, it is not possible to derive $E(x,z)$ from the recorded flux profile $\Phi(x_0)$. In the special case that the beam irradiance is

separable in spatial variables, i.e., $E(x,z) = E_1(x)E_2(z)$, eq. (4.22) simplifies to

$$\Phi(x_0) = \int_{-\infty}^{\infty}\int_{-\infty}^{x_0} E_1(x)E_2(z)\,\mathrm{d}x\,\mathrm{d}z = \int_{-\infty}^{\infty} E_2(z)\,\mathrm{d}z \cdot \int_{-\infty}^{x_0} E_1(x)\,\mathrm{d}x\,. \tag{4.23}$$

Importantly, the integral over z is constant with respect to x_0. Therefore, the derivative of the transmitted flux with respect to the knife-edge position becomes proportional to the beam irradiance profile along x:

$$\frac{\mathrm{d}\Phi}{\mathrm{d}x_0} = E_1(x_0) \cdot \int_{-\infty}^{\infty} E_2(z)\,\mathrm{d}z\,. \tag{4.24}$$

Thus, $E_1(x_0)$ and $\mathrm{d}\Phi/\mathrm{d}x_0$ only differ by a multiplicative constant that is given by the integral over z.

An example for a separable irradiance profile $E(x,z)$ is that of a Gaussian beam propagating along the y-axis,

$$E(x,z) = E_0 \exp\left(-\frac{2x^2}{w_0^2}\right)\exp\left(-\frac{2z^2}{w_0^2}\right)\,, \tag{4.25}$$

where w_0 is the radial distance at which the irradiance has dropped to E_0/e^2. Inserting into eq. (4.24) yields

$$\frac{\mathrm{d}\Phi}{\mathrm{d}x_0} = \frac{w_0 E_0\sqrt{2\pi}}{2}\exp\left(-\frac{2x_0^2}{w_0^2}\right)\,. \tag{4.26}$$

Hence, the Gaussian beam radius w_0 can be found by measuring $\Phi(x_0)$ and fitting a one-dimensional Gaussian function to the derivative of the measured flux profile. The flux profile was obtained by recording the photocurrent generated in the photodiode, I, which is proportional to the incident flux. An exemplary knife-edge measurement result is shown in fig. 4.15.

At the start of each characterization session of the cloaking samples, the interface of the sample was made sure to be positioned in the focal plane of the objective L2. For this purpose, after coarsely moving the sample to a position where the focus appeared smallest in the camera image, a series of knife-edge measurements at different positions along the optical axis were taken. For each of them, w_0 was determined by a Gaussian fit, and the position with the smallest w_0 was used for the subsequent characterization

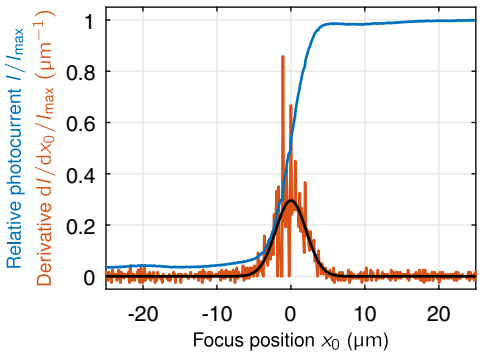

Figure 4.15: Photocurrent (blue curve) and derivative (red curve) recorded when the laser focus was scanned across the knife-edge. Fitting the experimental data with a Gaussian function (black curve) yielded a beam radius $w_0 = 4.1\,\mu m$.

measurements. Typical beam radii w_0 for the measurement results shown in the following were in the range of 4 µm to 4.5 µm. Similar values were found when measuring the focal irradiance profile along the z-direction indicating lateral symmetry of the focus. Considering the mode field diameter MFD = 9.5 µm of the single-mode fiber and the focal lengths $f_1 = 18\,mm$ and $f_2 = 12\,mm$ of the two objectives L1 and L2, respectively, the ideal beam waist is $w_0^{ideal} = f_2/f_1 \cdot \text{MFD} \approx 3.2\,\mu m$. That leads to a Rayleigh length $y_R^{ideal} = \pi w_0^2 n/\lambda \approx 32\,\mu m$ in a medium with refractive index $n = 1.5$. As the cloaking structures are several tens of micrometers high, some effect of the divergence of the beam is expected to be present in the measurement results. The residual discrepancy between theoretical and experimental beam waist is attributed to minor imperfections and sub-ideal alignment of the optical components.

RESULTS After adding GRIN and FFS cloaks to some regions along the metal fingers on the silicon chips via DLW, transmission profiles were recorded to characterize the cloaking performance. The metal fingers were $W = 20\,\mu m$ wide and—despite being arranged in an array—were understood representing individual unit cells of the problem (with width and period $P = 200\,\mu m$) that were equipped with cloaks separately. Like this, a solar cell with a contact finger filling fraction of $f = 10\,\%$ was emulated in this experiment.

The design parameters of the cloaks were chosen according to the discussion above, i.e., $R_1 = 0.6W = 12\,\mu m$ and $R_2 = 5W = 100\,\mu m$ for both types, and $y(0) = 0.6W = 12\,\mu m$, relevant to the FFS cloak only. While the transmission profile recorded was recorded for the range from $-R_2$ to R_2, i.e., for the full unit cell, the cloaking structures were extrapolated a bit beyond that range (see shaded region in fig. 4.16). This was done to avoid boundary artifacts in

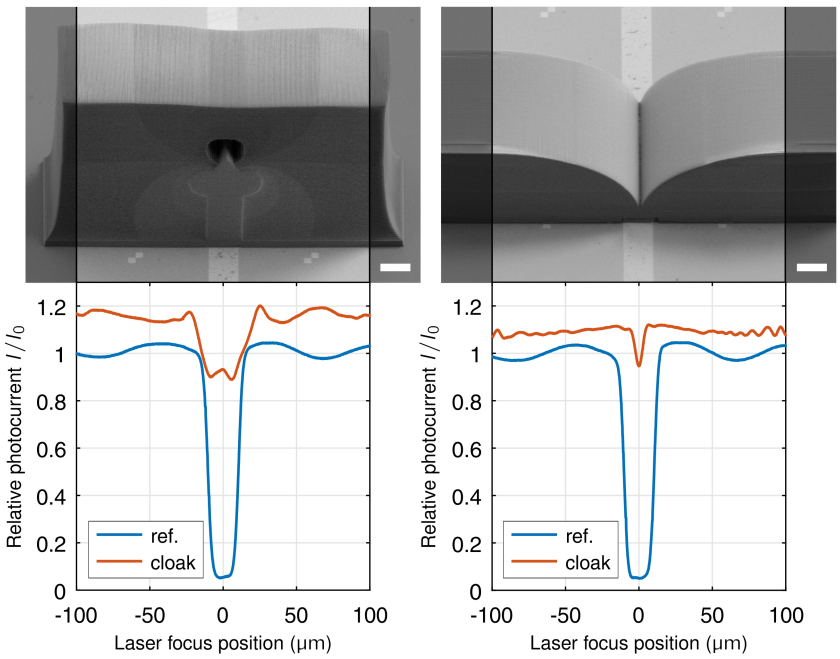

Figure 4.16: Oblique-view electron micrographs (top) and transmission profiles (bottom) of a GRIN cloak (left) and a FFS cloak (right) on a silicon wafer with metal strips. The photocurrent induced in the photodiode behind the sample, I, was normalized to the current measured when focusing the laser to a region far away from the metal finger, I_0. Scale bars are 20 µm. Adapted with permission from [136], © 2015 Optical Society of America.

the transmission profiles that arise when scanning the laser focus across the physical boundary of the structure. These artifacts would not be present in a real solar cell with a periodic arrangement of contact fingers and periodic cloaking devices. The GRIN cloak was extrapolated 15 µm beyond the unit cell limits, whereas 50 µm were added for the FFS cloak. Nearest-neighbor extrapolation of the relevant properties was applied, i.e., the GRIN cloak exhibited the same vertical refractive-index distribution as at $x = \pm R_2$ in the additional region, and the FFS was continued by a flat polymer block with constant height.

Transmission profiles were taken across metal fingers in regions with and without added cloaking devices (bottom row of fig. 4.16). Without the cloak, near-zero transmission was observed when the laser focus hit the metal finger. If the sample were a real solar cell with contact fingers, this observation would correspond to pronounced contact finger shadowing. With both of the cloaking devices, shadowing is reduced significantly, manifesting in a less

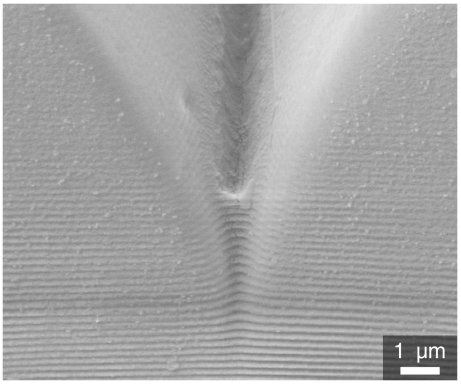

Figure 4.17: Oblique-view electron micrograph of the central notch of the FFS cloak, showing a rounded shape caused by the finite voxel size in DLW. The ripple pattern on the surface is caused by interference of the laser focus with its reflection off of the silicon substrate, leading to a spatially oscillating exposure dose during DLW.

pronounced transmission dip in the region of the metal finger. This shows that cloaking of the metal finger works in principle.

Cloaking is not perfect, however, since the transmission profiles are not completely flat, but still show a trace of the presence of the contact finger. This is especially true for the GRIN cloak. In this case, the prominent transmission dip above the contact finger is attributed to the fact that realization of the TO device via an effective material limits the range of accessible refractive indices to the interval $n \in [1, 1.5]$, as discussed above. While only a small relative area of the ideal cloak design exhibits indices outside of that interval, a numerical analysis presented in section 4.3 showed that especially the domains with $n < 1$ are essential for the cloaking to work properly, predicting zero transmission for a range of positions. In the experiment, transmission is not reduced to zero because the measured transmission is spatially averaged due to the finite focus size and averaged over angles of incidence because of the finite beam divergence.

For the FFS cloak, a much less pronounced central transmission dip was observed. Here, the finite resolution of DLW as the fabrication method is expected to be the cause for the dip. While by design the slit above the contact finger should be sharp, with zero radius of curvature, the finite voxel size leads to a rounded-off shape (see fig. 4.17). As a result, the surface inclination is lower than designed over a few micrometers in the center of the structure. Thus, light incident there is not refracted strongly enough to avoid the metal finger, leading to a dip in transmission.

Two more effects are visible in the measured transmission profiles. Firstly, there is a clear offset in transmission between the measurements of reference and cloak. For both types of cloaks, transmission is generally higher by several

percent as compared to the reference case without any cloaking measures. This is attributed to better impedance matching (hence lower reflectance) between air ($n = 1$) and silicon ($n = 3.5$) when an additional polymer layer with $n = 1.5$ is present in between. In a sense, the cloaks act as simple anti-reflection layers, enhancing transmission through the sample.

The second visible effect are oscillations with an amplitude of a few percent in the transmission profile that are especially clear in the reference measurements. These oscillations are attributed to interference within the silicon substrate. Due to its high refractive index of $n = 3.5$, the two air-silicon interfaces exhibit a reflectance of $R \approx 30\,\%$. This enables the silicon substrate to act as a Fabry-Perot etalon with a maximum reflectivity $R_{\mathrm{max}} = {}^{4R}/_{(1-R)^2} \approx 70\,\%$. For a fixed wavelength, etalon reflectivity oscillates with the resonator length between $R = 0$ and R_{max}. It can be expected that the silicon substrate used for the transmission experiments has a finite thickness variation. For instance, the normals of the two interfaces of the substrate can be tilted slightly toward each other. In this case, an oscillation in transmittance is expected when moving the sample laterally with respect to the incident beam. The amplitude of transmittance oscillations is reduced below the 70 % quoted above due to the finite size (causing spatial averaging) and divergence (causing angular averaging) of the incident beam. All in all, this effect can be regarded as being caused by the particular type of experimental setup chosen for characterization (including coherent illumination), and is considered irrelevant for real solar cells with cloaked contact fingers.

In conclusion, both GRIN and FFS contact finger cloaks were demonstrated to work for normal incidence in this proof-of-principle experiment.

4.3 Numerical analysis

Beyond demonstration of the principle, several questions had to be answered before implementing the contact finger cloak on a real solar cell: How do the cloaks behave when light comes from non-normal directions? How does an encapsulation of the solar cell influence cloaking? Can the concept be extended to work for a two-dimensional grid of contact fingers and bus bars? These questions were investigated by numerical analysis.

4.3.1 *Choice of method*

When simulating the performance of optical structures, several techniques are available, most prominently finite-element methods (FEMs) and ray-tracing. In general, the FEM is a numerical scheme to solve partial differential equations in discretized space. First, space is split into finite elements, polyhedra in a 3D problem or polygons in a 2D problem. Then, the partial differential equations are solved for each of the finite elements individually, taking into account boundary conditions as given by the surrounding elements.

As all electromagnetic phenomena, the propagation of light is described by Maxwell's equations, so these are the partial differential equations relevant for all optical problems. For accurate results, the finite elements must be small enough, i.e., their dimensions must be a fraction of the wavelength of light. The resulting spatial distributions of the electromagnetic fields include all wave effects of light propagation, such as diffraction or interference. Therefore, the FEM is especially suited when wave effects play an important role in the performance of the investigated optical device and its dimensions are not much larger than the wavelength.

Ray-tracing, on the other hand, ignores wave effects altogether, and is entirely based on geometrical optics. The method therefore provides a good approximation to reality whenever the wavelength of light is small compared to the dimensions of the structures interacting with the light. In realistic solar cells, the period of contact fingers is in the range of millimeters, with filling fractions of few percent. That means the unit cell of the problem as well as the width of the contact fingers are orders of magnitude larger than the wavelength of visible light. Therefore, diffraction at the grid of contact fingers can be safely neglected when simulating cloaking performance. Inside the cloaking structures, diffraction is expected to be largely irrelevant for the following reasons. For the GRIN cloak, the bulk of the refractive-index distribution features smooth, moderate variations of n. That means over a distance comparable to the medium wavelength, λ/n, only very small changes of n occur. While this is true for the majority of the GRIN distribution, light could in principle be diffracted at the position where the forbidden region forms a sharp tip. In case of the GRIN cloak with polymer core, the refractive index jumps from 1 to 1.5 at that position. Overall, however, the effect of diffraction at this sharp feature in the GRIN distribution is considered negligible, because most of the light should avoid this region anyway.

A similar argument can be made for the FFS cloak. Its surface shape

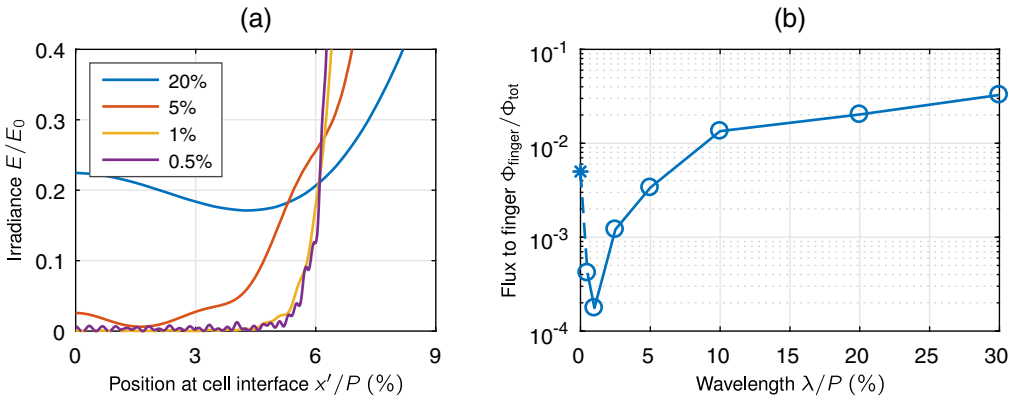

Figure 4.18: FEM simulations of the FFS cloak with finite notch diameter of 0.5 %P. (a) Irradiance profiles for several relative wavelengths λ/P in the vicinity of the forbidden region $|x'| < 6\,\%P$. (b) Relative flux to the region of the contact finger $|x'| < 5\,\%P$. The asterisk marks the ray-tracing result for a notch cut off at a width of 0.5 %P.

varies smoothly for the largest part, so that geometrical optics are a valid approximation there. The only sharp feature is the notch directly above the contact finger, where the FFS has its minimum height. In the fabricated structures, this notch had a finite radius of curvature of few micrometers. Since its dimensions are comparable to the wavelength, light can be diffracted there. To estimate the effect of diffraction, full-wave FEM simulations were carried out in the Wave Optics Module of Comsol Multiphysics. Here, a 2D cross-section of the polymeric FFS cloak was modeled and a TE-polarized plane wave was sent toward the cloak at normal incidence, along the negative y-direction. The wave was emitted by a port above the FFS and detected by a second port at $y = 0$, i.e., at the position where the solar cell interface would be in a real device. Both ports were backed by perfectly matched layers to avoid spurious reflections at the boundaries of the model. A full unit cell of the FFS cloak was modeled, including periodic boundary conditions. Solution of Maxwell's equation was carried out at a fixed frequency, corresponding to a given vacuum wavelength. The wavelength was varied between 20 % and 0.5 % of the contact finger period P. Smaller wavelengths were not accessible, because the discretized grid required for accurate results then exceeded the memory capacity of the simulation computer. The diameter of the rounded notch of the FFS was set to 0.5 %P, corresponding to the smallest simulated wavelength. The contact finger was assumed to cover $f = 10\,\%$ of the period, and the optimized parameters were used to design the FFS.

As a benchmark for similarity to geometric optics, irradiance profiles across the cloaked region were analyzed for the different wavelengths (fig. 4.18(a)). For large wavelengths, interference lead to a substantial fraction of the incident light reaching the forbidden region. The shorter the wavelength, however, the closer the irradiance profile approached the ideal shape—zero irradiance in the forbidden region, and a sharp rise at the boundary $x' = 6\,\%P$. For the smallest wavelength, corresponding to the diameter of the notch of the FFS, the irradiance profile shows an oscillatory modulation. This is attributed to diffraction at the notch.

From the irradiance profile it was concluded that the influence of diffraction was small. This qualitative argument was substantiated by a more quantitative analysis depicted in fig. 4.18(b). Here, the relative radiant flux to the region of the contact finger was computed for the set of incident wavelengths. It was found that—as expected from the irradiance profiles—the relative flux to the region of the finger decreases when reducing the wavelength. Diffraction effects caused a small increase of the relative flux for the shortest wavelength.

In the ray-tracer, the finite resolution of the FFS notch was modeled by cutting off the sharp notch, so that it was replaced by a flat region. Like this, at normal incidence all the rays traveling toward this region hit the FFS normal to its surface. Thus, the rays were not refracted away from the contact finger. That means in the ray-optics limit, the fraction of the light transmitted to the contact finger is given by the relative width of the notch. For a width of $0.5\,\%P$, the relative flux for the ray-optics situation was added to fig. 4.18(b) as an asterisk. Obviously, diffraction does not lead to an increase in relative flux to the contact finger region that is strong enough to surpass the estimation from ray-optics. Thus, cloaking performance will be underestimated slightly by ray-tracing simulations.

Moreover, diffraction at the notch of the FFS can only occur if light approaches the cloak at near-normal incidence. At oblique angles, all light is refracted in the smooth region of the FFS due to its rounded shape.

In conclusion, wave-optical effects were considered negligible for both GRIN and FFS cloaks, and ray-tracing was used as the method of choice for all simulations.

4.3.2 Figure of merit

As discussed in section 4.1, the ultimate figure of merit for quantification of solar cell performance is the PCE, η. Cloaking of the contact fingers is

expected to increase the total radiant flux to the active area of the solar cell, Φ, by several percent, thereby increasing its PCE. A reasonable figure of merit to quantify cloaking quality therefore is the relative increase of PCE caused by application of the cloak,

$$\zeta_{\mathrm{PCE}} = \frac{\eta_{\mathrm{cloak}}}{\eta_{\mathrm{ref}}} - 1\,. \tag{4.27}$$

Here, η_{ref} is the PCE found in a reference situation. If the reference was a solar cell without any additional layer, the relative PCE increase would include the trivial effect of reduced overall reflectance due to a polymer layer on the silicon surface. To exclude this effect from the discussion, a solar cell with contact fingers and a flat layer with a fixed refractive index of $n = 1.5$ was chosen as the reference situation for all simulations. The thickness of the reference layer was chosen to equal the half-period of the contact fingers, R_2.

According to eq. (4.6), PCE is given as the product of FF, V_{oc}, and I_{sc}, normalized by the incident flux Φ_0. While I_{sc} is proportional to the radiant flux to the active area of the cell, Φ, FF and V_{oc} depend only weakly on Φ. Thus, the relative increase in PCE can be approximated by the relative increase in I_{sc} or that in Φ:

$$\zeta_{\mathrm{PCE}} \approx \frac{I_{\mathrm{sc}}^{\mathrm{cloak}}}{I_{\mathrm{sc}}^{\mathrm{ref}}} - 1 = \frac{\Phi_{\mathrm{cloak}}}{\Phi_{\mathrm{ref}}} - 1 \equiv \zeta\,. \tag{4.28}$$

The fluxes were found by ray-tracing simulations (see section 3.4).

In general, the numerical values obtained from eq. (4.28) provide a measure of how much the cloak increases ($\zeta > 0$) or decreases ($\zeta < 0$) the amount of light that hits the active area in comparison to the reference situation. However, it is not obvious what value of ζ would be expected for an ideal cloak. Therefore, a special situation was considered for some simulations to ease assessment of the results: Partial Fresnel reflections were switched off, corresponding to fictitious ideal anti-reflection coatings at all interfaces. Nevertheless, *total* internal reflection and reflection at the contact finger were taken into account. Without partial reflections, all launched rays keep their initial flux value, $\delta\Phi$, throughout the simulation. Thus, the fluxes in eq. (4.28) can be expressed as $\Phi_{\mathrm{cloak}} = N_{\mathrm{cloak}}\delta\Phi$ and $\Phi_{\mathrm{ref}} = N_{\mathrm{ref}}\delta\Phi$, where N_{cloak} and N_{ref} are the number of rays that hit the active area of the solar cell with cloak and in the reference situation, respectively. Considering that the rays are launched with equidistant spacing, we find that N_{ref} is given by the total number of rays launched, N_0, and the contact finger filling fraction, f, as

$$N_{\mathrm{ref}} = N_0(1 - f)\,, \tag{4.29}$$

so that eq. (4.28) becomes

$$\zeta = \frac{N_{\text{cloak}}}{N_{\text{ref}}} - 1 = \frac{N_{\text{cloak}}}{N_0(1-f)} - 1\,. \tag{4.30}$$

If the cloak works perfectly, all launched rays will reach the active area of the cell. Consequently, $N_{\text{cloak}} = N_0$ and the maximum relative flux increase is found to be

$$\zeta_{\text{max}} = \frac{f}{1-f} \approx 11\,\%\,. \tag{4.31}$$

The numeric value was calculated for the filling fraction $f = 10\,\%$, as present in the transmission experiments. The result implies that the PCE of a solar cell with contact fingers covering 10 % of their front area can be increased by 11 %, given that the contact finger cloak shows ideal performance. This would raise the PCE of a cell with 20 % efficiency to 22 %, for instance.

4.3.3 Oblique incidence

To obtain an understanding of the cloaking performance under oblique incidence, the relative flux increase was computed for different angles of incidence via ray-tracing simulations. The direction of incidence was described by a normalized direction vector, $\boldsymbol{v}$. It was specified by two angles (ψ_1, ψ_2) related to its Cartesian coordinates as

$$\boldsymbol{v} = \begin{pmatrix} \sin\psi_1 \cos\psi_2 \\ -\cos\psi_1 \cos\psi_2 \\ \sin\psi_2 \end{pmatrix}\,. \tag{4.32}$$

Using this definition, ψ_1 is the azimuthal angle around the z-axis and ψ_2 is the polar angle toward the y-axis. $\psi_1 = \psi_2 = 0°$ characterizes a vector along the y-axis, i.e., normal incidence with respect to the solar cell surface.

In the simulations discussed in the following, ψ_1 was varied while fixing $\psi_2 = 0°$, so that all rays propagated in the xy-plane. Three different cloak configurations were compared for an exemplary contact finger filling fraction of $f = 10\,\%$: the FFS, using the same design parameters as for the transmission experiments, the GRIN cloak with its refractive index truncated to the interval $n \in [1, 1.5]$ with a solid core made of polymer, and with an air-filled core.

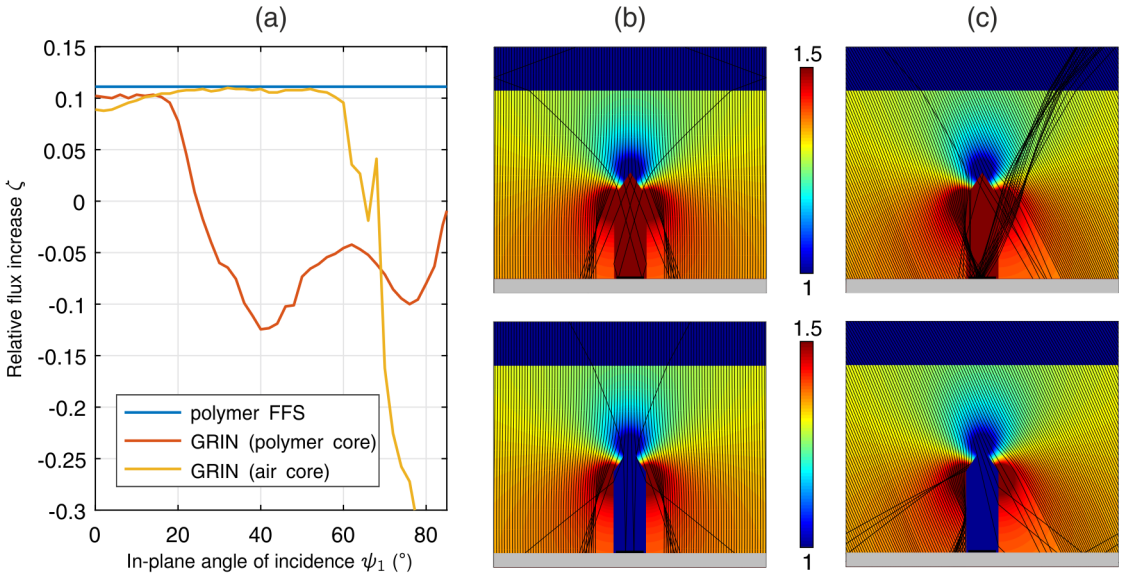

Figure 4.19: Simulated performance at oblique incidence for the FFS cloak and the GRIN cloak with its refractive index truncated to the interval $n \in [1, 1.5]$. Simulations neglected partial reflections for clarity. (a) Relative flux increase, showing ideal cloaking ($\zeta = \zeta_{max} \approx 11\,\%$) independent of ψ_1 for the FFS cloak. The angle-dependent performance of the GRIN cloaks can be understood from ray trajectories at (b) normal incidence ($\psi_1 = \psi_2 = 0°$) and (c) incidence at $\psi_1 = 30°$, $\psi_2 = 0°$ (see text). Adapted with permission from [136], © 2015 Optical Society of America.

IGNORING PARTIAL REFLECTIONS Figure 4.19(a) shows the relative flux increase ζ obtained from simulations where partial Fresnel reflections were switched off. Like this, the simulated ζ can be compared to the maximum achievable increase, $\zeta_{max} \approx 11\,\%$, to judge how perfect cloaking is. All three designs show good cloaking for angles up to 20°, with the FFS achieving full recovery of the shadowing effect. The FFS cloak keeps its perfect cloaking ability for all angles of incidence. For the GRIN cloak with solid polymer core, the relative flux increase drops strongly when the angle of incidence is increased beyond 20°. ζ even turns negative there, meaning that the addition of the cloak decreases the PCE of the solar cell. Interestingly, when replacing the polymer core by air, the angular dependence of the device becomes much more favorable, providing near-perfect cloaking for angles of incidence up to 60°.

The origin of this effect and other details of the angle-dependent flux increase for the two GRIN cloaks can be understood by considering the ray trajectories within the devices. At normal incidence (fig. 4.19(b)), rays

should follow the coordinate lines of the transformed space if the index values corresponded exactly to those resulting from the SC mapping (see fig. 4.7(a)). In the experimentally realizable device with truncated refractive index, however, rays follow coordinate lines only approximately. The deviation is especially pronounced in the central region, where the minimum and the maxima of the refractive-index distribution are located. Truncation of the minimum at the top of the forbidden region has the effect that rays are not redirected strongly enough. Thus, some rays enter the forbidden region and are back-reflected off of the contact finger, which impairs the cloaking effect. Truncation of the two maxima right and left of the forbidden region is less critical. The maxima only serve the purpose to homogenize illumination on the solar cell by deviating the rays coming from the minimum such that they travel along the vertical direction again. Truncation hinders this deviation from being as strong as designed, so that the illumination of the solar cell becomes inhomogeneous in the central region. In conclusion, it is the truncation of the minimum of the refractive-index distribution that leads to non-ideal cloaking at normal incidence.

Moreover, the ray trajectories in fig. 4.19(c) reveal why the GRIN cloak with air core is much more tolerant to oblique incidence. When filled with solid polymer, rays can enter the forbidden region and are even focused onto the contact finger by the refractive-index distribution. This decreases the cloaking performance drastically. Replacing the solid polymer by air, the core exhibits a refractive index considerably lower than the surrounding. Thus, rays approaching the boundary of the forbidden region at grazing angles are totally internally reflected, hence avoiding the contact finger. The effect breaks down when rays hit the interface of the forbidden region below the critical angle of total internal reflection. This happens for very oblique incidence, resulting in the dip in the relative flux increase at angles of incidence above 60°.

INFLUENCE OF FFS DESIGN PARAMETERS[6] The angle-independent ability of the FFS device for cloaking contact fingers without any losses is surprising at first sight, because when designing the FFS shape, normal incidence was assumed. As will be discussed in the following, it is the right choice of the design parameters that enables this angle-tolerant cloaking. As an example,

[6] While this paragraph focuses on a qualitative understanding of the role of the design parameters, a more quantitative analysis can be found in section 4.3.4.

let us consider the influence of $y(0)$, while R_1 and R_2 are fixed. Like this, the target region where rays hit the solar cell interface at normal incidence, is set. $y(0)$ defines the minimum height of the free-form surface, directly above the contact finger. The ray that intersects the FFS at $x = 0$ has to be refracted such that it hits $x' = \pm R_1$ on the cell surface. That requires only a small surface inclination if $y(0)$ is large, but a steep inclination if $y(0)$ is small. At the same time, the inclination at $x = R_2$ is bound to be zero. As a result, a FFS designed with a large $y(0)$ has a flatter shape than one for a small $y(0)$, which shows a stronger curvature.

But why does a stronger curvature lead to a better angle tolerance? This can be understood by considering the worst-case scenario in terms of incidence on the FFS. At any point on the FFS, the most oblique incidence is grazing, corresponding to a local angle of incidence of 90° against the surface normal. For simplicity, let us assume for now that incidence is fully within the xy-plane, so that rays incident tangentially to the FFS can either come from the right or from the left side. The situation is depicted in the left column of fig. 4.20, where 1.5 unit cells are shown. Light impinges onto the central half-unit cell, at grazing incidence from the right (red rays) and from the left (white rays). While the red rays hit the central part of the FFS tangentially, the white rays are tangential to the leftmost part of the FFS and hit the central part non-tangentially. All sensible in-plane angles of incidence lie between the angles assumed for the red and the white rays. Tracing the red and white ray from a fixed position on the FFS toward the solar cell, we obtain the hit positions corresponding to extreme angles of incidence, x'_{min} and x'_{max}. While x'_{min} is the intersection point of the red ray with the solar cell surface, x'_{max} follows from the white ray. Together, the two points define a spatial range in which rays refracted at position x on the FFS can land on the solar cell. Plotting the extreme intersection points versus the position of refraction at the FFS (right column of fig. 4.20), one can immediately see if cloaking is expected to work for all in-plane incidence angles. As soon as the range defined by x'_{min} and x'_{max} intersects with the position of a contact finger, cloaking becomes non-ideal.

For the optimized design parameters, this is not the case (fig. 4.20(a)), explaining why no angle-dependence was found when calculating the cloaking performance (see fig. 4.19). In fig. 4.20(b), the minimum height $y(0)$ was tripled as compared to the optimum value, leading to a flatter shape of the FFS as discussed above. Analysis of the extreme rays reveals that the smaller slope

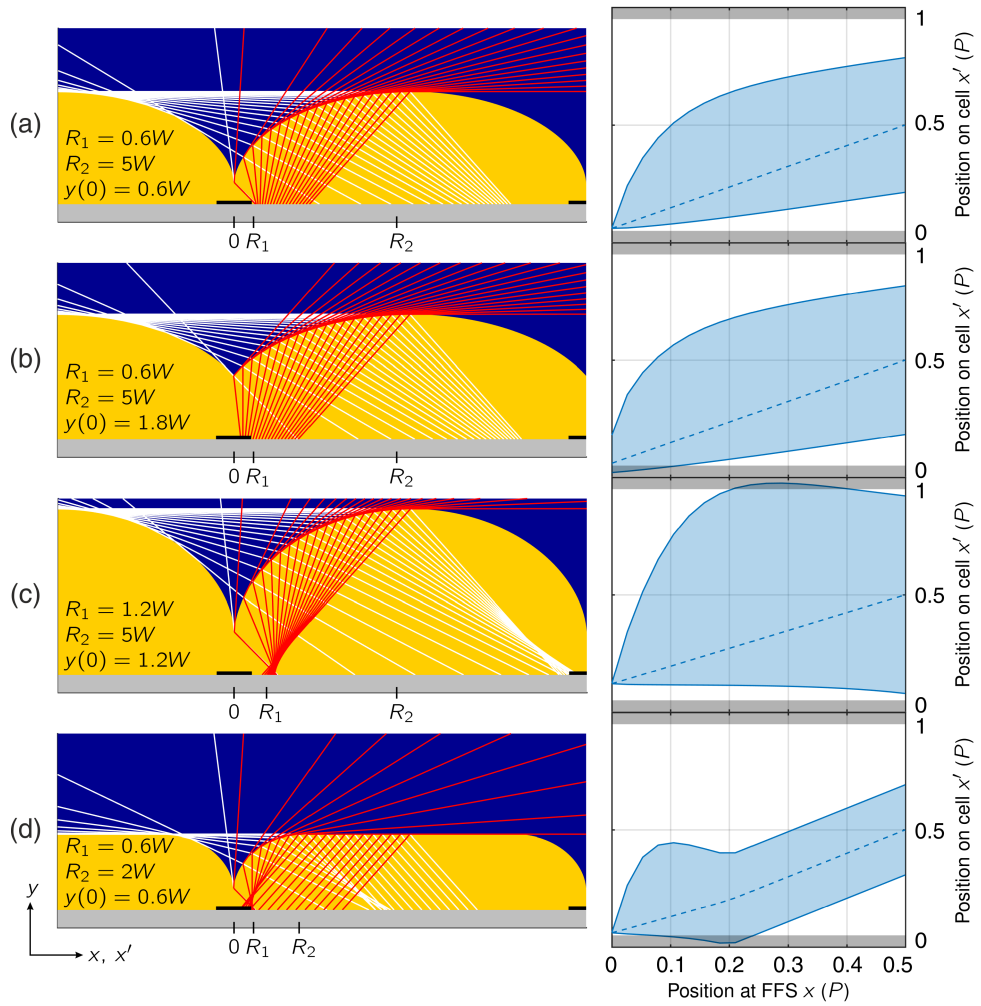

Figure 4.20: Tracing of rays at extreme in-plane angles of incidence through the FFS cloak (left column) for different sets of design parameters, while fixing $f = 10\,\% = {}^{W}/_{P}$. For every point on the FFS, minimum (red rays) and maximum (white rays) points of intersection with the solar cell surface were found, limiting the range of x' encountered when illuminating the FFS cloak from arbitrary in-plane angles (blue domains in right column). The dashed line corresponds to normal incidence. Cloaking is perfect in (a), where the range of x' does not extend beyond the position of contact fingers (gray domains).

leads to a failure of cloaking for the region above the contact finger. Here, the FFS is not steep enough anymore to refract the red rays sufficiently, and hence they hit the contact finger.

The influence of a non-ideal choice of R_1 is illustrated in fig. 4.20(c). Note that $y(0)$ had to be increased as well, because otherwise eq. (4.21) would be

violated. The ratio $y(0)/R_1$ was kept the same as for the optimum parameter set, though. At normal incidence, when increasing R_1, light is distributed to a smaller interval $x' \in [R_1, R_2]$ after refraction at the FFS. Therefore, the behavior of the FFS upon normal incidence is closer to that of a focusing cylindrical lens as for the optimum parameters. The surface shape required here has a stronger curvature and causes a lens-like behavior also at extreme incidence. Furthermore, the overall structure is relatively high, so that the white rays refracted at $x \approx 0.3P$ can reach the finger in the next unit cell. Both the focusing effect and reflection off of the adjacent contact finger can be detrimental to solar cell operation.

A similar effect is observed when reducing R_2, i.e., limiting the other side of the interval $x' \in [R_1, R_2]$. Again this makes the target region smaller, yielding a strong curvature and a comparable focusing behavior as for large R_1. In contrast, however, the total height of the structure is reduced here and FFS is horizontal in the domain $x \in [R_2, P - R_2]$. As a result, cloaking does not break down for the white rays, but for the red rays refracted at $x \approx 0.2P$. There, the surface is too steep as compared to the optimum case.

OUT-OF-PLANE INCIDENCE The above considerations limited the variation of the direction of incidence to the xy-plane for clarity. As will be shown in the following, it is also possible to draw conclusions about the FFS cloak performance under out-of-plane incidence from these results.

First, let us consider a point on the FFS at which incident rays with velocity $\boldsymbol{v_0}$ are refracted. For simplicity, the following description is done in the local coordinate system shown in fig. 4.21 whose xz-plane is tangential to the inclined surface. Refraction is governed by Snell's law, so that the angle after refraction, α only depends on the angle that the incident ray encloses with the surface normal, γ. Like this, Snell's law looks the same for all incident rays lying on a cone with opening angle γ around the surface normal. Thus, the refracted rays lie on another cone with opening angle α. Moreover, all refracted rays stay in the plane of incidence (defined by $\boldsymbol{v_0}$ and $\boldsymbol{n}$), so that a given ray lands exactly on the opposite side of the double-cone after refraction, with direction $\boldsymbol{v_1}$ (see fig. 4.21(a)). Furthermore, the contact finger problem is assumed to be invariant with respect to the z-direction. Therefore, only the projection onto the xy-plane is relevant for cloaking. More precisely, it is the component of α within the xy-plane that determines the distance between the contact finger and the intersection of the refracted ray with the cell surface.

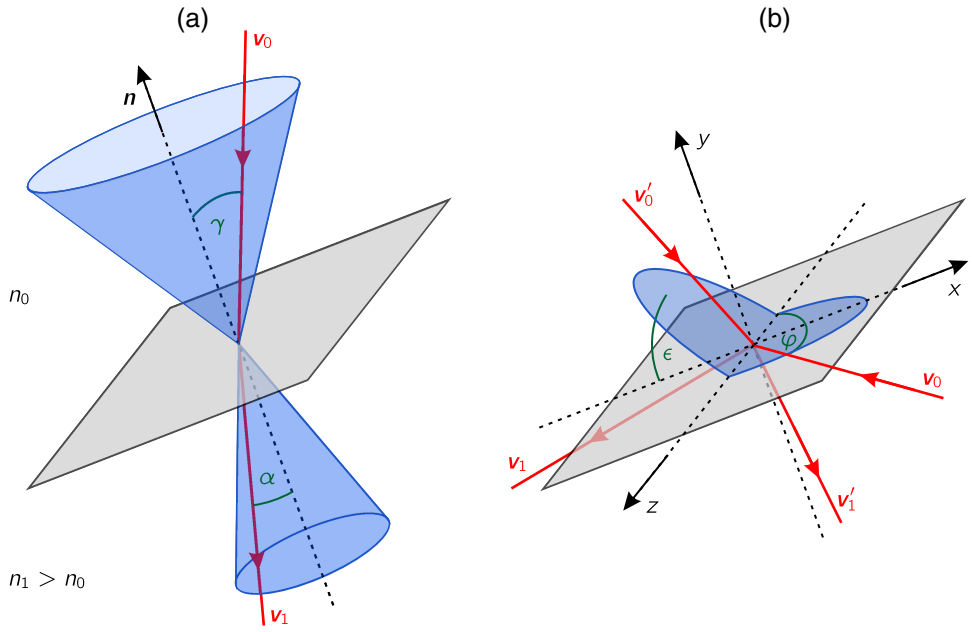

Figure 4.21: Refraction at a dielectric interface. (a) All rays with incident velocities lying on a cone with opening angle γ around the interface normal $\boldsymbol{n}$ lie on a cone with opening angle α after refraction. (b) In the limiting case of grazing incidence, the cone becomes a disk lying in the plane of the interface on the right. Incidence is characterized by azimuth φ. The left half of the disk is tilted upwards by an angle ϵ, because incident directions with lower ϵ are blocked by the adjacent FFS (see left column of fig. 4.20).

The in-plane component is calculated from

$$\tan \alpha_{xy} = -\frac{v_{1,x}}{v_{1,y}}, \tag{4.33}$$

so that the refracted rays hit the solar cell the further to the right the larger their α_{xy} is. All in all, the rays with extreme values of α_{xy} determine the range of hit positions on the solar cell for a given position on the FFS and for a fixed angle of incidence against its surface normal. Since the refracted rays lie on a cone around the surface normal, the rays with extreme α_{xy} are those that travel in the xy-plane.

This argument still holds when considering rays with grazing incidence as in the in-plane case. The single red and white ray refracted at a given point of the FFS, as shown in fig. 4.20, translate to a continuum of rays, coming from all possible directions that correspond to grazing incidence. Due to the translational symmetry along the z-axis, it is sensible to separate them into

rays coming from the right side (corresponding to the red rays), and those from the left side (white rays). For the rays coming from the right, there is no obstacle that hinders them from approaching the FFS tangentially, so that they all lie on a cone with an opening angle of 90°, i.e., a disk. This is different for the rays coming from the left, because their directions of incidence are limited by the edge of the adjacent FFS. That makes their direction vectors, $\boldsymbol{v}_0'$, lie on a tilted disk instead of a cone around the surface normal, as illustrated in fig. 4.21(b). This disk is rotated around the z-axis by an angle ϵ that follows from the position and shape of the FFS. In local coordinates,

$$\boldsymbol{v}_0' = \begin{pmatrix} -\cos\epsilon \sin\varphi \\ \sin\epsilon \sin\varphi \\ -\cos\varphi \end{pmatrix} , \tag{4.34}$$

where φ is the azimuthal angle around the surface normal with $180° \leq \varphi \leq 360°$, and $\epsilon > 0$ for incidence from the left. Applying Snell's law (eq. (3.2)), the direction after refraction becomes

$$\boldsymbol{v}_1' = -\begin{pmatrix} n_0/n_1 \cos\epsilon \sin\varphi \\ 1 \\ n_0/n_1 \cos\varphi \end{pmatrix} , \tag{4.35}$$

resulting in

$$\alpha_{xy} = -\arctan(n_0/n_1 \cos\epsilon \sin\varphi) . \tag{4.36}$$

Obviously, α_{xy} assumes its maximum value if $\varphi = 270°$, corresponding to incidence within the xy-plane from the left side. Letting $\epsilon = 0°$, the equation for α_{xy} holds for the rays incident from the right. As expected, α_{xy} assumes its minimum value at $\varphi = 90°$ in this case, i.e., at in-plane incidence from the right.

In conclusion, analyzing the performance of the FFS cloak under variation of in-plane incidence angles is sufficient to estimate its performance under arbitrary incidence. As a consequence, any combination of design parameters that leads to perfect cloaking independent of the in-plane angle of incidence is expected to yield perfect cloaking when averaging over the calendar year (see section 4.3.4), and vice versa.

INCLUDING PARTIAL REFLECTIONS When including partial Fresnel reflections at all interfaces in the ray-tracing simulations, there is no qualitative

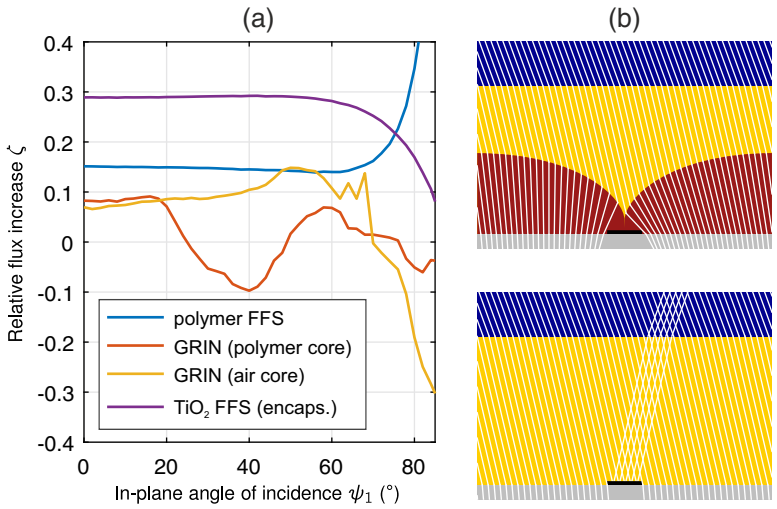

Figure 4.22: Simulated performance at oblique incidence for the FFS cloak made of polymer, a version of the FFS cloak made of titania for use in encapsulated solar cells, and the GRIN cloak with its refractive index truncated to the interval $n \in [1, 1.5]$. (a) Relative flux increase including partial reflections, showing angle-tolerant cloaking for the FFS designs. Global offsets between the curves arise from differences in reflectivity due to the different (average) refractive indices of the cloaks. (b) Exemplary ray trajectories for a FFS cloak made of titania ($n = 2.7$, red), encapsulated in EVA ($n = 1.5$, yellow), and corresponding reference situation (bottom). Adapted with permission from [136], © 2015 Optical Society of America.

change to the behavior of the cloaks for incidence angles below 40° (see fig. 4.22(a)). The absolute value of ζ, however, now differs significantly between the FFS and the GRIN cloaks. This can be explained by the different average refractive indices of the three designs, leading to different reductions in overall reflectivity.

To understand the phenomenon, let us consider a single dielectric layer with refractive index n_1 that is added to the silicon substrate with $n_{\mathrm{Si}} = 3.5$. Ignoring interference and multiple reflections, transmission from a surrounding medium with refractive index n_0 via the additional layer to silicon can be expressed as

$$\begin{aligned} T &= T_{0\to1} \cdot T_{1\to\mathrm{Si}} \\ &= \left(1 - \left(\frac{n_0 - n_1}{n_0 + n_1}\right)^2\right) \cdot \left(1 - \left(\frac{n_1 - n_{\mathrm{Si}}}{n_1 + n_{\mathrm{Si}}}\right)^2\right) \end{aligned} \tag{4.37}$$

at normal incidence. It is straight-forward to calculate that transmission is maximal if $n_1 = \sqrt{n_0 n_{\mathrm{Si}}}$. That means for silicon surrounded by air ($n_0 = 1$),

the refractive index of the additional layer resulting in the highest reduction of reflectivity is $n_1 = \sqrt{n_{Si}} \approx 1.9$.

While the average refractive index of the GRIN cloak is around 1.3, the refractive index of the FFS is 1.5. Since the latter lies closer to the optimum n_1, a stronger anti-reflective effect is expected for the FFS cloak. That is what leads to the higher relative flux increase for the FFS cloak in comparison with the GRIN cloaks.

The most prominent effect of switching on partial reflections was found for the polymer FFS cloak. At very oblique angles of incidence (above 60°), the relative flux increase rises steeply. This effect can be understood by considering the shape of the FFS. Due to its rounded profile, a large fraction of the incident light hits the FFS at angles close to the surface normal even at oblique incidence. Therefore, Fresnel reflection at the air-polymer interface is reduced, leading to a higher flux to the active area of the cell. This is different in the reference situation where we consider a flat polymer layer. There, Fresnel reflections increase rapidly for incidence angles above 60°, reducing the flux to the active area of the cell. As a consequence, the relative flux increase caused by the FFS cloak rises for very oblique angles.

INFLUENCE OF ENCAPSULATION Another important aspect is the influence of an encapsulation on the cloaking performance, because real-world silicon solar cells are typically encapsulated by an ethylene vinyl acetate (EVA) or silicone layer to protect them from environmental influences. These materials usually have refractive indices close to that of the polymer used for the FFS cloak [139]. Thus, embedding a polymeric FFS into such an encapsulant would reduce refraction at the encapsulant-polymer interface significantly and deteriorate cloaking performance.

Cloaking functionality can be restored by replacing the polymer by a material with higher refractive index, for instance titania ($n_1 = 2.7$ [140]), as illustrated in fig. 4.22(b). A FFS with a similar shape as the polymeric version can cause strong enough refraction to guide all incident light around the contact finger. Here, the design parameters $R_1 = 0.6W$, $R_2 = 5W, y(0) = 0.6W$ were chosen to be the same as for the polymeric FFS. The angle tolerance of the encapsulated FFS cloak can be seen from fig. 4.22(a) (purple curve). Only for very oblique incidence angles above 60° the relative flux increase evolves into the opposite direction as for the polymer version without additional encapsulation. This effect is attributed to the fact that the encapsulated FFS

constitutes a second interface at which back-reflections can occur that increase with the angle of incidence. In the reference situation of a flat encapsulation, this additional interface is absent, leading to lower back-reflections. Hence, the relative flux increase drops for high incidence angles in this case.

4.3.4 Averaging cloaking performance over a year

The figure of merit used so far, the relative flux increase ζ, is a quantity depending on the angle of incidence, as discussed above. This complicates comparison of different cloak designs, because the relative position of the sun and hence the angle of incidence varies with time. Therefore, it is desirable to condense the angle-dependent relative flux increase into a single figure of merit that also includes the variation of insolation over the course of the year. We call this quantity the annual average relative flux increase and define it as

$$\begin{aligned}\langle\zeta\rangle &= \frac{\text{energy deposited on active area with cloak}}{\text{energy deposited on active area with reference layer}} - 1 \\ &= \frac{\int_{\text{year}} E_{\text{dir}}(t)\Phi_{\text{ref}}(t)\,(\zeta(t)+1) + E_{\text{diff}}(t)\langle\Phi_{\text{cloak}}\rangle\,\mathrm{d}t}{\int_{\text{year}} E_{\text{dir}}(t)\Phi_{\text{ref}}(t) + E_{\text{diff}}(t)\langle\Phi_{\text{ref}}\rangle\,\mathrm{d}t} - 1\,. \end{aligned} \tag{4.38}$$

Here, E_{dir} and E_{diff} denote the direct and diffuse irradiance approaching the cell. Their values vary over the course of each day and also between seasons, depending on the location where the solar cell is installed. In general, direct irradiance dominates in arid climates (e.g. deserts), whereas the diffuse contribution is largest in regions that commonly have clouds (e.g. northern Europe). In Germany, direct and diffuse contributions are similar when averaging over the year [141].

The second factor in each term of eq. (4.38) takes care of the fact that not all the incident light ends up being absorbed by the solar cell: Φ_{ref} is the radiant flux that reaches the active area in the reference situation of a flat dielectric layer covering a solar cell with contact fingers. It depends on time as well, because the strength of Fresnel reflections off of the air-polymer interface varies with the direction of incidence. The direction was specified by two angles ψ_1, ψ_2 (defined in eq. (4.32)), which in turn vary with time as the sun moves in the local reference system. $\Phi_{\text{ref}}(\psi_1, \psi_2)$ was found by ray-tracing simulations for a discrete set of directions of incidence and was linearly interpolated in between. All flux factors are understood to be normalized to the incident flux Φ_0, so that they specify the relative amount of light that is

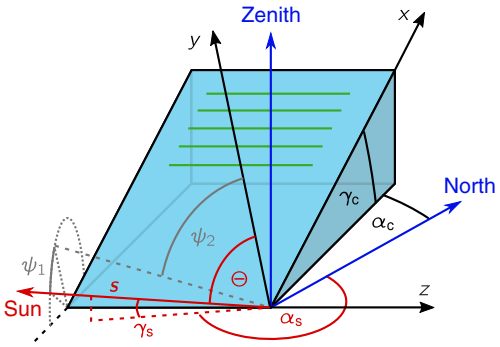

Figure 4.23: Illustration of a solar cell with contact fingers (green). Its orientation is characterized by inclination γ_c and azimuth α_c. The position of the sun is given by sun height γ_s and sun azimuth α_s, or direction vector $\boldsymbol{s}$. Axes labeled x, y, and z refer to the coordinate system used in ray-tracing simulations, with the y-direction perpendicular to the cell surface, contact fingers extended along z, and ψ_1, ψ_2 as defined in eq. (4.32). Adapted with permission from [136], © 2015 Optical Society of America.

transmitted to the active area. Φ_0 was omitted in the above equation, because it cancels out anyway (assuming all ray-tracing simulations are run with the same incident flux). For the diffuse contributions, the fluxes to the active area with cloak, Φ_{cloak}, and with reference layer, Φ_{ref}, were averaged over the hemisphere[7], i.e.,

$$\langle \Phi_{\text{ref}} \rangle = \frac{1}{2\pi} \int_{-\pi/2}^{\pi/2} \int_{-\pi/2}^{\pi/2} \Phi_{\text{ref}}(\psi_1, \psi_2) \cos\psi_2 \, \mathrm{d}\psi_1 \, \mathrm{d}\psi_2 \,,$$

$$\langle \Phi_{\text{cloak}} \rangle = \frac{1}{2\pi} \int_{-\pi/2}^{\pi/2} \int_{-\pi/2}^{\pi/2} (\zeta(\psi_1, \psi_2) + 1) \, \Phi_{\text{ref}}(\psi_1, \psi_2) \cos\psi_2 \, \mathrm{d}\psi_1 \, \mathrm{d}\psi_2 \,. \quad (4.39)$$

Note that eqs. (4.38) and (4.39) are valid for simulations that take partial Fresnel reflections into account. In the special case ignoring partial reflections, both equations keep their general form. The flux to the active area for the reference situation does not have to be computed via ray-tracing simulations in this case, but is given by the contact finger filling fraction as $\Phi_{\text{ref}} = (1 - f)\Phi_0$. That simplifies eqs. (4.38) and (4.39) considerably.

The time-dependent location of the sun can be specified by the sun azimuth $\alpha_s(t)$ and the sun height $\gamma_s(t)$ (see fig. 4.23). The two angles were computed according to DIN 5034, part 2 [142] for Karlsruhe conditions (latitude 49.007°N, longitude 8.404°E). The solar cell modelled by the ray-tracing simulations was assumed to be set up at the optimum orientation for a non-tracking solar cell

[7] The surface element on a unit sphere in the spherical coordinates according to eq. (4.32) is $\mathrm{d}A = \cos\psi_2 \, \mathrm{d}\psi_1 \, \mathrm{d}\psi_2$.

installed in Karlsruhe. This orientation is characterized by inclination $\gamma_c = 36°$ and azimuth $\alpha_c = 6°$ [143].

Note that the angles defining the position of the sun are measured toward the axes of the global coordinate system given by the Zenith and the North direction. Ray-tracing was carried out using a rotated coordinate system, with its x-axis parallel to the tilted edge of the solar cell, the y-axis along the surface normal, and the z-axis along the direction of the contact fingers, as shown in fig. 4.23. Therefore, the angle of incidence measured against the surface normal, $\Theta(t)$, was found by defining a vector $\boldsymbol{s}$ pointing toward the sun and expressing $\boldsymbol{s}$ in the rotated coordinates, so that

$$\Theta(t) = \arccos(\boldsymbol{s}(t) \cdot \hat{\boldsymbol{y}}) \ . \tag{4.40}$$

Here, $\hat{\boldsymbol{y}}$ is a vector along the y-direction of the rotated coordinate system with unit length.

Using the computed angles, the direct and diffuse irradiance on the oriented solar cell were obtained from the irradiance on the horizontal plane:

$$\begin{aligned} E_{\text{dir}}(t) &= E_{\text{dir,hor}}(t) \cdot \frac{\cos\Theta(t)}{\sin\gamma_s} \,, \\ E_{\text{diff}}(t) &= E_{\text{diff,hor}}(t) \cdot \frac{1}{2}\left(1 + \cos\gamma_c\right) \ . \end{aligned} \tag{4.41}$$

The time-dependent horizontal-plane irradiance data for Karlsruhe conditions was taken from the CM-SAF PVGIS database [143, 144]. The data did not include wavelength-dependent effects, but only the total irradiances, integrated over the full solar spectrum.

Finally, in order to carry out the integration over the year in eq. (4.38), $\boldsymbol{s}(t)$ was expressed in terms of the angles $\psi_1(t)$, $\psi_2(t)$. Then, the ray-tracing results for Φ_{ref} and ζ were inserted into eq. (4.38) as

$$\begin{aligned} \Phi_{\text{ref}}(t) &= \Phi_{\text{ref}}(\psi_1(t), \psi_2(t)) \,, \\ \zeta(t) &= \zeta(\psi_1(t), \psi_2(t)) \,. \end{aligned} \tag{4.42}$$

For all the computations of annual average flux increase presented in the following, ray-tracing was carried out for a discretized set of incidence angles. Here, ψ_1 was swept from 0° to 88° in steps of 2°, while ψ_2 was varied from 0° to 80° in steps of 10° and from 80° to 88° in steps of 4°. From the resulting relative flux increases, $\langle\zeta\rangle$ was computed for Karlsruhe conditions.

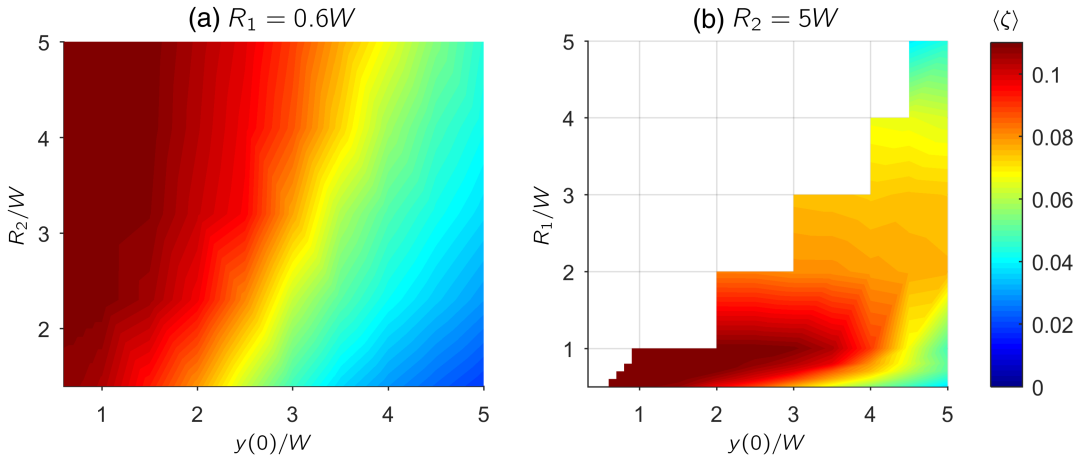

Figure 4.24: Calculated annual average flux increase $\langle\zeta\rangle$ depending on design parameters of the FFS cloak, for contact finger filling fraction $f = 10\,\%$, index contrast $n_0/n_1 = 2/3$, computed for Karlsruhe conditions without taking into account partial reflections. Cloaking performance is relatively tolerant against variations of R_2, but sensitive to changes of R_1 and $y(0)$.

Optimization of FFS design parameters As indicated in section 4.2.2, the optimum design parameters for the FFS cloak were found by maximizing $\langle\zeta\rangle$ for given refractive index contrast $n_0/n_1 = 2/3$, finger filling fraction $f = 10\,\%$, and finger period P. Neglecting partial reflections, the relationships shown in fig. 4.24 were found. When fixing R_1 to its optimum value (fig. 4.24(a)), variations of R_2 only slightly influence cloaking performance. The minimum height of the cloaking layer, $y(0)$, however, plays an important role for optimization of the annual average flux increase, $\langle\zeta\rangle$. For small values of $y(0)$, the performance of the FFS cloak approaches the ideal case, where $\langle\zeta\rangle = \zeta_{\max} \approx 11\,\%$. For fixed R_2 and varying R_1 and $y(0)$ (fig. 4.24(b)), optimum cloaking performance was found when both parameters were minimal. The region without any data shown corresponds to the part of the parameter space where $y(0)$ falls below the limit specified in eq. (4.20). The staircase-like boundary of the domain showing data reflects the discretization of the parameter sweep. For comparison, the computed annual average flux increase for the optimized FFS cloak is summarized in table 4.1, along with the data for the other cloak designs discussed so far.

Invisibility structure	$\langle \zeta_N \rangle$	$\langle \zeta_R \rangle$
GRIN (polymer core)	0.04	0.07
GRIN (air core)	0.09	0.10
FFS (polymeric)	0.11	0.20
FFS (TiO_2, encaps.)	0.11	0.29

Table 4.1: Annual average of the flux increase computed neglecting partial reflections, ζ_N, and including all reflections, ζ_R, for several cloak designs. Both calculations were referenced to a flat layer with refractive index 1.5 and thickness R_2. A contact finger filling fraction $f = 10\,\%$ was assumed and the half-width of the region to hide was $R_1 = 0.6W$.

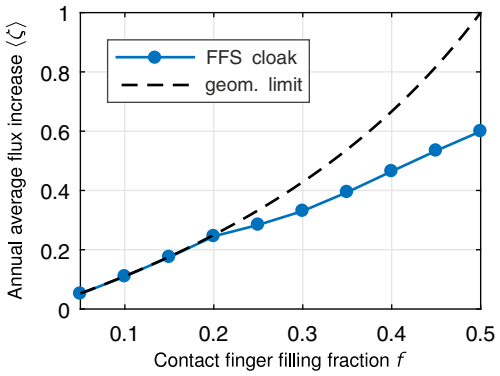

Figure 4.25: Calculated annual average relative flux increase obtained by the FFS cloak for Karlsruhe conditions, neglecting partial reflections. Perfect cloaking for contact fingers covering up to 20 % of the area is found. Adapted with permission from [136], © 2015 Optical Society of America.

MAXIMUM FILLING FRACTION An interesting question about the limitations of the FFS cloak is how dense the contact finger grid can be made without impairing perfect cloaking. This aspect was investigated by running ray-tracing simulations neglecting partial reflections for different f. A polymeric FFS ($n_1 = 1.5$) was employed to cloak the contact fingers. To change the filling fraction $f = W/P$, the finger width W was changed while keeping the period P constant. The design parameters were chosen the same way as above, i.e., $R_1 = 0.6W = 0.6fP$, $R_2 = P/2$, and $y_0 = R_1 = 0.6fP$. Since $y(0)$ increases with f, higher filling fractions generally lead to less compact FFS shapes.

The computed annual average flux increase for several filling fractions is depicted in fig. 4.25 together with the geometric limit given by $\zeta_{max} = f/1-f$. Again, this limit is only meaningful when considering the special situation where partial reflections are neglected. For filling fractions up to 20 %, the FFS cloak achieves perfect cloaking of the contact fingers when averaging over one calendar year. Increasing the filling fraction beyond this value, the relative flux increase does not correspond to complete elimination of the finger shadowing anymore. Nevertheless, addition of the cloak still leads to an appreciable flux increase as compared to a flat polymer layer. Considering the typical 5 % of area coverage for front metallization in current solar cells, this result

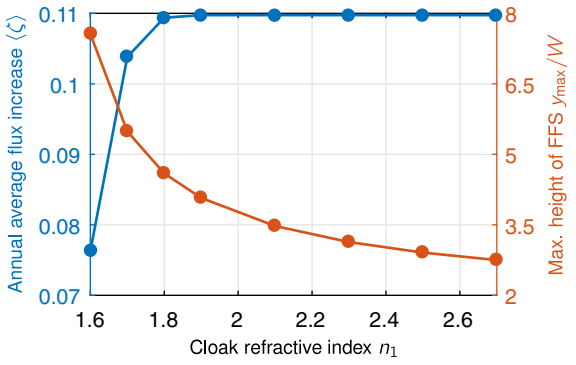

Figure 4.26: Calculated annual average relative flux increase (Karlsruhe conditions) for a solar cell ($f = 10\,\%$) with FFS cloak, encapsulated in a medium with refractive index $n_0 = 1.5$. Perfect cloaking is achieved for $n_1 > 1.8$. Increasing n_1 reduces the overall height of the cloak (measured from the solar cell surface, normalized to the contact finger width W).

illustrates the large potential of cloaking by dielectric free-form surfaces: By adding the FFS cloak, the density of the electrode grid could be increased significantly. Hence, series resistance could be minimized further without adding any optical losses from shadowing.

MINIMUM INDEX CONTRAST Another aspect relating to the limitations of the FFS cloak is the choice of the refractive index of the cloaking layer. As the working principle of the FFS cloak is based on a refractive interface, a certain index contrast between the constituting material of the cloak, n_1, and its surrounding, n_0, has to be present. As discussed in section 4.3.3, this aspect is especially important for solar cells that are encapsulated. For a FFS cloak made of titania ($n_1 = 2.7$), encapsulated in EVA ($n_0 = 1.5$), cloaking was observed for a large angular range. But what minimum index contrast is needed to enable perfect cloaking of the contact fingers?

The annual average flux increase for Karlsruhe conditions, $\langle\zeta\rangle$, again played the figure of merit in this consideration. $\langle\zeta\rangle$ was computed for different refractive indices of the cloaking layer, n_0, while keeping the index of the $10W$ thick encapsulant layer constant. The contact finger filling fraction was set to an exemplary value of $f = 10\,\%$. The design parameters $R_1 = 0.6W$ and $R_2 = 5W$ were chosen the same as earlier. $y(0)$, however, was not kept constant across the simulations for the following reason. According to eq. (4.21), the minimum and most favorable value for $y(0)$ changes with the ratio of the refractive indices, n_0/n_1. For the polymeric FFS cloak surrounded by air, $y(0) = 0.6W$ was chosen, larger than the optimum $y(0) \approx 0.45W$ roughly by a factor $4/3$. This resulted in a good compromise between large angle tolerance and ease of manufacturing of the structure by DLW. Therefore, for every n_1 investigated, the optimum $y(0)$ was calculated following eq. (4.21)

and multiplied by $4/3$ to yield the parameter $y(0)$ used for the design of the FFS cloak.

Figure 4.26 shows the result of the refractive index sweep. It can be seen that above a threshold refractive index of 1.8, the FFS cloak hides the contact fingers completely. At the same time, increasing n_1 leads to a reduction of the overall height of the FFS shape, making the cloak more compact. The titania FFS cloak discussed in section 4.3.3 exhibits perfect cloaking when its performance is averaged over the calendar year, because its refractive index $n_1 = 2.7$ lies well above the threshold value.

4.3.5 Extending the FFS cloak to include bus bars

When designing the FFS for contact finger cloaking, it was argued that the geometry is effectively two-dimensional, because the spacing of bus bars is typically much larger than the period of contact fingers. Nevertheless, as long as the bus bars are not removed entirely, they still contribute to shadowing of the active area. Apart from this potential practical relevance, it is an interesting academic question if the design method can be extended to include both bus bars and contact fingers. This aspect was investigated by Lukas Powalla in the scope of his Bachelor's thesis [145], which was done under the author's supervision. The results described in the following section are taken from this thesis.

To derive a FFS cloak for contact fingers only, a spatial mapping between one-dimensional domains was sufficient, hence we call this situation the 1D problem in the following. When taking into account bus bars, however, a mapping between 2D domains is necessary. For a rectangular grid of fingers and bus bars, the unit cell of the grid geometry is rectangular with an aspect ratio equal to the ratio of the respective periods. For simplicity, an aspect ratio of 1:10 was assumed here. Moreover, the relative coverage of the active area was assumed to be split equally between contact fingers and bus bars. The filling fractions, i.e., the ratios of their widths to their periods, was set to 10 %, so that in total $f = 19\,\%$ of the active area were shadowed by metal. Neglecting partial reflections, an ideal cloak would therefore increase the flux to the active area by $\zeta_{\mathrm{max}} \approx 23.5\,\%$.

The design of the cloak for the 2D problem was done similar to designing the FFS for contact finger cloaking. Again, the aim was to find a continuous surface of a homogeneous dielectric with refractive index $n = 1.5$ that refracts normally incident light such that it is homogeneously distributed in the region

between contact fingers and bus bars.

In analogy to eq. (4.13), a defining relation for the surface shape, $h(x,z)$, was derived. The result was an implicit, non-linear, inhomogeneous partial differential equation, and no method was found to solve the equation in a straight-forward way.

As an alternative, $h(x,z)$ was constructed from solutions to the 1D problem that were computed for the two directions individually. The two FFS shapes $h_1(x)$ and $h_2(y)$ were derived by the method described in section 4.2.2. Several ways of combining the two functions were tested, and the best was found to be the Pythagorean addition

$$h(x,z) = \sqrt{c_1 h_1^2(x) + c_2 h_2^2(z)} \tag{4.43}$$

with free parameters c_1 and c_2. The two parameters were optimized via a genetic algorithm provided by Matlab's ga function. Two different optimization strategies were investigated, corresponding to two different figures of merit. Both strategies were based on ray-tracing of rays through the FFS and calculating their intersection points with the solar cell interface. Partial reflections were neglected for straight-forward interpretation of the results.

The first figure of merit was meant to quantify how well refraction at the FFS realized the mapping of the ray positions prescribed for normal incidence. Therefore, for every ray, the distance between the hit point on the solar cell interface found by ray-tracing and that corresponding to a homogeneous distribution of the rays in the target region was calculated. The distance then was averaged across all rays, yielding the average mapping error. Optimizing this figure of merit using the genetic algorithm yielded a FFS cloak with good performance at normal incidence. Most importantly, no ray was found to reach the forbidden region around contact fingers and bus bars. Furthermore, the average mapping error was around 0.1 % of the bus bar period, so that the design requirement of homogeneous irradiance on the cell was fulfilled approximately. Finally, the annual average relative flux increase caused by the FFS cloak, $\langle\zeta\rangle$, was computed following the procedure described in section 4.3.4. In contrast to near-perfect cloaking at normal incidence, $\langle\zeta\rangle$ was found to be 10.5 % only. This is less than half of the relative flux increase expected for perfect cloaking, $\zeta_{\max} \approx 23.5\,\%$.

As an alternative approach, $\langle\zeta\rangle$ was used as the figure of merit for optimization of the two parameters c_1 and c_2. Again, cloaking performance was

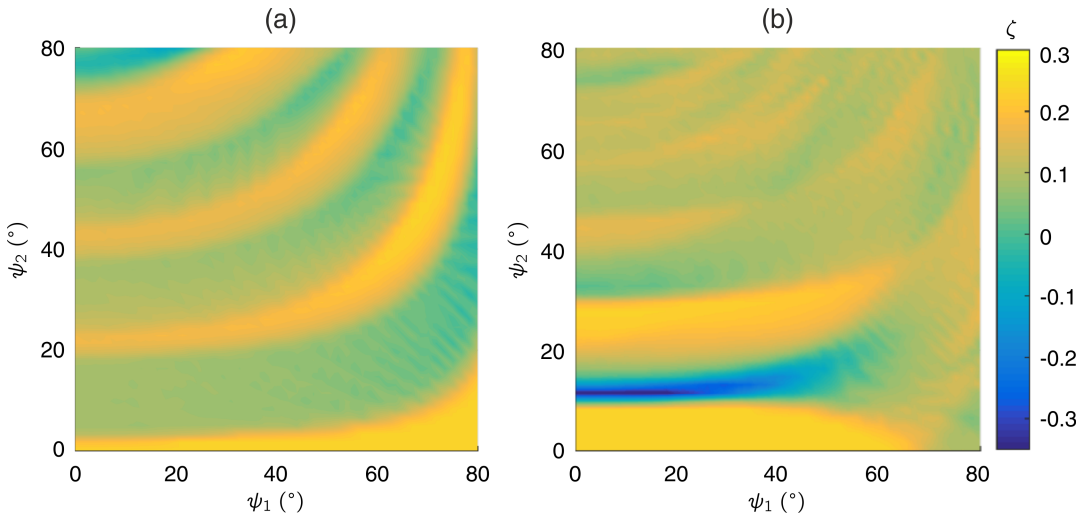

Figure 4.27: Angular dependence of the relative flux increase, ζ, caused by the FFS cloak for contact fingers (extended along x) and bus bars (extended along z) with total filling fraction $f = 19\,\%$. Cloaking of the bus bars is largely tolerant to in-plane incidence ($\psi_2 = 0$), but cloaking performance drops for out-of-plane directions of incidence. The FFS shape was optimized (a) to minimize mapping error at normal incidence and (b) to maximize the annual average relative flux increase. Adapted from [145].

good for normal incidence, but the annual average flux increase approached the same value, i.e., $\langle\zeta\rangle = 10.5\,\%$. As a comparison, the performance of a FFS cloak designed to hide only the bus bars was calculated. At $\langle\zeta\rangle = 10.2\,\%$, its annual average flux increase was only marginally lower.

The low annual average flux increase found in both cases was traced back to a much stronger sensitivity of the cloaking performance to variations in the angle of incidence as compared to the FFS for contact finger cloaking (see fig. 4.27). For the latter, the invariance along the direction of the contact finger was an essential ingredient when deriving that cloaking is independent of the angle of incidence, especially for out-of-plane incidence (see section 4.3.3). Therefore, as translational invariance is absent in the 2D case, the worse angle tolerance is understandable.

Apart from the continuous FFS cloak, two more concepts were investigated for hiding of contact fingers and bus bars. In one approach, a structure similar to a Fresnel lens was analyzed. The other scheme was based on generalized refraction at a metasurface. Both approaches, however, provided worse cloaking performance than the FFS cloak discussed above.

In conclusion, trying to extend the cloaking idea to include bus bars did not

lead to FFS designs providing significant enhancement over the situation with translational invariance. Additionally, the overall height of the 2D version is mainly determined by the period of the bus bars. That means the structure is approximately ten times as high (due to the 1:10 aspect ratio) as the cloak only hiding contact fingers. That hinders experimental realization, because the larger dimensions increase the time needed for printing the master by DLW significantly. Finally, the one-dimensional contact finger cloak was demonstrated to provide full relief of the shadowing problem for filling fractions up to 20 %. Thus, the need for bus bars within the active area could potentially be eliminated by increasing the density of contact fingers. For instance, if resistance in the contact fingers was small enough, the bus bars could be moved to a region of the solar cell where they do not cause shadowing.

For all these reasons, the FFS cloak based on the one-dimensional coordinate mapping was applied for the experimental prototyping discussed in the following section.

4.4 Prototype solar cells with FFS cloaks[8]

As a next step toward the implementation of contact finger cloaking on real-world solar cells, contact fingers of a prototype solar cell were cloaked using the FFS approach.

4.4.1 Solar cell fabrication

The silicon heterojunction (SHJ) solar cells equipped with a FFS cloak and characterized by the author were fabricated by collaborators at Forschungszentrum Jülich [146]. The structure of the SHJ cell is depicted in fig. 4.28(a). It is based on a 250 µm thick p-doped crystalline silicon wafer that acts as the absorber. On both sides of the wafer, buffer layers of intrinsic hydrogenated amorphous silicon oxide (a-SiO_x:H) were deposited via plasma-enhanced chemical vapor deposition (PECVD). These passivate the surface of the absorber layer to prevent detrimental recombination of the charger carriers via surface states. The layer of n-doped hydrogenated micro-crystalline silicon oxide (µc-SiO_x:H)

[8] The results presented in this section have been discussed in one of the author's journal publications [101].

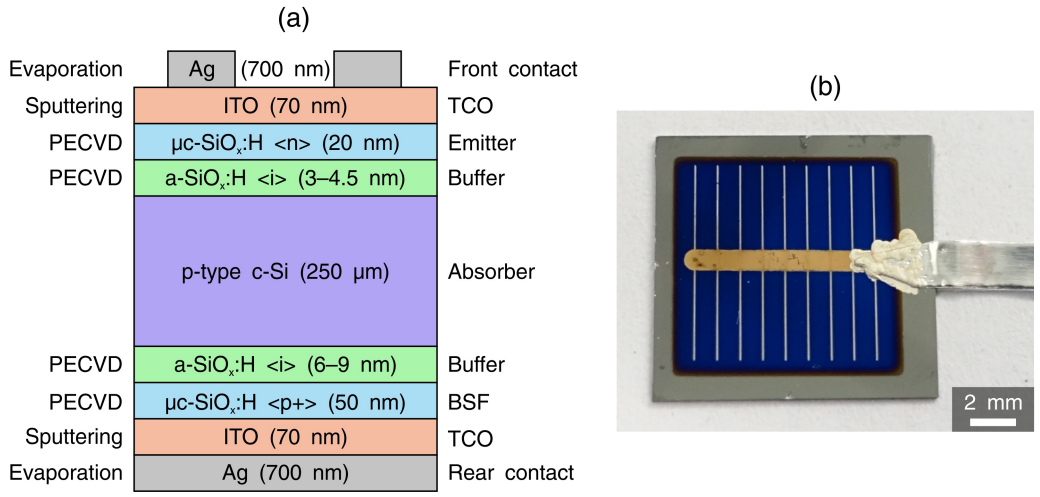

Figure 4.28: (a) Structure of the SHJ solar cells. Adapted with permission from [146], © 2012 WILEY-VCH Verlag GmbH & Co. KGaA, Weinheim. (b) Photograph of a pristine SHJ solar cell, featuring 18 contact fingers and a central bus bar. A conductive metal strip is attached to the bus bar to allow for electrical access after adding the polymer layer containing the cloaking structures.

on the front side creates a built-in field that attracts electrons generated in the absorber. A layer of heavily p-doped µc-SiO_x:H on the backside serves to create the back surface field, hindering electrons from reaching the rear contact, where they could easily recombine. Both layers of µc-SiO_x:H were deposited via PECVD. 70 nm of indium tin oxide (ITO) were sputtered onto both sides to create transparent conductive layers. At the front side, it additionally served as an anti-reflective layer: Its thickness was optimized to minimize reflections at the interface between air and the solar cell at wavelengths around 600 nm. The back electrode was formed by a 700 nm thick silver layer. On the front side, the current was extracted through a grid of contact fingers fabricated by thermal evaporation of silver through a shadow mask. The contact fingers were 700 nm thick, around $W = 64\,\mu m$ wide, and had a period of $P = 1\,mm$. To enable straight-forward external electrical contacting, a 1 mm wide bus bar crossed the contact fingers. A photograph of a typical cell featuring an active area of $1\,cm^2$ is shown in fig. 4.28(b).

4.4.2 Cloak design & realization

The FFS approach was employed to hide six of the contact fingers on one side of the bus bar. The cloak was fabricated via the soft-imprinting process

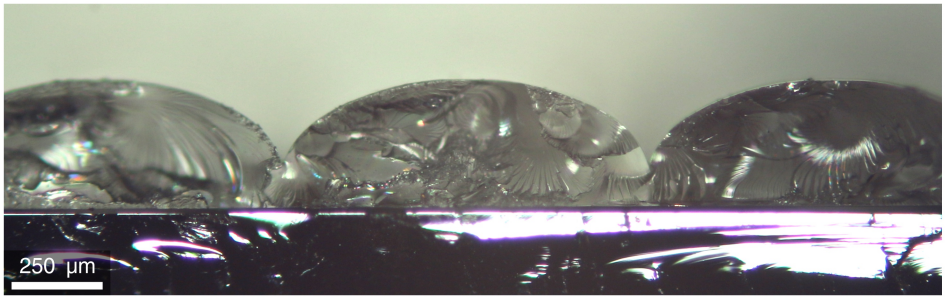

Figure 4.29: Optical micrograph of a cross-section of the soft-imprinted FFS cloaks on a solar cell. Visual inhomogeneities are caused by the rough topography resulting from cleaving the sample.

described in section 3.2, so that it consisted of the polymer OrmoComp. Hence, for the design of the cloak, a refractive index of $n_1 = 1.5$ was assumed. As in the transmission experiments (section 4.2.3), R_2 was set to the half-period of the contact fingers and the minimum height $y(0)$ was chosen close to its minimum possible value. The half-width of the cloaked region, R_1, was increased almost to the finger width to allow for sufficient alignment tolerance. All in all, the FFS shape was computed using the parameters

$$\begin{aligned} n_1/n_0 &= 1.5\,, \\ R_1 &= 60\,\mu\text{m}\,, \\ R_2 &= 500\,\mu\text{m}\,, \\ y(0) &= 60\,\mu\text{m}\,. \end{aligned} \tag{4.44}$$

It was confirmed by ray-tracing calculations that this combination of parameters provided all-angle cloaking for the given geometric contact finger filling fraction of $f_g = {}^{w}/_{p} = 6.4\,\%$. When neglecting partial reflections, the simulated cloaking performance corresponded to an angle-independent relative flux increase of $\zeta = \zeta_{\max} \approx 6.8\,\%$.

The inverse master structure for soft-imprinting was produced by DLW on an ITO-covered glass substrate using the $25\times/0.8\,\text{NA}$ objective and IP-S photoresist (see section 3.1 and appendix A.1.2). Shell-writing was employed, with exposure taking place at a speed of $8\,\text{cm/s}$ to reduce fabrication time. Like that, writing of the $6\,\text{mm} \times 4\,\text{mm}$ large master structure took close to 22 h. Converting the master into a soft version made of PDMS was a matter of a day, approximately. The resulting PDMS master was used to imprint the FFS cloak onto the SHJ solar cell (see section 3.2 and fig. 4.29). The final sample

was completely covered by polymer, showing the FFS shape at the position of six contact fingers, and flat everywhere else. As a consequence, the bus bar itself was not anymore physically accessible after imprinting. Therefore, a metallic strip was glued to the bus bar as an extension prior to the imprinting step.

4.4.3 Fabrication challenges

The fabrication protocol quoted above was the result of an optimization process during which several dozens of samples were produced with varying parameters and quality. The major challenges encountered while trying to find the optimum protocol are discussed in this section.

STITCHING ARTIFACTS The dimensions of the polymer master structure exceeded the field of view of the $25\times/0.8\,\mathrm{NA}$ objective used for DLW, which is limited to 400 µm in diameter. Therefore, it was not possible to scan the writing laser across the complete structure in a single step and thus expose it layer by layer. Instead, the overall structure was split into smaller blocks that fit into the writing field and each of the blocks was exposed layer by layer on its own. The coarse translation stage of the instrument served to move between the positions of the blocks. It is a common observation for stitched structures that visible stitching artifacts form at the block boundaries, most frequently grooves, bumps, or discontinuities of height. When fabricating the first FFS master structures, height discontinuities of up to 2 µm were observed. It was found that these were primarily caused by a tilt of the sample surface of about 0.1° against the plane in which the coarse translation stage moved. The tilt angle in turn depended on the position at which the substrate was fixed to the sample holder during writing. To mitigate the height discontinuities, a position with a tilt angle below 0.04° was chosen for the final masters.

Moreover, the DLW instrument showed a slight fall-off of the exposure dose toward the outer parts of the writing field. This can be attributed to the method by which the writing laser focus is positioned laterally: Displacements of the focus are achieved by varying the angle at which light is fed into the objective. Since the objective is optimized for normal incidence, light is focused less ideal in the outer parts, reducing the effective exposure dose there. This effect was observed to generate groove-like imperfections at the boundaries between blocks. Therefore, the dimensions of the individual blocks were

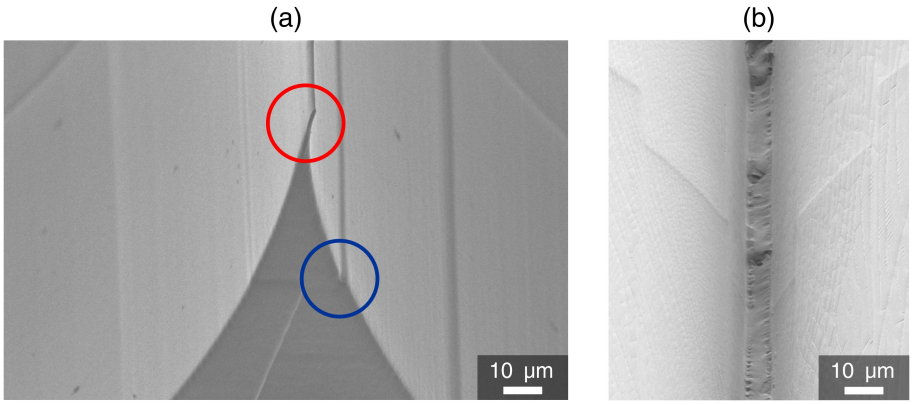

Figure 4.30: Oblique-view electron micrographs of FFS cloak fabrication steps. (a) Alumina-coated inverse polymer master showing a well-resolved, but slightly bent tip (red circle) with an approximate width of 1 µm. Stitching artifacts at block boundaries (blue circle) correspond to less than 0.5 µm height discontinuity between blocks. (b) 6 µm wide notch in the final FFS cloak after soft-imprinting on a solar cell.

optimized in order to establish a good compromise between short fabrication time (large blocks) and less pronounced stitching artifacts (small blocks).

Combining the two work-arounds, the height discontinuities between adjacent blocks were reduced to well below 0.5 µm (fig. 4.30(a)). Overall, this type of fabrication imperfection was not expected to severely impair cloaking performance of the FFS cloaks since the height discontinuities present only a limited number of localized deviations from the designed shape.

HARD OR SOFT MASTER? For the first imprints of the FFS cloak onto a solar cell, the polymeric master made by DLW was used. Before imprinting, alumina was deposited on the structure to allow for a hydrophobic silanization with OTS. Like this, the master was hardened and turned anti-adhesive toward the finished OrmoComp layer. This more direct approach of imprinting has the obvious advantage to spare the intermediate conversion of the master to a PDMS replica. However, the direct route was found to be less practical: The surface functionalization with OTS did not suffice to prevent adhesion between the master and the OrmoComp structure, supposedly due to mechanical tensions between the two relatively hard parts. Thus, the master had to be removed from the imprint in a quite violent procedure. Frequently, that lead to the formation of cracks or delamination of the OrmoComp layer from the substrate. Moreover, the master structure itself was damaged easily by the procedure, requiring to repeat the time-consuming DLW step to fabricate a

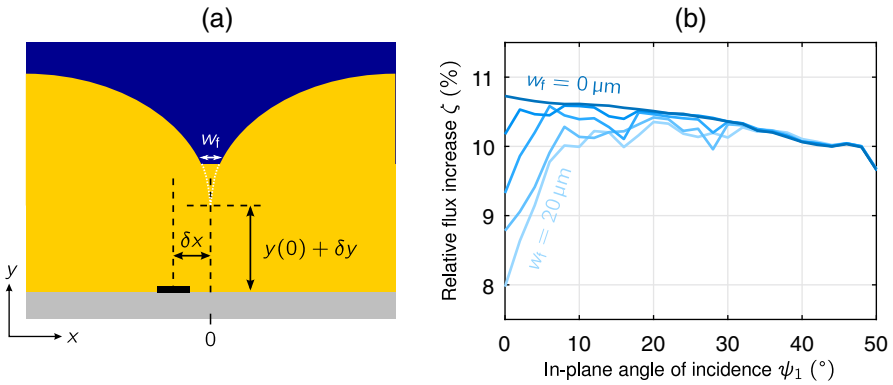

Figure 4.31: (a) Fabrication imperfections considered in ray-tracing simulations including partial reflections: finite notch width w_f, lateral misalignment δx, layer thickness discrepancy δy. (b) Effect of finite notch width for otherwise ideal FFS cloak. For angles $\psi_1 > 35°$, no difference in cloak performance was observed.

new master.

In contrast, when using the PDMS version of the master for imprinting, the master could be removed without applying violent force. Like this, the defects described above were avoided. A further advantage of this approach was that—in case the PDMS master got damaged—a new master could be obtained much quicker, by simply replicating the intermediate structure again. Finally, the PDMS master was more tolerant to deformations without taking damage because of its high elasticity. If, for instance, the master was erroneously approached too far during alignment so that it was pushed into the substrate, the PDMS stayed intact, whereas the alumina-coated polymer master was damaged severely.

FINITE NOTCH WIDTH In section 4.2.3 it was argued that the resolution of DLW limited the sharpness of the central notch in the FFS cloak. Since fabrication of the cloaks was based on DLW for the solar cell prototypes as well, a similar effect was expected. For some parts of the finished cloaks, however, the central notch was found to be around 6 µm wide (fig. 4.30(b)), i.e., larger than expected from the resolution when using the 25×/0.8 NA objective for writing (around 1 µm). This effect was attributed to mechanical damage of the master structures during replication and imprinting. Both the initial polymer master and the final PDMS master had the inverse geometry of the desired FFS cloak, i.e., they featured a sharp tip instead of the notch (fig. 4.30(a)). Due

to its delicacy, this tip could easily be deformed or even ripped off partially during removal of the master after replication or imprinting.

A less delicate tip would have resulted if the minimum layer height, $y(0)$, was chosen higher than the optimum value when designing the FFS cloak. On the other hand, as discussed in section 4.3.3, this would have lead to a diminished tolerance of cloaking performance to oblique incidence. Therefore, $y(0)$ was left at the optimum value. The effect of the finite width of the notch was studied in ray-tracing simulations including partial reflections. Here, the height given by the function $y(x)$ was truncated such that a flat region with finite width w_f formed in the central notch of the FFS cloak (fig. 4.31(a)). That mainly reduced the relative flux increase for near-normal incidence while having a negligible effect on oblique incidence, even if w_f was increased to 20 µm (fig. 4.31(b)). This can be understood from the fact that only for near-normal incidence rays can reach the notch. At more oblique angles, rays are instead refracted at the curved FFS.

LATERAL ALIGNMENT Before curing the OrmoComp resist during soft-imprinting, a proper alignment of the master with respect to the contact fingers on the solar cell had to be ensured. Lateral alignment was assessed optically using a stereo microscope. Cross-shaped markers added to the master structure in the DLW step served as guides. Like this, lateral alignment accuracies of well below 10 µm were achieved when aligning a single FFS cloak to a contact finger.

During the initial attempts to cloak several adjacent contact fingers it was found that the period of the master structure did not fit exactly the period of the contact fingers, hindering good lateral alignment in all unit cells. This was attributed to shrinkage through the fabrication process of the master. Shrinkage was found to occur during the PDMS replication step almost exclusively. The total shrinkage of 1.7 % corresponded to a maximum misalignment of around 100 µm over six periods of contact fingers, causing a clear drop of cloaking performance in the unit cell with the worst alignment. Luckily, shrinkage was reproducible enough to allow for pre-compensation: For the samples discussed in section 4.4.4, the designed cloak geometry was scaled up isotropically by a factor $1/1 - 0.017$ prior to fabrication via DLW. Like this, the overall lateral misalignment between the notches of the FFS cloaks and the contact fingers reduced to less than 20 µm. It was confirmed by ray-tracing simulations that lateral misalignments up to 60 µm did not have any influence

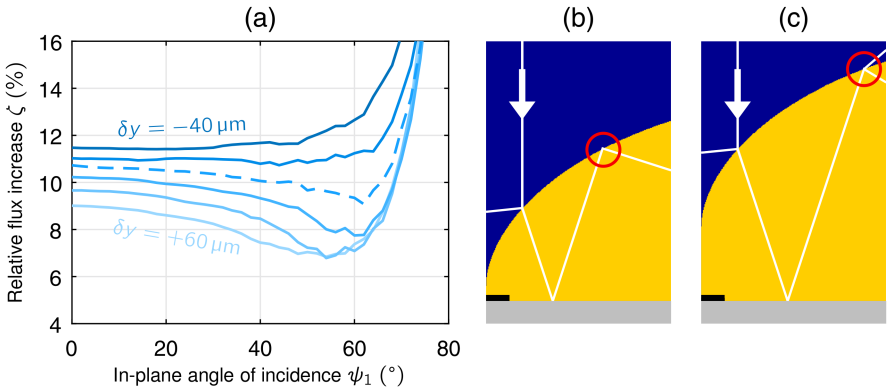

Figure 4.32: Simulated effect of layer thickness discrepancy δy. (a) Relative flux increase caused by the FFS cloak with respect to a flat layer (including partial reflections). The dashed curve corresponds to the design geometry ($\delta y = 0\,\mu m$). For $\delta y < 0$, more light is trapped by total internal reflection in the cloaking layer than for thicker layers, as illustrated for (b) $\delta y = -40\,\mu m$ and (c) $\delta y = +40\,\mu m$.

on the cloaking performance, even when including partial reflections and when averaging over the calendar year.

LAYER THICKNESS A more critical influence on cloaking performance was found to have the thickness of the cloaking layer. It was controlled by the height of a recess in the sample holder onto which the master was pressed during imprinting (see fig. 3.4). In order to produce polymer layers with a homogeneous thickness (excluding the region of the FFS itself), it had to be ensured that solar cell, sample holder, and master were not tilted with respect to each other. Possible relative tilts were corrected using a goniometer stage onto which the sample holder with the solar cell was mounted. Like this, the thickness of the fabricated polymer layer was typically within a $\pm 30\,\mu m$ range around the design thickness.

Ray-tracing simulations including partial reflections were run to understand the effect of the discrepancy of layer thickness, δy, on the angle-dependent cloaking performance (fig. 4.32(a)). For layers thicker than designed ($\delta y > 0$) cloaking performance worsened, as indicated by a lower relative flux increase at normal incidence and a less favorable tolerance to oblique incidence. Interestingly, the opposite behavior was found for $\delta y < 0$, so a deviation from the design height in this direction would in fact be beneficial. This effect can be explained by stronger light-trapping in the cloaking layer for lower

layer thicknesses (fig. 4.32(b-c)). In the experimental realization, δy must be larger than $-y(0) = -60\,\mu\text{m}$, because otherwise the tip of the master structure would penetrate into the substrate during imprinting. In order to avoid this while allowing for sufficient tolerance, $\delta y = 0\,\mu\text{m}$ was kept as the target value for imprinting.

4.4.4 Experimental characterization

Three different characterization methods were applied to assess cloaking quality of the soft-imprinted FFS cloaks on solar cells. All were based on comparing the optical performance of the solar cell in three distinct situations, namely

1. before soft-imprinting,
2. after soft-imprinting, when illuminated in the region with cloaked contact fingers,
3. after soft-imprinting, when illuminated in the region with a flat polymer layer burying the contact fingers.

As discussed in section 4.1, the optical performance of a solar cell manifests in its short-circuit current density, since J_{sc} is proportional to the irradiance on the active area.

For the pristine cell (before soft-imprinting), the contact fingers shadow a fraction f of the active area, reducing J_{sc} by a corresponding factor:

$$J_{sc}^{\text{pristine}} = (1 - f)\, J_{sc}^{0}\,. \tag{4.45}$$

Here, J_{sc}^{0} denotes the short-circuit current density that a hypothetical solar cell without contact finger shadowing, but otherwise identical optical and electrical properties would deliver.

Upon adding a polymer layer to the cell with contact fingers, two effects are expected. Firstly, transmittance from air to the solar cell changes because impedance matching is changed by the additional layer. This effect can be characterized by a transmission factor, T. Secondly, light being reflected off of the contact finger is not inevitably lost for current generation anymore, as it was for the pristine cell. Instead, it now has the chance to be back-reflected at the polymer-air interface toward the active area and eventually contribute to the light-induced current. This effect makes the shadowing caused by

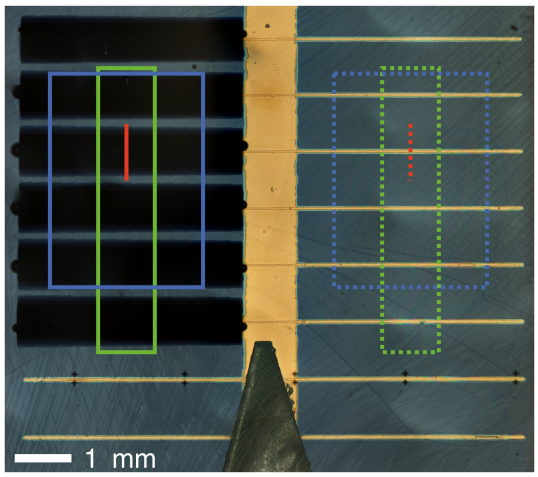

Figure 4.33: Optical micrograph of SHJ solar cell after soft-imprinting. Left of the bus bar, six contact fingers are cloaked by free-form surfaces; the rest of the cell is covered by a flat polymer layer. The region of the cloaks appears black in reflection because light is refracted away from the normal direction at the FFS, so that it cannot be collected by the imaging objective. The center between adjacent cloaks appears brighter due to the low local surface inclination, i.e., negligible refraction. Colored rectangles mark the regions where SISC (red), J–V (blue), and EQE (green) measurements took place for cloak (solid) and reference (dashed). Reproduced with permission from [101], © 2017 WILEY-VCH Verlag GmbH & Co. KGaA, Weinheim.

the finger appear smaller than implied by its geometrical shape. Hence, it can be described by an effective or optical filling fraction, f_{eff}, of the contact finger. Both effects are present in a flat polymer layer and in the FFS cloak. Additionally, the cloak reduces the effective filling fraction even further by refracting the light away from the contact finger. The short-circuit current density can therefore be expressed in terms of the effective filling fractions as

$$J_{\text{sc}}^{\text{flat}} = T\left(1 - f_{\text{eff}}^{\text{flat}}\right) J_{\text{sc}}^{0}\,, \quad J_{\text{sc}}^{\text{cloak}} = T\left(1 - f_{\text{eff}}^{\text{cloak}}\right) J_{\text{sc}}^{0}\,. \tag{4.46}$$

The results obtained by the three characterization methods were compared in terms of a common figure of merit, the relative increase in J_{sc} that the cloak caused over a flat polymer layer,

$$\zeta = \frac{J_{\text{sc}}^{\text{cloak}}}{J_{\text{sc}}^{\text{flat}}} - 1 = \frac{1 - f_{\text{eff}}^{\text{cloak}}}{1 - f_{\text{eff}}^{\text{flat}}} - 1\,. \tag{4.47}$$

Like that, the trivial effect of a changed transmittance is excluded from the discussion. This is considered a fair comparison, since real-world solar cells are usually encapsulated with materials of refractive indices $n \approx 1.5$ anyway.

The characterization methods were applied in regions of different size, as shown in fig. 4.33 for an exemplary solar cell after soft-imprinting.

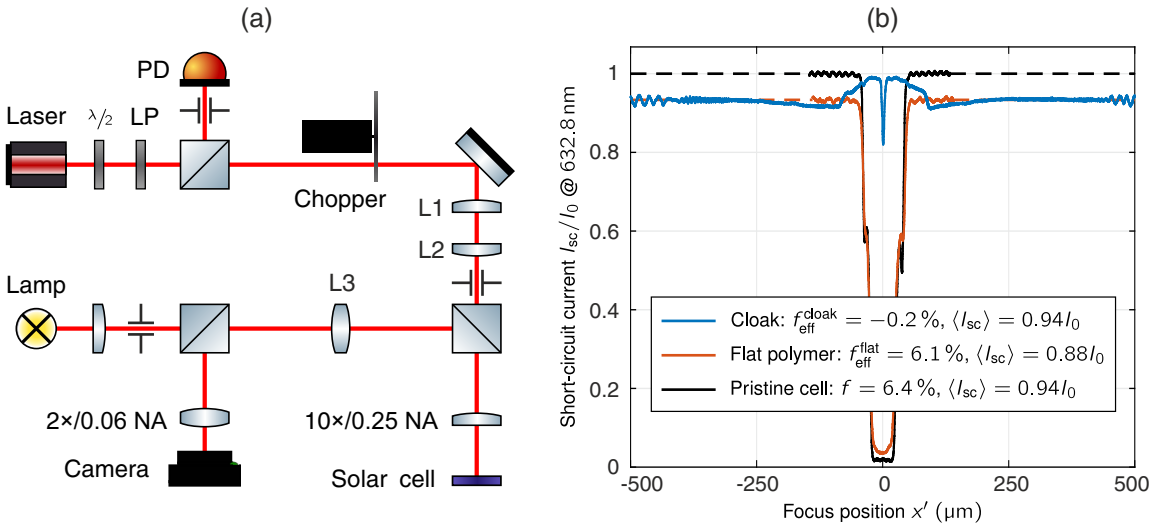

Figure 4.34: (a) Experimental setup for SISC measurements, where monochromatic light emitted from a helium-neon laser is focused on the surface of the solar cell. (b) Spatial profile of the short-circuit current generated by the cell upon localized irradiation. I_0 is the short-circuit current measured in the middle between two adjacent fingers for the pristine cell; the averages $\langle I_{sc}\rangle$ were calculated over one unit cell. Adapted with permission from [101], © 2017 WILEY-VCH Verlag GmbH & Co. KGaA, Weinheim.

4.4.4.1 *Spatially resolved current generation*

In the first experiment for characterization of the cloaking performance, the short-circuit current upon localized monochromatic illumination of the cell was measured. The focused illumination was scanned across a contact finger to obtain a corresponding spatial profile of I_{sc}.

MEASUREMENT SETUP The dedicated setup built to measure spatially resolved short-circuit current (SISC) profiles is depicted in fig. 4.34(a). A continuous-wave helium-neon laser[9] with a maximum output power of 4 mW served as the monochromatic light source at a wavelength of $\lambda = 632.8$ nm. The power was reduced by a combination of a half-wave plate and a Glan-Thompson polarizer (LP) which was set to transmit light with its electric field oriented along the z-axis. A silicon pin-type photodiode (PD) served to

[9]Laser: Coherent 31-2041-00, L1: $f_1 = 25.4$ mm, L2: $f_2 = 100$ mm, objective 10×/0.25 NA: Olympus 604490 ($f = 18$ mm), piezo stage: Piezosystem Jena PX400 and PZ100, L3: $f = 100$ mm, camera: Sony GigE Vision XCG-5005CR, objective 2×/0.06 NA: Edmund Optics 2× Mitutoyo compact objective, lock-in amplifier: Stanford Research SR830.

monitor the laser output power. The laser beam was modulated at a frequency of 1.1 kHz and expanded by a telescope made of two planoconvex lenses[9] (L1, L2) to fill the entrance pupil of the following 10×/0.25 NA objective[9]. Like this, the laser light was focused to the solar cell surface. Typical focus diameters were below 8 µm, as was confirmed by knife-edge measurements (see section 4.2.3). The cell was mounted to a piezo stage[9] allowing computer-controlled movement in the *xy*-plane. The surface of the solar cell was imaged to an intermediate plane by a biconvex lens[9] (L3), followed by imaging to a digital camera[9] using a finite-conjugate 2×/0.06 NA objective[9]. To measure the short-circuit current generated by the solar cell, it was electrically connected to a current pre-amplifier at zero bias voltage. Its output voltage was fed to a lock-in amplifier[9] for demodulation and amplification. The resulting signal was normalized to the current generated by the reference photodiode to account for variations of the output power of the laser.

RESULTS SISC profiles in the vicinity of the contact finger were recorded for the pristine cell and along the two paths shown in fig. 4.33 on the processed cell.

The profiles (fig. 4.34(b)) reveal what effect the contact fingers and the addition of the cloak has. For the pristine cell, I_{sc} drops to virtually zero in the central region where the contact finger is located. This finding indicates that the contact finger causes a near-complete shadowing of the active area. The shadowing effect does not change considerably when adding a flat polymer layer, as expected. What changes, however, is the short-circuit current generated in the region without a contact finger, which decreases by roughly 6 %. The lower I_{sc} is attributed to the anti-reflective performance of the ITO layer present on the front surface of the solar cell. As discussed in section 4.4.1, the thickness of the layer was optimized in order to minimize reflections when the cell was illuminated from air. Since the polymer layer has a different refractive index than air, the ITO layer is non-optimal in terms of reduction of reflectance. Thus, reflections at the interface between polymer and the solar cell increase (fig. 4.37(b)), leading to a reduced short-circuit current. This effect corresponds to the increase in transmission that was found in the proof-of-principle transmission experiments when adding the polymer structures (section 4.2.3). The direction of the effect, however, is reversed here, because the SHJ solar cell was optimized for operation at air in the first place. Real-world solar cells are typically encapsulated in materials with

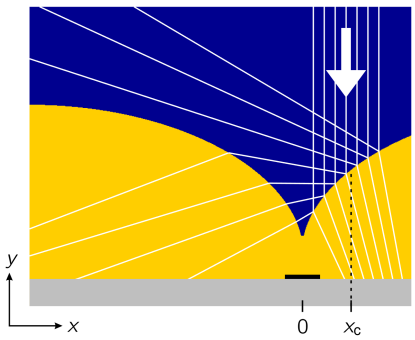

Figure 4.35: Ray-tracing of a bundle of normally incident rays, illustrating the light-gathering effect in the central region. Fresnel reflections are only drawn at the first interface for clarity. The reflected sub-rays of rays incident at $|x| < x_c = 0.09P$ hit the opposite side of the FFS, where they can be refracted toward the solar cell. For rays incident further away from the center, this is not possible.

refractive indices around 1.5, and their anti-reflective layer stack is designed accordingly. This argument thus once more motivates why it is sensible to choose the flat polymer layer as the reference situation for quantifying the cloaking performance.

The I_{sc} profile measured across a cloaked contact finger conforms to that of the reference situation between contact fingers. In the center, only a narrow dip indicates the presence of the contact finger. As in the transmission experiments, the dip is attributed to the finite resolution of the fabrication method, causing a flattening of the sharp notch of the FFS. Apart from this glitch, the cell produces the highest current when it is irradiated in the central region. This effect is attributed to enhanced light-gathering as illustrated in fig. 4.35. The FFS cloak allows for collection of the Fresnel-reflected portion of light incident in the central region. The effect is limited to a critical distance x_c around the contact finger. The value found in the ray-tracing simulations, $x_c = 0.09P$, conforms to the experimental observation. In the experiment, an increased current was observed for focus positions between $-80\,\mu m$ and $90\,\mu m$, corresponding to $x_c = 0.085P$.

For a more quantitative analysis of the cloaking effect, the (effective) contact finger filling fractions were extracted from the measured I_{sc} profiles for the three situations according to

$$f = 1 - \frac{\langle I_{sc} \rangle}{I_{sc}(x' = P/2)} \,. \tag{4.48}$$

Here, $\langle I_{sc} \rangle$ denotes the short-circuit current averaged over one unit cell of the contact finger grid, and the denominator represents the short-circuit current measured in the middle between two adjacent contact fingers. Like this, f measures the relative shadowing that the contact finger causes.

For the pristine cell, a filling fraction of $f = (6.4 \pm 0.7)\,\%$ was found.[10] Upon addition of the flat polymer layer, the filling fraction reduced marginally to $f_{\text{eff}}^{\text{flat}} = (6.1 \pm 0.7)\,\%$. In the region where the FFS cloak was employed, the contact finger was not causing any shadowing anymore, manifesting in an effective filling fraction close to zero, $f_{\text{eff}}^{\text{cloak}} = (-0.2 \pm 0.7)\,\%$. The reduction of f_{eff} when comparing cloak and flat polymer corresponded to a relative current increase of $\zeta = (6.7 \pm 1.1)\,\%$.

4.4.4.2 *Angle-resolved standardized characterization*

The second characterization experiment was meant to demonstrate the angle-dependent cloaking performance under realistic illumination conditions. For this purpose, current-density–voltage (J–V) characteristics of the solar cell were measured under illumination in a commercial solar simulator (WXS-90S-L2 by Wacom, Japan), whose output spectrum was certified to Class AAA. The results presented in the following were obtained from measurements under illumination with one sun that were calibrated to an AM1.5 spectrum.

The sample was mounted to a rotation stage, such that the in-plane angle of incidence ψ_1 could be varied. A shadow mask with a rectangular opening was fixed to the front side of the cell to restrict illumination to a defined area. The shadow mask was laser-cut from aluminum sheet metal, which was anodized subsequently to give it a matte black surface finish. This was essential to avoid spurious reflections on the side of the shadow mask facing the solar cell. The size of the mask opening was found from calibrated optical micrographs to be $3.76\,\text{mm} \times 2.70\,\text{mm}$. By aligning the mask as shown in fig. 4.33, the measurements were spatially averaged over $N = 4$ adjacent contact fingers.

Note that the length of the illuminated area, $l = 3.76\,\text{mm}$, is not an integer multiple of the period $P = 1\,\text{mm}$ of the contact fingers. Therefore, the (effective) filling fraction of the contact fingers is higher by a factor $NP/l = 4/3.76$ than in a hypothetical measurement where four full finger periods are illuminated. That reduces the light-induced current by a factor

$$c = \frac{1 - f}{1 - f\frac{NP}{l}}\,. \tag{4.49}$$

In both cases, the current density follows from relating the generated current to the total size of the mask opening. Thus, the measured current density is

[10] Details on the estimation of the measurement uncertainty can be found in appendix A.3.

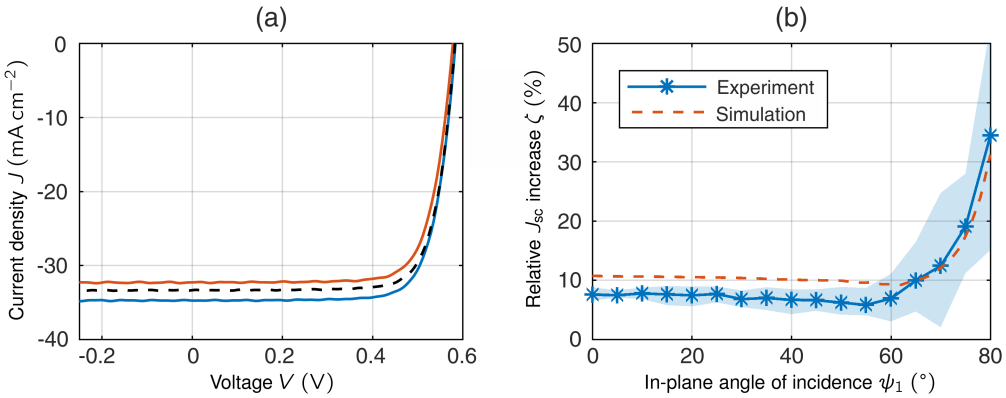

Figure 4.36: Standard solar cell characterization under one sun illumination. (a) J–V characteristics at normal incidence for the device shown in figs. 4.34 and 4.37(a). J_{sc} is 7.6 % higher in the cloaked region (blue curve) than in the reference region with flat polymer (red curve), efficiency increases by 9.9 %. (b) Relative increase in J_{sc} caused by the FFS cloak for varying in-plane angles of incidence ψ_1, averaged over a batch of six devices (blue curve). The shading represents the spread (minimum to maximum) of the measurements. Experimental results agree qualitatively with predictions from ray-tracing calculations (red dashed curve). Reproduced with permission from [101], © 2017 WILEY-VCH Verlag GmbH & Co. KGaA, Weinheim.

Table 4.2: Properties of the solar cell as extracted from the J–V characteristics shown in fig. 4.36(a).

	J_{sc} (mA cm^{-2})	V_{oc} (V)	FF (%)	η (%)
Cloak	34.8	0.584	76.5	15.5
Flat polymer	32.3	0.579	76.0	14.1
Pristine cell	33.4	0.583	76.9	15.0

also expected to be lower by the factor c than in the hypothetical situation. In order to enable a direct comparison among all three characterization methods, the current densities measured here were therefore adjusted by multiplying them with the correction factor c. Correction was omitted for measurements in the region with cloaked contact fingers, because the size of the illuminated area should not influence cloaking quality. In other words, the effective filling fraction was assumed to be close to zero for the FFS cloak. For the pristine cell and the reference situation of the flat polymer region, the (effective) filling fractions f and $f_{\text{eff}}^{\text{flat}}$ obtained from SISC measurements were used to determine c.

As for the SISC measurements, J–V characteristics were measured for the pristine cell and for illumination in the two regions of the processed cell indicated in fig. 4.33. For each of the three situations, short-circuit current density J_{sc}, open-circuit voltage V_{oc}, fill factor FF, and PCE η were extracted from the J–V curve (table 4.2). At normal incidence (fig. 4.36(a)), the cloak-induced relative increase in J_{sc} amounted to $\zeta = (7.6 \pm 0.5)\,\%$, whereas the efficiency of the cell increased by $\zeta_{PCE} = (9.9 \pm 0.5)\,\%$.[11] Both FF and V_{oc} did not change considerably in comparison to the pristine cell. Thus, the addition of the polymer layer to the cell did not seem to impede its electrical properties.

A set of five additional solar cells were prepared to verify reproducibility of the cloaking effect. For these cells, similar relative increases in J_{sc} were found (fig. A.2), while the increase in PCE was subject to variations. Note, however, that adding the cloak had a beneficial effect on PCE for all cells. The variations were attributed to fluctuations of FF and V_{oc} between measurements, which can be caused by varying quality of the electrical contacting, and fluctuations of the cell temperature, respectively.

The cloaking performance for oblique incidence was investigated by recording J–V characteristics at in-plane angles of incidence in the range $\psi_1 \in [0°, 80°]$, measured against the surface normal. The measurement was carried out for the complete six-device batch, where J_{sc} was determined for each of the cells. In order to determine the correction factor c, the respective contact finger filling fractions were measured via the SISC method. The dependence of the relative J_{sc} increase, ζ, on the angle of incidence, averaged over the six-device batch, is depicted in fig. 4.36(b). It can be seen that ζ shows a qualitative behavior compatible to ray-tracing calculations including all reflections. For $\psi_1 \leq 60°$, ζ stays relatively constant, showing values between 5 % and 8 %. At higher angle, a steep rise is observed, which can be explained by enhanced light-gathering (see section 4.3.3). The remaining quantitative discrepancy between measured and predicted current increase is attributed to remaining fabrication imperfections, such as surface roughness or a deviation of the FFS shape from the design. The relatively large spread in ζ, especially for angles of incidence above 60°, is expected to be caused by variations in the thickness of the cloaking layer among the six samples.

[11] Details on the estimation of the measurement uncertainty can be found in appendix A.3.

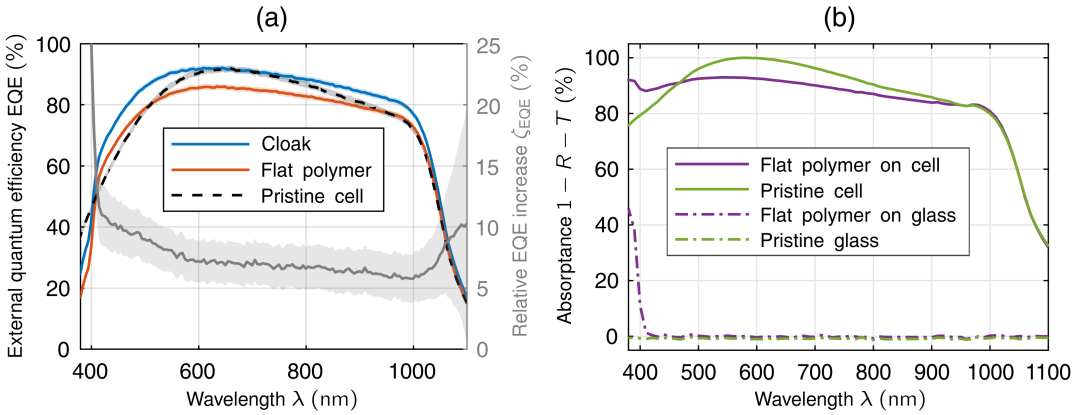

Figure 4.37: (a) Measured external quantum efficiency at normal incidence for the three test scenarios, showing a fairly constant increase in EQE between flat polymer and cloaked contact fingers. (b) Measured absorptance spectra for a solar cell without contact fingers (solid curves) and a glass substrate (dashed-dotted curves), before and after adding a flat OrmoComp polymer layer with similar thickness to that on the solar cells with cloaked contact fingers. Reproduced with permission from [101], © 2017 WILEY-VCH Verlag GmbH & Co. KGaA, Weinheim.

4.4.4.3 *Spectrally resolved current generation*

In a third characterization measurement, the wavelength-dependence of the cloaking performance at normal incidence was studied. Here, the EQE of the solar cell was measured using an experimental setup provided by Bryce Richard's group at Institute of Microstructure Technology at KIT. The cell was illuminated with a modulated monochromatic light source whose wavelength was swept through the range from 350 nm to 1100 nm in steps of 5 nm. For each wavelength, the short-circuit current was measured. By relating the measured wavelength-dependent I_{sc} to that of a reference solar cell with known EQE, the spectrally resolved EQE for the tested device was obtained. The region of measurement was restricted to the rectangular region shown in fig. 4.33 by inserting a mask in the beam path. With the region being approximately 1 mm × 5 mm in size, the resulting EQE is averaged over five full periods of contact fingers. No broadband bias light[12] was used to obtain the results shown in the following.

[12]When using bias light, the cell is illuminated with broadband light of approximately one sun additionally to the monochromatic light necessary for the actual EQE measurement. This can be sensible when the cell shows a different behavior upon global and localized illumination. For the SHJ cells characterized here, no difference between measurements with

Again, three situations were compared (no polymer, flat polymer, cloak), where the region with flat polymer served as the reference for the calculation of the relative EQE increase caused by the cloak. The measured spectrally resolved EQEs are depicted in fig. 4.37(a). Across the most relevant wavelength range between 400 nm and 1050 nm, a fairly constant relative increase of the EQE was found. By weighing the EQE data with the AM1.5 solar spectrum and averaging, the implied short-circuit current was computed, resulting in a relative current increase of $\zeta = (7.6 \pm 0.4)\,\%$.[13] While both the region with cloaked fingers and the reference region showed a similar spectral behavior in terms of their EQE, the EQE behaved somewhat differently for the pristine cell.

To allow for an understanding of this phenomenon, absorption spectra of a glass slide and a solar cell without contact fingers, before and after adding a flat layer of the OrmoComp polymer, were taken. The measurement was done in a commercial table-top spectrophotometer (Lambda 1050 by PerkinElmer, USA). The obtained spectra are depicted in fig. 4.37(b). Comparison of the two measurements at the glass slide (dashed-dotted lines) suggests that the polymer is highly transparent across the investigated spectral range, except for wavelengths below 400 nm, where absorption sets in. That explains why the pristine cell shows higher EQE at these wavelengths. Moreover, absorption in the polymer can, at least partly, explain the high relative increase in EQE between the flat polymer and the cloaked region: The average height of the cloak is lower than that of the region with flat polymer, and—on average—the cloak does not change direction of light propagation significantly. Therefore, the optical path length is shorter in the cloak than in the flat layer, mitigating the effect of absorption for the cloak.

The differences in behavior of EQE in the remaining spectral range can be understood by comparing the two absorption spectra measured on the solar cell without contact fingers (solid lines in fig. 4.37(b)). Overall, three distinct spectral ranges can be identified. For wavelengths between 400 nm and 470 nm, addition of the polymer layer increases the overall absorption. This indicates that at these wavelengths, the anti-reflective performance of the ITO layer is enhanced by the presence of the polymer. The opposite effect is present in the spectral range from 470 nm to 950 nm. As a result, the cell shows a reduced EQE in the region with flat polymer. Note that the EQE

and without bias light was found.

[13] Details on the estimation of the measurement uncertainty can be found in appendix A.3.

for the cloaked region exceeds that of the pristine cell nevertheless for the majority of this spectral range.

The fact that EQE is similar for pristine cell and cloaked region around a wavelength of 650 nm corresponds to the observations made in the SISC measurements at $\lambda = 632.8$ nm. There, pristine cell and cloaked region were found to deliver similar average short-circuit currents. For wavelengths above 950 nm, no influence of the polymer layer on overall absorption was found.

In conclusion, the cloaked region outperforms the flat polymer region across the complete spectral range. The detrimental increase in reflectivity caused by adding a polymer layer to the solar cell is overcompensated by contact finger cloaking for most wavelengths. Absorption in the ultraviolet could potentially be reduced by replacing the polymer by a different material. Apart from the trivial effects discussed above, no wavelength-dependence of the cloaking performance was found. This is in line with the ray-optical treatment of the cloaking effect.

In summary, both the GRIN and the FFS approach for cloaking of contact fingers on solar cells showed their potential for solving the shadowing problem. Interestingly, the FFS was predicted to show better performance than the GRIN device, especially at oblique incidence. Near-complete elimination of contact finger shadowing for all angles of incidence was found experimentally in a prototype device. This finding, along with the fairly low complexity of fabrication, makes the FFS cloak a good candidate for further boosting the efficiency of current real-world solar cells that rely on contact fingers.

Chapter 5

5 Cloaking metal electrodes on OLEDs[1]

In this chapter, after giving a brief introduction into the operation of organic light-emitting diodes, the design of a refractive free-form surface for cloaking of metallic electrode grids is discussed. Cloaking is demonstrated in a model experiment and on a top-emitting OLED. The remaining imperfections in cloaking quality are discussed based on ray-tracing simulations of the structure.

5.1 Operation of OLEDs

Broadly speaking, generation of light in LEDs is the inverse process of what happens in solar cells. While in the latter, photons are absorbed to create electron-hole pairs in a semiconducting material, in LEDs, electrons and holes recombine and create a photon in the process. As for solar cells, the semiconductor can be a solid-state or an organic material. Organic semiconductors owe their conductivity to the conjugation of the molecule which causes the electrons participating in π bonds to be delocalized. For such materials, the highest occupied molecular orbital (HOMO) and lowest unoccupied molecular orbital (LUMO) play the role that valence band and conduction band play in a solid-state semiconductor, respectively.

The simplest device architecture for an OLED is a single layer of an organic semiconductor that is sandwiched between an anode and a cathode. For the anode, a conductor with high work function is required so that its Fermi energy matches the HOMO level. A typical choice is ITO, yielding the additional

[1] Major parts of the results presented in this chapter have been discussed in one of the author's journal publications [147].

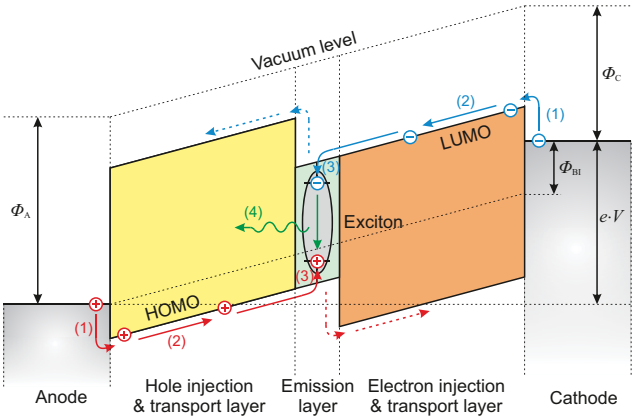

Figure 5.1: Energy diagram of a three-layer OLED under external bias voltage V, high enough to overcome the built-in potential Φ_{BI} given by the work function difference $\Phi_C - \Phi_A$. Charge carriers are injected from the electrodes (1), transported to the emission layer (2) where they form excitons (3) that decay radiatively (4). Reproduced with permission from [148], © 2012 WILEY-VCH Verlag GmbH & Co. KGaA, Weinheim.

benefit of a transparent anode. In contrast, the cathode is made of low work function materials such as calcium or aluminum with their Fermi energy close to the LUMO level of the emitting material.

The difference in the electrode work functions causes a built-in electrostatic potential, Φ_{BI}, that prevents electrons from leaving the cathode. The potential can be overcome by applying a negative bias voltage, V, at the cathode, so that electrons are injected into the LUMO of the organic semiconductor. Likewise, holes are injected into the HOMO from the anode. When the carriers meet in the semiconductor layer, they can form an exciton, which eventually decays into a photon.

While being straight-forward to understand, devices built with a single-layer architecture have long been believed to be limited to fairly low efficiencies. One reason for this is that no energetic barrier hinders the electrons from reaching the anode, where they can recombine without radiating a photon. This flaw can be alleviated by adding two more organic layers with carefully chosen electronic properties (see fig. 5.1). The resulting steps in the HOMO and LUMO levels lead to a confinement of electrons and holes to the emission layer, boosting the efficiency of exciton formation. Moreover, it is oftentimes challenging to find an anode material with high enough work function to allow for efficient injection of holes into the HOMO of the emission layer directly. In this case, an intermediate hole injection layer with a HOMO level between that of the emission layer and the work function of the anode can increase injection efficiency significantly. This is why most OLED devices under investigation today are based on some variation of this three-layer

architecture. Their internal quantum efficiencies were shown to approach 100 % [149], corresponding to near-lossless conversion of charge carriers into photons within the device. Out-coupling of the light can, however, still be a problem, as will be discussed in chapter 6.

OLEDs are usually fabricated by depositing the layer stack from the gas phase or from solution onto a glass or plastic substrate. That enables the cost-efficient production of large-area devices [150, 151] and has lead to widespread commercial application of OLEDs over the last years, most prominently in displays for consumer products. Moreover, OLEDs have proven to be power-efficient [152], can be mechanically flexible [153, 154] with tailored shapes [155], and can be transparent [156, 157].

These beneficial properties can also be exploited when using white-light OLEDs as large-area sources in lighting applications [158]. In that case, their mechanical flexibility [159] and the possibility to tune color rendering [160] can offer new degrees of design freedom. Especially for this application, it is desirable that the complete emissive area appears homogeneous, i.e., there are no variations in radiance[2] across the device. Achieving radiance homogeneity can be challenging because of the moderate conductivity of the transparent anode materials typically used. In devices with emissive areas above few square centimeters, a part of the externally applied bias voltage can drop at the resistance of the anode, thereby reducing the voltage available to drive light generation in the OLED stack. The effect increases with the distance from the metal contact connecting the anode to the external electric circuit. As a consequence, the emitted radiance can become inhomogeneous across the device [31].

Inhomogeneity can be mitigated by adding a grid of metallic electrodes to the front anode that reduce the series resistance [161–165], much as the metallic contact fingers on solar cells. For the OLED, the grid causes visible local variations in radiance by shadowing parts of the emissive area. These variations may be unwanted when using an OLED as a large-area light source.

[2] Radiance can be replaced by luminance here and in the following if the influence of the wavelength-dependent sensitivity of human vision shall be included. We stick with radiometric quantities to keep the discussion universal.

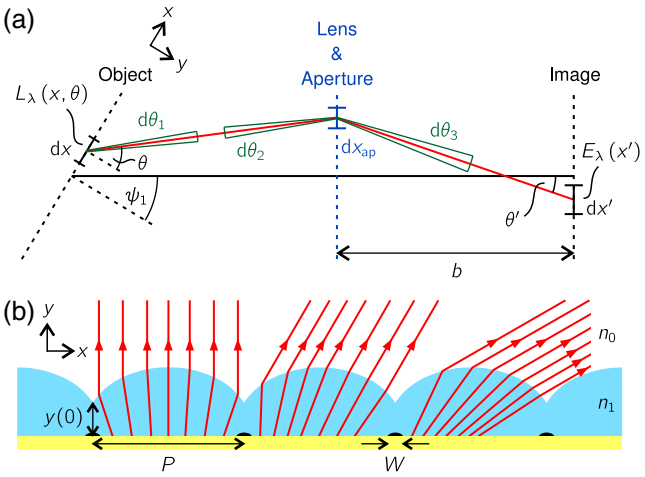

Figure 5.2: (a) Imaging of an object via an ideal lens at viewing angle ψ_1. (b) FFS cloak for grid electrodes with exemplary ray trajectories corresponding to paraxial imaging at $\psi_1 = 0°, -30°, -60°$. Adapted with permission from [147], © 2018 Optical Society of America.

5.2 Design of a cloak for electrode grids

For solar cells, a free-form refractive surface proved to be sufficient to hide contact fingers, so that all incident light was guided around them, unaffected of the angle of incidence. Can this concept be applied to the inverse problem as well? Can a similar FFS cloak hide metal electrodes on OLEDs so that they visually disappear for all viewing directions? Will the OLED with cloaked metal electrodes exhibit a homogeneous radiance?

In order to derive the requirements for cloaking of metal electrodes on OLEDs, let us assume that the problem is translationally invariant along the z-direction, so that electrodes are fully opaque strips with width W that are arranged with period P. Let us furthermore presume that the electrodes are positioned close together so that the spatial variation in radiance between adjacent electrodes is negligible.

The aim of hiding the metal electrodes from being seen can be formalized by considering imaging with magnification M of an object into an image plane at distance b from an ideal lens. This situation is sketched in fig. 5.2(a) for two dimensions for clarity, but the same point can be made in three dimensions. The object is rotated away from the optical axis by an angle ψ_1 around the z-axis, which determines the viewing direction. Suppose that the object is an OLED with opaque electrodes. It emits light with a spectral and angular distribution that is quantified by its spectral radiance,

$$L_\lambda(x,\theta) \equiv \frac{\mathrm{d}L(x,\theta)}{\mathrm{d}\lambda}\,. \tag{5.1}$$

Cloaking of the electrodes requires that the brightness in the image plane is perceived as homogeneous, meaning that the spectral irradiance,

$$E_\lambda(x') \equiv \frac{\mathrm{d}E(x')}{\mathrm{d}\lambda}\,, \tag{5.2}$$

has to be constant with respect to x'.

The spectral irradiance can be related to the spectral radiance in the image plane, $L'_\lambda(x', \theta')$, via eqs. (2.24) and (2.26) as

$$E_\lambda(x') = \int_{\text{ap.}} L'_\lambda(x', \theta') \cos\theta' \,\mathrm{d}\theta'\,, \tag{5.3}$$

where integration is carried out over the aperture. If Fresnel reflections are negligible, radiance is conserved along any ray, as discussed in section 2.3.2. Therefore, the spectral radiance at a given position x' in the image plane, L'_λ, can be replaced by the spectral radiance of the object, L_λ, at the corresponding position $x = x'/M$. Additionally changing the variable of integration leads to the relationship[3]

$$E_\lambda(x') = \frac{1}{b}\int_{\text{ap.}} L_\lambda(x, \theta) \cos^3\theta' \,\mathrm{d}x_{\text{ap}}\,. \tag{5.4}$$

Emission of an ideal OLED is Lambertian, i.e., the emitted spectral radiance is independent of the angle of emission for all wavelengths. As discussed above, its spatial dependence is solely determined by the shadowing that the metal electrodes cause. Assuming they are fully opaque, the spectral radiance of the object becomes $L_\lambda(x, \theta) = L^0_\lambda \Theta(|x| - W/2)$ in the unit cell centered at the contact finger at $x = 0$. Here, L^0_λ is a constant amplitude and Θ denotes the Heaviside step function. Inserting this result into eq. (5.4), the relationship

$$E_\lambda(x') = \frac{L^0_\lambda}{b}\int_{\text{ap.}} \Theta(|x'/M| - W/2) \cos^3\theta' \,\mathrm{d}x_{\text{ap}} \tag{5.5}$$

is found. Without the metal electrode, the Heaviside function would be absent from eq. (5.5), but apart from that, the relationship would be the same. Therefore, as expected when using an imaging system, the distribution of

[3] This equation is the two-dimensional version of the $\cos^4$ law that is well-known to describe the photographic vignetting effect.

spectral irradiance in the image plane reveals the presence of the electrode in the object plane. This fact is even more striking when assuming that the imaging lens has a low numerical aperture, so that the paraxial approximation $\cos\theta' \approx 1$ is justified. Then, integration becomes trivial and the irradiance in the image plane becomes proportional to the object radiance distribution. As a consequence, a sharp shadow is seen in the image that resembles the geometry of the metal electrode.

If a dielectric layer with refractive index n_1 is added to the OLED, light is refracted at the newly created interface between dielectric and the surrounding with refractive index n_0. Therefore, the relationship between positions in object and image plane cannot be described by a simple magnification factor M anymore. Instead, that relationship is given by a mapping function $x(x')$ whose behavior is dictated by the surface shape of the dielectric layer. Again neglecting Fresnel reflections at all interfaces, we arrive at the expression

$$E_\lambda(x') = \frac{n_0 L^0_\lambda}{n_1 b} \int_{\text{ap.}} \Theta\big(\big|x\big(x'\big)\big| - {}^{W}/_{2}\big) \cos^3\theta' \, \mathrm{d}x_{\text{ap}} \,. \tag{5.6}$$

The additional factor ${}^{n_0}/_{n_1}$ accounts for the fact that object plane and image plane are immersed in different media. In that case, basic radiance is the conservation quantity to be used, as discussed in section 2.3.2. The most important difference of eq. (5.6) with respect to eq. (5.5), however, is the occurrence of the mapping function $x(x')$ in the Heaviside function. The possibility to tune $x(x')$ by changing the shape of the dielectric-air interface enables us to prevent the Heaviside function from evaluating to zero during integration. Once this is achieved, the metal electrode is invisible in the image, because eq. (5.6) then takes the form that it would have if no electrode was present in the first place. In other words, the electrode can be hidden by refraction at a dielectric-air interface with an appropriate geometry: The interface shape has to ensure that all rays connecting image plane and object plane avoid the region of the metal electrode.

For a fixed angle of viewing ψ_1, it is sufficient when this requirement is fulfilled for a certain angular range $\delta\theta$ that depends on the size of the aperture. If one additionally requires that the electrodes shall be invisible independent of the direction of viewing, the above requirement has to be met for the full angular range $\theta \in [-90°, 90°]$. Apart from the reversed direction of propagation of the light rays, that requirement is similar to what was discussed in the context of cloaking of contact fingers on solar cells. There,

the free-form surface refracted the *incident* light in order to avoid the fingers. Cloaking was shown to be functional for all angles of incidence if the finger filling fraction was below 20 %.

Therefore, it can be expected that a FFS cloak is suitable for hiding metal electrodes on OLEDs from being seen from arbitrary directions, as long as the emission profile of the OLED is Lambertian for all emission wavelengths, Fresnel reflections are negligible, and the filling fraction of the electrodes is not too high. Exemplary ray trajectories for such a situation are depicted in fig. 5.2(b).

5.3 Realization & characterization

The ability of a FFS cloak to conceal electrode grids and homogenize the appearance of the emitting surface was validated experiments in two different situations. First, the FFS cloak was applied to an emissive surface with a near-ideal Lambertian intensity profile to demonstrate the principle of cloaking. Then, as a next step toward real-world application of the concept, the cloak was added to an actual top-emitting OLED prototype.

5.3.1 Model experiments

For the initial experiments, glass substrates with a light-scattering coating (Opal diffusing glass, Edmund Optics, USA) were chosen to model the surface of an OLED. Emission of the OLED was mimicked by illuminating the substrates from the backside using a white-light source (KL 300 LED, Schott, Germany). The emission emanating from the diffusive front side was confirmed experimentally to show a near-ideal Lambertian intensity profile (see inset in fig. 5.7(c)). A grid of 50 µm wide, 0.3 µm thick silver lines with a period of 500 µm was added to the diffusive side of the substrates via aerosol jet printing [166, 167].[4] Subsequently, a polymeric FFS cloak was added for hiding the silver lines. The FFS shape was computed following the recipe

[4]The measurement of radiant intensity profiles and the aerosol jet printing were done by Guillaume Gomard at Light Technology Institute, KIT, and Ralph Eckstein at InnovationLab Heidelberg, respectively. The following addition of the FFS cloak, experimental characterization, and ray-tracing simulations were carried out by the author.

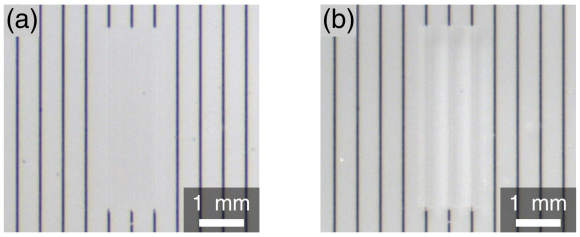

Figure 5.3: True-color photograph of the OLED model under (a) transmission illumination and (b) diffuse illumination by roomlight. The central three metal electrodes are equipped with an FFS cloak. Adapted with permission from [147], © 2018 Optical Society of America.

described in section 4.2.2, where the design parameters were chosen as

$$\begin{aligned} n_1/n_0 &= 1.5\,, \\ R_1 &= 50\,\mu\text{m}\,, \\ R_2 &= 250\,\mu\text{m}\,, \\ y(0) &= 110\,\mu\text{m}\,. \end{aligned} \tag{5.7}$$

As for the FFS cloaks for solar cells, an inverse polymer master was fabricated via DLW and converted to a softer copy made of PDMS that was finally used for imprinting the FFS shape into the polymer OrmoComp on the glass substrate with silver lines. Three of the silver lines were equipped with the FFS cloak, while the rest of the substrate was covered with a flat polymer layer.

The finished sample was characterized in a simple setup consisting of the white-light source for illumination from the backside and a camera (Blackfly PGE-50A2C-CS, FLIR, Canada) imaging the front surface of the sample. In a first test, two distinct situations were investigated, corresponding to an OLED in the on and the off state, respectively. Here, the OLED model was imaged using a camera objective with a focal length of $f = 35\,\text{mm}$ (C series fixed focal length lens, Edmund Optics, USA). Exemplary true-color photographs of the region around the three cloaked silver lines are depicted in fig. 5.3(a-b). To model an emitting OLED, backside illumination was switched on (fig. 5.3(a)). In that situation, the FFS cloak was found to hide the presence of the silver lines so that no trace of them was seen in the image. After switching off the backside illumination, the sample was only illuminated diffusively by the remaining roomlight. A considerable fraction of the light illuminated the sample from the front side, so that Fresnel reflections at the polymer-air interface revealed the presence of the cloaking structure (fig. 5.3(b)). Note, however, that also in this situation no trace of the silver lines themselves was visible in the image. The two photographs are also a good representation of

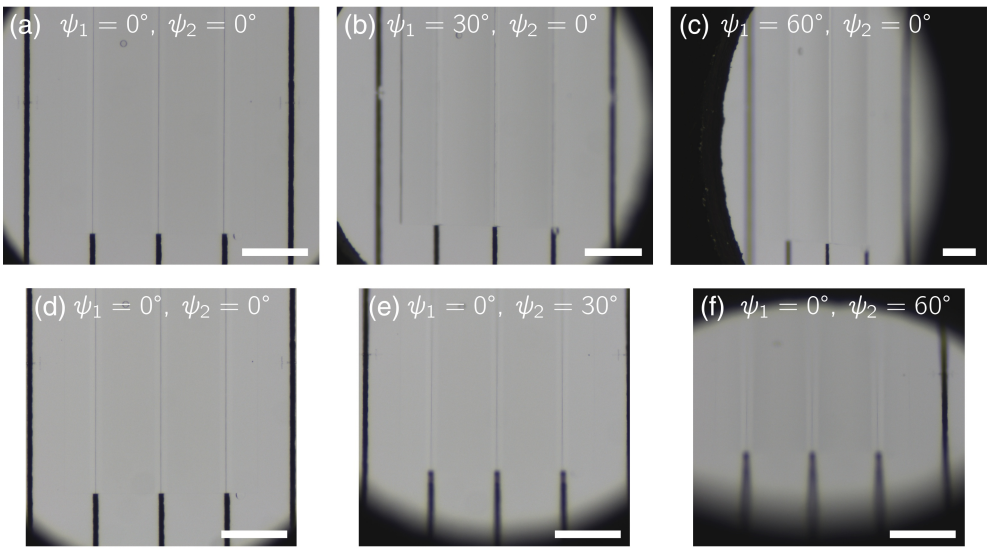

Figure 5.4: Gray-scale photographs of cloaked metal lines at different viewing directions on back-illuminated OLED model made from light-scattering glass substrates. An aperture was fixed directly to the front of the sample to suppress stray light. Positive values of ψ_1 indicate that the right side of the sample is closer to the observer than the left; at positive ψ_2 the top is closer than the bottom. Scale bars correspond to 0.5 mm along x (in the sample plane).

the impression of the OLED model when viewed by eye.

In both situations of illumination, no color-dependent effects were observed, as expected for an optical device operating in the limit of geometrical optics. Therefore, for the following quantitative analysis, the true-color images were converted to gray-scale by arithmetically averaging the three color channels. The resulting gray value of each pixel was taken to be proportional to the spectrally integrated irradiance at that position in the image plane. Proportionality was confirmed by comparing the gray values to the short-circuit current generated in a silicon photodiode (S2386-18K, Hamamatsu, Japan) upon illumination with varying radiant flux.

For the quantitative analysis, the objective for imaging the OLED model was replaced by a $2\times/0.06$ NA objective (Mitutoyo compact objective, Edmund Optics, USA) in order to provide a spatially more limited view with better resolution. Also, an aperture was added directly in front of the sample surface to avoid stray light from entering the objective and reducing the image contrast. Gray-scale photographs such as the ones depicted in fig. 5.4 provided the

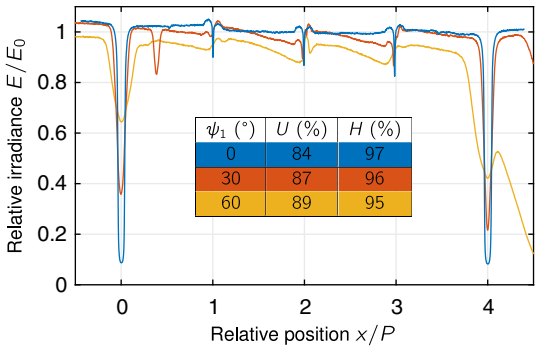

Figure 5.5: Irradiance profiles obtained from gray-scale images of the sample taken at different viewing angles. Profiles are normalized to the irradiance observed between electrodes in the region without cloak, E_0. Uniformity U and homogeneity H were measured over the central period. In the region without cloak, $U = 8\,\%$ and $H = 67\,\%$ for perpendicular viewing. Adapted with permission from [147], © 2018 Optical Society of America.

basis for further analysis. Both in-plane and out-of-plane angle of viewing (ψ_1 and ψ_2, respectively) were varied. Practically no effect of ψ_2 on the appearance of the cloaked metal grid was observed (see fig. 5.4(d-f)). This finding is in line with the argumentation in section 4.3.3, where it was shown analytically that independence of ψ_2 was expected for the FFS cloak for contact fingers on solar cells. Therefore, the following analysis focuses on the effect of variations of the in-plane angle of viewing, ψ_1.

Spatial profiles of irradiance were extracted from images as those shown in fig. 5.4(a-c); exemplary profiles for several values of ψ_1 are depicted in fig. 5.5. These were recorded with the transmission illumination switched on, simulating a light-emitting OLED. Here, the central three periods of electrodes were equipped with a FFS cloak, while the two outermost periods were buried under a flat polymer layer. A pronounced dip in irradiance can be seen at the position of the un-cloaked fingers. The relative depth of the dip is reduced considerably by adding the FFS cloak, corresponding to strongly reduced contrast of the shadowing effect.

To quantify these observations, two figures of merit were employed, uniformity U [168] and homogeneity H [169], defined as

$$U = \frac{\min(E)}{\max(E)}, \quad H = 1 - \frac{\langle |\Delta E/\Delta x'| \rangle}{\langle E \rangle / \langle |\Delta x'| \rangle}. \tag{5.8}$$

Both quantities were computed for the central period of contact fingers. Uniformity is the ratio of minimum and maximum irradiance and therefore describes the spread of irradiance within the unit cell. Homogeneity, on the other hand, is computed by averaging the discretized irradiance gradient over the unit cell; $\Delta x'$ is the pixel size of the camera sensor. Thus, H measures the average sharpness of features in the irradiance profile. This is a relevant measure

because human vision is sensitive to brightness gradients [170, 171]. Both figures of merit approach unity for a homogeneously emitting area without any electrode shadowing.

For viewing from the direction perpendicular to the sample surface, irradiance at the position of an un-cloaked metal electrode drops to 8 % of the reference value that was observed between electrodes. This results in a uniformity of $U = 8\,\%$ for that region, while homogeneity is $H = 67\,\%$ there. For all investigated angles of viewing $\psi_1 \in [-75°, 75°]$, the cloaked fingers showed irradiance uniformity above 80 %, and homogeneity above 90 %. Exemplary figures of merit for some viewing angles are summarized in the table in fig. 5.5.

Note that viewing the sample by eye, despite the imperfections seen in the quantitative analysis, the cloaked region appeared homogeneously bright and hardly any effect of oblique viewing directions could be seen.

5.3.2 *Discussion of cloaking imperfections*

Nevertheless, the source of the imperfections were analyzed numerically to study under which circumstances the FFS device can achieve ideal cloaking of the metal grid. For an ideally working cloak, the irradiance should be constant across the complete unit cell around one of the metal electrodes. Instead, the experimental profiles showed distinct features, such as a narrow dip in the center of the unit cell and an increased irradiance in the region around the center. Moreover, an irradiance offset between the profiles measured for different viewing angles was observed.

RADIANCE-BASED RAY-TRACING To understand the cause of these imperfections, 2D ray-tracing calculations of the unit cell around a metal electrode were carried out, using the same home-made simulation tool as for the cloaking of contact fingers on solar cells (section 4.3). The difference in terms of ray-tracing between the two scenarios of an illuminated solar cell and an emitting OLED are illustrated in fig. 5.6. Here, the simulations include all partial reflections.

For the solar cell, light enters the simulation region from the top. An exemplary ray at normal incidence is shown in fig. 5.6(a). It is attributed a radiant flux $\delta\Phi_0$. Upon hitting an interface, the ray is split into a transmitted and reflected sub-ray with flux values that are reduced by transmittance

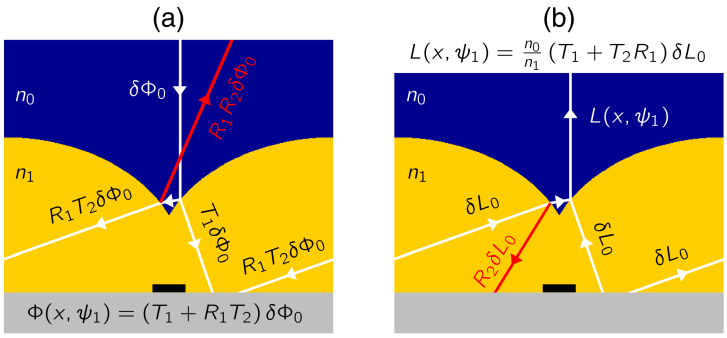

Figure 5.6: Ray-tracing including partial reflections (a) from top to bottom as for a solar cell with contact fingers and (b) from bottom to top as for an OLED. Besides the factor n_0/n_1, the relative radiance $L(x,\psi_1)/\delta L_0$ carried by the ray equals the relative flux $\Phi(x,\psi_1)/\delta\Phi_0$ received by the solar cell in (a), because the red rays do not contribute to flux and radiance, respectively.

and reflectance coefficients T and R, respectively. For the particular incident ray shown, two sub-rays reach the surface of the solar cell. Summing up their radiant fluxes yields the flux $\Phi(x,\psi_1)$ that the solar cell receives when illuminated from an angle ψ_1 by a ray passing through position x at the top of the simulation region. In this type of simulations, the figure of merit was calculated by summing $\Phi(x,\psi_1)$ over all positions x, yielding the total flux received by the cell when illuminated with parallel light from a certain angle ψ_1.

In the case of an OLED, it was the aim to simulate the irradiance profile on a screen that results from imaging the sample. The paraxial approximation $\cos\theta' \approx 1$ was applied, because the objective used for imaging had a low numerical aperture of NA $= 0.06$. As discussed in section 5.2, the irradiance distribution on the screen is then simply proportional to the radiance distribution $L(x,\psi_1)$ that the object emits toward the angle ψ_1. The radiance distribution was calculated at the top of the simulation region. Calculation of the radiance value for an exemplary position x and angle of emission $\psi_1 = 0°$ (i.e. normal viewing) is illustrated in fig. 5.6(b).

In contrast to the solar cell simulations, the rays now were attributed a radiance δL_0 instead of a radiant flux $\delta\Phi_0$. Like this, the radiance $L(x,\psi_1)$ of the ray leaving the simulation region at angle ψ_1 and position x could be found by summing the radiances of the sub-rays contributing to it. At the interface between the two media, the law of conservation of basic radiance—modified by transmittance and reflectance factors to account for Fresnel reflections—was applied. Apart from a factor n_0/n_1, the relative flux $\Phi/\delta\Phi_0$ found in the solar cell

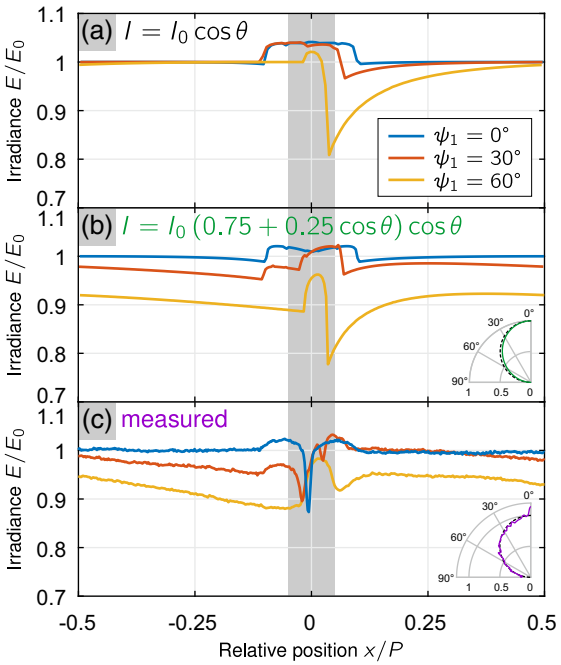

Figure 5.7: Irradiance profiles of one metal electrode with FFS cloak at different in-plane viewing angles ψ_1, simulated for (a) ideal and (b) non-ideal Lambertian emission, and (c) calculated from photographs of the back-illuminated sample. The irradiance offset between curves and the overall irradiance gradient observed in the experimental data is reproduced in the simulation of non-ideal Lambertian emission. Insets show the corresponding (b) simulated and (c) measured angular profiles of radiant intensity. All profiles are normalized to the irradiance in the center between adjacent contact fingers (at $x = \pm 0.5P$) for perpendicular viewing, E_0. Adapted with permission from [147], © 2018 Optical Society of America.

simulation equals the relative radiance $L/\delta L_0$ found in the OLED simulation. At first sight, this result is rather surprising, because the two situations are not exact time-reversed copies of each other. For both situations, one sub-ray is present that is absent in the other situation (red rays in fig. 5.6). But these rays do not contribute to the final flux and radiance, respectively, because they do not leave the medium that the initial rays were launched in.

In conclusion, the same algorithm as for simulations of light incident toward a solar cell could be used to find the radiance distribution for an emitting OLED with FFS cloak. For the simulations, the refractive index of the substrate (gray region in fig. 5.6) was set to equal that of the cloaking layer, $n_1 = 1.5$. Thus, no reflections occurred at the polymer-substrate interface. This should be a reasonable approximation of the experimental setting, because the refractive index of OrmoComp is close to that of the glass substrate. The radiance-based simulation approach was validated by comparing the results to those obtained when simulating the experimental situation in a commercial 3D ray-tracing software employing a Monte-Carlo approach (see appendix A.4). Good agreement was found, and the 2D radiance-based approach was selected as the method of choice for the simulations presented in the following. By design of the method, shot noise is absent, resulting in much shorter computation

times than for the Monte-Carlo approach.

IMPERFECTIONS IN CLOAKING The irradiance profiles resulting from the simulations of an emitter with an ideal Lambertian intensity profile are depicted in fig. 5.7(a). The profiles show a deviation from the behavior that is expected by design, namely a constant irradiance across the complete period. These discrepancies are caused entirely by Fresnel reflections that were not taken into account when designing the FFS cloak.

When viewing the sample from the normal direction (blue curve), irradiance is increased above the reference level in the central region. A similar effect was observed in the spatially resolved measurements of short-circuit current (SISC) discussed in section 4.4.4.1. There, the central I_{sc} bump was attributed to an enhanced light-gathering in the central region, as illustrated in fig. 4.35. For the emitting OLED, the inverse version of that effect is what causes the central irradiance increase. It can be understood by reversing the direction of light propagation in fig. 4.35. In the central region, rays traveling from the FFS toward the camera carry the radiance of two contributing sub-rays in the central region, but only carry that of a single sub-ray in the region with $x > x_c$.

For viewing from oblique angles, a second feature can be identified in the irradiance profiles, namely a sharp drop of irradiance close to $x = 0$, accompanied by a positive gradient at positive x. While the effect becomes stronger with increasing angle of viewing, the left half of the unit cell does not show this effect at all. This behavior can be understood by considering the angles at which light rays cross the polymer-air interface. For instance, consider the rightmost bundle of rays and the electrode left of it depicted in fig. 5.2. The rays closest to the electrode hit the FFS at the highest angles toward the surface normal, so that Fresnel reflectance is high. A considerable portion of the light is reflected back toward the emitting region, so that it cannot contribute to the irradiance observed in the image of the sample. Rays emitted further away from the electrode traverse the polymer-air interface at directions closer to the interface normal, so that Fresnel reflectance is reduced. Translating this argumentation to a unit cell that is centered to the metal electrode, the rays hitting the FFS close to the interface normal are those emitted from the left half of the unit cell.

As these imperfections in cloaking quality are solely caused by Fresnel reflections at the polymer-air interface, they could in principle be overcome by

applying some kind of anti-reflection layer. For instance, moth-eye structures could be suited to provide broadband reduction of reflections along with a wide angle tolerance [172–175].

The measured irradiance profiles depicted in fig. 5.7(c) were extracted from images similar to those shown in fig. 5.4. The profiles do not agree very well to the simulation of an ideal Lambertian emitter (fig. 5.7(a)). Most prominently, an irradiance offset between the curves for the different viewing angles and a negative irradiance gradient for oblique viewing are present. Moreover, a narrow dip is seen close to $x = 0$, similar to that seen in the SISC results. As for the solar cell measurements, this dip is attributed to the finite width of the notch of the FFS caused by fabrication imperfections. Offset and negative gradient, however, cannot be understood by comparison with the contact finger cloaks for solar cells. In fact, the ray-tracing results shown in fig. 5.7(b) suggest that deviations of the emission from an ideal Lambertian intensity profile can be the cause. In order to obtain the profiles shown, an intensity profile of the form $I(\theta) = I_0 \, (0.75 + 0.25 \cos\theta) \cos\theta$ was simulated. To achieve this, the angle of emission θ was taken into account when assigning a radiance to the constituting sub-rays, i.e., δL_0 (as shown in fig. 5.6) was replaced by $\delta L_0 \, (0.75 + 0.25 \cos\theta)$. This modification lead to a slight change of the intensity profile (inset in fig. 5.7(b)), but introduced both the experimentally observed offset and a negative gradient into the simulated irradiance profiles.

Measurements of the intensity profile emerging from the glass substrate when illuminated from the back confirmed that emission had a near-ideal Lambertian profile (inset in fig. 5.7(c)). Taking into account the measurement uncertainty, both simulated situations, i.e., ideal and non-ideal Lambertian emission, were compatible with the measured data. Therefore, it was concluded that it is a deviation from ideal Lambertian emission that caused the offset and negative gradient in the measured irradiance profiles.

5.3.3 OLEDs with metal fingers

As a next step toward real-world application, the FFS cloak was applied to a top-emitting OLED prototype. The OLED had an emissive area of few cm^2 only, so that it did not require a metallic grid to enable homogeneous emission across the complete area. Therefore, an electrode grid was mimicked

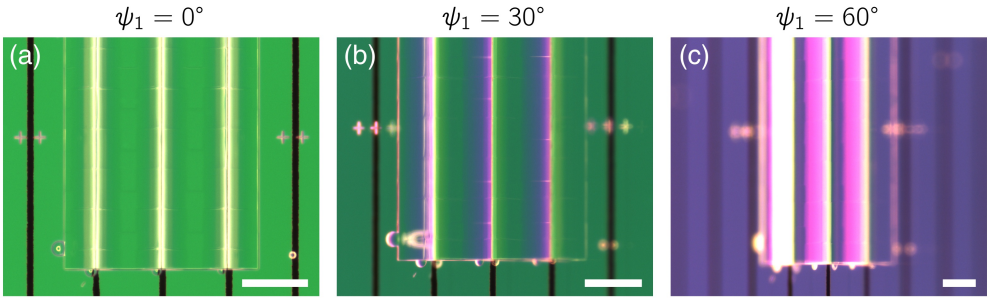

Figure 5.8: True-color photographs of cloaked metal lines at different in-plane viewing angles on an actual top-emitting OLED. The dependence of the emitted spectral radiance on the emission angle results in an inhomogeneous appearance with variations in perceived brightness and color. Positive values of ψ_1 indicate that the right side of the sample is closer to the observer than the left. Scale bars correspond to 0.5 mm along x (in the sample plane).

by adding silver lines via aerosol jet printing.[5] They had the same dimensions as for the model OLEDs, so that a FFS cloak with the same design parameters could be employed for hiding them. Photographs of the region with cloaked silver lines were recorded at several viewing angles; exemplary ones are depicted in fig. 5.8.

It can be seen that in the region with FFS cloak, no shadow is caused by the silver fingers. That means as expected, the light ending up in the image of the sample is only collected in the region between the fingers. In that sense, cloaking is still functional.

The spectral irradiance in the image, however, is strongly inhomogeneous across the cloaked region, resulting in variations of perceived brightness and color. At perpendicular viewing for instance, the region above the contact fingers has a bright yellowish appearance, while the rest of the OLED has a dimmer greenish look.

BRIGHTNESS INHOMOGENEITY Before discussing the origin for the inhomogeneity in color, let us first focus on the cause for the variations in (spectrally integrated) irradiance. These variations cannot be caused by Fresnel reflections at the polymer-air interface alone: Since the same FFS shape was used as for the model OLEDs, reflections at the polymer-air interface should have a comparable strength. Thus, they should cause variations of irradiance in the

[5] Again, aerosol jet printing was carried out by Ralph Eckstein at InnovationLab Heidelberg.

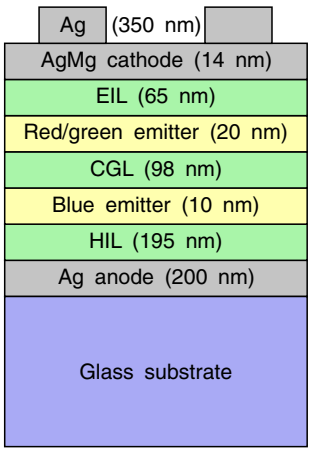

Figure 5.9: Layer stack of the OLEDs processed on a glass substrate, comprising red/green and blue emitters separated by a charge generation layer (CGL), sandwiched between a hole injection layer (HIL) and an electron injection layer (EIL). Note the silver-magnesium cathode is thin enough to be transparent, while the anode layer is highly reflective.

range of a few percents only, much weaker than the observed inhomogeneity. Instead, the variation of irradiance is attributed to an aspect that was not considered in the design of the cloak and that was not present in the OLED models: The OLED shows a relatively high specular reflectance, whereas for the OLED models, reflectance at the interface between glass and the cloaking layer was negligible. Therefore, when considering the actual OLED, light can be guided in the polymer layer by specular reflection at the OLED-polymer interface and total internal reflection at the polymer-air interface. As a consequence, light initially emitted in adjacent unit cells can efficiently reach the one that is imaged and be refracted toward the camera. Like this, more light can contribute to the irradiance seen in the image. This effect, however, can only occur when light travels along directions with a large x-component in the polymer layer, enabling total internal reflection. For perpendicular viewing (fig. 5.8(a)), the effect of increased irradiance is therefore limited to the central region, where the FFS shows the strongest surface inclination. Due to the high inclination, rays traveling along directions with large x-component can be refracted toward the camera.

When viewing the OLED at $\psi_1 = 60°$ (fig. 5.8(c)), the same light-guiding effect furthermore causes the region of the left FFS to appear brighter than the other two: In the flat polymer layer to the left, light is efficiently guided by the process just discussed. A large portion of this light is refracted toward the camera by the first FFS it encounters, making it appear brighter. Indeed, when the viewing angle was changed to $\psi_1 = -60°$, it was the right FFS that appeared brightest.

COLOR INHOMOGENEITY The observed inhomogeneity in color is attributed to the fact that the spectrum of emission of the OLED depends on the emission angle. Put more formally, this corresponds to an angle dependence of the spectral radiance, contradicting the ideal Lambertian nature assumed when designing the FFS cloak in section 5.2. The effect of this angle dependence can be seen in the photographs (fig. 5.8) in the region without FFS cloak. Here, where the OLED was only covered by a flat polymer layer, the emitted color changed depending on the viewing angle. While for normal viewing, this region appeared green, it had a purple tint when viewed at $\psi_1 = 60°$. This fact can be understood when considering the layer stack of the OLED (fig. 5.9). It comprises organic layers that emit at red, green, and blue wavelengths. The emissive layers are sandwiched between several additional layers with sub-wavelength thicknesses. Therefore, the overall stack can act as a Fabry–Perot filter whose transmitted spectrum depends on the direction at which light is emitted from the OLED.

In the cloaked region, this effect caused an inhomogeneity in color. By design, light ending up in the camera at a given viewing angle ψ_1 has been collected by the FFS cloak from a range of emission angles. Particularly in the region close to the contact finger, where the inclination of the FFS is highest, light emitted at oblique angles dominates. This leads to a color shift towards longer wavelengths in that region, as most prominently observed in fig. 5.8(b).

In order to mitigate both effects, a scattering layer could be added to the OLED. Like this, specular reflections at the OLED-polymer interface would be reduced, so that the guiding effect would be mitigated. Moreover, the presence of scatterers has been shown to stabilize the emitted spectrum when viewing the device from varying directions [176].

All in all, a similar FFS cloak as for hiding contact fingers on solar cells proved to be suited for concealing metal grids on light sources within certain limits. An emitter with metal grid exhibiting a near-ideal Lambertian intensity distribution showed a nearly-perfectly homogeneous brightness after adding the FFS cloak for a large range of viewing directions. For an actual top-emitting OLED suffering from pronounced optical cavity effects, however, the presence of the cloak lead to strong spatial variations of the color of emission. Thus, the application of this approach is limited to OLEDs that provide near-ideal Lambertian emission for the complete spectral range of interest.

Chapter 6

6 All-angle light-extraction for LEDs[1]

In this chapter, the design of a graded-refractive-index light-extraction structure for (O)LEDs is presented. Its omniangle single-pass unity extraction efficiency is demonstrated in ray-tracing simulations. The influence of the extractor on the angular distribution of the emitted intensity is investigated as well as the effect of different modifications to the extractor design.

6.1 Extraction challenges for (O)LEDs

LEDs are optoelectronic devices with the inverse functionality of solar cells. Therefore, their efficiency can be quantified in a similar manner. The ultimate figure quantifying their performance is the EQE, i.e., the ratio of generated photons and injected charge carriers. EQE can be expressed as a product of the internal quantum efficiency (IQE) and the extraction efficiency, η_{ex}:

$$\mathrm{EQE} = \eta_{ex} \cdot \mathrm{IQE}\,. \tag{6.1}$$

While IQE quantifies how efficiently charge carriers are converted into photons within the LED, extraction efficiency describes what fraction of the generated photons are coupled out to free space. By careful optimization of their electrical properties, near-unity IQE has been obtained for organic [149] and solid-state [178] LEDs.

[1] The results presented in this chapter have been discussed in one of the author's journal publications [177].

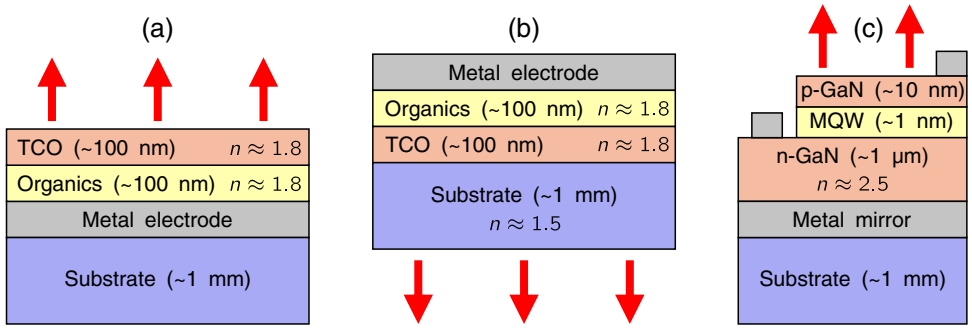

Figure 6.1: Schematic layer stacks of (a) top-emitting and (b) bottom-emitting OLED, and (c) of a top-emitting solid-state LED with a multi-quantum-well (MQW) architecture. Extraction of the generated light is hindered by waveguiding in the TCO-organic layers (a,b), by total internal reflection in the substrate (b) or in the semiconductor layers (c).

For both types of devices, however, optimization of light extraction is still subject to intense research [30]. The most prominent mechanisms leading to a reduced extraction efficiency can be understood by considering the typical (O)LED device structures depicted in fig. 6.1. In organic LEDs, light is generated in a layer stack made of organic semiconductors that is usually sandwiched between a transparent conductive oxide (TCO) layer and a metal electrode. Both the organic stack and the TCO typically exhibit a similar refractive index around 1.8. Depending on the sequence of layer depositions, the light generated in the final device is emitted away from the substrate ("top-emitting") or through the substrate ("bottom-emitting"). In both variants, light can form guided modes in the TCO-organic layer stack, as it has a combined thickness comparable to the wavelength of the emitted light. Due to the high index contrast between the TCO-organic stack and air as the surrounding material, waveguiding can be fairly efficient in top-emitting OLEDs, lowering the extraction efficiency significantly. For bottom-emitting OLEDs, the effect is mitigated due to the reduced index contrast, but instead light can be trapped in the substrate via total internal reflection at the substrate-air interface. Depending on the thickness of the emitter layer, the formation of surface plasmons at the metal interface can constitute a further loss mechanism. In combination, the three effects can lead to reductions of efficiency by more than 60 %, for both top- and bottom-emitting architectures [29, 148, 179].

Figure 6.1(c) shows the schematic structure of a solid-state LED made from gallium nitride. Light is emitted from the active region comprising several periods of InGaN/GaN quantum wells that is sandwiched between p- and

n-doped GaN layers. Due to the high refractive index of GaN, only light emitted to a cone with an opening angle of 24° around the normal direction is coupled out to free space, while a large fraction of the light is trapped in the GaN layers by total internal reflection.

Despite the different architectures, Fresnel reflections (particularly total internal reflections) at the air-facing surface of the LEDs thus present a major contribution to low extraction efficiencies. Several approaches to mitigate Fresnel reflections have been studied in the literature. For instance, macroscopic hemisphere lenses, so-called macro-extractors, can be added to the LED to suppress total internal reflection [180, 181]. These are several orders of magnitude thicker than the LED stack, rendering the approach impractical for pixelated LEDs with small emissive areas, for instance. Arrays of microlenses can provide a more compact alternative [182, 183], but they leave unpatterned regions between adjacent lenses. Moreover, cross-coupling between lenses can redirect light toward the LED stack. This is unfavorable especially for OLEDs, since only 70 % to 90 % of the light is reflected by the stack, while the rest is absorbed. Therefore, extraction schemes involving multiple passes of the light through the LED stack cannot achieve unity extraction efficiency [184]. GRIN structures that gradually adapt the refractive index between substrate and air have also been investigated [185, 186], but none of them completely eliminated Fresnel reflections to enable single-pass and omniangle extraction.

In order to extract light guided in the LED stack, the application of (quasi-)periodic [174, 187–189] and random [190–192] scattering structures has been investigated. Periodic structures have been shown to achieve good extraction efficiencies. Since they are based on diffraction, however, the efficiency of this scheme is inherently wavelength- and direction-dependent. While light extraction via random scatterers can be broadband and fairly efficient [180], this approach does not enable single-pass extraction.

6.2 Design of a GRIN extractor

In this work, a GRIN structure that eliminates Fresnel reflections at an interface entirely, including total internal reflection, was designed. Such an extractor structure can for instance be added to the glass substrate of a bottom-emitting LED, where it enables complete outcoupling of substrate modes. Alternatively, the device can be placed onto the transparent anode of a top-emitting LED. In this configuration, the extractor promotes outcoupling of modes guided

in the LED stack that leak into the extractor region. The working principle of the extractor is equivalent in both situtations, as it is solely based on complete suppression of Fresnel reflections at an interface between materials of different refractive index. As an example, we consider coupling between a homogeneous isotropic dielectric with refractive index $n_0 = 1.8$ and air ($n_1 = 1$) in the following. In this case, n_0 is close to that of ITO at $\lambda \approx 600\,\mathrm{nm}$, which is a common material choice for LED top anodes.

The geometry is taken to be translationally invariant, so that the extractor structure can be designed in two spatial dimensions. Moreover, the exit facet of the LED (width w_0) is assumed to be large enough to justify a ray-optical treatment. As long as this constraint is satisfied, the resulting extractor structure can be scaled isotropically without changing its performance. That means the device can be applied to the emissive area between opaque interconnection lines in pixelated LEDs as well as to a large-area OLEDs, for instance.

To design the extractor structure, we recall that a change in refractive index corresponds to an opposite change in the extension of physical space, as long as optical path length is conserved (see section 2.1). Therefore, physical space in a homogeneous isotropic dielectric with refractive index $n_0 > n_1$ appears compressed with respect to space in the low-index region. An abrupt interface between the two media therefore presents a metric discontinuity—corresponding to a mismatch of the wave impedance—at which Fresnel reflections occur [193]. Vice versa, reflections are eliminated if metric discontinuities are absent. This can be achieved by employing a GRIN distribution that mimics a smooth transition between the two spaces. As the transition from n_0 to n_1 corresponds to an expansion of space (compensated by the decreasing refractive index), the ratio of the widths of entrance and exit facet of the extractor is bound to be $w_0/w_1 = n_1/n_0$.

The GRIN distribution featuring metric continuity was found by optical conformal mapping (section 2.1.2). Obviously, no Fresnel reflections occur within a homogeneous medium, i.e., it corresponds to a space free of metric discontinuities. Therefore, a rectangular semi-infinite strip of a homogeneous medium with refractive index $n_0 = 1.8$ was chosen as the starting point for the transformation. It was conformally mapped to a semi-finite polygon as depicted in fig. 6.2. The target polygon was obtained from the rectangular strip by linearly expanding its width in a transition region. The ratio of widths w_0 and w_1 were chosen to reflect the ratio of refractive indices. As for the GRIN cloak for contact fingers on solar cells, the conformal map was

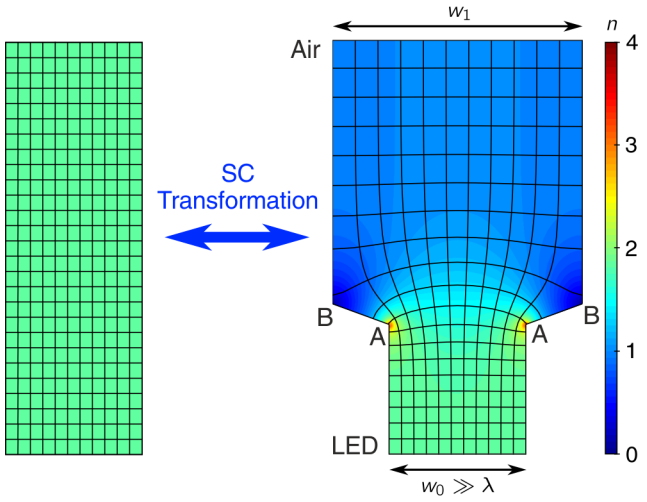

Figure 6.2: Design of a reflectionless extractor by SC mapping from a semi-infinite strip of a homogeneous medium to a semi-infinite polygon. No absolute lengths are given, because the performance of the structure is invariant upon isotropic scaling. Reproduced with permission from [177], © 2015 Optical Society of America.

found numerically using the SC toolbox for Matlab [55]. As expected, the transformed coordinate lines do not show discontinuities and the refractive index derived from the mapping continuously transforms from $n_0 = 1.8$ at the entrance to $n_1 = 1$ at the exit facet of the extractor.

Strictly, the SC mapping transforms all space since it is conformal. The GRIN distribution therefore has to be truncated spatially in order to obtain an extractor design with finite dimensions. As a consequence, the refractive index along entrance and exit facets shows variations, whose severity depends on how far away from the transition region the distribution has been truncated. Here, the length of the device was chosen such that the variation of refractive index along the entrance and exit facet was well below 0.1 % of the design value of $n_0 = 1.8$ and $n_1 = 1$, respectively.

Another design parameter is the length of the transition region. The smaller it is, the sharper are the corners of the polygon (A, B in fig. 6.2). Sharp corners imply a strong deformation of the coordinate grid, which leads to the formation of an extended region in the vicinity of the corner with extreme refractive indices. In contrast, if the transition region is made very long, the requirement for an extreme index is limited to the immediate surrounding of the corner.[2] This benefit toward experimental realization, however, comes at the cost of geometric compactness. The design analyzed in the following had a transition region with a 20° slope with respect to the x-axis; this situation was found to provide a good compromise.

[2] Extreme values never vanish completely from the refractive-index distribution, because the SC mapping function either diverges or approaches zero at the positions of the vertices.

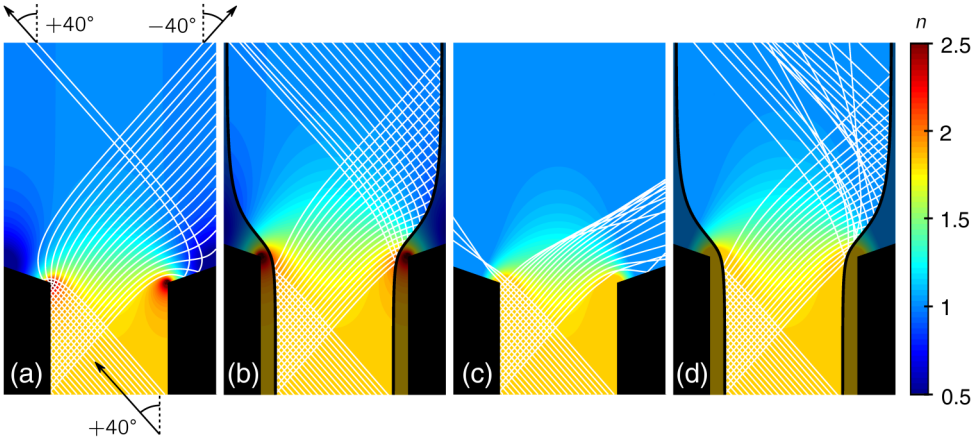

Figure 6.3: Exemplary ray trajectories in the extractor for a launch angle of $\psi = 40°$ for (a) the full refractive-index distribution without and (b) with geodesic truncation. (c) Extractor with the refractive index truncated to the interval $n \in [1, 1.8]$ without and (d) with additional geodesic truncation. The color scale is saturated between $n = 0.5$ and $n = 2.5$ for visibility. Reproduced from [177], © 2015 Optical Society of America.

Apart from the full extractor design resulting from the conformal mapping, several post-modified versions were analyzed numerically using the ray-tracing tool described in section 3.4. For the simulations it was assumed that the GRIN distribution was realized by an absorption-free dielectric. Moreover, the boundaries of the high-index part of the extractor were set to be perfect reflectors in order to confine the light to the extractor until it had passed the transition region.

Exemplary ray trajectories for four different extractor configurations are shown in fig. 6.3. Here, all rays were launched at an angle $\psi = 40°$ at the entrance facet of the extractor. Without the GRIN device, light propagating at this angle could not escape the high-index material. At a refractive index of $n_0 = 1.8$, total internal reflection occurs at angles above 33°.

For the unmodified extractor (fig. 6.3(a)), all rays exit from the low-index region at angles close to $\pm 40°$. The trajectories also show that light is more spatially spread at the exit facet. This is expected for a device that expands optical space as light travels from the entrance toward the exit facet. Reflections at the boundaries of the extractor can lead to flips of the sign of the exit angle. The sign is irrelevant in practice as long as the input intensity profile is symmetric about $\psi = 0°$. All in all, the full GRIN design provides the target functionality of reflectionless light extraction. Moreover, it preserves the

absolute value of the launch angle. A downside of this design, however, is that it relies on extreme refractive indices, which might impede practical realization using lossless dielectric materials.

Extreme indices are not required for efficient light-extraction per se, but their occurrence is rather a consequence of the choice of spatial transformation. Luckily, extreme index values are concentrated to the vicinity of the corners of the polygon, i.e., they do not occur in the central region. Therefore, they can be avoided by truncating the width of the extractor. In fig. 6.3(b), the GRIN distribution was truncated along a coordinate line corresponding to the y-direction in virtual space, called a *vertical geodesic* in the following. The boundary was set to be a perfect reflector to avoid light from escaping the truncated extractor. Like that, the only remaining boundary for coupling to the surrounding air was the top exit facet. Whenever light is reflected off of one of the geodesic mirrors, the component of velocity parallel to the geodesic is conserved. In other words, the angle of propagation with respect to the local surface normal only flips its sign. As the absolute value of the propagation angle is conserved while traveling through the GRIN distribution, such a reflection can only change the sign of the angle at which light leaves the extractor.

Note that the position of the geodesic mirrors influences the range of refractive indices needed: The closer the mirrors are put together, the larger is the excluded region in the vicinity of the polygon corners. As a consequence, a narrower range of refractive indices suffices to realize the remaining structure. Moreover, the ratio of entrance and exit facet (as defined by the geodesic mirrors) is not changed by geodesic truncation. Their absolute widths, however, are reduced. In order to provide an entrance facet of the same width as the unmodified structure, the design with geodesic mirrors was scaled up isotropically. That makes the device slightly less compact compared to the full structure.

It might seem artificial to first calculate the refractive-index distribution for a polygon-shaped extractor, calculate the geodesics, and then post-modify the structure by geodesic truncation to find an extractor with smooth boundaries. Indeed, it would be possible as well to start by mapping the rectangular virtual space to a physical domain with some sort of smooth boundaries and compute the index distribution directly. Finding a conformal mapping function, however, can be challenging in that case, whereas it is straightforward when mapping to a polygon-shaped physical domain.

A more radical approach to avoid extreme refractive indices is demonstrated

in fig. 6.3(c), where n was truncated to the interval $n \in [1, 1.8]$. At the shown launch angle of $\psi = 40°$, extraction is still functional, but angles are no longer preserved. Instead, the exit angles vary among rays and their absolute value tends to be larger than for the extractor designs without index truncation.

Combining the two modifications of index and geodesic truncation, angle-preservation is improved (fig. 6.3(d)). This can be understood because geodesic truncation now excludes the regions affected most by index truncation. In fact, the smaller the distance between the geodesic mirrors, the more exactly $|\psi|$ is preserved along the extractor. This can be used to tune the behavior of the index-truncated device: For a small enough spacing of the geodesic mirrors, the extractor behaves exactly as the one in fig. 6.3(b); for larger spacings, the behavior approaches that of the index-truncated device without additional geodesic truncation.

6.3 Quantitative analysis of extraction performance

Apart from the qualitative analysis described above, the extraction performance was assessed quantitatively, again via ray-tracing simulations. The numerical treatment required spatial and angular discretization: launch angles in the interval $\psi \in [0°, 88°]$ were simulated with a discretization of $\Delta\psi = 0.5°$, and for each of the angular bins, $N_x = 500$ rays were launched spread equidistantly across the entrance of the extractor. Like this, the simulated intensity distribution represents the spatial average across the entrance facet of the extractor. Each of the launched rays was assigned a radiant flux $\delta\Phi(\psi)$, whose value followed from a prescribed intensity distribution at the entrance, $I_{\text{in}}(\psi)$ as

$$\delta\Phi(\psi) = \frac{\Phi_{\text{in}}(\psi)}{N_x} = \frac{I_{\text{in}}(\psi)\Delta\psi}{N_x}\,. \tag{6.2}$$

Here, $\Phi_{\text{in}}(\psi)$ denotes the radiant flux launched at an angle ψ according to the intensity distribution.

6.3.1 Extraction efficiency

In order to quantify the efficiency of light extraction in dependence of the launch angle ψ, the extraction efficiency η was calculated as

$$\eta(\psi) = \frac{\Phi_{\text{out}}(\psi)}{\Phi_{\text{in}}(\psi)} = \frac{N_{x,\text{out}}(\psi)}{N_x}\,, \tag{6.3}$$

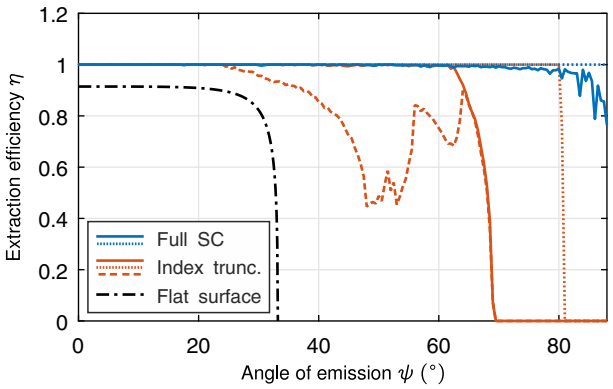

Figure 6.4: Extraction efficiency as a function of the launch angle from the LED stack for different extractor configurations: full refractive-index distribution as obtained from SC mapping (blue) without (solid) and with geodesic truncation (dotted); index-truncated version (red) without (solid) and with geodesic truncation (dotted) and with periodic boundaries (dashed). The dashed-dotted black curve corresponds to the polarization-averaged Fresnel transmittance through the interface between media with $n_0 = 1.8$ and $n_1 = 1$. Adapted with permission from [177], © 2015 Optical Society of America.

where $\Phi_{\text{out}}(\psi)$ is the flux reaching the exit of the extractor when light was launched at an angle ψ. $N_{x,\text{out}}(\psi)$ is the corresponding number of rays, so that $\Phi_{\text{out}}(\psi) = N_{x,\text{out}}(\psi)\delta\Phi(\psi)$.

The simulated angle-dependent extraction efficiency is depicted in fig. 6.4 for the four configurations discussed above and additionally for the index-truncated extractor with periodic boundaries. For all configurations, extraction is significantly better than for a flat interface between the two media underlying Fresnel back-reflection. At launch angles below 25° toward the interface normal, all GRIN structures provide ideal light extraction.

The full device with and without geodesic truncation extends the angular range of perfect light extraction to very oblique angles. With geodesic truncation, ideal extraction was found for all angles. For the full device, a slight decrease in efficiency was obtained for angles above 70°. This is considered to be a numerical artifact caused by the finite spatial discretization of the refractive-index distribution: In the regions around the corners of the SC polygon, the distribution of refractive index exhibits spatially narrow peaks that cannot be represented appropriately using the given discretization. Therefore, light rays approaching these index peaks can show a behavior deviating from the design. When light is launched at near-normal directions, only rays

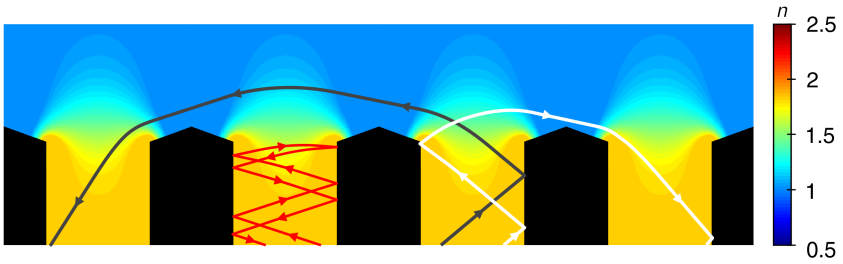

Figure 6.5: Exemplary ray trajectories in the index-truncated extractor. At very oblique launch angles (red rays, $\psi = 70°$), total internal reflection at the GRIN distribution can occur. In a periodic arrangement of extractors, light can be coupled into adjacent extractors and reach the LED surface at launch angles around $\psi = 50°$ (black and white rays).

launched close to the boundaries can approach the index peak. Thus, only a small fraction of the light is affected by this numerical inaccuracy. For very oblique launch angles, however, the propagation velocity of the rays has only a small y-component. Therefore, light bounces between the reflecting boundaries many times before it eventually reaches the transition region. Since the points of reflection of the rays advance very slowly in the y-direction, chances are much higher that a given ray approaches one of the index peaks. Hence, a larger fraction of rays is subject to the misbehavior, leading to a decreased extraction efficiency.

Perfect outcoupling performance is found for the index-truncated extractor for launch angles up to 62°, followed by a rapid decrease of extraction efficiency. This effect corresponds to the onset of total internal reflection within the extractor (see fig. 6.5). Note that for the devices featuring the refractive-index distributions as calculated by the SC mapping, total internal reflection cannot happen because metric continuity forbids Fresnel reflections entirely. Once the index distribution is truncated, however, metric continuity is not guaranteed anymore, so that argument does not hold for the index-truncated version of the extractor. By additionally truncating the device spatially along a vertical geodesic, the perfect extraction ability is restored for angles up to 80°. In fact, the critical angle of total internal reflection can be tuned by choosing the position of the geodesic mirrors.

Finally, the influence of periodic boundaries was studied. Here, rays leaving the simulation region through the vertical boundaries above the transition region re-entered at the opposite boundary while keeping their direction of propagation. Like this, cross-coupling between adjacent extractors was simu-

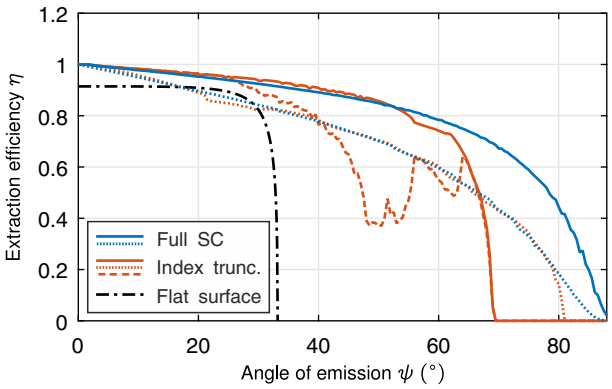

Figure 6.6: Extraction efficiency as a function of the launch angle from the LED stack for the same extractor configurations as in fig. 6.4, additionally attributing a non-ideal reflectance of $R = 90\,\%$ and an absorptance of $A = 10\,\%$ to all reflecting surfaces.

lated. As expected, no effect of the periodic boundaries on the performance of the full device and the configurations with geodesic truncation was observed. For the index-truncated version, however, switching on periodic boundaries lead to a significant decrease in extraction efficiency for angles well below the critical angle of total internal reflection. At launch angles around 50°, roughly half of the radiant flux was coupled into an adjacent extractor, where it then propagated toward the LED surface (see fig. 6.5). In a real device, the LED stack typically shows some reflectivity, so that the reflected part of the light could have reached the exit of that extractor eventually. In the simulations, however, the stack was set to be fully absorbing to incident light, so that the results provide a worst-case estimation of the extraction efficiency.

In the simulations just discussed, the flux that each of the rays transported was considered to be conserved upon reflection at one of the (geodesic) boundaries. This implies unity reflectance for the corresponding interfaces. Realizing near-unity reflectances experimentally, however, can be challenging. Therefore, the effect of non-ideal reflectivity on the extraction efficiency was investigated. Here, the reflecting boundaries in the high-index region of the extractor as well as geodesic mirrors (where applicable) were set to have a reflectance of 90 %. The remaining 10 % of the light were assumed to be absorbed. As can be seen in fig. 6.6, extraction efficiency suffers most prominently for high launch angles and when geodesic mirrors are in place. In these situations, light is reflected more often before reaching the exit facet, leading to stronger losses. Nevertheless, extraction efficiency is still superior to a plain flat surface, apart from a narrow angular range for the structures with geodesic truncation.

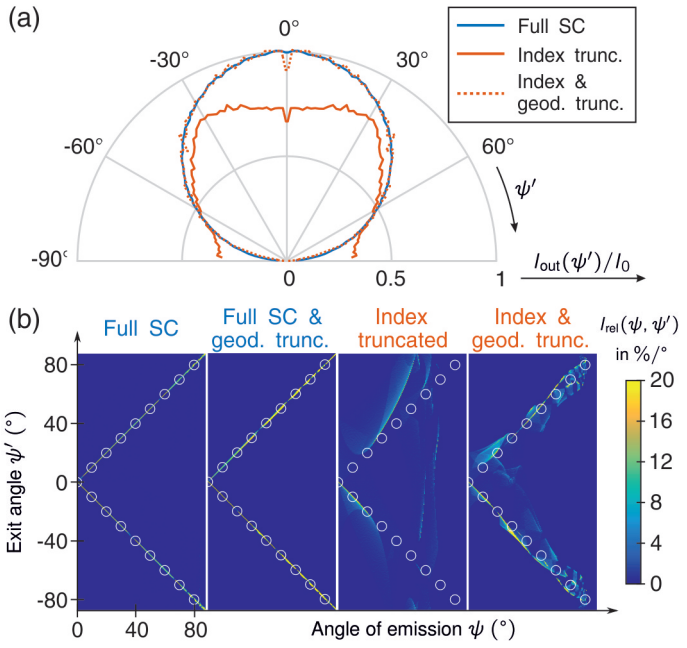

Figure 6.7: (a) Simulated intensity profiles emerging from the extractor for a Lambertian input profile. (b) Maps of relative intensity for the four extractor configurations. Ideal preservation of the absolute value of the emission angle corresponds to a narrow peak of $I_{\mathrm{rel}}(\psi, \psi')$ along the two lines indicated by white circles. The color scale is saturated at 20 %/° for visibility. Adapted with permission from [177], © 2015 Optical Society of America.

6.3.2 *Angular distribution of intensity*

Moreover, the influence of the extractor structure on the angular distribution of light was studied. The intensity distribution at the exit of the extractor, $I_{\mathrm{out}}(\psi')$, was found by summing the fluxes of all rays leaving the structure at an angle in the interval $\Psi' = [\psi' - \frac{\Delta\psi'}{2}, \psi' + \frac{\Delta\psi'}{2}]$ for a given input intensity distribution, $I_{\mathrm{in}}(\psi)$:

$$I_{\mathrm{out}}(\psi') = \frac{\mathrm{d}\Phi_{\mathrm{out}}}{\mathrm{d}\psi'} = \frac{1}{\Delta\psi'} \sum_{\psi'_k \in \Psi'} \delta\Phi_k = \frac{\Delta\psi}{\Delta\psi' N_x} \sum_{\psi'_k \in \Psi'} I_{\mathrm{in}}(\psi_k)\,. \tag{6.4}$$

Here, k iterates over all launched rays, $\delta\Phi_k$ denotes the flux carried by the k-th ray, and ψ'_k is the angle at which it leaves the extractor. As an example, the influence of the extractor structure on the angular distribution of a Lambertian emitter was studied. In that case, the intensity distribution at the entrance of the extractor is given as

$$I_{\mathrm{in}}(\psi) = I_0 \cos\psi\,. \tag{6.5}$$

Figure 6.7(a) depicts the calculated intensity distributions at the exit of the extractor structure for three different configurations. Using the full refractive-index distribution as calculated from the SC transformation, the ideal Lambertian intensity profile is preserved. Geodesic truncation of the structure

does not change this behavior (not shown in the plot). For the design with truncated refractive index values, however, the intensity profile emerging from the exit facet of the extractor deviates from an ideal Lambertian shape. The intensity at near-normal directions is reduced because the index distribution is missing the regions with extreme refractive indices. Therefore, parallel light entering the extractor along the y-direction is weakly spread, but not re-collimated properly as for the full design. As expected when considering the ray trajectories shown in fig. 6.3(c), the index-truncated extractor tends to increase angles of propagation, leading to a higher intensity at $\psi' > 60°$ than expected for an ideal Lambertian distribution. Applying geodesic truncation at the position shown in fig. 6.3(d), however, a near-ideal Lambertian profile is restored.

Another quantity of interest is the relative intensity $I_{\mathrm{rel}}(\psi, \psi')$ that exits the extractor for a given combination of angle of emission ψ and exit angle ψ'. It directly shows how well the extractor conserves the angular specificity of the light. If angles were exactly preserved during extraction, $I_{\mathrm{rel}}(\psi, \psi')$ would become proportional to the Dirac delta function $\delta(\psi - \psi')$. Here, however, reflection at boundaries can flip the sign of the angle. Therefore, only the absolute value of the propagation angle is conserved. This corresponds to

$$I_{\mathrm{rel}}(\psi, \psi') \propto c(\psi)\delta\left(\psi - \psi'\right) + \left(1 - c(\psi)\right)\delta\left(\psi + \psi'\right) \,, \tag{6.6}$$

where $c(\psi)$ determines how intensity is split among positive and negative sign of the propagation angle. The factor varies with the emission angle ψ, because the direction of emission influences how many reflections the rays undergo before leaving the extractor.

The computed relative intensity map was normalized to $I_{\mathrm{in}}(\psi)$, making the results universally applicable to arbitrary input intensity profiles. In analogy to eq. (6.4), $I_{\mathrm{rel}}(\psi, \psi')$ was found by summation over the rays that were launched at an angle ψ and exited the extractor in the angle interval Ψ' centered at ψ'.

$$\begin{aligned} I_{\mathrm{rel}}(\psi, \psi') &= \frac{1}{I_{\mathrm{in}}(\psi)} \frac{\mathrm{d}I_{\mathrm{out}}}{\mathrm{d}\psi} = \frac{1}{I_{\mathrm{in}}(\psi)} \frac{\mathrm{d}^2\Phi_{\mathrm{out}}}{\mathrm{d}\psi' \,\mathrm{d}\psi} = \frac{1}{I_{\mathrm{in}}(\psi)\Delta\psi'\Delta\psi} \sum_{\substack{\psi_k = \psi \\ \psi'_k \in \Psi'}} \delta\Phi_k \\ &= \frac{1}{I_{\mathrm{in}}(\psi)\Delta\psi' N_x} \sum_{\substack{\psi_k = \psi \\ \psi'_k \in \Psi'}} I_{\mathrm{in}}(\psi_k) = \frac{1}{\Delta\psi' N_x} \sum_{\psi'_k \in \Psi'} 1 \end{aligned} \tag{6.7}$$

Maps of relative intensity are depicted in fig. 6.7(b) for several configurations of the extractor. For the full device and its version with geodesic truncation, the shape of I_{rel} fits to the description in eq. (6.6). Thus, the two configurations conserve the absolute value of the propagation angle. This is expected for a device following from a conformal transformation. The index-truncated structure shows a different behavior. Here, intensity accumulates in the region above and below the two lines of ideal preservation of $|\psi|$. This confirms the above finding for a Lambertian input: the absolute value of the propagation angle is increased by this version of the extractor. Moreover, $I_{\mathrm{rel}}(\psi, \psi')$ is practically zero in the region $\psi > 70°$. This is a manifestation of total internal reflection occurring at very oblique emission angles in the index-truncated extractor. Adding geodesic mirrors to truncate the structure geometrically brings $I_{\mathrm{rel}}(\psi, \psi')$ closer to the behavior of the unmodified structure. Here, however, the relative intensity is scattered around the two lines of preservation of $|\psi|$, indicating that the absolute value of the propagation angle is only approximately conserved in this case. For a Lambertian input, this deviation had practically no effect on the conservation of the intensity distribution (fig. 6.7(a)).

CONSERVATION OF ETENDUE As discussed in section 2.3.2, conservation of etendue can be understood to cause total internal reflection at interfaces between dielectrics. Apart from the index-truncated version, total internal reflection is absent, and the devices show an omniangle unity outcoupling efficiency. How can this conform to the conservation of etendue?

To understand this, let us consider the extractor as a 2D optical system with entrance and exit apertures of width w_0 and w_1, respectively. The entrance shall be coupled to a half-space filled with a medium of refractive index n_0, the exit shall be coupled to air. According to eq. (2.42), the etendue of the largest ray bundle entering the entrance facet from the dielectric half-space is

$$G_0 = n_0 \int^{\psi_{\max}} \int^{w_0} \mathrm{d}x \cos\psi \, \mathrm{d}\psi \,, \tag{6.8}$$

where $\psi_{\max}$ is the acceptance angle of the optical system, i.e., the extractor. Light that enters the structure at higher angles is rejected (for example by total internal reflection somewhere within the device). The etendue at the exit facet, G_1, takes an analogous form. Requiring the conservation of etendue of light traveling through the extractor, we find

$$n_0 w_0 \sin\psi_{\max} = n_1 w_1 \sin\psi'_{\max} \,. \tag{6.9}$$

Here, $\psi'_{\max}$ denotes the maximum angle at which light leaves the extractor. For the devices discussed here, the widths of the exit and entrance facet fulfill the relationship $w_0/w_1 = n_1/n_0$. Inserting this into eq. (6.9), it follows that the acceptance angle is equal to the maximum emission angle. This finding is compatible to the observed behavior of the extractor structures (except for the index-truncated version), where both $\psi_{\max}$ and $\psi'_{\max}$ were found to be 90°. This is obviously different from an abrupt transition between the two refractive indices, where total internal reflection would lead to a reduced acceptance angle. Therefore, expansion of space along the extractor can be seen a requirement for enabling omniangle light extraction.

In the index-truncated extractor, space expansion is present as well, but the maximum exit angle exceeds the acceptance angle. This is an indication that the device does not perform ideally, because the etendue of light increases on its way through the extractor. As discussed above, the limited performance can be attributed to total internal reflection in the extractor. But why does it occur in the index-truncated GRIN distribution and not in the others? This can be understood by considering the evolution of the available phase space along the structure.

Inside the extractor, at an axial distance y away from the entrance facet, the system can transport light with a maximum etendue of $G_0(y)$ according to

$$G_0(y) = \sin \psi_{\max}(y) \int^{w(y)} n(x, y)\, \mathrm{d}x\,, \tag{6.10}$$

where $w(y)$ is the width of the device and $n(x, y)$ the spatial distribution of refractive index.

Generally, if a ray bundle with a given etendue shall be transmitted through an optical system without change in etendue or back-reflection, the system must provide sufficient phase space volume at every position along the optical axis. Considering the largest ray bundle fitting into the entrance of the extractor, this requirement takes the form

$$G_0(y) \geq G_0(0) = \sin \psi_{\max}(0) \int^{w(0)} n(x, 0)\, \mathrm{d}x\,, \tag{6.11}$$

where the entrance facet is bound to be at $y = 0$.

For a device that accepts all angles at the entrance, $\sin \psi_{\max}(0) = 1$. Therefore, eq. (6.11) can only be fulfilled if

$$\int^{w(y)} n(x, y)\, \mathrm{d}x \geq \int^{w(0)} n(x, 0)\, \mathrm{d}x\,. \tag{6.12}$$

In the index-truncated design, this is not given for all y: At the height of the polygon corner A (as in fig. 6.2), the integrated refractive index is lower than at the entrance of the extractor. Consequently, the acceptance angle $\sin\psi_{\max}(0)$ must be reduced in order to fulfill eq. (6.11), manifesting as the occurrence of total internal reflection. For the other designs, the lower values of refractive index in the central region are compensated by maxima at the polygon corners. Therefore, the integrated refractive index does not fall below that at the entrance, and no reduction of the acceptance angle is observed.

All in all, the designed extraction device can offer omniangle light extraction from LEDs by complete elimination of Fresnel reflections. The need for extreme refractive indices can be mitigated by spatial truncation along geodesics without impacting extraction performance. By directly truncating the occurring refractive index values the angular distribution of the extracted intensity can be tuned to some degree, at the cost of reduced overall efficiency.

7 Chapter 7
Conclusions & Outlook

In this work, the viability of transformation optics as a design method for optical structures on optoelectronic devices was explored.

First, an overview of the theoretical background was given in chapter 2. After reviewing the mathematical foundation of transformation optics, the realizability of TO devices was discussed. Here, the focus was laid on 2D optical structures designed from conformal transformations, as these can be realized by dielectric materials. Schwarz-Christoffel mappings between a half-plane and a polygon were found to provide a straight-forward route to computing the distribution of refractive index realizing the spatial transformation. This type of mapping was employed to design structures for cloaking of contact fingers on solar cells and for all-angle light extraction from light-emitting diodes.

The refractive-index distributions were experimentally realized by photonic crystals. In section 2.2, the procedure to compute their band structure was sketched. The band structure provided the basis for mapping the volume filling fraction of the crystal (i.e., a geometrical property) to its effective refractive index, hence enabling realization of the GRIN structure for contact finger cloaking on solar cells.

The chapter was concluded by the introduction of radiometric quantities and their conservation laws in section 2.3. The concepts described here were most prominently used when deriving an optical structure for visually hiding metal grids on OLEDs, but also enabled a detailed understanding of the behavior of the GRIN extractor for LEDs.

A discussion of the fabrication methods followed in chapter 3, where DLW was introduced as a flexible printing scheme for 3D polymer structures. After discussing the working principle, its practical limitations in terms of resolution, throughput, and structure quality were examined. These restrictions hindered

the use of DLW to print optical structures for contact finger cloaking directly on solar cells. Therefore, a soft-imprinting scheme was used that was described in section 3.2.

The performance of all optical structures designed in this work were evaluated numerically via ray-tracing simulations. The algorithm employed for tracing of light through homogeneous and inhomogeneous dielectric materials was discussed in section 3.4.

In chapter 4, after giving an overview of the physics of generation of electricity in solar cells, two distinct approaches to solve the problem of contact finger shadowing were discussed in sections 4.2 and 4.3.

The design based on a Schwarz-Christoffel mapping between 2D spatial coordinates resulted in a GRIN micro-optical structure that smoothly guided the incident light around the contact fingers. The spatial distribution of refractive index was realized by woodpile photonic crystals with varying polymer filling fraction. These were fabricated using DLW and employed in the long-wavelength limit. The cloaking principle was proven in infrared transmission experiments at normal incidence, where the GRIN structures provided fairly good cloaking of the contact fingers. Simulations of non-normal incidence showed a reduced cloaking performance for oblique angles of incidence, also reflecting in a sub-ideal annual average current increase predicted for typical Karlsruhe conditions.

A simplified cloaking device was designed based on a mapping from the one-dimensional spatial position of incidence to the surface inclination of a homogeneous dielectric. This free-form surface cloak was realized experimentally on a prototypical silicon heterojunction solar cell, as discussed in section 4.4. The cloaking layer was fabricated by DLW of a master structure and subsequent soft-imprinting into a highly transparent polymer. Cloaking performance was assessed in standard solar cell characterization measurements at varying angles of incidence, measurements of the spectrally resolved external quantum efficiency, and spatially resolved measurements of the short-circuit current generated in the cell. The FFS cloak was found to provide complete relief to the shadowing problem for all angles of incidence: For solar cells with a relative metal coverage of 6.4 %, the short-circuit current density was enhanced by 7.3 %, while the PCE was increased by 9.3 %. Ray-tracing simulations revealed that the overcompensation of the shadowing loss is enabled by additional light incoupling and trapping functionality that the FFS cloak offers. Judging from the annual average current increase for Karlsruhe conditions, the cloak was found to completely eliminate shadowing loss for

contact finger filling fractions up to 20 %.

An implementation of the GRIN cloak on a real-world solar cell is technologically challenging, because the refractive index of the constituent material has to be controlled in three spatial dimensions. The method chosen here has a fairly low throughput, so that it cannot provide a route that is commercially viable for large-area solar cells in the near future. Moreover, when sticking to the idea of using an effective dielectric medium, structuring of 3D materials with features well below the wavelengths of the visible spectral range would be required to implement a GRIN cloak working under illumination with the spectrum of the sun. While such structures have been demonstrated in academia in the context of invisibility cloaking [25], a realization on an industrial scale still seems a long way to go.

For the FFS cloak, upscaling the fabrication process appears more straightforward, because the working principle is only based on a single homogeneous dielectric layer. It is conceivable that the surface shape may be created by an imprinting process that is embedded into an industrial workflow. Nevertheless, several technological questions remain to be answered before a large-scale application of the FFS cloak comes into reach, for instance about the choice of material for the cloaking layer and its durability under varying environmental conditions. Moreover, the FFS cloak has to be aligned to the contact fingers of the cell with an accuracy in the order of 10 µm, which might be challenging in an industrial workflow. After all, in order to provide a commercially viable route, the costs of producing conventional solar cells with added FFS cloaks have to undercut those of alternative solar cell designs with reduced or no contact finger shadowing, such as back-contact cells.

Apart from hiding of contact fingers, the FFS cloaking approach can also be applied to related problems. For instance, thin-film solar modules oftentimes comprise monolithically connected cells [194]. As the cells are fairly small, they do not necessarily need metallic contact fingers, but a transparent front electrode can suffice to efficiently extract the generated current. The electrical interconnects between cells, however, present optically dead areas that reduce the module efficiency. It is conceivable that adding FFS cloaks designed for the geometry of the interconnects can help to mitigate this problem.

In chapter 5, it was demonstrated that a refractive FFS can be used to conceal metal grids on emitting surfaces with Lambertian emission characteristics. Interestingly, a radiometric discussion of the problem revealed that—when neglecting Fresnel reflections—the FFS shape originally derived for cloaking of contact fingers on solar cells could be applied for the reverse problem as

well.

In a model experiment, uniformity across the emissive area was enhanced substantially and homogeneity became near-ideal after applying a polymeric FFS cloak to a near-ideal Lambertian emitter. The remaining deviations from completely homogeneous and uniform radiance across the device were analyzed in 2D ray-tracing simulations. They were found to be caused by Fresnel reflections at the polymer-air interface, the non-ideal intensity profile emerging from the emitter, and fabrication imperfections. To improve these aspects, an anti-reflective coating could be added to the polymer structure and the soft-imprinting procedure could be optimized further. Also, in order for this concept to be viable, the light emitter has to show an intensity profile that is reasonably close to an ideal Lambertian distribution. Experiments at top-emitting OLEDs revealed that the quality of cloaking of metal grids on real-world devices also depends on the spectral behavior of their emission profile. In conclusion, the concept of FFS cloaking was found to be primarily suited for OLEDs providing spectrally homogenized, near-Lambertian emission.

A TO-based extraction device for enhanced out-coupling of light from (O)LEDs was discussed in chapter 6. The device was designed to provide omniangle and single-pass perfect outcoupling via the complete elimination of Fresnel reflections at a dielectric interface. The concept is applicable either to the glass substrate of bottom-emitting LEDs or to the transparent anode of top-emitting devices. By applying geodesic truncation, the range of refractive indices needed for realization of the GRIN extractor was reduced without impairing its outcoupling performance. Additional truncation of the refractive index allowed for tuning the extracted intensity distribution, between perfectly preserving the intensity profile emitted by the LED and a more spread-out version of the input profile. This feature could be useful to homogenize emission when applying the extractor to an LED with a directional intensity profile. The GRIN extractor is particularly suited to be employed on pixelized LEDs because of its compactness: The height of the device is in the same order of magnitude as the width of the emissive facet. Moreover, opaque interconnection lines between pixels can be concealed when placed in the region separating the entrance facets of the periodic arrangement of extractors (black regions in fig. 6.5). Finally, as the design is based on ray optics, its functionality is inherently wavelength-tolerant—as long as the materials realizing the refractive-index distribution show negligible dispersion over the spectral range of interest.

The extractor could be realized similarly to the GRIN contact finger cloaks

for solar cells, i.e., by DLW-fabricated woodpile photonic crystals with rod spacings smaller than the wavelength of the emitted light. Due to the finite resolution of DLW, operation of such devices would be limited to infrared and longer wavelengths, unless resolution-enhancing techniques such as stimulated-emission-depletion–inspired DLW [195] would be employed. The refractive index of the polymer made in the DLW process is typically around 1.5. Polymeric woodpiles would therefore only be able to suppress Fresnel reflections at an interface to a glass substrate with similar refractive index. In order to apply the extractor on the top anode of an OLED with a refractive index around 1.8 or on the semiconductor stack of a solid-state LED with a refractive index near 2.5, the polymeric structure would have to be converted to a different material. This could, for instance, be achieved by using a double-inversion process that replaces the polymer by titania ($n \approx 2.5$) [78]. Realization of the reflective parts of the extractor (for instance the geodesic mirrors) could be challenging if near-unity reflectance is targeted. As an alternative, the boundaries could be fabricated in the DLW step, so that Fresnel reflection at a polymer-air interface would replace a metallic mirror. In that case, some light would be able to escape through these sidewalls, which could eventually affect the preservation of the angular distribution of intensity.

Since the design was based on a 2D coordinate transformation, the resulting GRIN device is immediately applicable to systems exhibiting translational invariance along the third spatial direction. In principle, the design strategy can also be applied to three-dimensional geometries. The material realizing the 3D conformal mapping would, however, be an anisotropic magnetodielectric, i.e., the extractor could not be realized by a mere spatial distribution of refractive index. Using an approximate design based on quasi-conformal mapping, however, the material requirements for a 3D device could potentially be reduced significantly [36, 196].

All in all, transformation optics proved as a powerful tool for the design of practical optical structures for optoelectronic devices. Two-dimensional structures based on conformal mappings were realized by spatial distributions of refractive index, but their experimental implementation outside of academic applications remains a challenge. A simplified approach based on a one-dimensional spatial mapping allowed for near-complete remedy for the shadowing problem on solar cells and OLEDs and is potentially amenable to large-scale implementation.

Appendix A

A Supplementary material

A.1 DLW PARAMETERS

A.1.1 Cloaks for transmission experiments

The GRIN and FFS cloaks presented in section 4.2.3 were fabricated via dip-in DLW using the 63×/1.4 NA objective and IP-Dip photoresist. The GWL files containing the control commands for the instrument were generated by a Matlab script for the GRIN cloaks. Those for the FFS cloaks were prepared by importing an STL file specifying the surface shape into the DeScribe software. The parameters used during the STL import and for the writing of the structures are summarized in the following, using the DeScribe nomenclature.

A.1.1.1 GRIN cloaks

- Writing configuration
  - GalvoScanMode
  - ContinuousMode
  - PiezoSettlingTime 5
  - GalvoSettlingTime 2
  - GalvoAcceleration 20
- Writing parameters
  - PowerScaling 1.0
  - ScanSpeed 30000

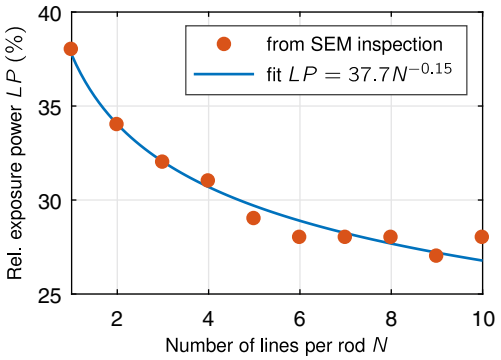

Figure A.1: Relationship between optimum exposure power and number of lines per rod of the woodpile photonic crystal. Power values are given on the calibrated power scale provided by the DLW instrument.

The relative power of exposure, LP, was not set globally, but depending on the local number of lines that were written per woodpile rod, N. Like this, an optimum exposure for all volume filling fractions was achieved. The relationship used for fabricating the GRIN cloaks presented in section 4.2.3 is shown in fig. A.1. For each N, the optimum relative exposure power was

determined by SEM inspection of woodpiles written at different exposure powers; the data was fitted by a polynomial function.

A.1.1.2 FFS cloaks

- Slicing
  - SlicingMode: Fixed
  - Distance: 0.3
  - SimplificationTolerance: 0
  - FixSelfIntersections: on
- Hatching
  - HatchingDistance: 0.2
  - ContourCount: 1
  - Angle: auto
  - ConcaveCornerMode: Beveled
- Output options
  - ScanMode: Galvo
  - HatchLines: Alternate
  - ZAxis: Piezo
  - ZDirection: Up
  - Exposure: Constant
- Writing configuration
  - GalvoScanMode
  - ContinuousMode
  - PiezoSettlingTime 5
  - GalvoSettlingTime 2
  - GalvoAcceleration 20
- Writing parameters
  - PowerScaling 1.0
  - LaserPower 40
  - ScanSpeed 50000

A.1.2 FFS masters for soft-imprinting

The master structures for soft-imprinting of all FFS cloaks presented in this work were fabricated via dip-in DLW using the 25×/0.8 NA objective and IP-S photoresist on an ITO-covered glass substrate. The GWL files containing the control commands for the instrument were prepared by importing an STL file specifying the surface shape into the DeScribe software. The parameters used during the STL import and for the writing of the master structures are summarized here, following the DeScribe nomenclature.

- Slicing
  - SlicingMode: Fixed
  - Distance: 0.3
  - SimplificationTolerance: 0

  - FixSelfIntersections: on
- Shell
  - HatchingDistance: 0.5
  - ContourCount: 30
  - BaseSliceCount: 30
  - Angle: auto
  - ConcaveCornerMode: Beveled
- Scaffold
  - HatchingDistance: 0.5
  - Type: Triangles
  - WallSpacing: 60
  - FloorSpacing: 50
  - WallLineCount: 1
  - FloorSliceCount: 1
  - Offset X: 0 Y: 0 Z: 0
  - Stagger: off
- Splitting
  - Mode: Rectangular
  - BlockSize X: 258 Y: 259 Z: 50
  - Offset X: 9 Y: -6 Z: -34
  - Shear: 20
  - Overlap: 2
  - BlockOrder: Lexical
  - BacklashCorrection: on
- Output options
  - ScanMode: Galvo
  - HatchLines: Alternate
  - ZAxis: Piezo
  - ZDirection: Up
  - Exposure: Variable
- Writing configuration
  - GalvoScanMode
  - ContinuousMode
  - PiezoSettlingTime 10
  - GalvoSettlingTime 2
  - GalvoAcceleration 20
- Writing parameters
  - PowerScaling 1.0
  - ShellLaserPower 70
  - ShellScanSpeed 80000
  - ScaffoldLaserPower 90
  - ScaffoldScanSpeed 100000
  - BaseLaserPower 65
  - BaseScanSpeed 80000
- Stage settings
  - StageVelocity 1000
  - StageCorrectionStretchX 1
  - StageCorrectionStretchY 1.012
  - StageCorrectionAngleX -0.2
  - StageCorrectionAngleY -0.1

A.2 J–V CHARACTERISTICS OF THE SIX-DEVICE BATCH

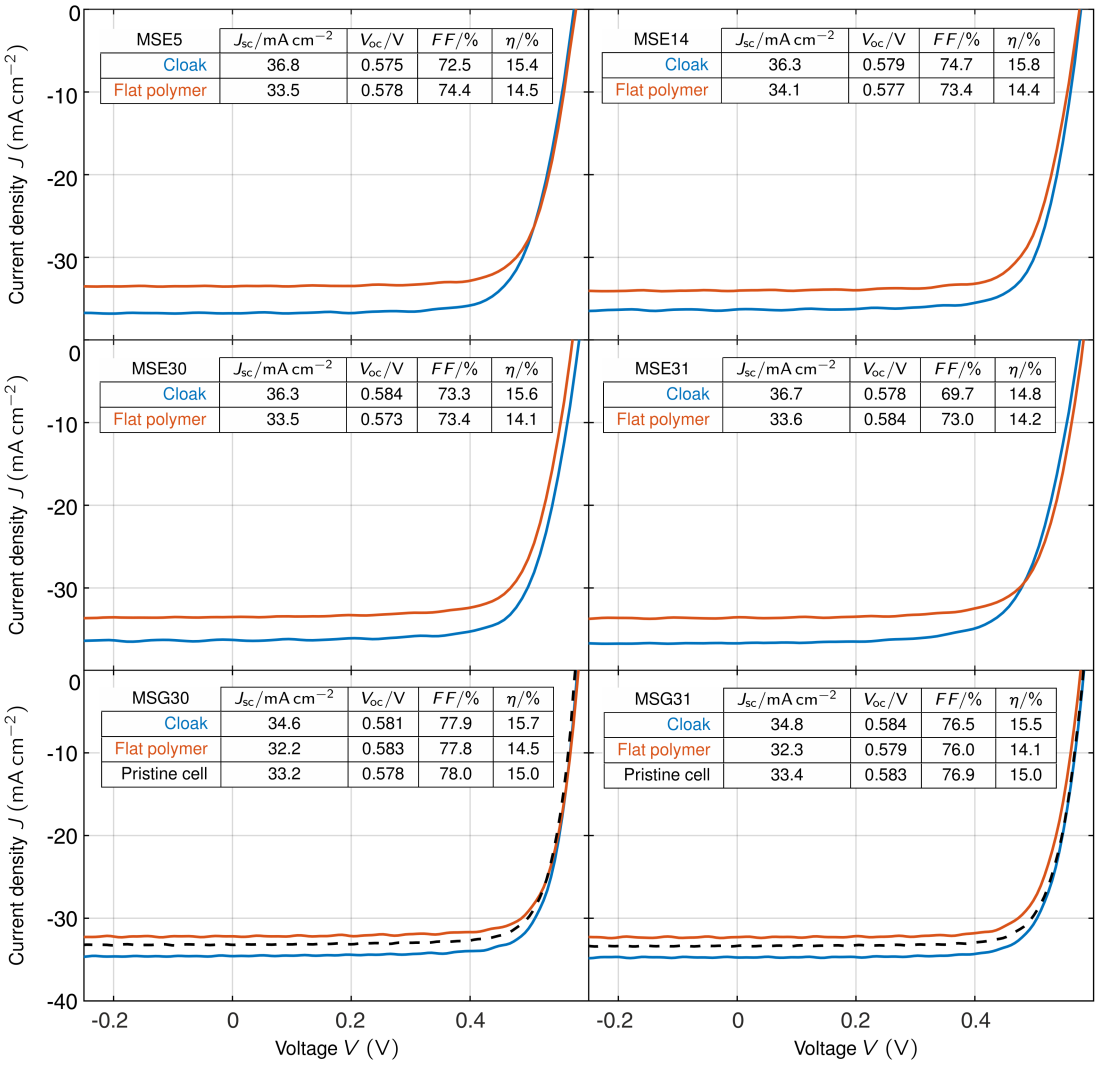

Figure A.2: J–V characteristics for the six cells discussed in section 4.4.4.2. The values for cell MSG31 (bottom right) are quoted in the main text. Reproduced from [101]. © 2017 WILEY-VCH Verlag GmbH & Co. KGaA, Weinheim.

A.3 Uncertainties in characterizing SHJ solar cells with FFS cloaks

In the following section, measurement uncertainties in the characterization of the SHJ solar cells with FFS cloaks are discussed, leading to the uncertainties quoted in section 4.4.4.

SISC measurements Despite the fact that the short-circuit current was measured relative to the signal of a reference photodiode, the resulting I_{sc} fluctuated by few percent over the course of several hours. The effect was attributed to temperature variations that caused changes in the alignment of the optics. Therefore, in order to reduce the influence of this error source, the data presented here was recorded within a two-hour window. The measurement uncertainties given in section 4.4.4.1 resulted from the following consideration. The piezo stage used to record the SISC profiles allowed a maximum displacement of 400 µm. Thus, the profile for the cloaked region had to be stitched from 400 µm long, overlapping profiles. The signal in the overlapping region showed discrepancies near 0.3 % of I_0, so this value was taken as the uncertainty in measuring both the reference and average short-circuit current, $\Delta I_{sc}(x' = P/2)$ and $\Delta\langle I_{sc}\rangle$, respectively. These were propagated to yield the uncertainty in the contact finger filling fraction,

$$\Delta f = \left|\frac{\langle I_{sc}\rangle}{I_{sc}(x' = P/2)}\right| \sqrt{\left(\frac{\Delta\langle I_{sc}\rangle}{\langle I_{sc}\rangle}\right)^2 + \left(\frac{\Delta I_{sc}(x' = P/2)}{I_{sc}(x' = P/2)}\right)^2}. \tag{A.1}$$

An analogous equation was found for the uncertainty in the relative current increase, which was derived by propagation of the uncertainties in the filling fractions through eq. (4.47).

J–V characteristics The main sources of uncertainty when computing the relative J_{sc} increase from the standard solar cell characterization were a statistical variation in the results for J_{sc} and the uncertainty in the (effective) contact finger filling fraction. The latter aspect was relevant because J_{sc} found for the reference situation was corrected by the factor c with a dependence on the filling fraction as given by eq. (4.49). Thus, the uncertainty in the relative current increase was calculated according to

$$\Delta\zeta = \left|\frac{J_{sc}^{cloak}}{J_{sc}^{flat}}\right| \sqrt{\left(\frac{\Delta J_{sc}^{cloak}}{J_{sc}^{cloak}}\right)^2 + \left(\frac{\Delta J_{sc}^{flat}}{J_{sc}^{flat}}\right)^2 + \left(\frac{c(l - NP)}{l(1 - f)^2}\Delta f\right)^2}, \tag{A.2}$$

where $N = 4$. While the uncertainty in f was inserted from the SISC results, the fluctuation in J_{sc} was estimated from repeated measurements under nominally equal conditions. Here, a variation corresponding to $^{\Delta J_{sc}}/_{J_{sc}} = 0.3\,\%$ was found. The uncertainty for the relative increase in PCE quoted in section 4.4.4.2 follows from an equation analogous to eq. (A.2). The measurement uncertainty for the PCE was estimated as $\Delta\eta = 0.1\,\%$, again based on the variation observed in repeated measurements.

EQE MEASUREMENTS Measuring EQE several times under the same conditions revealed a variation of approximately $\pm 1\,\%$ in the EQE values. The measurement spot was approximately $l = 5\,\mathrm{mm}$ long, but had a somewhat blurred appearance in the visible spectral range. Moreover, at infrared and ultraviolet wavelengths it was not possible to visually measure the size of the spot, so that an uncertainty of $\Delta l = 0.2\,\mathrm{mm}$ was estimated. Propagation of the uncertainties lead to the expression

$$\Delta\zeta_{\mathrm{EQE}} = \left|\frac{\mathrm{EQE}^{\mathrm{cloak}}}{\mathrm{EQE}^{\mathrm{flat}}}\right| \sqrt{\left(\frac{\Delta\mathrm{EQE}^{\mathrm{cloak}}}{\mathrm{EQE}^{\mathrm{cloak}}}\right)^2 + \left(\frac{\Delta\mathrm{EQE}^{\mathrm{flat}}}{\mathrm{EQE}^{\mathrm{flat}}}\right)^2 + \left(\frac{fNP\Delta l}{l^2(1-f)^2}\right)^2}, \tag{A.3}$$

with $N = 5$, for the resulting uncertainty of the relative increase in EQE. An analogous expression was used to derive the uncertainty of the relative increase in implied short-circuit current, $\Delta\zeta$. In that case, the variation found in the implied short-circuit current amounted to $^{\Delta J_{sc}}/_{J_{sc}} = 0.2\,\%$, as quoted in section 4.4.4.3.

A.4 Validation of the radiance-based ray-tracing simulations

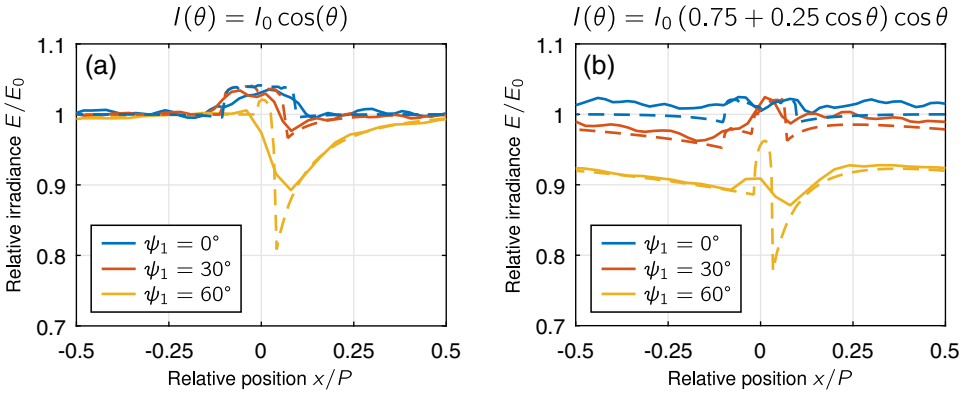

Figure A.3: Simulated irradiance profiles for (a) ideal Lambertian emission and (b) a near-Lambertian angular profile of intensity. In both cases, the results obtained by the radiance-based approach (dashed lines) agree well to the 3D simulations done in the commercial ray-tracing software (solid lines).

The validity of the radiance-based simulation approach employed in section 5.3.2 was verified by additional simulations run in a commercial ray-tracing software (LightTools, Synopsys, USA) based on a Monte-Carlo approach. These simulations were carried out by Benjamin Fritz (Light Technology Institute, KIT). Here, the relevant part of the experimental situation comprising seven periods of metal fingers was modeled in three dimensions. The central three fingers were equipped with a FFS cloak embedded in a flat layer of a material with refractive index $n_1 = 1.5$ that also covered the remaining two fingers. The area in between the fingers was set to emit light with a predefined angular profile of radiant intensity.

The sample was imaged to a screen by a spherical lens. Its diameter, focal length, and position with respect to sample and screen were chosen such that it provided a $2\times$ magnification and a numerical aperture of 0.06. The two-dimensional irradiance distribution registered in the screen plane was converted to an irradiance profile by averaging along the y-direction. After normalizing the profile to the irradiance observed at $x = 0$, the profile could be compared to the results from the radiance-based simulations. Figure A.3 shows the irradiance profiles for the two situations of an ideal Lambertian intensity pattern and for the modified version discussed in section 5.3.2.

Generally, good agreement between the two simulation methods was found, indicating that the radiance-based approach is valid in the considered scenario. The irradiance profiles from the 3D simulations showed less sharp features, because the binning in the screen plane was chosen fairly coarse. This was required because rays were launched at random directions from the emissive area. Therefore, only a small fraction of the launched light finally hit the screen plane, drastically increasing shot noise in the irradiance distribution. Several hundred million rays had to be traced in order to generate the irradiance profiles depicted in fig. A.3, which still show clear signs of shot noise.

Bibliography

[1] I. E. Tamm, "The Electrodynamics of Anisotropic Media in the Special Theory of Relativity", J. Russ. Phys. Chem. Soc. **56**, 248 (1924) (cited on page 1).

[2] I. E. Tamm, "Crystal-Optics of the Theory of Relativity Pertinent to the Geometry of a Biquadratic Form", J. Russ. Phys. Chem. Soc. **57** (1925) (cited on page 1).

[3] A. Einstein, "Die Grundlage Der Allgemeinen Relativitätstheorie", Ann. Phys. **354**, 769–822 (1916) (cited on page 1).

[4] L. S. Dolin, "On a Possibility of Comparing Three-Dimensional Electromagnetic Systems with Inhomogeneous Filling", Izv. Vuz. Radiofiz. **4**, 964–967 (1961) (cited on page 1).

[5] M. Lax and D. F. Nelson, "Maxwell Equations in Material Form", Phys. Rev. B **13**, 1777–1784 (1976) (cited on pages 1, 6).

[6] C. M. Soukoulis and M. Wegener, "Past Achievements and Future Challenges in the Development of Three-Dimensional Photonic Metamaterials", Nat. Photonics **5**, 523–530 (2011) (cited on pages 2, 7).

[7] J. B. Pendry, A. J. Holden, W. J. Stewart, and I. Youngs, "Extremely Low Frequency Plasmons in Metallic Mesostructures", Phys. Rev. Lett. **76**, 4773–4776 (1996) (cited on page 2).

[8] J. B. Pendry, A. J. Holden, D. J. Robbins, and W. J. Stewart, "Magnetism from Conductors and Enhanced Nonlinear Phenomena", IEEE Trans. Microw. Theory Tech. **47**, 2075–2084 (1999) (cited on page 2).

[9] J. B. Pendry, "Negative Refraction Makes a Perfect Lens", Phys. Rev. Lett. **85**, 3966–3969 (2000) (cited on page 2).

[10] J. B. Pendry, D. Schurig, and D. R. Smith, "Controlling Electromagnetic Fields", Science **312**, 1780–1782 (2006) (cited on pages 2, 5, 47).

[11] U. Leonhardt and T. G. Philbin, "General Relativity in Electrical Engineering", New J. Phys. **8**, 247 (2006) (cited on pages 2, 6).

[12] U. Leonhardt, "Optical Conformal Mapping", Science **312**, 1777–1780 (2006) (cited on pages 2, 5, 8, 9).

[13] D. H. Werner, Z. H. Jiang, J. P. Turpin, Q. Wu, and M. D. Gregory, "Transformation Electromagnetics Inspired Lens Designs and Associated Metamaterial Implementations for Highly Directive Radiation", in *Transformation Electromagnetics and Metamaterials: Fundamental Principles and Applications*, edited by D. H. Werner and D.-H. Kwon (Springer London, UK, 2014), pp. 221–261 (cited on page 2).

[14] N. Kundtz and D. R. Smith, "Extreme-Angle Broadband Metamaterial Lens", Nat. Mater. **9**, 129 (2010) (cited on page 2).

[15] H. F. Ma and T. J. Cui, "Three-Dimensional Broadband Ground-Plane Cloak Made of Metamaterials", Nat. Commun. **1**, 21 (2010) (cited on pages 2, 8).

[16] P.-H. Tichit, S. N. Burokur, D. Germain, and A. de Lustrac, "Design and Experimental Demonstration of a High-Directive Emission with Transformation Optics", Phys. Rev. B **83**, 155108 (2011) (cited on page 2).

[17] D. A. Roberts, M. Rahm, J. B. Pendry, and D. R. Smith, "Transformation-Optical Design of Sharp Waveguide Bends and Corners", Appl. Phys. Lett. **93**, 251111 (2008) (cited on page 2).

[18] Z. Liang and J. Li, "Scaling Two-Dimensional Photonic Crystals for Transformation Optics", Opt. Express **19**, 16821–16829 (2011) (cited on page 2).

[19] T. Han, C.-W. Qiu, and X. Tang, "Adaptive Waveguide Bends with Homogeneous, Nonmagnetic, and Isotropic Materials", Opt. Lett. **36**, 181–183 (2011) (cited on page 2).

[20] L. H. Gabrielli, D. Liu, S. G. Johnson, and M. Lipson, "On-Chip Transformation Optics for Multimode Waveguide Bends", Nat. Commun. **3**, 1217 (2012) (cited on page 2).

[21] R. Fleury, F. Monticone, and A. Alù, "Invisibility and Cloaking: Origins, Present, and Future Perspectives", Phys. Rev. Appl. **4**, 037001 (2015) (cited on page 2).

[22] D. Schurig, J. J. Mock, B. J. Justice, S. A. Cummer, J. B. Pendry, A. F. Starr, and D. R. Smith, "Metamaterial Electromagnetic Cloak at Microwave Frequencies", Science **314**, 977–980 (2006) (cited on pages 2, 47).

[23] J. Li and J. B. Pendry, "Hiding under the Carpet: A New Strategy for Cloaking", Phys. Rev. Lett. **101**, 203901 (2008) (cited on pages 2, 8).

[24] J. Valentine, J. Li, T. Zentgraf, G. Bartal, and X. Zhang, "An Optical Cloak Made of Dielectrics", Nat. Mater. **8**, 568–571 (2009) (cited on page 2).

[25] T. Ergin, N. Stenger, P. Brenner, J. B. Pendry, and M. Wegener, "Three-Dimensional Invisibility Cloak at Optical Wavelengths", Science **328**, 337–339 (2010) (cited on pages 2, 8, 21, 50, 52, 145).

[26] M. Gharghi, C. Gladden, T. Zentgraf, Y. Liu, X. Yin, J. Valentine, and X. Zhang, "A Carpet Cloak for Visible Light", Nano Lett. **11**, 2825–2828 (2011) (cited on page 2).

[27] International Technology Roadmap for Photovoltaic, *ITRPV Eighth Edition*, 2016 Results, http://www.itrpv.net (2017) (cited on pages 2, 45).

[28] M. A. Green, Y. Hishikawa, E. D. Dunlop, D. H. Levi, J. Hohl-Ebinger, and A. W. Y. Ho-Baillie, "Solar Cell Efficiency Tables (Version 51)", Prog. Photovolt. Res. Appl. **26**, 3–12 (2018) (cited on page 2).

[29] K. Hong and J.-L. Lee, "Review Paper: Recent Developments in Light Extraction Technologies of Organic Light Emitting Diodes", Electron. Mater. Lett. **7**, 77–91 (2011) (cited on pages 2, 128).

[30] M. C. Gather and S. Reineke, "Recent Advances in Light Outcoupling from White Organic Light-Emitting Diodes", J. Photonics Energy **5**, 057607 (2015) (cited on pages 2, 128).

[31] K. Neyts, M. Marescaux, A. U. Nieto, A. Elschner, W. Lövenich, K. Fehse, Q. Huang, K. Walzer, and K. Leo, "Inhomogeneous Luminance in Organic Light Emitting Diodes Related to Electrode Resistivity", J. Appl. Phys. **100**, 114513 (2006) (cited on pages 2, 111).

[32] H. Chen, C. T. Chan, and P. Sheng, "Transformation Optics and Metamaterials", Nat. Mater. **9**, 387–396 (2010) (cited on page 5).

[33] G. W. Milton, M. Briane, and J. R. Willis, "On Cloaking for Elasticity and Physical Equations with a Transformation Invariant Form", New J. Phys. **8**, 248 (2006) (cited on page 6).

[34] E. J. Post, *Formal Structure of Electromagnetics - General Covariance and Electromagnetics* (North-Holland Publishing Co., Amsterdam, Netherlands, 1962) (cited on page 6).

[35] D. Schurig, J. B. Pendry, and D. R. Smith, "Calculation of Material Properties and Ray Tracing in Transformation Media", Opt. Express **14**, 9794 (2006) (cited on pages 6, 34).

[36] N. Landy, Y. Urzhumov, and D. R. Smith, "Quasi-Conformal Approaches for Two and Three-Dimensional Transformation Optical Media", in *Transformation Electromagnetics and Metamaterials*, edited by D. H. Werner and D.-H. Kwon (Springer London, UK, 2014) (cited on pages 7, 8, 147).

[37] E. Cubukcu, K. Aydin, E. Ozbay, S. Foteinopoulou, and C. M. Soukoulis, "Electromagnetic Waves: Negative Refraction by Photonic Crystals", Nature **423**, 604–605 (2003) (cited on page 7).

[38] V. M. Shalaev, W. Cai, U. K. Chettiar, H.-K. Yuan, A. K. Sarychev, V. P. Drachev, and A. V. Kildishev, "Negative Index of Refraction in Optical Metamaterials", Opt. Lett. **30**, 3356–3358 (2005) (cited on page 7).

[39] G. Dolling, C. Enkrich, M. Wegener, C. M. Soukoulis, and S. Linden, "Simultaneous Negative Phase and Group Velocity of Light in a Metamaterial", Science **312**, 892–894 (2006) (cited on page 7).

[40] I. Liberal and N. Engheta, "Near-Zero Refractive Index Photonics", Nat. Photonics **11**, 149–158 (2017) (cited on page 7).

[41] J. Elser and V. A. Podolskiy, "Scattering-Free Plasmonic Optics with Anisotropic Metamaterials", Phys. Rev. Lett. **100**, 066402 (2008) (cited on page 7).

[42] A. Fang, T. Koschny, and C. M. Soukoulis, "Optical Anisotropic Metamaterials: Negative Refraction and Focusing", Phys. Rev. B **79**, 245127 (2009) (cited on page 7).

[43] J. Luo, P. Xu, H. Chen, B. Hou, L. Gao, and Y. Lai, "Realizing Almost Perfect Bending Waveguides with Anisotropic Epsilon-near-Zero Metamaterials", Appl. Phys. Lett. **100**, 221903 (2012) (cited on page 7).

[44] S. Hrabar, J. Bartolic, and Z. Sipus, "Waveguide Miniaturization Using Uniaxial Negative Permeability Metamaterial", IEEE T. Antenn. Propag. **53**, 110–119 (2005) (cited on page 7).

[45] Q. Zhao, L. Kang, B. Du, B. Li, J. Zhou, H. Tang, X. Liang, and B. Zhang, "Electrically Tunable Negative Permeability Metamaterials Based on Nematic Liquid Crystals", Appl. Phys. Lett. **90**, 011112 (2007) (cited on page 7).

[46] S. Linden, C. Enkrich, M. Wegener, J. Zhou, T. Koschny, and C. M. Soukoulis, "Magnetic Response of Metamaterials at 100 Terahertz", Science **306**, 1351–1353 (2004) (cited on page 7).

[47] D. R. Smith, W. J. Padilla, D. C. Vier, S. C. Nemat-Nasser, and S. Schultz, "Composite Medium with Simultaneously Negative Permeability and Permittivity", Phys. Rev. Lett. **84**, 4184 (2000) (cited on page 7).

[48] J. P. Turpin, A. T. Massoud, Z. H. Jiang, P. L. Werner, and D. H. Werner, "Conformal Mappings to Achieve Simple Material Parameters for Transformation Optics Devices", Opt. Express **18**, 244–252 (2010) (cited on page 8).

[49] H. F. Ma and T. J. Cui, "Three-Dimensional Broadband and Broad-Angle Transformation-Optics Lens", Nat. Commun. **1**, 124 (2010) (cited on page 8).

[50] Y. Kim, I. Seo, I.-S. Koh, and Y. Lee, "Design Method for Broadband Free-Space Electromagnetic Cloak Based on Isotropic Material for Size Reduction and Enhanced Invisibility", Opt. Express **24**, 22708 (2016) (cited on page 8).

[51] J. Fischer, T. Ergin, and M. Wegener, "Three-Dimensional Polarization-Independent Visible-Frequency Carpet Invisibility Cloak", Opt. Lett. **36**, 2059–2061 (2011) (cited on page 8).

[52] Y. G. Ma, N. Wang, and C. K. Ong, "Application of Inverse, Strict Conformal Transformation to Design Waveguide Devices", J. Opt. Soc. Am. A **27**, 968–972 (2010) (cited on page 8).

[53] L. Tang, J. Yin, G. Yuan, J. Du, H. Gao, X. Dong, Y. Lu, and C. Du, "General Conformal Transformation Method Based on Schwarz-Christoffel Approach", Opt. Express **19**, 15119–15126 (2011) (cited on page 10).

[54] T. A. Driscoll and L. N. Trefethen, *Schwarz-Christoffel Mapping* (Cambridge University Press, Cambridge, UK, 2002) (cited on page 10).

[55] T. A. Driscoll, "Algorithm 756: A MATLAB Toolbox for Schwarz-Christoffel Mapping", ACM Trans. Math. **22**, 168–186 (1996) (cited on pages 10, 131).

[56] T. A. Driscoll, "Algorithm 843: Improvements to the Schwarz-Christoffel Toolbox for MATLAB", ACM Trans. Math. Softw. **31**, 239–251 (2005) (cited on page 10).

[57] S. John, "Strong Localization of Photons in Certain Disordered Dielectric Superlattices", Phys. Rev. Lett. **58**, 2486–2489 (1987) (cited on page 12).

[58] E. Yablonovitch, "Inhibited Spontaneous Emission in Solid-State Physics and Electronics", Phys. Rev. Lett. **58**, 2059–2062 (1987) (cited on page 12).

[59] Y. A. Vlasov, M. O'Boyle, H. F. Hamann, and S. J. McNab, "Active Control of Slow Light on a Chip with Photonic Crystal Waveguides", Nature **438**, 65–69 (2005) (cited on page 12).

[60] S. Y. Lin, J. G. Fleming, D. L. Hetherington, B. K. Smith, R. Biswas, K. M. Ho, M. M. Sigalas, W. Zubrzycki, S. R. Kurtz, and J. Bur, "A Three-Dimensional Photonic Crystal Operating at Infrared Wavelengths", Nature **394**, 251–253 (1998) (cited on page 12).

[61] M. Arcari, I. Söllner, A. Javadi, S. Lindskov Hansen, S. Mahmoodian, J. Liu, H. Thyrrestrup, E. H. Lee, J. D. Song, S. Stobbe, and P. Lodahl, "Near-Unity Coupling Efficiency of a Quantum Emitter to a Photonic Crystal Waveguide", Phys. Rev. Lett. **113**, 093603 (2014) (cited on page 12).

[62] A. Blanco-Redondo, C. Husko, D. Eades, Y. Zhang, J. Li, T. F. Krauss, and B. J. Eggleton, "Observation of Soliton Compression in Silicon Photonic Crystals", Nat. Commun. **5**, 3160 (2014) (cited on page 12).

[63] C. Fenzl, T. Hirsch, and O. S. Wolfbeis, "Photonic Crystals for Chemical Sensing and Biosensing", Angew. Chem. Int. Ed. **53**, 3318–3335 (2014) (cited on page 12).

[64] Y. Zhao, L. Shang, Y. Cheng, and Z. Gu, "Spherical Colloidal Photonic Crystals", Acc. Chem. Res. **47**, 3632–3642 (2014) (cited on page 12).

[65] H. S. Lee, T. S. Shim, H. Hwang, S.-M. Yang, and S.-H. Kim, "Colloidal Photonic Crystals toward Structural Color Palettes for Security Materials", Chem. Mater. **25**, 2684–2690 (2013) (cited on page 12).

[66] T. Ergin, "Photonic Metamaterials for Transformation Optics", Dissertation (Karlsruhe Institute of Technology, Karlsruhe, Germany, Jan. 20, 2012) (cited on page 13).

[67] J. D. Joannopoulos, S. G. Johnson, J. N. Winn, and R. D. Meade, *Photonic Crystals: Molding the Flow of Light* (Princeton University Press, Princeton, USA, 2008) (cited on page 13).

[68] S. G. Johnson and J. D. Joannopoulos, "Block-Iterative Frequency-Domain Methods for Maxwell's Equations in a Planewave Basis", Opt. Express **8**, 173–190 (2001) (cited on page 14).

[69] R. U. Datla and A. C. Parr, "Introduction to Optical Radiometry", in *Optical Radiometry*, Vol. 41, edited by A. C. Parr, R. U. Datla, and J. L. Gardner, red. by R. Celotta and T. Lucatorto, Experimental methods in the physical sciences (Elsevier Academic Press, San Diego, USA, 2005) (cited on pages 14, 15).

[70] J. Chaves, *Introduction to Nonimaging Optics*, 2nd edition (CRC Press, Boca Raton, USA, 2016) (cited on page 18).

[71] S. Kawata, H.-B. Sun, T. Tanaka, and K. Takada, "Finer Features for Functional Microdevices", Nature **412**, 697–698 (2001) (cited on page 21).

[72] C. Kern, M. Kadic, and M. Wegener, "Experimental Evidence for Sign Reversal of the Hall Coefficient in Three-Dimensional Metamaterials", Phys. Rev. Lett. **118**, 016601 (2017) (cited on page 21).

[73] J. K. Gansel, M. Thiel, M. S. Rill, M. Decker, K. Bade, V. Saile, G. von Freymann, S. Linden, and M. Wegener, "Gold Helix Photonic Metamaterial as Broadband Circular Polarizer", Science **325**, 1513–1515 (2009) (cited on page 21).

[74] J. Qu, M. Kadic, A. Naber, and M. Wegener, "Micro-Structured Two-Component 3D Metamaterials with Negative Thermal-Expansion Coefficient from Positive Constituents", Sci. Rep. **7**, 40643 (2017) (cited on page 21).

[75] M. S. Rill, C. Plet, M. Thiel, I. Staude, G. von Freymann, S. Linden, and M. Wegener, "Photonic Metamaterials by Direct Laser Writing and Silver Chemical Vapour Deposition", Nat. Mater. **7**, 543–546 (2008) (cited on page 21).

[76] T. Bückmann, N. Stenger, M. Kadic, J. Kaschke, A. Frölich, T. Kennerknecht, C. Eberl, M. Thiel, and M. Wegener, "Tailored 3D Mechanical Metamaterials Made by Dip-in Direct-Laser-Writing Optical Lithography", Adv. Mater. **24**, 2710–2714 (2012) (cited on page 21).

[77] A. Radke, T. Gissibl, T. Klotzbücher, P. V. Braun, and H. Giessen, "Three-Dimensional Bichiral Plasmonic Crystals Fabricated by Direct Laser Writing and Electroless Silver Plating", Adv. Mater. **23**, 3018–3021 (2011) (cited on page 21).

[78] A. Frölich, J. Fischer, T. Zebrowski, K. Busch, and M. Wegener, "Titania Woodpiles with Complete Three-Dimensional Photonic Bandgaps in the Visible", Adv. Mater. **25**, 3588–3592 (2013) (cited on pages 21, 147).

[79] V. Melissinaki, A. A. Gill, I. Ortega, M. Vamvakaki, A. Ranella, J. W. Haycock, C. Fotakis, M. Farsari, and F. Claeyssens, "Direct Laser Writing of 3D Scaffolds for Neural Tissue Engineering Applications", Biofabrication **3**, 045005 (2011) (cited on page 21).

[80] F. Klein, B. Richter, T. Striebel, C. M. Franz, G. von Freymann, M. Wegener, and M. Bastmeyer, "Two-Component Polymer Scaffolds for Controlled Three-Dimensional Cell Culture", Adv. Mater. **23**, 1341–1345 (2011) (cited on pages 21, 26).

[81] A. M. Greiner, B. Richter, and M. Bastmeyer, "Micro-Engineered 3D Scaffolds for Cell Culture Studies", Macromol. Biosci. **12**, 1301–1314 (2012) (cited on page 21).

[82] A. Ovsianikov, M. Gruene, M. Pflaum, L. Koch, F. Maiorana, M. Wilhelmi, A. Haverich, and B. Chichkov, "Laser Printing of Cells into 3D Scaffolds", Biofabrication **2**, 014104 (2010) (cited on page 21).

[83] A. Selimis, V. Mironov, and M. Farsari, "Direct Laser Writing: Principles and Materials for Scaffold 3D Printing", Microelectron. Eng. **132**, 83–89 (2015) (cited on page 21).

[84] M. Schumann, T. Bückmann, N. Gruhler, M. Wegener, and W. Pernice, "Hybrid 2D–3D Optical Devices for Integrated Optics by Direct Laser Writing", Light Sci. Appl. **3**, e175 (2014) (cited on page 21).

[85] S. Juodkazis, "Manufacturing: 3D Printed Micro-Optics", Nat. Photonics **10**, 499–501 (2016) (cited on page 21).

[86] S. Fischbach, A. Schlehahn, A. Thoma, N. Srocka, T. Gissibl, S. Ristok, S. Thiele, A. Kaganskiy, A. Strittmatter, T. Heindel, S. Rodt, A. Herkommer, H. Giessen, and S. Reitzenstein, "Single Quantum Dot with Microlens and 3D-Printed Micro-Objective as Integrated Bright Single-Photon Source", ACS Photonics **4**, 1327–1332 (2017) (cited on page 21).

[87] T. Gissibl, S. Thiele, A. Herkommer, and H. Giessen, "Two-Photon Direct Laser Writing of Ultracompact Multi-Lens Objectives", Nat. Photonics **10**, 554–560 (2016) (cited on page 21).

[88] H. Huang, S. Chen, H. Zou, Q. Li, J. Fu, F. Lin, and X. Wu, "Fabrication of Micro-Axicons Using Direct-Laser Writing", Opt. Express **22**, 11035–11042 (2014) (cited on page 21).

[89] B. Xu, W.-Q. Du, J.-W. Li, Y.-L. Hu, L. Yang, C.-C. Zhang, G.-Q. Li, Z.-X. Lao, J.-C. Ni, J.-R. Chu, D. Wu, S.-L. Liu, and K. Sugioka, "High Efficiency Integration of Three-Dimensional Functional Microdevices inside a Microfluidic Chip by Using Femtosecond Laser Multifoci Parallel Microfabrication", Sci. Rep. **6**, 19989 (2016) (cited on page 21).

[90] B.-B. Xu, Y.-L. Zhang, H. Xia, W.-F. Dong, H. Ding, and H.-B. Sun, "Fabrication and Multifunction Integration of Microfluidic Chips by Femtosecond Laser Direct Writing", Lab Chip **13**, 1677–1690 (2013) (cited on page 21).

[91] A. S. van de Nes, L. Billy, S. F. Pereira, and J. J. M. Braat, "Calculation of the Vectorial Field Distribution in a Stratified Focal Region of a High Numerical Aperture Imaging System", Opt. Express **12**, 1281–1293 (2004) (cited on page 22).

[92] C. M. Sparrow, "On Spectroscopic Resolving Power", Astrophys. J. **44**, 76 (1916) (cited on page 23).

[93] J. Fischer and M. Wegener, "Three-Dimensional Optical Laser Lithography beyond the Diffraction Limit", Laser Photonics Rev. **7**, 22–44 (2013) (cited on page 23).

[94] S. H. Park, T. W. Lim, D.-Y. Yang, N. C. Cho, and K.-S. Lee, "Fabrication of a Bunch of Sub-30-Nm Nanofibers inside Microchannels Using Photopolymerization via a Long Exposure Technique", Appl. Phys. Lett. **89**, 173133 (2006) (cited on page 23).

[95] D. Tan, Y. Li, F. Qi, H. Yang, Q. Gong, X. Dong, and X. Duan, "Reduction in Feature Size of Two-Photon Polymerization Using SCR500", Appl. Phys. Lett. **90**, 071106 (2007) (cited on page 23).

[96] T. H. P. Chang, "Proximity Effect in Electron-beam Lithography", J. Vac. Sci. Technol. **12**, 1271–1275 (1975) (cited on page 23).

[97] E. H. Waller and G. von Freymann, "Spatio-Temporal Proximity Characteristics in 3D µ-Printing via Multi-Photon Absorption", Polymers **8**, 297 (2016) (cited on page 24).

[98] J. B. Mueller, J. Fischer, Y. J. Mange, T. Nann, and M. Wegener, "In-Situ Local Temperature Measurement during Three-Dimensional Direct Laser Writing", Appl. Phys. Lett. **103**, 123107 (2013) (cited on page 24).

[99] R. Buestrich, F. Kahlenberg, M. Popall, P. Dannberg, R. Müller-Fiedler, and O. Rösch, "ORMOCER®s for Optical Interconnection Technology", J. Sol-Gel Sci. Techn. **20**, 181–186 (2001) (cited on page 26).

[100] J. P. Matinlinna and L. V. Lassila, "Experimental Novel Silane System in Adhesion Promotion between Dental Resin and Pretreated Titanium. Part II: Effect of Long-Term Water Storage", Silicon **2**, 79–85 (2010) (cited on page 26).

[101] M. F. Schumann, M. Langenhorst, M. Smeets, K. Ding, U. W. Paetzold, and M. Wegener, "All-Angle Invisibility Cloaking of Contact Fingers on Solar Cells by Refractive Free-Form Surfaces", Adv. Opt. Mater. **5**, 1700164 (2017) (cited on pages 28, 90, 99, 100, 104, 106, 153).

[102] Nanoscribe GmbH, *IP Photoresists*, (2017) http://www.nanoscribe.de/en/products/ip-photoresists/ (visited on 10/10/2017) (cited on page 29).

[103] Micro Resist Technology GmbH, *OrmoComp® and OrmoClear®FX*, (11–2015) http://microresist.de/sites/default/files/download/PI_OrmoComp_OrmoClearFX_2015_0.pdf (visited on 10/10/2017) (cited on page 29).

[104] J. C. Halimeh, R. Schmied, and M. Wegener, "Newtonian Photorealistic Ray Tracing of Grating Cloaks and Correlation-Function-Based Cloaking-Quality Assessment", Opt. Express **19**, 6078–6092 (2011) (cited on page 34).

[105] J. Molcho and D. Censor, "A Simple Derivation and an Example of Hamiltonian Ray Propagation", Am. J. Phys. **54**, 351–353 (1986) (cited on page 34).

[106] P. S. J. Russel and T. A. Birks, "Hamiltonian Optics of Nonuniform Photonic Crystals", J. Lightwave Technol. **17**, 1982–1988 (1999) (cited on page 34).

[107] S. J. Fonash, *Solar Cell Device Physics* (Academic Press, Burlington, USA, 2010) (cited on page 37).

[108] C. Gueymard, *SMARTS2: A Simple Model of the Atmospheric Radiative Transfer of Sunshine: Algorithms and Performance Assessment*, Professional Paper FSEC-PF-270-95 (Florida Solar Energy Center, Cocoa, FL, USA, 1995) (cited on page 38).

[109] C. A. Gueymard, "Parameterized Transmittance Model for Direct Beam and Circumsolar Spectral Irradiance", Sol. Energy **71**, 325–346 (2001) (cited on page 38).

[110] P. A. Lynn, *Electricity from Sunlight: An Introduction to Photovoltaics* (John Wiley & Sons, West Sussex, UK, 2010) (cited on page 41).

[111] W. Shockley and H. J. Queisser, "Detailed Balance Limit of Efficiency of P-n Junction Solar Cells", J. Appl. Phys. **32**, 510–519 (1961) (cited on page 41).

[112] S. Rühle, "Tabulated Values of the Shockley–Queisser Limit for Single Junction Solar Cells", Sol. Energy **130**, 139–147 (2016) (cited on page 41).

[113] T. Tiedje, E. Yablonovitch, G. D. Cody, and B. G. Brooks, "Limiting Efficiency of Silicon Solar Cells", IEEE Trans. Electron Devices **31**, 711–716 (1984) (cited on page 41).

[114] M. J. Kerr, P. Campbell, and A. Cuevas, "Lifetime and Efficiency Limits of Crystalline Silicon Solar Cells", in Conference Record of the 29th IEEE Photovoltaic Specialists Conference (2002), pp. 438–441 (cited on page 41).

[115] A. Richter, J. Benick, F. Feldmann, A. Fell, M. Hermle, and S. W. Glunz, "N-Type Si Solar Cells with Passivating Electron Contact: Identifying Sources for Efficiency Limitations by Wafer Thickness and Resistivity Variation", Sol. Energy Mater. Sol. Cells **173**, 96–105 (2017) (cited on page 42).

[116] M. Glatthaar, J. Haunschild, M. Kasemann, J. Giesecke, W. Warta, and S. Rein, "Spatially Resolved Determination of Dark Saturation Current and Series Resistance of Silicon Solar Cells", Phys. Status Solidi (RRL) **4**, 13–15 (2010) (cited on page 43).

[117] L. Kuna, G. C. Eder, C. Leiner, and G. Peharz, "Reducing Shadowing Losses with Femtosecond-Laser-Written Deflective Optical Elements in the Bulk of EVA Encapsulation: Reducing Optical Shadowing by Volume Optics in Encapusulant", Prog. Photovolt. Res. Appl. **23**, 1120–1130 (2014) (cited on page 45).

[118] M. F. Stuckings and A. W. Blakers, "A Study of Shading and Resistive Loss from the Fingers of Encapsulated Solar Cells", Sol. Energy Mater. Sol. Cells **59**, 233–242 (1999) (cited on page 45).

[119] J. Schneider, M. Turek, M. Dyrba, I. Baumann, B. Koll, and T. Booz, "Combined Effect of Light Harvesting Strings, Anti-Reflective Coating, Thin Glass, and High Ultraviolet Transmission Encapsulant to Reduce Optical Losses in Solar Modules", Prog. Photovolt. Res. Appl. **22**, 830–837 (2014) (cited on page 45).

[120] Ebner, R., Schwark, M., Kubicek, B., Újvári, G., Mühleisen, W., Hirschl, C., Neumaier, L., Pedevilla, M., Scheurer, J., Plösch, A., Kogler, A., Krumlacher, W., and Muckenhuber, H., "Increased Power Output of Crystalline Silicon PV Modules by Alternative Interconnection Applications", in Proceedings of the 28th European Photovoltaic Solar Energy Conference and Exhibition (2013), pp. 489–494 (cited on page 45).

[121] "Solar Cells and Methods of Manufacturing Solar Cells Incorporating Effectively Transparent 3D Contacts", US20160322514 (H. A. Atwater, R. Saive, A. M. Borsuk, H. Emmer, C. Bukowsky, and S. Yalamanchili, Mar. 11, 2016) (cited on page 45).

[122] R. Saive, A. M. Borsuk, H. S. Emmer, C. R. Bukowsky, J. V. Lloyd, S. Yalamanchili, and H. A. Atwater, "Effectively Transparent Front Contacts for Optoelectronic Devices", Adv. Opt. Mater. **4**, 1470–1474 (2016) (cited on page 45).

[123] I. Mingareev, R. Berlich, T. J. Eichelkraut, H. Herfurth, S. Heinemann, and M. C. Richardson, "Diffractive Optical Elements Utilized for Efficiency Enhancement of Photovoltaic Modules", Opt. Express **19**, 11397 (2011) (cited on page 45).

[124] J. Jaus, H. Pantsar, J. Eckert, M. Duell, H. Herfurth, and D. Doble, "Light Management for Reduction of Bus Bar and Gridline Shadowing in Photovoltaic Modules", in 35th IEEE Photovoltaic Specialists Conference (2010), pp. 979–983 (cited on page 45).

[125] P. Jahelka, R. Saive, and H. Atwater, "Total Internal Reflection for Effectively Transparent Solar Cell Contacts", ArXiv:1610.01047v1 (2016) (cited on page 45).

[126] F.-h. Chen, S. Pathreeker, J. Kaur, and I. D. Hosein, "Increasing Light Capture in Silicon Solar Cells with Encapsulants Incorporating Air Prisms to Reduce Metallic Contact Losses", Opt. Express **24**, A1419–A1430 (2016) (cited on page 45).

[127] E. San Román, A. Vitrey, J. Buencuerpo, I. Prieto, J. M. Llorens, A. García-Martín, B. Alén, A. Chaudhuri, A. Neumann, S. R. J. Brueck, and J. M. Ripalda, "Cloaking of Solar Cell Contacts at the Onset of Rayleigh Scattering", Sci. Rep. **6**, 28669 (2016) (cited on page 45).

[128] J. Schneider, P. Rohner, D. Thureja, M. Schmid, P. Galliker, and D. Poulikakos, "Electrohydrodynamic NanoDrip Printing of High Aspect Ratio Metal Grid Transparent Electrodes", Adv. Funct. Mater. **26**, 833–840 (2016) (cited on page 45).

[129] Q.-D. Ou, H.-J. Xie, J.-D. Chen, L. Zhou, Y.-Q. Li, and J.-X. Tang, "Enhanced Light Harvesting in Flexible Polymer Solar Cells: Synergistic Stimulation of Plasmonic Meta-Mirror and Transparent Silver Mesowire Electrode", J. Mater. Chem. A **4**, 18952–18962 (2016) (cited on page 45).

[130] E. V. Kerschaver and G. Beaucarne, "Back-Contact Solar Cells: A Review", Prog. Photovolt. Res. Appl. **14**, 107–123 (2006) (cited on page 45).

[131] K. Yoshikawa, H. Kawasaki, W. Yoshida, T. Irie, K. Konishi, K. Nakano, T. Uto, D. Adachi, M. Kanematsu, H. Uzu, and K. Yamamoto, "Silicon Heterojunction Solar Cell with Interdigitated Back Contacts for a Photoconversion Efficiency over 26%", Nat. Energy **2**, 17032 (2017) (cited on page 45).

[132] J. Zhao, A. Wang, and M. A. Green, "An Optimized Prismatic Cover Design for Concentrator and Nonconcentrator Solar Cells", J. Appl. Phys. **68**, 1345–1350 (1990) (cited on page 45).

[133] A. Meulenberg, "The Sawtooth Coverslide - A New Means of Coupling Light into Solar Cells", J. Energy **1**, 151–154 (1977) (cited on page 45).

[134] A. Boca, K. M. Edmondson, and R. R. King, "Prismatic Covers for Boosting the Efficiency of High-Concentration PV Systems", in 34th IEEE Photovoltaic Specialists Conference (2009), pp. 131–136 (cited on page 45).

[135] V. M. Andreev, A. B. Kazantsev, V. P. Khvostikov, E. V. Paleeva, V. D. Rumyantsev, and M. Z. Shvarts, "High-Efficiency (24.6% AM 0) LPE Grown AlGaAs/GaAs Concentrator Solar Cells and Modules", in Conference Record of the 24th IEEE Photovoltaic Specialists Conference, Vol. 2 (1994), pp. 2096–2099 (cited on page 45).

[136] M. F. Schumann, S. Wiesendanger, J. C. Goldschmidt, B. Bläsi, K. Bittkau, U. W. Paetzold, A. Sprafke, R. B. Wehrspohn, C. Rockstuhl, and M. Wegener, "Cloaked Contact Grids on Solar Cells by Coordinate Transformations: Designs and Prototypes", Optica **2**, 850 (2015) (cited on pages 46, 47, 54, 64, 72, 79, 82, 85).

[137] S. Wiesendanger, "Photonmanagement in Dünnfilmsolarzellen" (Friedrich-Schiller-Universität Jena, Jena, Germany, Sept. 3, 2015) (cited on page 47).

[138] I. Staude, "Functional Elements in Three-Dimensional Photonic Bandgap Materials" (Karlsruhe Institute of Technology, Karlsruhe, Germany, Feb. 11, 2011) (cited on page 51).

[139] K. McIntosh, J. Cotsell, J. Cumpston, A. Norris, N. Powell, and B. Ketola, "An Optical Comparison of Silicone and EVA Encapsulants for Conventional Silicon PV Modules: A Ray-Tracing Study", in 34th IEEE Photovoltaic Specialists Conference (2009), pp. 544–549 (cited on page 80).

[140] J. Kischkat, S. Peters, B. Gruska, M. Semtsiv, M. Chashnikova, M. Klinkmüller, O. Fedosenko, S. Machulik, A. Aleksandrova, G. Monastyrskyi, Y. Flores, and W. Ted Masselink, "Mid-Infrared Optical Properties of Thin Films of Aluminum Oxide, Titanium Dioxide, Silicon Dioxide, Aluminum Nitride, and Silicon Nitride", Appl. Opt. **51**, 6789–6798 (2012) (cited on page 80).

[141] H. C. Power, "Trends in Solar Radiation over Germany and an Assessment of the Role of Aerosols and Sunshine Duration", Theor. Appl. Climatol. **76**, 47–63 (2003) (cited on page 81).

[142] S. C. W. Krauter, *Solar Electric Power Generation - Photovoltaic Energy Systems* (Springer Berlin Heidelberg, Germany, 2006) (cited on page 82).

[143] European Union, *PV Potential Estimation Utility*, `http://re.jrc.ec.europa.eu/pvgis/apps4/pvest.php` (visited on 03/27/2015) (cited on page 83).

[144] T. Huld, R. Müller, and A. Gambardella, "A New Solar Radiation Database for Estimating PV Performance in Europe and Africa", Sol. Energy **86**, 1803–1815 (2012) (cited on page 83).

[145] L. Powalla, "Cloaked Contact Grids on Solar Cells", B.Sc. Thesis (Karlsruhe Institute of Technology, Karlsruhe, Germany, Sept. 5, 2016) (cited on pages 87, 89).

[146] K. Ding, U. Aeberhard, F. Finger, and U. Rau, "Silicon Heterojunction Solar Cell with Amorphous Silicon Oxide Buffer and Microcrystalline Silicon Oxide Contact Layers", Phys. Status Solidi (RRL) **6**, 193–195 (2012) (cited on pages 90, 91).

[147] M. F. Schumann, B. Fritz, R. Eckstein, U. Lemmer, G. Gomard, and M. Wegener, "Cloaking of Metal Grid Electrodes on Lambertian Emitters by Free-Form Refractive Surfaces", Opt. Lett. **43**, 527–530 (2018) (cited on pages 109, 112, 116, 118, 121).

[148] W. Brütting, J. Frischeisen, T. D. Schmidt, B. J. Scholz, and C. Mayr, "Device Efficiency of Organic Light-Emitting Diodes: Progress by Improved Light Outcoupling", Phys. Status Solidi A **210**, 44–65 (2013) (cited on pages 110, 128).

[149] C. Adachi, M. A. Baldo, M. E. Thompson, and S. R. Forrest, "Nearly 100% Internal Phosphorescence Efficiency in an Organic Light-Emitting Device", J. Appl. Phys. **90**, 5048–5051 (2001) (cited on pages 111, 127).

[150] J.-H. Jou, S. Kumar, A. Agrawal, T.-H. Li, and S. Sahoo, "Approaches for Fabricating High Efficiency Organic Light Emitting Diodes", J. Mater. Chem. C **3**, 2974–3002 (2015) (cited on page 111).

[151] A. E. Nikolaenko, M. Cass, F. Bourcet, D. Mohamad, and M. Roberts, "Thermally Activated Delayed Fluorescence in Polymers: A New Route toward Highly Efficient Solution Processable OLEDs", Adv. Mater. **27**, 7236–7240 (2015) (cited on page 111).

[152] S. Park, J. T. Lim, W.-Y. Jin, H. Lee, B.-H. Kwon, N. S. Cho, J.-H. Han, J.-W. Kang, S. Yoo, and J.-I. Lee, "Efficient Large-Area Transparent OLEDs Based on a Laminated Top Electrode with an Embedded Auxiliary Mesh", ACS Phot. **4**, 1114–1122 (2017) (cited on page 111).

[153] A. Sugimoto, H. Ochi, S. Fujimura, A. Yoshida, T. Miyadera, and M. Tsuchida, "Flexible OLED Displays Using Plastic Substrates", IEEE J. Sel. Top. Quant. **10**, 107–114 (2004) (cited on page 111).

[154] J.-S. Park, H. Chae, H. K. Chung, and S. I. Lee, "Thin Film Encapsulation for Flexible AM-OLED: A Review", Semicond. Sci. Technol. **26**, 034001 (2011) (cited on page 111).

[155] B. O'Connor, K. H. An, Y. Zhao, K. P. Pipe, and M. Shtein, "Fiber Shaped Light Emitting Device", Adv. Mater. **19**, 3897–3900 (2007) (cited on page 111).

[156] V. Bulovic, G. Gu, P. E. Burrows, S. R. Forrest, and M. E. Thompson, "Transparent Light-Emitting Devices", Nature **380**, 29–29 (1996) (cited on page 111).

[157] P. Görrn, M. Sander, J. Meyer, M. Kröger, E. Becker, H.-H. Johannes, W. Kowalsky, and T. Riedl, "Towards See-Through Displays: Fully Transparent Thin-Film Transistors Driving Transparent Organic Light-Emitting Diodes", Adv. Mater. **18**, 738–741 (2006) (cited on page 111).

[158] Y. Chen, J. Wang, Z. Zhong, Z. Jiang, C. Song, Z. Hu, J. Peng, J. Wang, and Y. Cao, "Fabricating Large-Area White OLED Lighting Panels via Dip-Coating", Org. Electron. **37**, 458–464 (2016) (cited on page 111).

[159] T.-H. Han, Y. Lee, M.-R. Choi, S.-H. Woo, S.-H. Bae, B. H. Hong, J.-H. Ahn, and T.-W. Lee, "Extremely Efficient Flexible Organic Light-Emitting Diodes with Modified Graphene Anode", Nat. Photonics **6**, 105–110 (2012) (cited on page 111).

[160] G. Tan, S. Chen, C.-H. Siu, A. Langlois, Y. Qiu, H. Fan, C.-L. Ho, P. D. Harvey, Y. Hsing Lo, L. Liu, and W.-Y. Wong, "Platinum(II) Cyclometallates Featuring Broad Emission Bands and Their Applications in Color-Tunable OLEDs and High Color-Rendering WOLEDs", J. Mater. Chem. **4**, 6016–6026 (2016) (cited on page 111).

[161] K. Neyts, A. Real, M. Marescaux, S. Mladenovski, and J. Beeckman, "Conductor Grid Optimization for Luminance Loss Reduction in Organic Light Emitting Diodes", J. Appl. Phys. **103**, 093113 (2008) (cited on page 111).

[162] L. Kinner, S. Nau, K. Popovic, S. Sax, I. Burgués-Ceballos, F. Hermerschmidt, A. Lange, C. Boeffel, S. A. Choulis, and E. J. W. List-Kratochvil, "Inkjet-Printed Embedded Ag-PEDOT:PSS Electrodes with Improved Light out Coupling Effects for Highly Efficient ITO-Free Blue Polymer Light Emitting Diodes", Appl. Phys. Lett. **110**, 101107 (2017) (cited on page 111).

[163] J. Park, J. Lee, and Y.-Y. Noh, "Optical and Thermal Properties of Large-Area OLED Lightings with Metallic Grids", Org. Electron. **13**, 184–194 (2012) (cited on page 111).

[164] H. Tang, Y. Jiang, C. Tang, and H.-S. Kwok, "Grid Optimization of Large-Area OLED Lighting Panel Electrodes", J. Disp. Technol. **12**, 605–609 (2016) (cited on page 111).

[165] M. Slawinski, M. Weingarten, M. Heuken, A. Vescan, and H. Kalisch, "Investigation of Large-Area OLED Devices with Various Grid Geometries", Org. Electron. **14**, 2387–2391 (2013) (cited on page 111).

[166] R. Eckstein, G. Hernandez-Sosa, U. Lemmer, and N. Mechau, "Aerosol Jet Printed Top Grids for Organic Optoelectronic Devices", Org. Electron. **15**, 2135–2140 (2014) (cited on page 115).

[167] R. Eckstein, M. Alt, T. Rödlmeier, P. Scharfer, U. Lemmer, and G. Hernandez-Sosa, "Digitally Printed Dewetting Patterns for Self-Organized Microelectronics", Adv. Mater. **28**, 7708–7715 (2016) (cited on page 115).

[168] Society for Information Display, *Information Display Measurements Standard Version 1.03*, http://www.icdm-sid.org (2012) (cited on page 118).

[169] T. Gerloff and K. Diekmann, "Luminance Homogeneity of OLEDs", in *OLED100.Eu Newsletter – February 2010*, edited by S. Grabowski (OLED100.eu, 2010) (cited on page 118).

[170] L. Pessoa, E. Mingolla, and H. Neumann, "A Contrast- and Luminance-Driven Multiscale Network Model of Brightness Perception", Vision Res. **35**, 2201–2223 (1995) (cited on page 119).

[171] O. Penacchio, X. Otazu, and L. Dempere-Marco, "A Neurodynamical Model of Brightness Induction in V1", PLoS ONE **8**, e64086 (2013) (cited on page 119).

[172] X. Gao, X. Yan, X. Yao, L. Xu, K. Zhang, J. Zhang, B. Yang, and L. Jiang, "The Dry-Style Antifogging Properties of Mosquito Compound Eyes and Artificial Analogues Prepared by Soft Lithography", Adv. Mater. **19**, 2213–2217 (2007) (cited on page 123).

[173] S. A. Boden and D. M. Bagnall, "Optimization of Moth-Eye Antireflection Schemes for Silicon Solar Cells", Prog. Photovolt. Res. Appl. **18**, 195–203 (2010) (cited on page 123).

[174] L. Zhou, Q.-D. Ou, J.-D. Chen, S. Shen, J.-X. Tang, Y.-Q. Li, and S.-T. Lee, "Light Manipulation for Organic Optoelectronics Using Bio-Inspired Moth's Eye Nanostructures", Sci. Rep. **4**, 4040 (2014) (cited on pages 123, 129).

[175] X. Liu, Y. Da, and Y. Xuan, "Full-Spectrum Light Management by Pseudo-Disordered Moth-Eye Structures for Thin Film Solar Cells", Opt. Express **25**, A824–A839 (2017) (cited on page 123).

[176] A. Heinrichsdobler, M. Engelmayer, D. Riedel, C. J. Brabec, and T. Wehlus, "Inkjet-Printed Polymer-Based Scattering Layers for Enhanced Light Outcoupling from Top-Emitting Organic Light-Emitting Diodes", in Organic Light Emitting Materials and Devices XXI, Proc. SPIE Vol. 10362 (2017), 103622B (cited on page 126).

[177] M. F. Schumann, A. Abass, G. Gomard, S. Wiesendanger, U. Lemmer, M. Wegener, and C. Rockstuhl, "Single-Pass and Omniangle Light Extraction from Light-Emitting Diodes Using Transformation Optics", Opt. Lett. **40**, 5626 (2015) (cited on pages 127, 131, 132, 135, 138).

[178] T. Nishida, H. Saito, and N. Kobayashi, "Efficient and High-Power AlGaN-Based Ultraviolet Light-Emitting Diode Grown on Bulk GaN", Appl. Phys. Lett. **79**, 711–712 (2001) (cited on page 127).

[179] R. Meerheim, M. Furno, S. Hofmann, B. Lüssem, and K. Leo, "Quantification of Energy Loss Mechanisms in Organic Light-Emitting Diodes", Appl. Phys. Lett. **97**, 253305 (2010) (cited on page 128).

[180] M. Harada, H. Wakana, S. Nobuki, H. Sakuma, M. Kawasaki, and S. Aratani, "Characterization of Light Extraction Efficiency for WOLEDS with Light-out-Coupling Layer", J. Soc. Info. Display, 1–6 (2015) (cited on page 129).

[181] C. F. Madigan, M.-H. Lu, and J. C. Sturm, "Improvement of Output Coupling Efficiency of Organic Light-Emitting Diodes by Backside Substrate Modification", Appl. Phys. Lett. **76**, 1650–1652 (2000) (cited on page 129).

[182] S. Möller and S. R. Forrest, "Improved Light Out-Coupling in Organic Light Emitting Diodes Employing Ordered Microlens Arrays", J. Appl. Phys. **91**, 3324–3327 (2002) (cited on page 129).

[183] J. P. Yang, Q. Y. Bao, Z. Q. Xu, Y. Q. Li, J. X. Tang, and S. Shen, "Light Out-Coupling Enhancement of Organic Light-Emitting Devices with Microlens Array", Appl. Phys. Lett. **97**, 223303 (2010) (cited on page 129).

[184] J. J. Shiang and A. R. Duggal, "Application of Radiative Transport Theory to Light Extraction from Organic Light Emitting Diodes", J. Appl. Phys. **95**, 2880–2888 (2004) (cited on page 129).

[185] J. K. Kim, A. N. Noemaun, F. W. Mont, D. Meyaard, E. F. Schubert, D. J. Poxson, H. Kim, C. Sone, and Y. Park, "Elimination of Total Internal Reflection in GaInN Light-Emitting Diodes by Graded-Refractive-Index Micropillars", Appl. Phys. Lett. **93**, 221111 (2008) (cited on page 129).

[186] F. W. Mont, A. J. Fischer, A. N. Noemaun, D. J. Poxson, J. Cho, E. F. Schubert, M. H. Crawford, D. D. Koleske, and K. W. Fullmer, "Enhanced Light-Extraction from a GaN Waveguide Using Micro-Pillar TiO2-SiO2 Graded-Refractive-Index Layers", Phys. Status Solidi A **209**, 2277–2280 (2012) (cited on page 129).

[187] C. S. Choi, S.-M. Lee, M. S. Lim, K. C. Choi, D. Kim, D. Y. Jeon, Y. Yang, and O. O. Park, "Improved Light Extraction Efficiency in Organic Light Emitting Diodes with a Perforated WO 3 Hole Injection Layer Fabricated by Use of Colloidal Lithography", Opt. Express **20**, A309–A317 (2012) (cited on page 129).

[188] R. Wang, L.-H. Xu, Y.-Q. Li, L. Zhou, C. Li, Q.-D. Ou, J.-D. Chen, S. Shen, and J.-X. Tang, "Flexible Electronics: Broadband Light Out-Coupling Enhancement of Flexible Organic Light-Emitting Diodes Using Biomimetic Quasirandom Nanostructures", Adv. Opt. Mater. **3**, 139–139 (2015) (cited on page 129).

[189] J. Y. Kim, C. S. Choi, W. H. Kim, D. Y. Kim, D. H. Kim, and K. C. Choi, "Extracting Optical Modes of Organic Light-Emitting Diodes Using Quasi-Periodic WO_3 Nanoislands", Opt. Express **21**, 5424–5431 (2013) (cited on page 129).

[190] W.-Y. Park, Y. Kwon, C. Lee, and K.-W. Whang, "Light Outcoupling Enhancement from Top-Emitting Organic Light-Emitting Diodes Made on a Nano-Sized Stochastic Texture Surface", Opt. Express **22**, A1687 (2014) (cited on page 129).

[191] C.-H. Shin, E. Y. Shin, M.-H. Kim, J.-H. Lee, and Y. Choi, "Nanoparticle Scattering Layer for Improving Light Extraction Efficiency of Organic Light Emitting Diodes", Opt. Express **23**, A133–A139 (2015) (cited on page 129).

[192] I. Schnitzer, E. Yablonovitch, C. Caneau, T. J. Gmitter, and A. Scherer, "30% External Quantum Efficiency from Surface Textured, Thin-Film Light-Emitting Diodes", Appl. Phys. Lett. **63**, 2174 (1993) (cited on page 129).

[193] M. Rahm, D. Schurig, D. A. Roberts, S. A. Cummer, D. R. Smith, and J. B. Pendry, "Design of Electromagnetic Cloaks and Concentrators Using Form-Invariant Coordinate Transformations of Maxwell's Equations", Photonics Nanostruct. **6**, 87–95 (2008) (cited on page 130).

[194] M. W. Rowell and M. D. McGehee, "Transparent Electrode Requirements for Thin Film Solar Cell Modules", Energy Environ. Sci. **4**, 131–134 (2010) (cited on page 145).

[195] J. Fischer and M. Wegener, "Three-Dimensional Direct Laser Writing Inspired by Stimulated-Emission-Depletion Microscopy", Opt. Mater. Express **1**, 614–624 (2011) (cited on page 147).

[196] N. I. Landy, N. Kundtz, and D. R. Smith, "Designing Three-Dimensional Transformation Optical Media Using Quasiconformal Coordinate Transformations", Phys. Rev. Lett. **105**, 193902 (2010) (cited on page 147).

Acknowledgments

It is my pleasure to thank many people that have contributed to the success of my work that eventually allowed me to write this thesis.

First of all, I would like to thank my supervisor, Prof. Dr. Martin Wegener, for giving me the opportunity to work in his group on this exciting topic. His continuous scientific support of my work was invaluable. I also enjoyed very much the chance to present my work at several international conferences.

I also thank Prof. Dr. Carsten Rockstuhl, who agreed to serve as the second reviewer of the thesis and was part of the collaborations about GRIN cloaks and light extractors.

Thanks go to all collaborators I had the pleasure to work with in the last four years. Special gratitude deserve Dr. Samuel Wiesendanger, who preceded me in the project about cloaking of contact fingers on solar cells, Dr. Kaining Ding, who fabricated the prototype cells, Dr. Ulrich Paetzold, who gave me the opportunity to use the equipment of his group for solar cell characterization, and Malte Langenhorst, who supported me taking the measurements and who continues my work by developing further free-form surface cloaking.

It was an equally great pleasure to work with Dr. Aimi Abass and Dr. Guillaume Gomard on the light-extraction project. I also very much enjoyed investigating metal grid cloaking on light emitters together with Dr. Guillaume Gomard and Benjamin Fritz, who tortured his computer with many simulations for the project.

I want to thank all researchers involved in projects that have not been covered in this thesis. Explicit thanks go to Sujoy Paul and Prof. Dr. Arkadi Chipouline, with whom I successfully applied DLW-fabricated phase masks to integrated tunable filters and who promoted the project at several scientific conferences. I have enjoyed working with Zheqin Dong, Kevin Edelmann, and Dr. Lukas Gerhard on two projects that are still ongoing. Thank you!

I want to express my gratitude to all my current and former colleagues in the Wegener group, for the extraordinary team spirit and mutual support, for countless coffee breaks filled with informative or entertaining discussions, and for spending time together on leisure activities.

Special thanks go to Dr. Aimi Abass, Vincent Hahn, Christian Kern, Malte Langenhorst, Frederik Mayer, Patrick Müller, and Andreas Wickberg for proofreading the thesis and providing their valuable feedback.

Great gratitude deserve the staff supporting the scientific work: the secretaries Ursula Mösle, Claudia Alaya, and Monica Brenkmann helped to keep our amount of paperwork minimal. Our technician Johann Westhauser was always helpful in placing orders and designing essential mechanical parts for the experimental setups that were made in the mechanical workshop with incredible accuracy. The staff of the electronics workshop, Michael Hippe, Helmut Lay, and Werner Gilde, helped making custom electronic components for the measurement setups and always ensured a perfect IT environment. Thanks to all of them!

Finally, I would like to thank my parents who always supported me and gave me the freedom to study the subject that I liked. Most of all, it is my pleasure to thank my lovely wife Anne, who has always been there for me when I needed her. I feel blessed to have her.